

DTIC FILE COPY

SA/TR-3/89

②

A003 : FINAL REPORT

**COMPUTER ALGORITHMS AND ARCHITECTURES
FOR THREE-DIMENSIONAL
EDDY-CURRENT NONDESTRUCTIVE EVALUATION**

Contract No. N 00019-86-C-0219

with

**Sabbagh Associates, Inc.
4639 Morningside Drive
Bloomington, IN 47401**

for

Naval Air Systems Command

20 January, 1989

Volume II

CHAPTERS I-V

**DTIC
ELECTE
4 APR 1989
S D
Q E**

\int_A

This document has been approved
for public release and sale in
distribution is unlimited.

AD-A206 628

89 4 04 083

SECURITY CLASSIFICATION OF THIS PAGE

[illegible]

18. Digital signal processing, image processing, classification

(A)

19. ABSTRACT

In this report, we develop an electromagnetic model for three-dimensional inversion of eddy-current data, an inversion algorithm based on the conjugate gradient technique, and a special purpose computer that we estimate can execute this algorithm in times comparable to high speed main-frames. This computer has a pipeline architecture and is designed around our parallel implementation of the inversion algorithm and makes use of high-speed DSP chips. The inversion process achieves a higher performance measure when more than one data set is inverted. The sequential order of the inversion scheme restricts the number of active elements in the pipe for a single problem. When more than one inversion problem enters the pipe, then more than one element could be active to improve the overall performance of the system.

The basic electromagnetic model starts with the integral equations for electromagnetic scattering, which are then discretized by means of the method of moments. This gives us the fundamental inversion model, which is then solved using the conjugate gradient algorithm. In order to accomplish the three-dimensional inversion, we acquire data at a number of frequencies; therefore, our inversion process is called a multifrequency method. The choice of frequencies, and the number of frequencies to be used, depend upon the conductivity of the host material, and the depth resolution sought.

The method of conjugate gradients has a number of attractive features for our purposes. Chief among them is that it allows a large problem to be solved efficiently, and, because it is an iterative algorithm, it allows us to take advantage of the special Toeplitz structure of the discretized model. We also derive an algorithm that allows us to constrain the solution, use preconditioning and a Levenberg-Marquardt parameter. Preconditioning is often useful in improving the convergence of the conjugate gradient algorithm, and the Levenberg-Marquardt parameter is needed to stabilize the solution against the effects of noise and modeling inaccuracies.

The inversion algorithms may require *a priori* information about the flaw regions. The information can be used to concentrate the inversion efforts on regions of interest rather than unflawed regions. Statistical pattern recognition and computer vision techniques have been examined to achieve this goal. The purpose of applying statistical pattern recognition techniques, is to detect the flaw regions and the background regions in the spatial domain. In addition, a graphical tool can be used to analyze the raw data when used as input features, and evaluate the classifiability of the measurement (any two features).



Accession For	
NTIS GRA&I	<input checked="" type="checkbox"/>
DTIC TAB	<input type="checkbox"/>
Unannounced	<input type="checkbox"/>
Justification	
By	
Distribution/	
Availability Codes	
Dist	Avail and/or Special
A-1	

CHAPTER I

DEVELOPMENT OF THE MODEL

1. Introduction

In this chapter we describe mathematical models that were developed to be the basis for our inversion algorithms. These models make use of a bulk conductivity model of an anisotropic material. The bulk conductivity approach and the associated Green's functions for a flat plate are described in Sabbagh Associates' report SA/TR-3/88. Here we develop direct and inverse models based on a whip source probe and a ring source probe. In laboratory tests these probes have been used successfully to detect flaws and so we develop these models to allow for the reconstruction of three-dimensional flaws.

2. Whip Source Direct Model

(a) Computation of the Incident Fields Due to a Whip Source

The infinitely long 'whip' is oriented parallel to the y -axis, with x -coordinate equal to x_0 and z -coordinate equal to z_0 . Hence, we have for the current density

$$\mathbf{J}_0(x, y, z) = I_0 \delta(x - x_0) \delta(z - z_0) \mathbf{a}_y, \quad -\infty < y < \infty. \quad (1)$$

The Fourier transform of \mathbf{J} is given by

$$\begin{aligned} \tilde{\mathbf{J}}_0(k_x, k_y, z) &= \mathbf{a}_y \delta(z - z_0) \frac{I_0}{4\pi^2} \int \int_{-\infty}^{\infty} \delta(x - x_0) e^{j(k_x x + k_y y)} dx dy \\ &= \mathbf{a}_y \frac{I_0}{2\pi} e^{jk_x x_0} \delta(k_y) \delta(z - z_0). \end{aligned} \quad (2)$$

We have, from (15) of NSWC TR 85-304:

$$\begin{aligned} \tilde{\mathbf{e}}_i(z) &= \int \tilde{\mathbf{G}}_{21}(z|z') \cdot \tilde{\mathbf{J}}_0(z') dz' \\ &= \mathbf{a}_y \frac{I_0}{2\pi} e^{jk_x x_0} \delta(k_y) \tilde{\mathbf{G}}_{21}(z|z_0), \end{aligned} \quad (3)$$

where the tilde denotes a function of (k_x, k_y) , and $\tilde{\mathbf{G}}_{21}(z|z_0)$ is the external Green's function. From here on we suppress the subscripts on the Green's function and replace them with the superscript, '(e)'.

Hence, the electric field at level z , within the slab, is given by

$$\begin{aligned} \tilde{E}_{0x}(z, z_0) &= \frac{I_0}{2\pi} e^{jk_x x_0} \delta(k_y) \tilde{G}_{12}^{(e)}(z|z_0) \\ \tilde{E}_{0y}(z, z_0) &= \frac{I_0}{2\pi} e^{jk_x x_0} \delta(k_y) \tilde{G}_{22}^{(e)}(z|z_0), \end{aligned} \quad (4)$$

where the subscripts refer to a 4×3 tensor (because there are four transverse field components in \tilde{e}_i , and the applied current can point in three directions.)

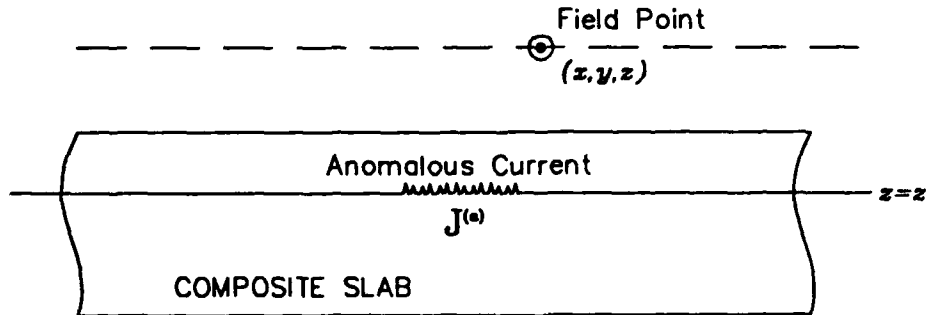
Upon taking the inverse Fourier transform of (4), we get

$$\begin{aligned} E_{0z}(x, y, z) &= \frac{I_0}{2\pi} \int_{-\infty}^{\infty} \tilde{G}_{12}^{(e)}(k_x, 0; z, z_0) e^{-jk_z(z-z_0)} dk_x \\ &= F_{0z}(x_0 - x, 0; z, z_0) \\ E_{0y}(x, y, z) &= \frac{I_0}{2\pi} \int_{-\infty}^{\infty} \tilde{G}_{22}^{(e)}(k_x, 0; z, z_0) e^{-jk_z(z-z_0)} dk_x \\ &= F_{0y}(x_0 - x, 0; z, z_0). \end{aligned} \quad (5)$$

These are the functions that are to be used in the next section.

(b) Computation of the Scattered Fields Due to the Whip Source

We will analyze the problem shown in the figure:



We have, from (15) of NSWC TR 85-304:

$$\tilde{e}_i(z) = \int \tilde{G}_{12}(z|z') \cdot \tilde{J}^{(a)}(z') dz', \quad (6)$$

where the tilde denotes a function of (k_x, k_y) ; i.e., (6) is in the Fourier domain. $\tilde{G}_{12}(z|z')$ is the "internal Green's function".

We assume that the only significant currents lie in the transverse plane; i.e., $\tilde{J}^{(a)}(z') = J_z^{(a)} a_z(z') + J_y^{(a)} a_y(z')$. From here on we suppress the subscripts, 12, on the Green's

function and understand that this is the internal Green's function. We also suppress, for the moment, the independent variable, z' , and understand that $\tilde{J}^{(a)}$ refers to the anomalous current at some depth z' . Hence, the electric fields at the sensor level z due to the anomalous current at level z' are

$$\begin{aligned}\tilde{E}_x &= \tilde{G}_{11} \tilde{J}_x^{(a)} + \tilde{G}_{12} \tilde{J}_y^{(a)} \\ \tilde{E}_y &= \tilde{G}_{21} \tilde{J}_x^{(a)} + \tilde{G}_{22} \tilde{J}_y^{(a)},\end{aligned}\quad (7)$$

where the subscripts refer to a 4×3 tensor (because there are four transverse field components in $\tilde{\mathbf{E}}$, and the anomalous current can point in three directions).

We are really interested in \tilde{B}_z at the sensor. According to (10)(b) of NSWC TR 85-304, we have

$$\tilde{B}_z = \mu_0 \tilde{H}_z = -\frac{k_y}{\omega} \tilde{E}_x + \frac{k_x}{\omega} \tilde{E}_y, \quad (8)$$

which, according to (7), implies that

$$\begin{aligned}\tilde{B}_z &= -\frac{k_y}{\omega} [\tilde{G}_{11} \tilde{J}_x^{(a)} + \tilde{G}_{12} \tilde{J}_y^{(a)}] + \frac{k_x}{\omega} [\tilde{G}_{21} \tilde{J}_x^{(a)} + \tilde{G}_{22} \tilde{J}_y^{(a)}] \\ &= \left(\frac{-k_y \tilde{G}_{11} + k_x \tilde{G}_{21}}{\omega} \right) \tilde{J}_x^{(a)} + \left(\frac{-k_y \tilde{G}_{12} + k_x \tilde{G}_{22}}{\omega} \right) \tilde{J}_y^{(a)}.\end{aligned}\quad (9)(a)$$

For completeness we write the other two components of \mathbf{B} :

$$\begin{aligned}\tilde{B}_x &= \mu_0 \tilde{G}_{31} \tilde{J}_x^{(a)} + \mu_0 \tilde{G}_{32} \tilde{J}_y^{(a)} \\ \tilde{B}_y &= \mu_0 \tilde{G}_{41} \tilde{J}_x^{(a)} + \mu_0 \tilde{G}_{42} \tilde{J}_y^{(a)}.\end{aligned}\quad (9)(b)$$

Let's call

$$\begin{aligned}\tilde{H}_{xx} &= \mu_0 \tilde{G}_{31}, & \tilde{H}_{xy} &= \mu_0 \tilde{G}_{32} \\ \tilde{H}_{yx} &= \mu_0 \tilde{G}_{41}, & \tilde{H}_{yy} &= \mu_0 \tilde{G}_{42} \\ \tilde{H}_{zx} &= (-k_y \tilde{G}_{11} + k_x \tilde{G}_{21})/\omega, & \tilde{H}_{zy} &= (-k_y \tilde{G}_{12} + k_x \tilde{G}_{22})/\omega.\end{aligned}\quad (10)$$

Then, from (9)(a):

$$\begin{aligned}B_z(x, y, z) &= \iint_{-\infty}^{\infty} \tilde{H}_{zx}(k_x, k_y; z, z') \tilde{J}_x^{(a)}(k_x, k_y) e^{-j(k_x x + k_y y)} dk_x dk_y \\ &\quad + \iint_{-\infty}^{\infty} \tilde{H}_{zy}(k_x, k_y; z, z') \tilde{J}_y^{(a)}(k_x, k_y) e^{-j(k_x x + k_y y)} dk_x dk_y,\end{aligned}\quad (11)$$

or, in convolution form:

$$\begin{aligned}B_z(x, y, z) &= \frac{1}{4\pi^2} \iint_{-\infty}^{\infty} H_{zx}(x - \xi, y - \eta; z, z') J_x^{(a)}(\xi, \eta) d\xi d\eta \\ &\quad + \frac{1}{4\pi^2} \iint_{-\infty}^{\infty} H_{zy}(x - \xi, y - \eta; z, z') J_y^{(a)}(\xi, \eta) d\xi d\eta.\end{aligned}\quad (12)$$

In order to compute emf's, we integrate B_z over the appropriate sensing coil. This computation should be done in (11), because it is very easy to integrate the exponential in (x, y) . The result is to introduce new \tilde{H} functions for the emf's, and these functions can then be transformed for use in the convolution integrals of (12), *et seq.* (The derivation of these \tilde{H} functions is described more fully in Appendix A of Chapter IV; see (A.33), *et seq.*)

Let the conductivity of the flawed region at level z' be the scalar function $\sigma^{(f)}(x, y, z')$ (for a void region $\sigma^{(f)} = 0$). We are assuming, therefore, that the flaws are isotropic. The incident field at z' is $E_0(x, y, z') = E_{0x}(x, y, z')\mathbf{a}_x + E_{0y}(x, y, z')\mathbf{a}_y$. If the source of the incident field is an infinitely long 'whip' oriented parallel to the y -axis, with x coordinate equal to q , then it is straightforward to show that $E_{0x}(x, y, z') = F_{0x}(q - x, 0, z')$, $E_{0y}(x, y, z') = F_{0y}(q - x, 0, z')$, where F_{0x} and F_{0y} are given in (5). The zero in the second argument of the F 's implies that the incident field is independent of y , as we know.

The anomalous conductivity tensor is the difference between the flaw conductivity tensor and the host conductivity tensor:

$$\bar{\sigma}^{(a)} = \begin{bmatrix} \sigma^{(f)} & 0 & 0 \\ 0 & \sigma^{(f)} & 0 \\ 0 & 0 & \sigma^{(f)} \end{bmatrix} - \begin{bmatrix} \sigma_{11} & \sigma_{12} & 0 \\ \sigma_{12} & \sigma_{22} & 0 \\ 0 & 0 & \sigma_{33} \end{bmatrix}.$$

Hence,

$$\begin{aligned} J_x^{(a)}(x, y) &= \sigma_{11}^{(a)}(x, y)F_{0x}(q - x, 0, z') + \sigma_{12}^{(a)}(x, y)F_{0y}(q - x, 0, z') \\ J_y^{(a)}(x, y) &= \sigma_{12}^{(a)}(x, y)F_{0x}(q - x, 0, z') + \sigma_{22}^{(a)}(x, y)F_{0y}(q - x, 0, z'), \end{aligned} \quad (13)$$

and we note that $\sigma_{12}^{(a)} = \sigma_{12}$, which is known. Of course, if we work in the principal-axis system, then $\sigma_{12} = 0$.

When this is substituted into (12) we get

$$\begin{aligned} B_z(x, y, z) &= \frac{1}{4\pi^2} \iint_{-\infty}^{\infty} H_{zx}(x - \xi, y - \eta; z, z') F_{0x}(q - \xi, 0, z') \sigma_{11}^{(a)}(\xi, \eta) d\xi d\eta \\ &+ \frac{1}{4\pi^2} \iint_{-\infty}^{\infty} H_{zy}(x - \xi, y - \eta; z, z') F_{0y}(q - \xi, 0, z') \sigma_{22}^{(a)}(\xi, \eta) d\xi d\eta \\ &+ \frac{1}{4\pi^2} \iint_{-\infty}^{\infty} [H_{zx}(x - \xi, y - \eta; z, z') F_{0y}(q - \xi, 0, z') \\ &\quad + H_{zy}(x - \xi, y - \eta; z, z') F_{0x}(q - \xi, 0, z')] \sigma_{12}^{(a)}(\xi, \eta) d\xi d\eta. \end{aligned} \quad (14)$$

Because we sense the field at the same location as the whip, $x = q$, we can replace q

by x in (14) and get

$$\begin{aligned}
 B_z(x, y, z) = & \frac{1}{4\pi^2} \iint_{-\infty}^{\infty} T_{11}(x - \xi, y - \eta; z, z') \sigma_{11}^{(a)}(\xi, \eta) d\xi d\eta \\
 & + \frac{1}{4\pi^2} \iint_{-\infty}^{\infty} T_{22}(x - \xi, y - \eta; z, z') \sigma_{22}^{(a)}(\xi, \eta) d\xi d\eta \\
 & + \frac{1}{4\pi^2} \iint_{-\infty}^{\infty} T_{12}(x - \xi, y - \eta; z, z') \sigma_{12}^{(a)}(\xi, \eta) d\xi d\eta,
 \end{aligned} \tag{15}$$

where

$$\begin{aligned}
 T_{11}(x - \xi, y - \eta; z, z') &= H_{zx}(x - \xi, y - \eta; z, z') F_{0x}(x - \xi, 0, z') \\
 T_{22}(x - \xi, y - \eta; z, z') &= H_{zy}(x - \xi, y - \eta; z, z') F_{0y}(x - \xi, 0, z') \\
 T_{12}(x - \xi, y - \eta; z, z') &= H_{zx}(x - \xi, y - \eta; z, z') F_{0y}(x - \xi, 0, z') \\
 &\quad + H_{zy}(x - \xi, y - \eta; z, z') F_{0x}(x - \xi, 0, z').
 \end{aligned} \tag{16}$$

The last integral in (15) is known, because $\sigma_{12}^{(a)} = \sigma_{12}$. Indeed, if we are operating in the principal-axis system of the host conductivity tensor, then $\sigma_{12} = 0$.

For three-dimensional flaws, we need only perform a spatial integration of (15) with respect to z' . We consider the slab to be partitioned into N_z discrete 'layers' and consider $\bar{\sigma}^{(a)}$ to be constant with respect to z' for each layer. The transfer function $T_{11}^{(n)}$, for example, for a layer bounded by $z_n^{(-)}$ and $z_n^{(+)}$ is

$$T_{11}^{(n)}(x - \xi, y - \eta; z, z_n) = \int_{z_n^{(-)}}^{z_n^{(+)}} H_{zx}(x - \xi, y - \eta; z, z') F_{0x}(x - \xi, 0; z, z') dz' \tag{17}$$

The total field due to flaws in a slab, then, is the sum of the fields due to flaws in each of the 'layers'. This will be fully explained in Section 4.

Equation (15) is the same equation that we derived for reconstructing $\bar{\sigma}^{(a)}$ using an infinite current sheet for excitation. The only difference is that for the whip the transfer functions T_{11} , T_{22} , and T_{12} consist of the product of two arrays, rather than the product of one array (H_{zx} , or H_{zy}) and a scalar (E_{0x} , or E_{0y}), as was the case with a current sheet excitation. Clearly, if the excitation source is bounded in the y -direction, then the transfer function is the product of two two-dimensional arrays. Hence, it appears that we can apply all of the inversion algorithms that were developed for excitation with infinite current sheets, but that there must be a little more pre-processing to generate the appropriate transfer functions.

3. Ring Source Direct Model

(a) Computation of the Incident Fields Due to a Ring Source

The source is a single filament ring parallel to the slab workpiece. The ring has radius r_0 and is centered at (x_0, y_0, z_0) . The current density is

$$\mathbf{J}_0(x, y, z) = I_0 \delta(z - z_0) (-a_x \sin \theta + a_y \cos \theta) \delta(r - r_0) \quad (18)$$

The transform of \mathbf{J} is given by

$$\tilde{\mathbf{J}}_0(k_x, k_y, z) = \delta(z - z_0) \frac{I_0}{4\pi^2} \int \int_{-\infty}^{\infty} (-a_x \sin \theta + a_y \cos \theta) \delta(r - r_0) e^{j(k_x x + k_y y)} dx dy \quad (19)$$

From Appendix C of NSWC TR 85-304, this transform is

$$\tilde{\mathbf{J}}_0(k_x, k_y, z) = \frac{j I_0 r_0 \delta(z - z_0)}{2\pi} J_1(k_r r_0) \left(-a_x \frac{k_y}{k_r} + a_y \frac{k_x}{k_r} \right) \quad (20)$$

where $k_r = \sqrt{k_x^2 + k_y^2}$.

From (15) of NSWC TR 85-304, the fields due to this current ring are

$$\begin{aligned} \tilde{\mathbf{e}}_i(z) &= \int \tilde{\mathbf{G}}^{(e)}(z|z_0) \cdot \tilde{\mathbf{J}}_0(z_0) dz_0 \\ &= \tilde{\mathbf{G}}^{(e)}(z|z_0) \cdot \frac{j I_0 r_0 \delta(z - z_0)}{2\pi} J_1(k_r r_0) \left(-a_x \frac{k_y}{k_r} + a_y \frac{k_x}{k_r} \right) \end{aligned} \quad (21)$$

where the tilde denotes a function of (k_x, k_y) and $\tilde{\mathbf{G}}^{(e)}(z|z_0)$ is the external Green's function which is a 4×3 tensor (because there are four transverse field components in $\tilde{\mathbf{e}}_i$ and the applied current can point in three directions).

The electric field at level z within the slab, then, is

$$\begin{aligned} \tilde{E}_{0x}(z, z_0) &= \frac{j I_0 r_0 \delta(z - z_0)}{2\pi k_r} J_1(k_r r_0) \left[-k_y \tilde{G}_{11}^{(e)}(z|z_0) + k_x \tilde{G}_{12}^{(e)}(z|z_0) \right] \\ \tilde{E}_{0y}(z, z_0) &= \frac{j I_0 r_0 \delta(z - z_0)}{2\pi k_r} J_1(k_r r_0) \left[-k_y \tilde{G}_{21}^{(e)}(z|z_0) + k_x \tilde{G}_{22}^{(e)}(z|z_0) \right] \end{aligned} \quad (22)$$

Taking the inverse Fourier transform of (22) we obtain

$$\begin{aligned} E_{0x}(x, y, z) &= \frac{j I_0 r_0}{2\pi} \int \int_{-\infty}^{\infty} \frac{J_1(k_r r_0)}{k_r} \left[-k_y \tilde{G}_{11}^{(e)}(k_x, k_y) + k_x \tilde{G}_{12}^{(e)}(k_x, k_y) \right] e^{-j(k_x(x_0-x) + k_y(y_0-y))} dk_x dk_y \\ &= F_{0x}(x_0 - x, y_0 - y; z, z_0) \\ E_{0y}(x, y, z) &= \frac{j I_0 r_0}{2\pi} \int \int_{-\infty}^{\infty} \frac{J_1(k_r r_0)}{k_r} \left[-k_y \tilde{G}_{21}^{(e)}(k_x, k_y) + k_x \tilde{G}_{22}^{(e)}(k_x, k_y) \right] e^{-j(k_x(x_0-x) + k_y(y_0-y))} dk_x dk_y \\ &= F_{0y}(x_0 - x, y_0 - y; z, z_0) \end{aligned} \quad (23)$$

(b) Computation of the Scattered Fields Due to the Ring Source

The computation of the scattered fields due to the ring source is identical to that of the whip source (Section 2(b)) through (12). For the ring source, though, the incident field is not independent of y . If the ring source has x coordinate q and y coordinate r , the incident electric fields are $E_{0x}(x, y, z') = F_{0x}(q - x, r - y, z')$ and $E_{0y}(x, y, z') = F_{0y}(q - x, r - y, z')$, where F_{0x} and F_{0y} are given in (23). If we choose x and y to correspond to the principle directions of the host material, then $\sigma_{12} = \sigma_{21} = 0$ and the anomalous currents are

$$\begin{aligned} J_x^{(a)}(x, y) &= \sigma_{11}^{(a)} F_{0x}(q - x, r - y, z') \\ J_y^{(a)}(x, y) &= \sigma_{22}^{(a)} F_{0y}(q - x, r - y, z') \end{aligned} \quad (24)$$

When equations (24) are substituted into (12), we obtain

$$\begin{aligned} B_z(x, y, z) &= \\ &\frac{1}{4\pi^2} \int \int_{-\infty}^{\infty} H_{zx}(x - \xi, y - \eta; z, z') F_{0x}(q - \xi, r - \eta, z') \sigma_{11}^{(a)}(\xi, \eta) d\xi d\eta \\ &+ \frac{1}{4\pi^2} \int \int_{-\infty}^{\infty} H_{yz}(x - \xi, y - \eta; z, z') F_{0y}(q - \xi, r - \eta, z') \sigma_{22}^{(a)}(\xi, \eta) d\xi d\eta \end{aligned} \quad (25)$$

The sensor is a single filament loop. If the source ring remains stationary while the sensor loop is moved around, then the electric fields do not change as the sensor loop is moved. In this case, F_{0x} is a function of ξ and η only and (25) becomes

$$\begin{aligned} B_z(x, y, z) &= \frac{1}{4\pi^2} \int \int_{-\infty}^{\infty} H_{zx}(x - \xi, y - \eta) F_{0x}(\xi, \eta) \sigma_{11}^{(a)}(\xi, \eta) d\xi d\eta \\ &+ \frac{1}{4\pi^2} \int \int_{-\infty}^{\infty} H_{yz}(x - \xi, y - \eta) F_{0y}(\xi, \eta) \sigma_{22}^{(a)}(\xi, \eta) d\xi d\eta \end{aligned} \quad (26)$$

So, B_z is computed by

$$\tilde{B}_z = \tilde{H}_{zx} \tilde{\Pi}_x + \tilde{H}_{yz} \tilde{\Pi}_y \quad (27)$$

where

$$\begin{aligned} \Pi_x(x, y) &= F_{0x}(x, y) \sigma_{11}^{(a)}(x, y) \\ \Pi_y(x, y) &= F_{0y}(x, y) \sigma_{22}^{(a)}(x, y) \end{aligned}$$

On the other hand, if the source ring and the sensor loop always move together (and are concentric), then $q = x$ and $r = y$. In this case, (25) becomes

$$\begin{aligned} B_z(x, y, z) &= \frac{1}{4\pi^2} \int \int_{-\infty}^{\infty} H_{zx}(x - \xi, y - \eta) F_{0x}(x - \xi, y - \eta) \sigma_{11}^{(a)}(\xi, \eta) d\xi d\eta \\ &+ \frac{1}{4\pi^2} \int \int_{-\infty}^{\infty} H_{yz}(x - \xi, y - \eta) F_{0y}(x - \xi, y - \eta) \sigma_{22}^{(a)}(\xi, \eta) d\xi d\eta \end{aligned} \quad (28)$$

and B_z is computed by

$$\tilde{B}_z = \tilde{T}_{11}\tilde{\sigma}_{11}^{(a)} + \tilde{T}_{22}\tilde{\sigma}_{22}^{(a)} \quad (29)$$

where

$$T_{11}(x, y) = H_{zz}(x, y)F_{0z}(x, y)$$

$$T_{22}(x, y) = H_{zy}(x, y)F_{0y}(x, y)$$

Finally, if the source ring and the sensor loop move together but are not concentric, then the offset must be considered in (25). If the offset in the x direction is a and the offset in the y direction is b , then equation (25) becomes

$$\begin{aligned} B_z(x, y, z) = & \frac{1}{4\pi^2} \int \int_{-\infty}^{\infty} H_{zz}(x - \xi, y - \eta; z, z') F_{0z}(x - \xi - a, y - \eta - b, z') \sigma_{11}^{(a)}(\xi, \eta) d\xi d\eta \\ & + \frac{1}{4\pi^2} \int \int_{-\infty}^{\infty} H_{zy}(x - \xi, y - \eta; z, z') F_{0y}(x - \xi - a, y - \eta - b, z') \sigma_{22}^{(a)}(\xi, \eta) d\xi d\eta \quad (30) \end{aligned}$$

and B_z is computed by

$$\tilde{B}_z = \tilde{T}_{11}\tilde{\sigma}_{11}^{(a)} + \tilde{T}_{22}\tilde{\sigma}_{22}^{(a)} \quad (31)$$

where

$$T_{11}(x, y) = H_{zz}(x, y)F_{0z}^{(off)}(x, y)$$

$$T_{22}(x, y) = H_{zy}(x, y)F_{0y}^{(off)}(x, y)$$

and

$$\tilde{F}_{0z}^{(off)}(x, y) = e^{j(k_x a + k_y b)} \tilde{F}_{0z}(x, y)$$

$$\tilde{F}_{0y}^{(off)}(x, y) = e^{j(k_x a + k_y b)} \tilde{F}_{0y}(x, y)$$

For three dimensional flaws, the transfer functions must be integrated with respect to z' .

4. Whip Source Inverse Model

(a) The Discretized Integral Equation

We assume that we are operating in the principal-axis system, so that the last integral in (15) vanishes. If the whip is oriented along the y -axis, then we know from theoretical considerations that the electric field, $F_{0z}(x - \xi, 0, z')$, vanishes. Thus, (15) reduces to an integral equation for a single unknown, the anomalous conductivity, $\sigma_{22}^{(a)}(\xi, \eta, z')$ at layer z' :

$$B_z(x, y, z) = \frac{1}{4\pi^2} \iint_{-\infty}^{\infty} T_{22}(x - \xi, y - \eta; z, z') \sigma_{22}^{(a)}(\xi, \eta, z') d\xi d\eta. \quad (32)$$

This is the contribution of the layer that is located at z' . The net contribution of all layers is given by the integral of (32) over the flawed region:

$$\begin{aligned} B(x, y) &= \int_{\text{flaw}} \left\{ \frac{1}{4\pi^2} \iint_{-\infty}^{\infty} T(x - \xi, y - \eta, z') \sigma^{(a)}(\xi, \eta, z') d\xi d\eta \right\} dz' \\ &= \int_{\text{flaw}} \left\{ \iint_{-\infty}^{\infty} \tilde{T}(k_x, k_y, z') \tilde{\sigma}^{(a)}(k_x, k_y, z') e^{-j(k_x x + k_y y)} dk_x dk_y \right\} dz'. \end{aligned} \quad (33)$$

From here on we will suppress the sensor z -coordinate, because it is fixed; we also suppress the subscripts on T and $\sigma^{(a)}$.

Next, expand the unknown conductivity in a series of pulse functions (defined on a regular grid of spacing $(\delta x, \delta y, \delta z)$):

$$\sigma^{(a)}(x, y, z) = \sum_{l=0}^{N_x} \sum_{m=0}^{N_y} \sum_{n=0}^{N_z} \sigma_{lmn} P_l(x/\delta x) P_m(y/\delta y) P_n(z/\delta z), \quad (34)$$

where the $\{\sigma_{lmn}\}$ are real-valued, positive constants. Any other functions that are defined over this grid, such as the sinc functions, could work as well; the pulse functions, however, and functions derived from them by convolution, are particularly nice.

The Fourier transform of (34) is

$$\begin{aligned} \tilde{\sigma}(k_x, k_y, z) &= \frac{\delta x \delta y}{4\pi^2} \sum_{l=0}^{N_x} \sum_{m=0}^{N_y} \sum_{n=0}^{N_z} \sigma_{lmn} e^{jk_x(l+1/2)\delta x} e^{jk_y(m+1/2)\delta y} \\ &\quad \left(\frac{\sin(k_x \delta x/2)}{k_x \delta x/2} \right) \left(\frac{\sin(k_y \delta y/2)}{k_y \delta y/2} \right) P_n(z/\delta z), \end{aligned} \quad (35)$$

and when this is substituted into (33) we get

$$\begin{aligned} B(x, y) &= \frac{\delta x \delta y}{4\pi^2} \sum_{l=0}^{N_x} \sum_{m=0}^{N_y} \sum_{n=0}^{N_z} \sigma_{lmn} \iint_{-\infty}^{\infty} \tilde{T}^{(n)}(k_x, k_y) \left(\frac{\sin(k_x \delta x/2)}{k_x \delta x/2} \right) \left(\frac{\sin(k_y \delta y/2)}{k_y \delta y/2} \right) \\ &\quad e^{-j[k_x(x-(l+1/2)\delta x) + k_y(y-(m+1/2)\delta y)]} dk_x dk_y. \end{aligned} \quad (36)$$

$\tilde{T}^{(n)}(k_x, k_y, \omega)$ is the Fourier transform of

$$T_{22}^{(n)}(x - \xi, y - \eta; \omega) = \int_{z_n^{(-)}}^{z_n^{(+)}} H_{zy}(x - \xi, y - \eta; \omega, z') F_{0y}(x - \xi, 0; \omega, z') dz', \quad (37)$$

which was derived in (17). We are explicitly showing the dependence of the transfer function on frequency, in anticipation of the multifrequency model for inversion.

We take moments of (36) by multiplying by "testing functions", and then integrating. For testing functions we will use the same pulse functions, $P_L(x/\delta x)$, $P_M(y/\delta y)$, that were used in the expansion of the unknown (thus, this is Galerkin's variant of the method of moments). The integration on the right-hand side introduces another Fourier transform, so that the result is

$$\begin{aligned} B_{LM} &= \iint P_L(x/\delta x) P_M(y/\delta y) B(x, y) dx dy \\ &= \frac{(\delta x \delta y)^2}{4\pi^2} \sum_{l=0}^{N_x} \sum_{m=0}^{N_y} \sum_{n=0}^{N_z} \sigma_{lmn} \iint_{-\infty}^{\infty} \tilde{T}^{(n)}(k_x, k_y) \left(\frac{\sin(k_x \delta x/2)}{k_x \delta x/2} \right)^2 \left(\frac{\sin(k_y \delta y/2)}{k_y \delta y/2} \right)^2 \\ &\quad e^{-j[k_x \delta x(L-l) + k_y \delta y(M-m)]} dk_x dk_y. \end{aligned} \quad (38)$$

This equation can be written as the sum of Toeplitz operations

$$B_{LM} = \sum_{n=0}^{N_z} \sum_{l=0}^{N_x} \sum_{m=0}^{N_y} T^{(n)}(L-l, M-m) \sigma_{lmn}, \quad (39)$$

where the two-dimensional Toeplitz matrix, $T^{(n)}$, is given by the integral in (38). This is the discrete version of the integral equation, (33), and is the basis of our inversion method.

(b) The Multifrequency Model

Equation (39) consists of $(N_x + 1) \times (N_y + 1)$ equations in $(N_x + 1) \times (N_y + 1) \times (N_z + 1)$ unknowns. Hence, we need more equations. The easiest way to generate these equations is to repeat (39) at a number of different frequencies. This is easy to do in the lab (where we must measure B at these frequencies), and on the computer (where we generate a new transfer function, T , at the same frequencies). This approach is plausible because the anomalous conductivity is assumed to be independent of frequency. Thus, assuming that we use N_f frequencies, we have

$$\begin{aligned} B_1 &= T_{1,1} \otimes \sigma_1 + \cdots + T_{1,N_x} \otimes \sigma_{N_x} \\ &\vdots \\ B_{N_f} &= T_{N_f,1} \otimes \sigma_1 + \cdots + T_{N_f,N_x} \otimes \sigma_{N_x}. \end{aligned} \quad (40)$$

Each of the B 's in (40) is a $(N_x+1) \times (N_y+1)$ -dimensional data array, the subscript denoting the frequency at which the data is taken. The operator \otimes denotes the two-dimensional Toeplitz operation

$$T_{f,n} \otimes \sigma_n \equiv \sum_{l=0}^{N_x} \sum_{m=0}^{N_y} T^{(n)}(L-l, M-m; f) \sigma_{lmn}. \quad (41)$$

We write (40) in a block-matrix form, in which the real and imaginary parts are separated

$$\begin{bmatrix} B_1^{(R)} \\ \vdots \\ B_{N_f}^{(R)} \\ B_1^{(I)} \\ \vdots \\ B_{N_f}^{(I)} \end{bmatrix} = \begin{bmatrix} T_{1,1}^{(R)} & \cdots & T_{1,N_x}^{(R)} \\ \vdots & & \vdots \\ T_{N_f,1}^{(R)} & \cdots & T_{N_f,N_x}^{(R)} \\ T_{1,1}^{(I)} & \cdots & T_{1,N_x}^{(I)} \\ \vdots & & \vdots \\ T_{N_f,1}^{(I)} & \cdots & T_{N_f,N_x}^{(I)} \end{bmatrix} \odot \begin{bmatrix} \sigma_1 \\ \vdots \\ \sigma_{N_x} \end{bmatrix}. \quad (42)$$

Equations (40) or (42) are our basic system of discrete equations, and constitute the 'multifrequency model' for the whip source. These equations may contain several thousand unknowns, so we must use efficient methods of inverting them. In Chapter II we will apply the method of conjugate gradients, together with the Fast Fourier Transform (FFT), to accomplish this task.

The question arises as to the best number, N_f , of frequencies to use, and what is the optimum range of frequencies. Generally, this can be answered by trial-and-error, with the following ideas as a guide. Least-squares methods, such as the conjugate gradient algorithm, often work better with overdetermined systems, because the variance of the error is reduced as the number of equations increases, for a given number of unknowns. Hence, we would like N_f to generally be much larger than N_x . It is time consuming, however, to generate too much data, so there is a trade-off that can only be determined by conducting numerical experiments with typical problems.

The same can be said in determining the frequency range, but we know intuitively, if for no other reason, that we should use as broad a frequency range as possible. We can be a little bit more definite here, and rely upon the phenomenon of skin effect to guide us. If we want a resolution of δ_z in depth, then our upper limit of frequency should produce a skin depth that is smaller than δ_z , though, as we will see in Chapter III, we have gotten good results with simulated data at lower frequencies.

5. Ring Source Inverse Model

The inverse algorithm developed in the previous section for the whip probe is equally applicable for the ring probe. For the whip probe, we noted that if the grid was oriented parallel to the principle axes of the workpiece, $\sigma_{12}^{(a)} = 0$ and the third integral in (15) vanishes. Also, since the whip is also oriented parallel to the y axis, $F_{0x} = 0$ and the first integral in (15) vanishes. Hence, (32) includes only the second integral. For the ring probe it is still true that we can choose to orient our reference grid parallel to the principle axes of the workpieces and so we can eliminate the third integral in (15). However, the first integral must be retained. The basic inversion equation for the ring probe, then, involves T_{11} and $\sigma_{11}^{(a)}$ as well as T_{22} and $\sigma_{22}^{(a)}$. For isotropic materials, $\sigma_{11}^{(a)} = \sigma_{22}^{(a)}$ and the transfer functions can be combined. For anisotropic materials, we can either treat the two principle conductivities as independent unknowns and double the size of the problem or we can assume a constant ratio for the conductivities and combine the transfer functions.

CHAPTER II

APPLICATION OF CONJUGATE GRADIENTS

1. Introduction

The discretized system of equations, (I-40), which resulted from the application of the method of moments to the operator equations in Chapter I, will, in general, have a large number of unknowns. In subsequent chapters we demonstrate some problems with 4000 to 10,000 unknowns. In addition, we found that this system has a very special structure; it was Toeplitz in two of the three dimensions. This means that we should apply a solution technique that can accommodate a large number of variables, while, at the same time, taking advantage of the special structure. This suggests the use of iterative techniques, such as the conjugate gradient (CG) method.

We have successfully applied the CG method to a number of problems involving volume integral equations in nondestructive evaluation [1-3]. Much of the rest of this report deals with the application of this method to three-dimensional inverse problems.

In this chapter, we will simply sketch the important features of the CG algorithm; references [4-6] should be consulted for further details on the method.

2. The Conjugate Gradient Method

Let us write the complex vector-matrix equation (I-40) as the operator equation

$$Y = \mathcal{A} \circ X, \quad (1)$$

where

$$Y = \begin{bmatrix} B_1 \\ \vdots \\ B_{N_f} \end{bmatrix}, \quad (2)$$

$$X = \begin{bmatrix} \sigma_1 \\ \vdots \\ \sigma_{N_s} \end{bmatrix}, \quad (3)$$

and

$$\mathcal{A} \circ X = \begin{bmatrix} T_{1,1} & \cdots & T_{1,N_s} \\ \vdots & & \vdots \\ T_{N_f,1} & \cdots & T_{N_f,N_s} \end{bmatrix} \odot \begin{bmatrix} \sigma_1 \\ \vdots \\ \sigma_{N_s} \end{bmatrix}. \quad (4)$$

Keep in mind that each of the B 's and σ 's is a two-dimensional array, say of dimension 32×32 , and each $T_{i,j}$ in (4) is a two-dimensional Toeplitz matrix, $T_{i,j}(l-m, l-M)$. l, m index the 'row' in each of the two dimensions, while L, M index the 'column' of each dimension.

We will need the adjoint operator, \mathcal{A}^* , which corresponds to the conjugate transpose of the block-matrix in (4):

$$\mathcal{A}^* \circ Y = \begin{bmatrix} T_{1,1}^H & \cdots & T_{N_f,1}^H \\ \vdots & & \vdots \\ T_{1,N_s}^H & \cdots & T_{N_f,N_s}^H \end{bmatrix} \odot \begin{bmatrix} B_1 \\ \vdots \\ B_{N_f} \end{bmatrix}. \quad (5)$$

$T_{i,j}^H$ is the Hermitian transpose of the two-dimensional Toeplitz matrix $T_{i,j}$; i.e., $T_{i,j}^H(l-M, m-M) = T_{i,j}^*(L-l, M-m)$, where $*$ denotes the complex-conjugate. The operator formalism is precisely the same if we use the real system, (I-42), except that the Hermitian transpose is replaced by the ordinary transpose in defining the adjoint operator in (5).

We remind the reader that the \odot operation that appears in (4) and (5) stands for the sum of a number of two-dimensional Toeplitz operations, as in (I-40).

The conjugate gradient algorithm starts with an initial guess, X_0 , from which we compute $R_0 = Y - \mathcal{A} \circ X_0$, $P_1 = Q_0 = \mathcal{A}^* \circ R_0$. In addition, we have a convergence parameter, ϵ . Then for $k = 1, \dots$, if $Test = \|R_k\|/\|Y\| < \epsilon$, stop; X_k is the optimal solution of (1). Otherwise, update X_k by the following steps:

$$\begin{aligned} S_k &= \mathcal{A} \circ P_k \\ a_k &= \frac{\|Q_{k-1}\|^2}{\|S_k\|^2} \\ X_k &= X_{k-1} + a_k P_k \\ R_k &= R_{k-1} - a_k S_k \\ Q_k &= \mathcal{A}^* \circ R_k \\ b_k &= \frac{\|Q_k\|^2}{\|Q_{k-1}\|^2} \\ P_{k+1} &= Q_k + b_k P_k. \end{aligned} \quad (6)$$

comment (1): The algorithm terminates at the M th step when $Q_{M+1} = 0$, so that X_{M+1} is the least-squares solution of $Y = \mathcal{A} \circ X$. The vectors Q_0, Q_1, Q_2, \dots , are mutually orthogonal, as are the vectors, S_1, S_2, S_3, \dots . In addition

$$S_k^H P_j = \begin{cases} 0, & \text{if } j < k; \\ \|Q_k\|^2, & \text{otherwise.} \end{cases}$$

comment (2): This suggests that we monitor the iterates $\{Q_k\}$ for loss of orthogonality, and restart when the condition $|Q_k^H Q_{k+1}| \geq \epsilon_1 Q_{k+1}^H Q_{k+1}$ is satisfied, where $\epsilon_1 = 0.2$ (say). When this occurs, we set $b_k = 0$ in the last line, and then continue (i.e., we restart with a pure gradient step).

comment (3): Allen McIntosh, *Fitting Linear Models: An Application of Conjugate Gradient Algorithms*, Springer-Verlag, 1982, gives an alternative expression for b_k :

$$b_k = \frac{Q_k^H (Q_k - Q_{k-1})}{\|Q_{k-1}\|^2},$$

which seems to produce Q_k 's that are more orthogonal, when using the criterion of comment (2). This definition requires, however, that an extra array to store Q_{k-1} be made available. This is no problem if we monitor for orthogonality for the purpose of restarting, because that array is required anyway.

The convolution and correlation operations that are a part of A and A^* are evaluated by using the FFT, as described in Appendix A. This, together with the fact that the storage requirements are reasonably modest, are the reasons why the conjugate gradient algorithm becomes attractive for large problems in our model.

3. Conjugate Gradients with Constraints

The conjugate gradient algorithm that was just described does not constrain the solution. In solving an inverse problem, we often need to constrain the solution in order to get meaningful solutions. Hestenes [6, Chapter III] presents algorithms that involve general linear inequality constraints (such as bounds on the solution). We show one such algorithm, the active set method, using Hestenes' notation.

The problem is to minimize the quadratic function,

$$F(x) = \frac{1}{2}x^T Ax - h^T x + C_0,$$

on the set, S , of all points, x , satisfying a set of inequality constraints

$$g_i(x) = w_i^T x - k_i \leq 0 \quad (i = 1, \dots, M). \quad (7)$$

We assume that A is $N \times N$ and symmetric; later, we will consider the more general case that can be solved using least-squares.

A special case of (7), which will be of interest to us, are the bounds

$$c^i \leq x^i \leq d^i \quad (i = 1, \dots, N).$$

This can be put into the form (7):

$$\begin{aligned} g_i(x) &= -x^i + c^i \leq 0 \\ g_{i+N}(x) &= x^i - d^i \leq 0 \quad (i = 1, \dots, N). \end{aligned} \quad (8)$$

Hence, $M = 2N$; w^i in (7) is the unit vector pointing in the negative i th-coordinate direction, for $i = 1, \dots, N$, and in the positive $(i - N)$ th-coordinate direction, for $i = N + 1, \dots, 2N$. These vectors, of course, are the outer normal vectors to the feasible region, S , which, in this case, is a cuboid whose edges are parallel to the coordinate axes.

(a) CG-Algorithm for Minimizing F on S [6, p. 224]

Step 1. Select a point x_1 in S . Compute

$$r_1 = -F'(x_1) = h - Ax_1, \quad g_{i1} = g_i(x_1) \quad (i = 1, \dots, 2N).$$

If $r_1 = 0$, stop; algorithm terminates.

Else, let I be the set of indices, i , such that $g_{i1} = 0$ (the 'active set'), and go to Step 2.

Step 2. If I is empty, i.e., no constraints are active, let H be the identity matrix, and go to Step 3.

Else, let H be the nonnegative symmetric matrix that annihilates the vectors, w_i , $i \in I$.

comment: Note that if the first N constraints are active, or the last N , then H is the zero matrix, because that is the only matrix that jointly annihilates all of the coordinate vectors. This is the case when x is at a vertex of the feasible region (which corresponds to a corner of the cuboid). In general, the columns of H are orthogonal to the normal vectors of the surfaces that intersect to form the part of the cuboid on which x lies. (Consider the case in which x lies on a face of the cube, or on an edge.) It will be quite apparent how we apply H , so that no matrix multiplies will be involved.

If $H = 0$ go to Step 5, with x_1 playing the role of x_{k+1} .

Else go to Step 3.

Step 3. CG-subroutine. Set

$$p_1 = \bar{r}_1 = Hr_1. \quad (a)$$

comment: If H is not the identity matrix, then when it operates on a vector it merely nulls certain components. Thus, the resulting vector lies in the constraint subspace in which x is located. This means that the correction vector, p , lies in the constraint boundary, if x starts there.

Starting with $k = 1$ compute

$$s_k = Ap_k, \quad c_k = p_k^T r_k, \quad d_k = p_k^T s_k, \quad a_k = \frac{c_k}{d_k}, \quad (b)$$

$$q_{ik} = \begin{cases} 0, & i \in I \\ w_i^T p_k, & i \notin I, \end{cases} \quad (c)$$

$$x_{k+1} = x_k + a_k p_k, \quad g_{j,k+1} = g_{jk} + a_k q_{jk} \quad (j = 1, \dots, 2N). \quad (d)$$

$$\text{If for some } j \notin I, g_{j,k+1} \geq 0, \text{ go to Step 4.} \quad (e)$$

Else

$$r_{k+1} = r_k - a_k s_k, \quad \bar{r}_{k+1} = Hr_{k+1}. \quad (f)$$

$$\text{If } \bar{r}_{k+1} = 0, \text{ or } k = N, \text{ go to Step 5.} \quad (g)$$

Else

$$p_{k+1} = \bar{r}_{k+1} + b_k p_k, \quad b_k = -\frac{s_k^T \bar{r}_{k+1}}{d_k}. \quad (h)$$

Replace k by $k + 1$ and go to (b).

Step 4. Scale back to the boundary of the feasible region and update the active set. Let J be all indices $j \notin I, \exists g_{j,k+1} \geq 0$. Let \bar{a}_k be the smallest of the ratios

$$a_{jk} = -\frac{g_{jk}}{q_{jk}}, \quad j \in J.$$

Reset

$$x_1 = x_k + \bar{a}_k p_k, \quad r_1 = h - Ax_1, \quad g_{j1} = g_{j,k} + \bar{a}_k q_{jk}, \quad (j = 1, \dots, 2N).$$

Update the active set by adjoining to I all indices $j \notin I, \exists g_{j1} = 0$. Then go to Step 2.

comment: Instead of scaling back to the boundary along the conjugate direction, we can return to the boundary along the orthogonal direction from the current estimate point. This seems to speed up the algorithm.

Step 5. If $r_{k+1} = 0$, stop; algorithm is terminated.

Else select shortest v of the form

$$v = r_{k+1} - \sum w_i y_i, \text{ summed for all } i \in I \text{ with } y_i \geq 0. \quad (i)$$

comment: It is easy to do this because the w_i are unit coordinate vectors. The y_i are called either Lagrange multipliers or components of the dual vector.

If $v = 0$, stop; Kuhn-Tucker conditions are satisfied, and algorithm is terminated at minimum point of F on S .

Else, choose $a > 0$, such that

$$g_{j,k+1} + av^T w_j \leq 0 \quad (j = 1, \dots, 2N), \quad F(x_{k+1} + av) < F(x_{k+1}). \quad (j)$$

comment: The last inequality holds when $0 < a \leq 2v^T r_{k+1} / v^T A v$.

Restart the algorithm at Step 1 with

$$x_1 = x_{k+1} + av$$

as the initial point.

(b) CG-Algorithm for Least-Squares on S

comment: The algorithm follows from the preceding one, after observing that the new functional to be minimized is

$$\begin{aligned} F(X) &= \frac{1}{2} \|Y - AX\|^2 \\ &= \frac{1}{2} X^T A^* A X - X^T (A^* Y) + \frac{1}{2} \|Y\|^2, \end{aligned}$$

where we are returning to our usual notation. The constraints are the same as before, (8).

Step 1. Select a point X_1 in S . Compute

$$R_1 = Y - AX_1, \quad Q_1 = A^* R_1 = -F'(X_1), \quad g_{i1} = g_i(X_1) \quad (i = 1, \dots, 2N).$$

If $Q_1 = 0$, stop; algorithm terminates.

Else, let I be the set of indices, i , such that $g_{i1} = 0$ (the 'active set'), and go to Step 2.

Step 2. If I is empty, i.e., no constraints are active, let H be the identity matrix, and go to Step 3.

Else, let H be the nonnegative symmetric matrix that annihilates the vectors, W_i , $i \in I$.
comment: This is the same matrix as above.

If $H = 0$ go to Step 5, with X_1 playing the role of X_{k+1} .

Else go to Step 3.

Step 3. CG-subroutine. Set

$$P_1 = \bar{Q}_1 = HQ_1. \quad (a)$$

Starting with $k = 1$ compute

$$S_k = AP_k, \quad a_k = \frac{\|\bar{Q}_k\|^2}{\|S_k\|^2} \quad (b)$$

$$l_{ik} = \begin{cases} 0, & i \in I \\ W_i^T P_k, & i \notin I, \end{cases} \quad (c)$$

$$X_{k+1} = X_k + a_k P_k, \quad g_{j,k+1} = g_{jk} + a_k l_{jk} \quad (j = 1, \dots, 2N). \quad (d)$$

$$\text{If for some } j \notin I, g_{j,k+1} \geq 0, \text{ go to Step 4.} \quad (e)$$

Else

$$R_{k+1} = R_k - a_k S_k, \quad Q_{k+1} = A^* R_{k+1}, \quad \bar{Q}_{k+1} = HQ_{k+1}. \quad (f)$$

$$\text{If } \bar{Q}_{k+1} = 0, \text{ or } k = N, \text{ go to Step 5.} \quad (g)$$

Else

$$b_k = \frac{\|\bar{Q}_{k+1}\|^2}{\|\bar{Q}_k\|^2}, \quad P_{k+1} = \bar{Q}_{k+1} + b_k P_k. \quad (h)$$

Replace k by $k + 1$ and go to (b).

comment: The definitions of a_k , b_k force the orthogonality conditions: $\bar{Q}_k^T \bar{Q}_{k+1} = 0$, $S_k^T S_{k+1} = 0$. This suggests that we monitor the iterates $\{\bar{Q}_k\}$ for loss of orthogonality, and restart when the condition $|\bar{Q}_k^T \bar{Q}_{k+1}| \geq \epsilon_1 \bar{Q}_k^T \bar{Q}_{k+1}$ is satisfied, where $\epsilon_1 = 0.2$ (say). When this occurs, we set $b_k = 0$ in (h), and then continue.

Step 4. Scale back to the boundary of the feasible region and update the active set. Let J be all indices $j \notin I, \exists g_{j,k+1} \geq 0$. Let \bar{a}_k be the smallest of the ratios

$$a_{jk} = -\frac{g_{jk}}{l_{jk}}, \quad j \in J.$$

Reset

$$X_1 = X_k + \bar{a}_k P_k, \quad R_1 = Y - AX_1, \quad Q_1 = A^* R_1, \quad g_{j1} = g_{j,k} + \bar{a}_k l_{jk}, \quad (j = 1, \dots, 2N).$$

Update the active set by adjoining to I all indices $j \notin I, \exists g_{j1} = 0$. Then go to Step 2.

comment: Instead of scaling back to the boundary along the conjugate direction, we can return to the boundary along the orthogonal direction from the current estimate point. This seems to speed up the algorithm.

Step 5. If $Q_{k+1} = 0$, stop; algorithm is terminated.

Else select shortest V of the form

$$V = Q_{k+1} - \sum W_i \lambda_i, \text{ summed for all } i \in I \text{ with } \lambda_i \geq 0. \quad (i)$$

If $V = 0$, stop; Kuhn-Tucker conditions are satisfied, and algorithm is terminated at minimum point of F on S .

Else, choose $a > 0$, such that

$$g_{j,k+1} + aV^T W_j \leq 0 \quad (j = 1, \dots, 2N), \quad F(X_{k+1} + aV) < F(X_{k+1}). \quad (j)$$

comment: The last inequality holds when $0 < a \leq 2V^T Q_{k+1} / V^T A^* AV$.

Restart the algorithm at Step 1 with

$$X_1 = X_{k+1} + aV$$

as the initial point.

(c) Example Calculation

Let

$$A = \begin{bmatrix} 0 & 1 \\ 1 & 1 \\ 1 & 1 \end{bmatrix}, \quad A^* = \begin{bmatrix} 0 & 1 & 1 \\ 1 & 1 & 1 \end{bmatrix}, \quad Y = \begin{bmatrix} 2 \\ 0 \\ 8 \end{bmatrix}.$$

Then the solution of the normal equation

$$A^* AX = \begin{bmatrix} 2 & 2 \\ 2 & 3 \end{bmatrix} X = A^* Y = \begin{bmatrix} 8 \\ 10 \end{bmatrix}$$

is $X = \begin{bmatrix} 2 \\ 2 \end{bmatrix}$. The outer-normal vectors to the two-dimensional constraint region (which is a square) are

$$W_1 = \begin{bmatrix} -1 \\ 0 \end{bmatrix}, \quad W_2 = \begin{bmatrix} 0 \\ -1 \end{bmatrix}, \quad W_3 = \begin{bmatrix} 1 \\ 0 \end{bmatrix}, \quad W_4 = \begin{bmatrix} 0 \\ 1 \end{bmatrix}.$$

Start with $X_1 = \begin{bmatrix} 0 \\ 0 \end{bmatrix}$. Then $g_1(X_1) = 0$, $g_2(X_1) = 0$, $g_3(X_1) = -1$, $g_4(X_1) = -1$. Hence, the active index set is $I = (1, 2)$, which means that the H matrix is the null-matrix. The initial residual and gradient vectors are, respectively,

$$R_1 = \begin{bmatrix} 2 \\ 0 \\ 8 \end{bmatrix}, \quad Q_1 = A^* R_1 = \begin{bmatrix} 8 \\ 10 \end{bmatrix}.$$

Enter 5: Minimize V with nonnegative λ_1, λ_2 , where,

$$V = \begin{bmatrix} 8 \\ 10 \end{bmatrix} - \lambda_1 \begin{bmatrix} -1 \\ 0 \end{bmatrix} - \lambda_2 \begin{bmatrix} 0 \\ -1 \end{bmatrix} = \begin{bmatrix} 8 + \lambda_1 \\ 10 + \lambda_2 \end{bmatrix}.$$

Hence, $\lambda_1 = \lambda_2 = 0$, and $V = \begin{bmatrix} 8 \\ 10 \end{bmatrix}$. Next, consider

$$g_{1,1} + a[8 \ 10] \begin{bmatrix} -1 \\ 0 \end{bmatrix} = -8a \leq 0 \Rightarrow a > 0$$

$$g_{2,1} + a[8 \ 10] \begin{bmatrix} 0 \\ -1 \end{bmatrix} = -10a \leq 0 \Rightarrow a > 0$$

$$g_{3,1} + a[8 \ 10] \begin{bmatrix} 1 \\ 0 \end{bmatrix} = -1 + 8a \leq 0 \Rightarrow a < 1/8$$

$$g_{4,1} + a[8 \ 10] \begin{bmatrix} 0 \\ 1 \end{bmatrix} = -1 + 10a \leq 0 \Rightarrow a < 1/10$$

$$0 < a \leq \frac{328}{10^2 + 18^2 + 18^2} = \frac{328}{748}.$$

Thus, $a = 0.1$, and we leave step 5 with

$$X_1 = \begin{bmatrix} 0 \\ 0 \end{bmatrix} + \begin{bmatrix} 0.8 \\ 1.0 \end{bmatrix} = \begin{bmatrix} 0.8 \\ 1.0 \end{bmatrix}.$$

Enter step 1 with this value of X_1 and compute

$$R_1 = \begin{bmatrix} 2 \\ 0 \\ 8 \end{bmatrix} - \begin{bmatrix} 0 & 1 \\ 1 & 1 \\ 1 & 1 \end{bmatrix} \begin{bmatrix} 0.8 \\ 1.0 \end{bmatrix} = \begin{bmatrix} 1 \\ -2.8 \\ 5.2 \end{bmatrix}.$$

$$Q_1 = A^* R_1 = \begin{bmatrix} 0 & 1 & 1 \\ 1 & 1 & 1 \end{bmatrix} \begin{bmatrix} 1 \\ -2.8 \\ 5.2 \end{bmatrix} = \begin{bmatrix} 2.4 \\ 3.4 \end{bmatrix}.$$

$$g_1 = -0.8, \quad g_2 = -1.0, \quad g_3 = -0.2, \quad g_4 = 0.$$

$$I = (4), \quad H = \begin{bmatrix} 1 & 0 \\ 0 & 0 \end{bmatrix}.$$

Enter step 3:

$$P_1 = \bar{Q}_1 = \begin{bmatrix} 2.4 \\ 0 \end{bmatrix}$$

$$S_1 = AP_1 = \begin{bmatrix} 0 & 1 \\ 1 & 1 \\ 1 & 1 \end{bmatrix} \begin{bmatrix} 2.4 \\ 0 \end{bmatrix} = \begin{bmatrix} 0 \\ 2.4 \\ 2.4 \end{bmatrix}$$

$$a_1 = \frac{(2.4)^2}{2(2.4)^2} = 0.5$$

$$l_{11} = -2.4, \quad l_{21} = 0, \quad l_{31} = 2.4, \quad l_{41} = 0$$

$$X_2 = X_1 + \frac{1}{2}P_1 = \begin{bmatrix} 0.8 \\ 1.0 \end{bmatrix} + \frac{1}{2} \begin{bmatrix} 2.4 \\ 0 \end{bmatrix} = \begin{bmatrix} 2.0 \\ 1.0 \end{bmatrix}.$$

$$g_{1,2} = -0.8 + \frac{1}{2}(-2.4) = -2.0$$

$$g_{2,2} = -1.0 + \frac{1}{2}(0) = -1.0$$

$$g_{3,2} = -0.2 + \frac{1}{2}(2.4) = 1.0$$

$$g_{4,2} = 0$$

Enter step 4:

$$\bar{a} = \frac{0.2}{2.4} = 1/12, \quad I = (3, 4)$$

$$X_1 = \begin{bmatrix} 0.8 \\ 1.0 \end{bmatrix} + \frac{1}{12} \begin{bmatrix} 2.4 \\ 0 \end{bmatrix} = \begin{bmatrix} 1.0 \\ 1.0 \end{bmatrix}$$

$$R_1 = \begin{bmatrix} 2 \\ 0 \\ 8 \end{bmatrix} - \begin{bmatrix} 0 & 1 \\ 1 & 1 \\ 1 & 1 \end{bmatrix} \begin{bmatrix} 1 \\ 1 \end{bmatrix} = \begin{bmatrix} 1 \\ -2 \\ 6 \end{bmatrix}$$

$$Q_1 = \begin{bmatrix} 0 & 1 & 1 \\ 1 & 1 & 1 \end{bmatrix} \begin{bmatrix} 1 \\ -2 \\ 6 \end{bmatrix} = \begin{bmatrix} 4 \\ 5 \end{bmatrix}$$

$$g_1 = -1.0, \quad g_2 = -1.0, \quad g_3 = 0, \quad g_4 = 0.$$

Enter step 2:

$$H = \begin{bmatrix} 0 & 0 \\ 0 & 0 \end{bmatrix}$$

Enter step 5: Find smallest V with nonnegative λ_3, λ_4 , such that

$$V = \begin{bmatrix} 4 \\ 5 \end{bmatrix} - \lambda_3 \begin{bmatrix} 1 \\ 0 \end{bmatrix} - \lambda_4 \begin{bmatrix} 0 \\ 1 \end{bmatrix} = \begin{bmatrix} 4 - \lambda_3 \\ 5 - \lambda_4 \end{bmatrix}.$$

Hence, $\lambda_3 = 4$, $\lambda_4 = 5$, and $V = \begin{bmatrix} 0 \\ 0 \end{bmatrix}$. Hence, stop with solution

$$X = \begin{bmatrix} 1 \\ 1 \end{bmatrix}, \quad \lambda = \begin{bmatrix} 4 \\ 5 \end{bmatrix}.$$

4. Preconditioned Conjugate Gradients

The rate of convergence of the conjugate gradient method depends upon the condition number of the matrix operator, \mathcal{A} . Hence, in order to speed up the convergence, we precondition \mathcal{A} . There are several ways to do this (see Allen McIntosh, *Fitting Linear Models: An Application of Conjugate Gradient Algorithms*, New York: Springer-Verlag, 1982); we are going to consider only one method, scaling to produce columns of \mathcal{A} that are unit vectors.

Return to the basic equation

$$\begin{aligned} Y &= \mathcal{A}X \\ &= \mathcal{A}B B^{-1}X \\ &= \mathcal{A}BU, \end{aligned} \tag{9}$$

where B is some invertible operator (matrix), and $U = B^{-1}X$. B is chosen to improve the condition number of \mathcal{A} . We will take it to be a diagonal matrix, whose n th entry is the reciprocal of the norm of the n th column of \mathcal{A} .

We do not multiply \mathcal{A} with B , because that would destroy the special convolutional structure of \mathcal{A} . We introduce a new operator, \mathcal{A}' , which is the composition of B followed by \mathcal{A} . The adjoint of \mathcal{A}' is then $\mathcal{A}'^* = B^T \mathcal{A}^*$. Note that because B is diagonal, then $B^T = B$. In multidimensional problems, in which we don't actually write out the operator equations as matrix equations, we interpret a "diagonal operator" to be an operator that multiplies the n th component of the solution vector by the n th component of B .

The conjugate gradient algorithm remains unchanged, except that \mathcal{A} is replaced by \mathcal{A}' . The solution, U , of the scaled equation is then unscaled to get the original solution: $X = BU$. Keep in mind that this also introduces scaled bounds in the constrained conjugate gradient algorithm for U . That is, if $c^i \leq x^i \leq d^i$, then $(c^i/B^i) \leq u^i \leq (d^i/B^i)$.

5. Conjugate Gradients with the Levenberg-Marquardt Parameter

In our discussion of deconvolution via Fourier transforms, we introduced a filter parameter, α , which smoothed the solution. Here, we introduce a similar parameter, λ , called a Levenberg-Marquardt parameter. We want to see how it enters into the conjugate gradient algorithm.

We start with the augmented functional

$$\begin{aligned} F(X) &= \frac{1}{2} \|Y - AX\|^2 + \frac{1}{2} \lambda^2 \|X\|^2 \\ &= \frac{1}{2} X^T A^* AX - X^T A^* Y + \frac{1}{2} \|Y\|^2 + \frac{1}{2} \lambda^2 \|X\|^2 \\ &= \frac{1}{2} X^T A'^* A' X - X^T A'^* Y' + \frac{1}{2} \|Y'\|^2, \end{aligned} \quad (10)$$

where the augmented operator, A' , is defined by

$$A' = \begin{bmatrix} A \\ \lambda I \end{bmatrix}, \quad (11)$$

and the augmented right-hand side is

$$Y' = \begin{bmatrix} Y \\ 0 \end{bmatrix}. \quad (12)$$

I in (11) is the $N \times N$ identity matrix (where N is the number of unknowns), and the zero vector in (12) is of length N .

The vectors in the conjugate gradient algorithm that are affected by these definitions are S and Q . We define new vectors, S' and Q' , in terms of the old ones by

$$S' = A'P = \begin{bmatrix} AP \\ \lambda P \end{bmatrix} = \begin{bmatrix} S \\ \lambda P \end{bmatrix}, \quad (13)$$

$$\begin{aligned} Q' &= -F'(X) = A^*Y - (A^*A + \lambda^2)X \\ &= A^*R - \lambda^2 X \\ &= Q - \lambda^2 X. \end{aligned} \quad (14)$$

It is easy to see that $\|S'\|^2 = \|S\|^2 + \lambda^2 \|P\|^2$.

We can use the Levenberg-Marquardt parameter to solve a constrained least-squares problem. First, let us approximate the cuboidal constraint set, that was defined in Section 3, by the inscribed hypersphere, whose center is at the centroid, X_c , of the cuboid. Then we replace the functional of (10) by

$$F(X) = \frac{1}{2} \|Y - AX\|^2 + \frac{1}{2} \lambda^2 \|X - X_c\|^2, \quad (15)$$

which, under the change of variables, $U = X - X_c$, becomes

$$G(U) = \frac{1}{2} \|Y - AX_c - AU\|^2 + \frac{1}{2} \lambda^2 \|U\|^2. \quad (16)$$

Hence, the previous algorithm is unchanged, except that the inhomogeneous term, Y , in (12) is replaced by $Y - AX_c$.

Now the question arises, how do we determine λ ? In a statistical approach to deconvolution, λ can be given in terms of signal-to-noise ratio, as is done in Chapter IX. Without this data, however, we look for something else. In our discussion of deconvolution via Fourier transforms, we showed that the smoothing parameter, α , could be determined by solving a nonlinear equation, given certain prior information. We do something similar with the Levenberg-Marquardt parameter, but first we quote the following theorem: (Charles L. Lawson and Richard J. Hanson, *Solving Least Squares Problems*, Englewood Cliffs: Prentice-Hall, Inc., 1974, p. 193)

Theorem. For a fixed nonnegative value of λ , say, $\bar{\lambda}$, let \bar{X} be the solution vector for the problem of minimizing (10), and let $\bar{\Omega} = \frac{1}{2} \|Y - A\bar{X}\|^2$. Then $\bar{\Omega}$ is the minimum value of $\frac{1}{2} \|Y - AX\|^2$ for all vectors X satisfying $\|X\| \leq \|\bar{X}\|$.

The proof of this theorem is simple, and is given in Lawson and Hanson. The meaning of the theorem is clear: Given the radius of the hypersphere constraint set (which follows from the original hypercube constraint set), $\|\bar{X}\|$, we minimize (10) by means of conjugate gradients, for a collection of λ 's. We choose that solution for which $\|X\| = \|\bar{X}\|$. This yields the optimum λ , and gives us the optimum, constrained, least-squares solution of $Y = AX$.

This approach is equivalent to solving for λ using a trial-and-error method. This is inevitable when using conjugate gradients. If we were solving a much smaller problem, we could determine the singular value expansion of A , and use that result in setting up an analytic equation for λ , which could then be solved using Newton's method, as indicated in Lawson and Hanson. It remains to be seen whether this approach is faster than that which constrains each component of the solution vector individually.

There is a serious problem with this approach, however. The inscribed hypersphere in N -dimensional space has a volume that is much smaller than the N -dimensional constraint cuboid, when N is only reasonably large, whereas the circumscribed hypersphere has a volume that is much larger. Hence, using the inscribed hypersphere results in a very strong (and undoubtedly incorrect) constraint, whereas using the circumscribed hypersphere results in a very weak constraint.

6. References

- [1] J. R. Bowler, L. D. Sabbagh, and H. A. Sabbagh, "A Theoretical and Computational Model of Eddy-Current Probes Incorporating Volume Integral and Conjugate Gradient Methods," to be published in *IEEE Trans. Magnetics*, 1989.

- [2] H. A. Sabbagh, L. D. Sabbagh, and J. R. Bowler, "A Model of Ferrite-Core Probes Over Composite Workpieces," in D. O. Thompson and D. E. Chimenti, eds., *Review of Progress in Quantitative Nondestructive Evaluation*, Vol. 7A, New York: Plenum, 1987, pp. 479-486.
- [3] H. A. Sabbagh, J. R. Bowler, and L. D. Sabbagh, "A Volume Integral Code for Eddy-Current Nondestructive Evaluation," accepted for publication in *J. App. Comp. Elect. Soc.*, 1989.
- [4] T. K. Sarkar, E. Arvas, and S. M. Rao, "Application of FFT and Conjugate Gradient Method for the Solution of Electromagnetic Radiation from Electrically Large and Small Bodies," *IEEE Trans. Ant. Prop.*, Vol. AP-34, May 1986, pp. 635-640.
- [5] A. F. Peterson and R. Mittra, "On the Implementation and Performance of Iterative Methods for Computational Electromagnetics," *Electromagnetic Communication Laboratory Technical Report No. 85-9*, University of Illinois, Urbana, 1985.
- [6] Magnus Hestenes, *Conjugate Direction Methods in Optimization*, New York: Springer-Verlag, 1982.

APPENDIX A

Efficient Computation of Convolutions and Correlations

If we attempt to solve (1) using an iterative technique, such as the conjugate gradient method, it will be necessary to evaluate the vector-matrix product many times. This is a PQ -step operation, where P is the number of rows (equations), and Q is the number of columns (unknowns) of the matrix T . If the matrix is square, with dimension $N \times N$, this process can be reduced to $N \log_2 N$ operations by using the Fast Fourier Transform (FFT) for evaluating discrete convolutions.

The appropriate theorems (in one dimension) that relate discrete Fourier transforms and convolutions and correlations are (\iff denotes a discrete transform-pair):

$$\begin{aligned} \text{If} \quad & g(j) \iff G(n) \\ & h(j) \iff H(n) \end{aligned}$$

$$\begin{aligned} \text{Then} \quad \frac{1}{N} \sum_{k=0}^{N-1} g(j+k)h(k) &= \frac{1}{N} \sum_{k=0}^{N-1} g(k)h(k-j) \\ &\iff G(n)H(-n) \\ &= G(n)H(N-n) \end{aligned} \tag{A.1}(a)$$

$$\begin{aligned} \frac{1}{N} \sum_{k=0}^{N-1} g(k)h(j+k) &= \frac{1}{N} \sum_{k=0}^{N-1} g(k-j)h(k) \\ &\iff G(-n)H(n) \\ &= G(N-n)H(n) \end{aligned} \tag{A.1}(b)$$

$$\frac{1}{N} \sum_{k=0}^{N-1} g(k)h(j-k) = \frac{1}{N} \sum_{k=0}^{N-1} g(j-k)h(k) \quad (\text{A.1})(c)$$

$$\iff G(n)H(n),$$

where $j = 0, \dots, N-1$, $n = 0, \dots, N-1$ in all of these. Several points should be made: first note that correlation summing is not commutable, and that one must use negative frequencies in the discrete Fourier transform (which, of course, introduces the term $N-n$).

Let's look at the matrix structure of convolution and correlation sums and see how we can use FFT techniques to compute them. We'll work in one dimension. Consider the following convolution sum, which is written as a vector-matrix equation:

$$\begin{bmatrix} y_0 \\ y_1 \\ y_2 \\ y_3 \end{bmatrix} = \begin{bmatrix} m_0 & m_{-1} & m_{-2} & m_{-3} \\ m_1 & m_0 & m_{-1} & m_{-2} \\ m_2 & m_1 & m_0 & m_{-1} \\ m_3 & m_2 & m_1 & m_0 \end{bmatrix} \begin{bmatrix} x_0 \\ x_1 \\ x_2 \\ x_3 \end{bmatrix} \quad (\text{A.2})$$

Rewrite this in the expanded form (padding with zeros to get a power of two) in order to achieve a circulant-matrix:

$$\begin{bmatrix} y_0 \\ y_1 \\ y_2 \\ y_3 \\ * \\ * \\ * \\ * \end{bmatrix} = \begin{bmatrix} m_0 & m_{-1} & m_{-2} & m_{-3} & 0 & m_3 & m_2 & m_1 \\ m_1 & m_0 & m_{-1} & m_{-2} & m_{-3} & 0 & m_3 & m_2 \\ m_2 & m_1 & m_0 & m_{-1} & m_{-2} & m_{-3} & 0 & m_3 \\ m_3 & m_2 & m_1 & m_0 & m_{-1} & m_{-2} & m_{-3} & 0 \\ 0 & m_3 & m_2 & m_1 & m_0 & m_{-1} & m_{-2} & m_{-3} \\ m_{-3} & 0 & m_3 & m_2 & m_1 & m_0 & m_{-1} & m_{-2} \\ m_{-2} & m_{-3} & 0 & m_3 & m_2 & m_1 & m_0 & m_{-1} \\ m_{-1} & m_{-2} & m_{-3} & 0 & m_3 & m_2 & m_1 & m_0 \end{bmatrix} \begin{bmatrix} x_0 \\ x_1 \\ x_2 \\ x_3 \\ 0 \\ 0 \\ 0 \\ 0 \end{bmatrix}, \quad (\text{A.3})$$

where the * denotes a discarded entry. Hence, the sequences to be FFT'd are: $(m_0, m_1, m_2, m_3, 0, m_{-3}, m_{-2}, m_{-1})$ and $(x_0, x_1, x_2, x_3, 0, 0, 0, 0)$, and the output sequence is $(y_0, y_1, y_2, y_3, *, *, *, *)$. The order of the entries in the sequences is very important.

Now for correlations:

$$\begin{bmatrix} y_0 \\ y_1 \\ y_2 \\ y_3 \end{bmatrix} = \begin{bmatrix} m_0 & m_1 & m_2 & m_3 \\ m_1 & m_2 & m_3 & m_4 \\ m_2 & m_3 & m_4 & m_5 \\ m_3 & m_4 & m_5 & m_6 \end{bmatrix} \begin{bmatrix} x_0 \\ x_1 \\ x_2 \\ x_3 \end{bmatrix} \quad (\text{A.4})$$

Rewrite this in the expanded form (padding with zeros to get a power of two) in order to achieve a circulant-matrix:

$$\begin{bmatrix} y_0 \\ y_1 \\ y_2 \\ y_3 \\ * \\ * \\ * \\ * \end{bmatrix} = \begin{bmatrix} m_0 & m_1 & m_2 & m_3 & m_4 & m_5 & m_6 & 0 \\ m_1 & m_2 & m_3 & m_4 & m_5 & m_6 & 0 & m_0 \\ m_2 & m_3 & m_4 & m_5 & m_6 & 0 & m_0 & m_1 \\ m_3 & m_4 & m_5 & m_6 & 0 & m_0 & m_1 & m_2 \\ m_4 & m_5 & m_6 & 0 & m_0 & m_1 & m_2 & m_3 \\ m_5 & m_6 & 0 & m_0 & m_1 & m_2 & m_3 & m_4 \\ m_6 & 0 & m_0 & m_1 & m_2 & m_3 & m_4 & m_5 \\ 0 & m_0 & m_1 & m_2 & m_3 & m_4 & m_5 & m_6 \end{bmatrix} \begin{bmatrix} x_0 \\ x_1 \\ x_2 \\ x_3 \\ 0 \\ 0 \\ 0 \\ 0 \end{bmatrix}, \quad (\text{A.5})$$

where the * denotes a discarded entry. Hence, the sequences to be FFT'd are: $(m_0, m_1, m_2, m_3, m_4, m_5, m_6, 0)$ and $(x_0, x_1, x_2, x_3, 0, 0, 0, 0)$, and the output sequence is $(y_0, y_1, y_2, y_3, *, *, *, *)$. The order of the entries in the sequences is very important, and also don't forget to negate the frequencies in the transform of the x -sequence.

To summarize: we expand the original data, padding with zeros, as necessary, to get a circulant matrix, and then take FFT's.

APPENDIX B

Bi-Conjugate Gradients

Let us consider the following equation,

$$AX = Y, \quad (B.1)$$

where A is a known operator, X is the unknown, and Y is the known vector. For a non-Hermitian operator, the conjugate gradient method solves the normal equation,

$$A^*AY = A^*Y, \quad (B.2)$$

where A^* is the adjoint operator of A . It is noted that the condition number of the original equation (B.1) is squared in the solution of (B.2). In the bi-conjugate gradient method, one solves the non-Hermitian operator equation (B.1) directly. For this algorithm an additional $2N$ storage spaces is required, where N is the dimension of the unknown vector X .

Method of Solution

To solve (B.1), one starts with an initial guess, X_0 , for X , and then defines the residual $R_0 = Y - AX_0$, and an initial search direction $P_0 = R_0$. In parallel, we define the bi-residual $\tilde{R}_0 = R_0^*$ and bi-directional $\tilde{P}_0 = P_0^*$, where $(*)$ denotes the complex conjugate. In addition, we have a convergence parameter, ϵ . Then for $k = 1, 2, \dots$, if $\text{Test} = \|R_k\|/\|Y\| < \epsilon$, stop. Otherwise, update X_k by the following steps:

$$\begin{aligned} S_k &= AP_k & ; & & \tilde{S}_k &= A^* \tilde{P}_k \\ a_k &= \frac{\langle R_k, \tilde{R}_k \rangle}{\langle S_k, \tilde{P}_k \rangle} & ; & & b_k &= \frac{\langle R_{k+1}, \tilde{R}_{k+1} \rangle}{\langle R_k, \tilde{R}_k \rangle} \\ X_{k+1} &= X_k + a_k P_k & & & & \\ P_{k+1} &= R_{k+1} + b_k P_k & ; & & \tilde{P}_{k+1} &= \tilde{R}_{k+1} + b_k^* \tilde{P}_k \\ R_{k+1} &= R_k - a_k S_k & ; & & \tilde{R}_{k+1} &= \tilde{R}_k - a_k^* \tilde{S}_k. \end{aligned} \quad (B.3)$$

The scalar $\{a_k\}$ is chosen so as to force the bi-orthogonality conditions,

$$\langle \tilde{R}_n, R_m \rangle = \langle R_n, \tilde{R}_m \rangle = 0 \quad ; \quad 0 \leq m < n < N,$$

and $\{b_k\}$ is chosen to force the bi-conjugacy conditions,

$$\langle \tilde{P}_n, S_m \rangle = \langle S_n, \tilde{P}_m \rangle = 0 \quad ; \quad 0 \leq m < n < N,$$

provided that the algorithm does not break down; i.e., for all i for which

$$\langle S_i, \tilde{P}_i \rangle \neq 0 \quad ; \quad \langle R_i, \tilde{R}_i \rangle \neq 0.$$

The algorithm must terminate with $R_n = \tilde{R}_n = 0$ in at most N iterations. It is important to point out that the bi-conjugate gradient algorithm does not minimize the norm of the residual, $\|R\|$, at each iteration. Nevertheless, if the algorithm does not break down, it converges at a much faster rate than the normal conjugate gradient algorithm. From our experience with large size and ill-conditioned operators, however, the bi-conjugate gradient algorithm does seem to break down; (i.e., $|\langle S_i, \tilde{P}_i \rangle| < \delta$; $|\langle R_i, \tilde{R}_i \rangle| < \delta$, where δ is a very small positive number), before it meets the convergence criteria.

CHAPTER III

RECONSTRUCTIONS USING SIMULATED AND LABORATORY DATA

1. Introduction

The goal of our work is to reliably reconstruct three dimensional flaws in workpieces from emf measurements that are inherently noisy. First, though we tested the algorithm using simulated data, that is, computer generated data. Through these tests, we were able to learn how the conjugate gradient (CG) algorithm performs as a function of the frequency range of the emf data and the degree of overdeterminedness of the system. Also, the equations we are trying to solve are ill-conditioned and so we needed to know if acceptable solutions could be expected using this form of the CG algorithm. The results of the tests using simulated data are very encouraging. We also include some preliminary results based on actual measured data.

2. Reconstructions Using Simulated Data

(a) Simulating the EMF Data

Two types of synthetic data were available. Since, in the fourier domain, we are solving an equation of the form $Az = B$, we can provide a test solution z_t and calculate $B_t = Az_t$. Then, using A and B_t , we can try to reconstruct z_t using the CG algorithm. This type of synthetic data will be referred to as "exact" data.

Another type of synthetic data resulted from our model of the direct problem. In the direct problem, we calculate emf data from a flaw definition and a transfer function derived from internal and external Green's functions (see Chapter I). This transfer function is discretized using the method of moments and becomes the operator A in the inverse model. The discretization introduces error so that the emf calculated using the direct model differs slightly from the emf calculated using the discrete operator A . The difference between the two diminishes as more terms are used to approximate the operator. This type of synthetic data will be referred to as "direct model" data.

All tests using simulated data used the "direct model" data.

(b) Material and Data Collection Parameters

The emf that is measured depends on the material parameters and the parameters of the data collection system. Figure 1 shows the typical arrangement of workpiece, source (whip) and sensor. For the synthetic data tests the distances shown were as follows.

$$\begin{aligned} z_{source} &= 0.013 \text{ in.} \\ z_{sensor} &= 0.019 \text{ in.} \\ z_{return} &= 0.273 \text{ in.} \end{aligned}$$

The sensor consisted of ten square turns from 0.10 inch to 0.55 inch. The workpiece was 0.11 inch thick. The conductivity tensor was (mhos/m)

$$\begin{bmatrix} 10^4 & 0 & 0 \\ 0 & 10^4 & 0 \\ 0 & 0 & 1 \end{bmatrix}$$

This represents a graphite-epoxy composite material that is isotropic in-plane and essentially nonconducting through its thickness.

Data measurements were simulated at each point of a 32×32 grid in the sensor plane at a resolution of 0.1 inch. The thickness was discretized into four layers, each also a 32×32 grid. A test flaw, then, could be defined as a collection of "voxels" each with dimension $0.1 \times 0.1 \times 0.0275$.

(c) Convergence Test

A convergence test variable was defined in terms of the L_2 norms of the simulated data and the residual. Specifically, at iteration i , the convergence test variable δ_i is

$$\delta_i = \frac{\|Y - AX_i\|_2}{\|Y\|_2}$$

where Y is the simulated emf data, X_i is the flaw function at iteration i and $Y - AX_i$ is the residual.

(d) Test Set #1

A flaw in the shape of a cross was chosen as the standard test flaw. This test flaw was placed in the center of each of the four layers (one at a time) and an attempt was made to reconstruct the flaw from emf data. The conductivity was scaled so that flaw locations had a value of 1 and host material locations had a value of 0. For ease of reference, we will refer to a particular flaw using the word 'flaw' followed by digit(s) indicating the layer(s) that contain the test flaw. This first test set, then, involves flaw1, flaw2, flaw3 and flaw4. Data was simulated at 5 frequencies: 1, 3, 5, 7 and 9 MHz. The unconstrained version of the CG algorithm was used and the initial guess was no flaw, that is, all zeroes.

The number of unknowns in this problem is $32 \times 32 \times 4 = 4096$. Because the emf data is complex and our solution (conductivity) is real, each set of emf data provides $2 \times 32 \times 32 = 2048$ equations. For 5 sets of emf data and 4 layers, the overdeterminedness of the system is 2.5.

The purpose of this set of tests was to determine the ability of the CG algorithm to isolate the flaw to the proper layer. Also, we wanted to find out the effect of depth on the convergence.

Figure 2 shows grayscale plots of the attempted reconstruction of flaw1 at four stages during the iterative process: 100, 500, 1000 and 2048 iterations. Table 1 below shows

the value of the convergence measure, δ_i , as well as the minimum and maximum values of the solution for each layer.

Table 1

flaw1		Layer 1		Layer 2		Layer 3		Layer 4	
Iterations	δ_i	min	max	min	max	min	max	min	max
100	0.00397	-0.270	1.343	-0.068	0.142	-0.118	0.025	-0.074	0.053
500	0.00067	-0.215	1.216	-0.164	0.176	-0.093	0.037	-0.034	0.047
1000	0.00027	-0.293	1.300	-0.170	0.171	-0.065	0.044	-0.050	0.027
2048	0.00011	-0.350	1.364	-0.156	0.139	-0.044	0.050	-0.037	0.036

Figure 3 shows three-dimensional plots of the solution after 2048 iterations. The solution exhibits overshooting at the transition from host material to flaw. That is, near the base of the flaw "tower" some values drop to -0.350 and at the edges of the top of the "tower" some values reach 1.364.

Figures 4 through 9 are similar plots for flaw2, flaw3 and flaw4. Likewise, Tables 2 through 4 show the convergence measure and upper and lower limits of these solutions.

Table 2

flaw2		Layer 1		Layer 2		Layer 3		Layer 4	
Iterations	δ_i	min	max	min	max	min	max	min	max
100	0.00972	-0.066	0.154	-0.259	1.108	-0.107	0.455	-0.221	0.149
500	0.00166	-0.165	0.166	-0.257	1.220	-0.154	0.333	-0.152	0.086
1000	0.00079	-0.170	0.165	-0.192	1.258	-0.158	0.248	-0.175	0.131
2048	0.00036	-0.155	0.133	-0.136	1.232	-0.191	0.239	-0.182	0.111

Table 3

flaw3		Layer 1		Layer 2		Layer 3		Layer 4	
Iterations	δ_i	min	max	min	max	min	max	min	max
100	0.01762	-0.120	0.026	-0.108	0.456	-0.152	0.615	-0.120	0.472
500	0.00431	-0.089	0.040	-0.156	0.322	-0.279	0.976	-0.170	0.507
1000	0.00199	-0.060	0.041	-0.160	0.237	-0.203	1.042	-0.176	0.442
2048	0.00088	-0.041	0.046	-0.184	0.238	-0.208	1.049	-0.208	0.365

Table 4

flaw4		Layer 1		Layer 2		Layer 3		Layer 4	
Iterations	δ_i	min	max	min	max	min	max	min	max
100	0.03249	-0.066	0.048	-0.219	0.141	-0.114	0.470	-0.199	0.668
500	0.00600	-0.029	0.041	-0.153	0.080	-0.170	0.512	-0.290	1.048
1000	0.00268	-0.047	0.031	-0.172	0.135	-0.171	0.452	-0.242	1.151
2048	0.00123	-0.041	0.043	-0.184	0.112	-0.214	0.369	-0.180	1.181

The results of this first set of tests are encouraging. Flaw3 and flaw4 are more difficult to isolate and this is to be expected. Figure 10 is a plot of the convergence measure, δ_i , for the first 500 iterations. Notice that the deeper the flaw is, the slower the convergence is. The "skin effect" phenomena suggests that the results should be better if some of the data were taken at higher frequencies. With this in mind, more tests were performed.

(e) Test Set #2

The error in our solutions reported in the previous section was greatest in the layers immediately adjacent to the layer that contained the flaw. The worst case for layer discrimination, then, would seem to be having a flaw in layers 2 and 4. The error that would appear in layer 3 may be large enough to lead us to believe that there is a flaw in that layer also. We will call this flaw arrangement flaw24. First we tried to reconstruct flaw24 using data taken at the same five frequencies as above (i.e, at 1, 3, 5, 7 and 9 MHz). The results are shown in Figures 11 and 12 and in Table 5.

Table 5

flaw24		Layer 1		Layer 2		Layer 3		Layer 4	
Iterations	δ_i	min	max	min	max	min	max	min	max
100	0.00992	-0.048	0.142	-0.221	1.096	-0.198	0.927	-0.166	0.639
500	0.00251	-0.170	0.194	-0.206	1.097	-0.253	0.820	-0.245	0.930
1000	0.00120	-0.177	0.181	-0.133	1.110	-0.291	0.674	-0.175	0.998
2048	0.00053	-0.128	0.128	-0.123	1.118	-0.402	0.489	-0.186	1.045

At 9 MHz, the skin depth of the workpiece is 0.066 inches or 2.4 times the layer thickness. A second reconstruction was performed for flaw24 using data simulated over a wider frequency range. The frequencies used were 1, 5, 10, 20 and 30 MHz. At 30 MHz, the skin depth is 0.036 inches or 1.3 times the layer thickness. The results of this second reconstruction are displayed in Figures 13 and 14 and in Table 6 below. As expected, the higher frequency data improves the solution.

Table 6

flaw24		Layer 1		Layer 2		Layer 3		Layer 4	
Iterations	δ_i	min	max	min	max	min	max	min	max
100	0.02541	-0.029	0.034	-0.323	1.381	-0.147	0.499	-0.329	0.693
500	0.00452	-0.062	0.065	-0.210	1.270	-0.184	0.308	-0.310	1.148
1000	0.00189	-0.044	0.042	-0.151	1.239	-0.196	0.198	-0.321	1.315
2048	0.00072	-0.024	0.024	-0.238	1.242	-0.185	0.255	-0.291	1.398

Earlier we noted that 5 sets of emf data made the system overdetermined by a factor of 2.5. To see if additional data sets from the same frequency range would improve the solution, we tried a third reconstruction using 9 sets of emf data (1, 2, 3, 4, 5, 6, 7, 8 and

9 MHz). This increased the factor of overdetermination to 4.5. The results are shown in Figures 15 and 16 and in Table 7. Note that the results in Table 7 are essentially identical to those in Table 5. The additional data sets may be important, though, when data with noise is used.

Table 7

flaw24		Layer 1		Layer 2		Layer 3		Layer 4	
Iterations	δ_i	min	max	min	max	min	max	min	max
100	0.00953	-0.048	0.146	-0.219	1.088	-0.199	0.932	-0.165	0.647
500	0.00244	-0.174	0.198	-0.206	1.091	-0.243	0.826	-0.243	0.926
1000	0.00117	-0.182	0.187	-0.131	1.106	-0.290	0.684	-0.176	1.000
2048	0.00052	-0.134	0.133	-0.123	1.120	-0.399	0.490	-0.184	1.043

In Chapter II a method of constraining the solution was considered. A final reconstruction was performed with all variables constrained to the interval $[-0.0001, 1.0]$. The results are shown in Figures 17 and 18 and in Table 8 below.

Table 8

flaw24		Layer 1		Layer 2		Layer 3		Layer 4	
Iterations	δ_i	min	max	min	max	min	max	min	max
100	0.1041	-0.001	0.714	-0.001	1.000	-0.001	1.000	-0.001	1.000
500	0.1035	-0.001	0.706	-0.001	1.000	-0.001	1.000	-0.001	1.000
1000	0.1035	-0.001	0.706	-0.001	1.000	-0.001	1.000	-0.001	1.000
2048	0.0400	-0.001	0.379	-0.001	1.000	-0.001	1.000	-0.001	1.000

These results are not very good compared to the unconstrained solutions we have generated. More work is needed in this area to determine whether our implementation of constraints should be modified. The results are interesting in that the convergence measure δ_i goes from 1.0 to 0.104 in about 100 iterations and then changes very little through iteration 1460. Then, at some point between iteration 1460 and iteration 1470, a direction for significant improvement is found and the solution improves steadily through iteration 1560 and then again little changes until some point between iteration 1960 and iteration 1970 when another "good direction" is found. Figure 19 is a plot of δ_i illustrating this phenomenon. More work is needed to determine if convergence can be speeded up for the constrained case.

To make sure that there is nothing fundamentally incorrect with the constrained CG algorithm, we used the actual flaw as the initial guess. This guess would yield $\delta_0=0$ and terminate the algorithm if we were using "exact" data. Since we are using "direct model" data, though, our initial guess is not the best fit. Figures 20 and 21 and Table 9 show the results of this last run.

Table 9

flaw24		Layer 1		Layer 2		Layer 3		Layer 4	
Iterations	δ_i	min	max	min	max	min	max	min	max
100	0.01504	-0.001	0.116	-0.001	1.000	-0.001	0.275	-0.001	1.000
500	0.01256	-0.001	0.110	-0.001	1.000	-0.001	0.674	-0.001	1.000
1000	0.01254	-0.001	0.110	-0.001	1.000	-0.001	0.704	-0.001	1.000
2048	0.01253	-0.001	0.110	-0.001	1.000	-0.001	0.706	-0.001	1.000

Notice that although some isolated points build up to help match the data, the flaw locations from the initial guess are unaltered. Also, the convergence measure is much smaller in Table 9 than than in Table 8. Hopefully this means that our previous test (Figures 17 and 18) will eventually evolve (albeit slowly) to this same solution.

Post-processing Using Classification Theory

Returning to the unconstrained results, post-processing based on some classification theory results seems to "clean up" the solutions. Using some of the solutions as a "training set", 0.23 was determined to be the optimum value for partitioning the data into two classes, host material and flaw (see Chapter VI). If we filter our first test from Test Set #2 by assigning 0 to all variables less than 0.23, we obtain the solution shown in Figure 22.

3. Some Preliminary Results Using Measured Data

Several tests that use actual measured data have been performed to validate the model. Results of a few of those tests will be presented in the following.

A 0.11 inches-thick work-piece of graphite epoxy, in the form of woven fiber, has been used for measurement in the laboratory. Holes at various depths have been drilled into this work-piece, as shown in Figures 23-25. A multi-frequency measurement of the work-piece has been performed, as explained in Chapter V. For the test, an algorithm based on a ten-layer, five-frequency model has been chosen. Figures 26-30 show the plots of the real and imaginary parts of the measured data, B , for the frequencies of 2, 4, 8, 12 and 16 MHz.

In order to reconstruct the flaws from the measured data, a normalization process is performed. First, the left hand side, Y , of equation (II - 1) is calculated by using the flaw as the unknown X ; these results are shown in Figures 31-35. Next, the real and imaginary parts of the measured data, B , are normalized with respect to Y at each frequency. This normalization procedure attempts to compensate for amplitude and phase variations during the data acquisition. The sup-norm of the real and imaginary parts of B , as well as Y , versus frequency are depicted in Figure 36. It is noted that the real and imaginary sup-norms of B are greater than the real and imaginary sup-norms of Y at all frequencies. The normalized value of B is then used to solve for the unknown X of (II - 1).

Figures 37-39 are samples of the real and imaginary parts of the 64×64 elements of the operator, A , that appears in (II - 1), for different layers and frequencies. The elements of the operator are highly localized around the origin, as indicated in Figures 37-39. This simply states that the coupling effect is localized in physical space.

Figures 40-42 show the results of the reconstruction of the flaw. The constraint of positive conductivity is used; the Levenberg-Marquardt parameter is set to 1.5, the number of iterations is 500 and the threshold is 0.3. Figure 43 shows the flaw and its reconstruction in gray scale. The flaws of layers two to six have been somewhat reconstructed. Excessive noise is accumulated in layers one, two, seven and ten, which makes the flaws somewhat unrealisable.

Although the reconstruction with actual data is not perfect at this preliminary stage, it is very promising for further investigations. This shortcoming is in part due to the fact that the theoretical model for this study is based on the Born approximation. For the future study a more accurate and realistic model for reconstruction is proposed, which is discussed in the following chapter.

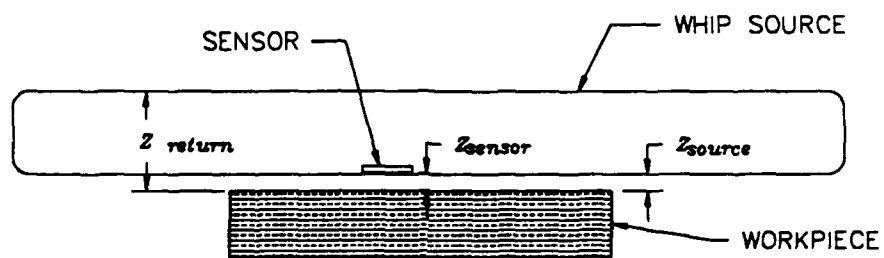


Figure 1
Probe-Sensor-Workpiece Arrangement

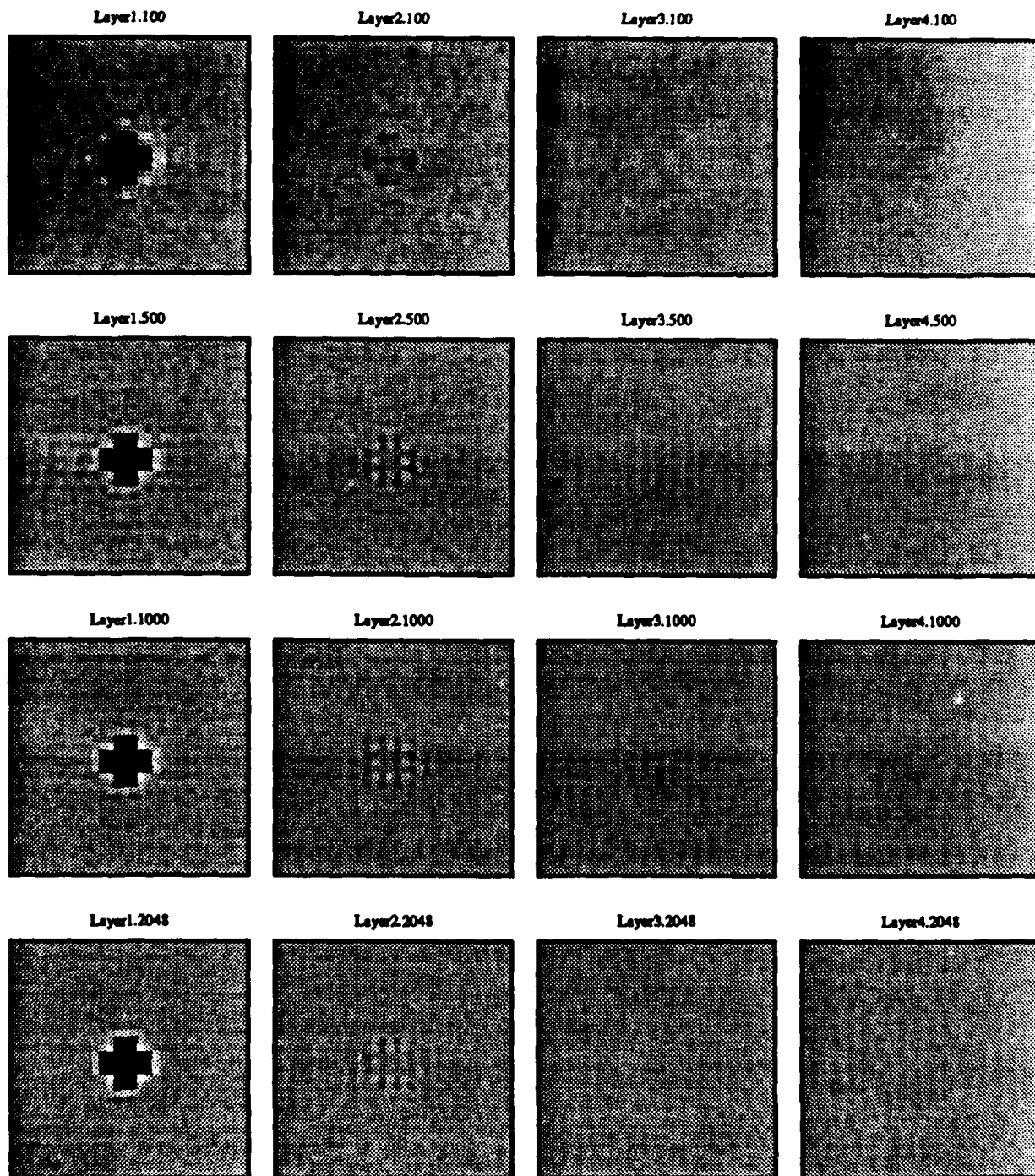


Figure 2
Reconstruction of flaw1
5 Frequencies: 1 3 5 7 9 MHz

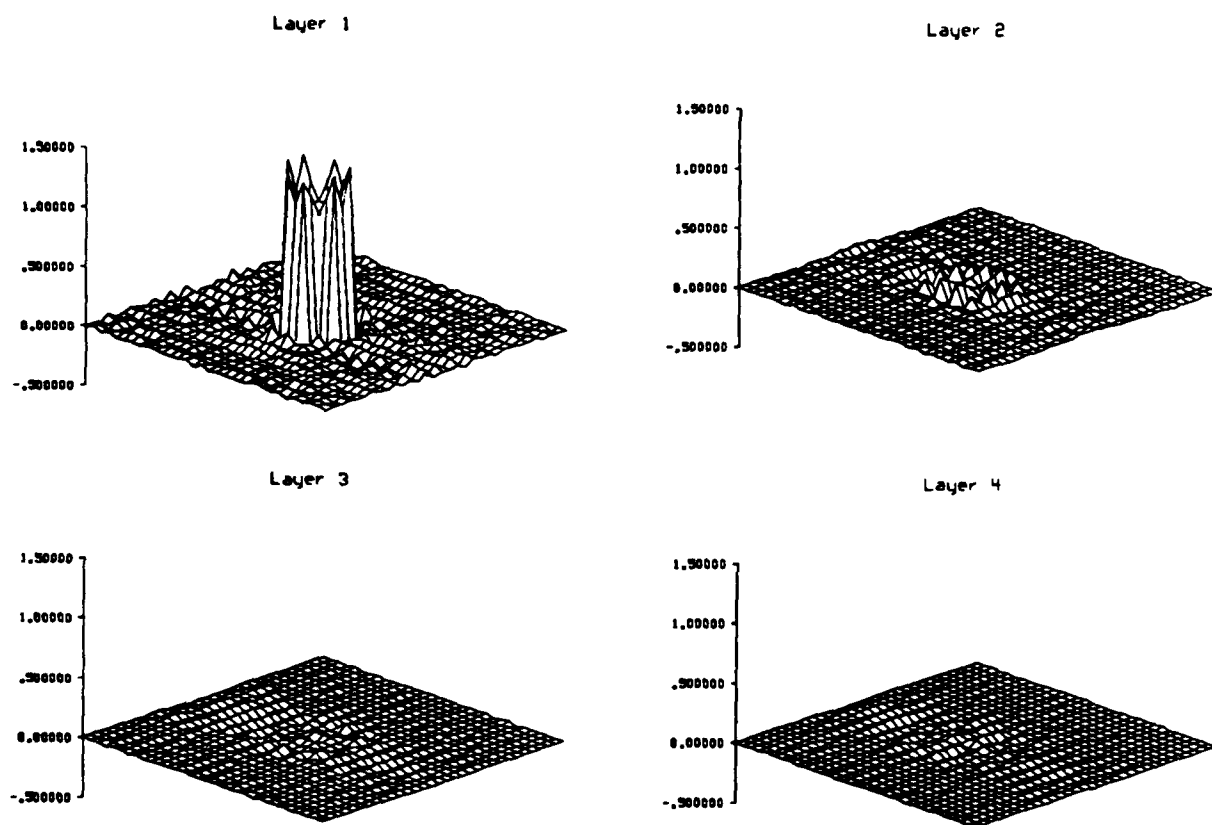


Figure 3
 3D Reconstruction of flaw1
 5 Frequencies: 1 3 5 7 9 MHz
 2048 Unconstrained Iterations

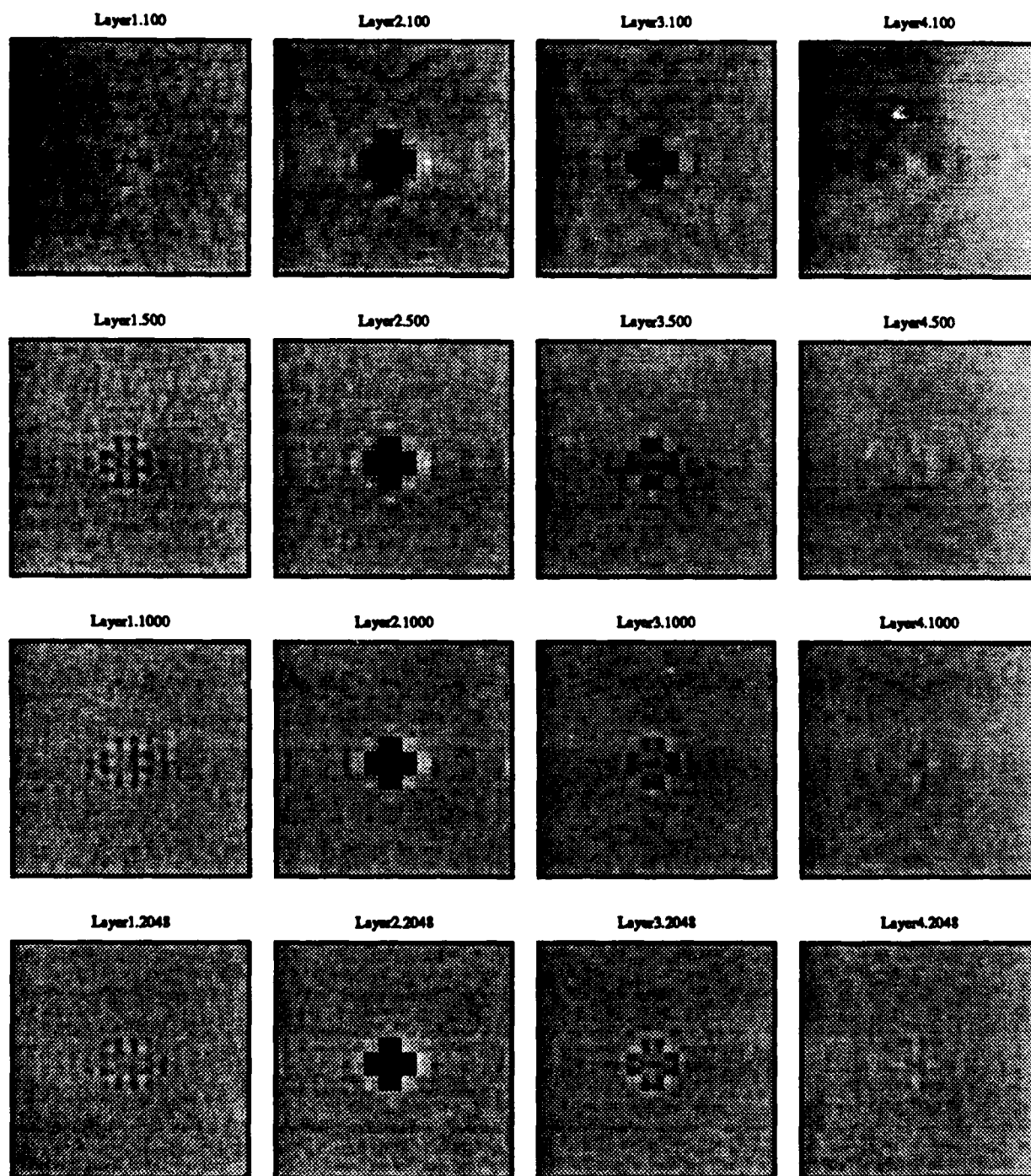


Figure 4
Reconstruction of flaw2
5 Frequencies: 1 3 5 7 9 MHz

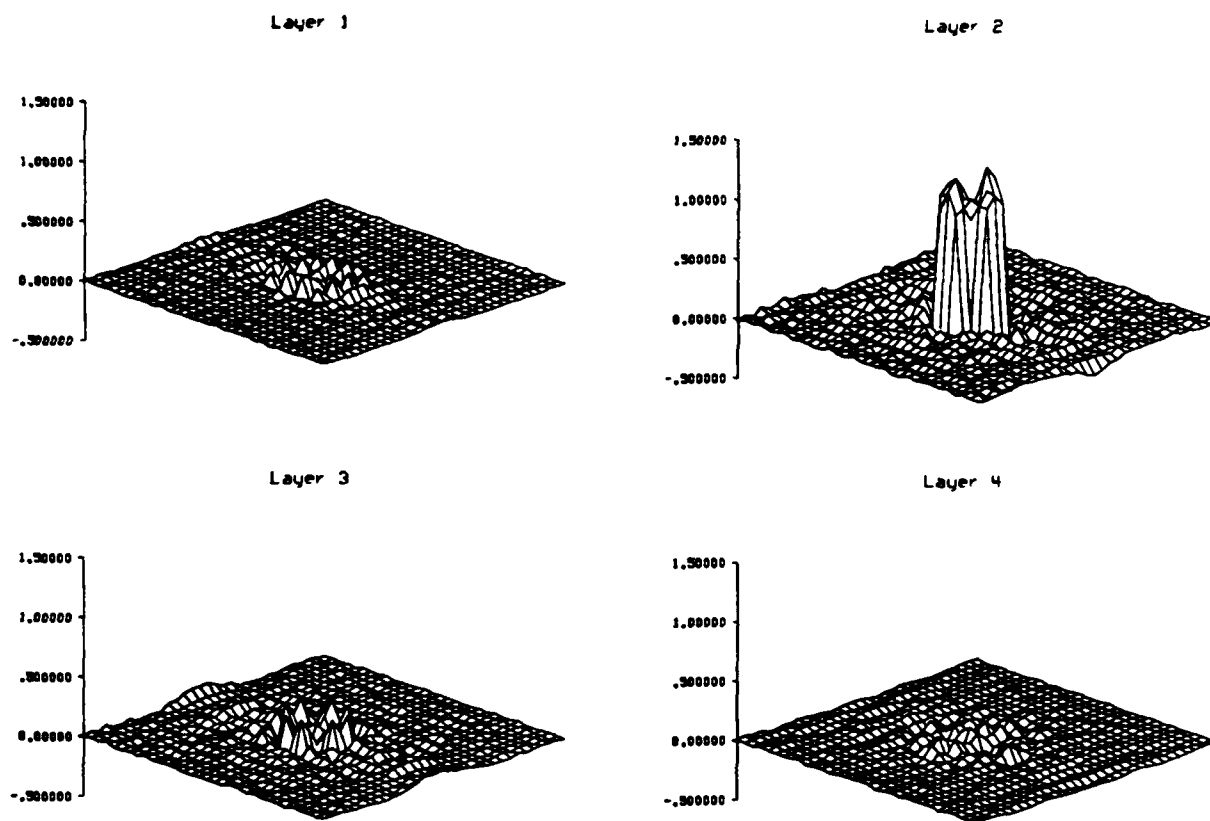


Figure 5
3D Reconstruction of flaw2
5 Frequencies: 1 3 5 7 9 MHz
2048 Unconstrained Iterations

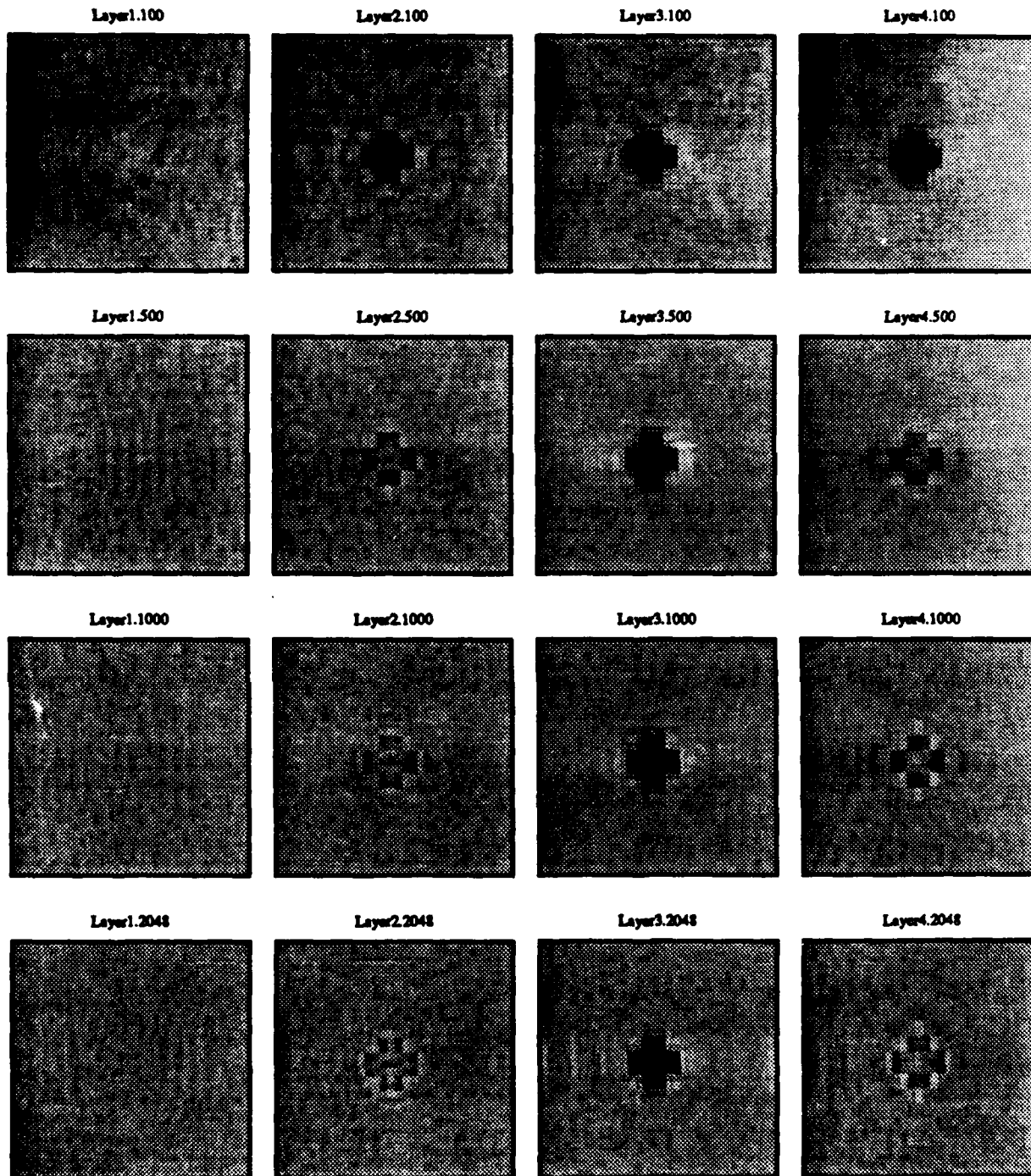


Figure 6
Reconstruction of flaw3
5 Frequencies: 1 3 5 7 9 MHz

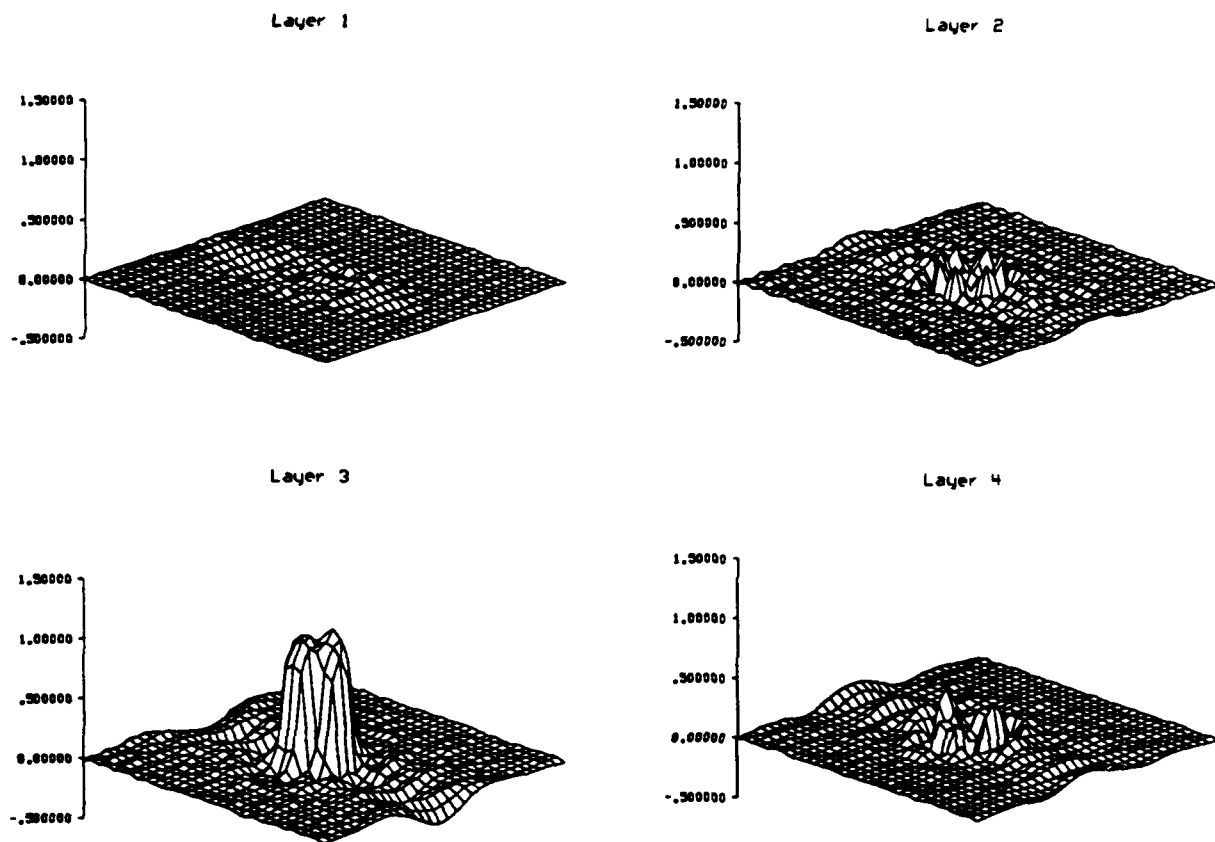


Figure 7
 3D Reconstruction of flaw3
 5 Frequencies: 1 3 5 7 9 MHz
 2048 Unconstrained Iterations

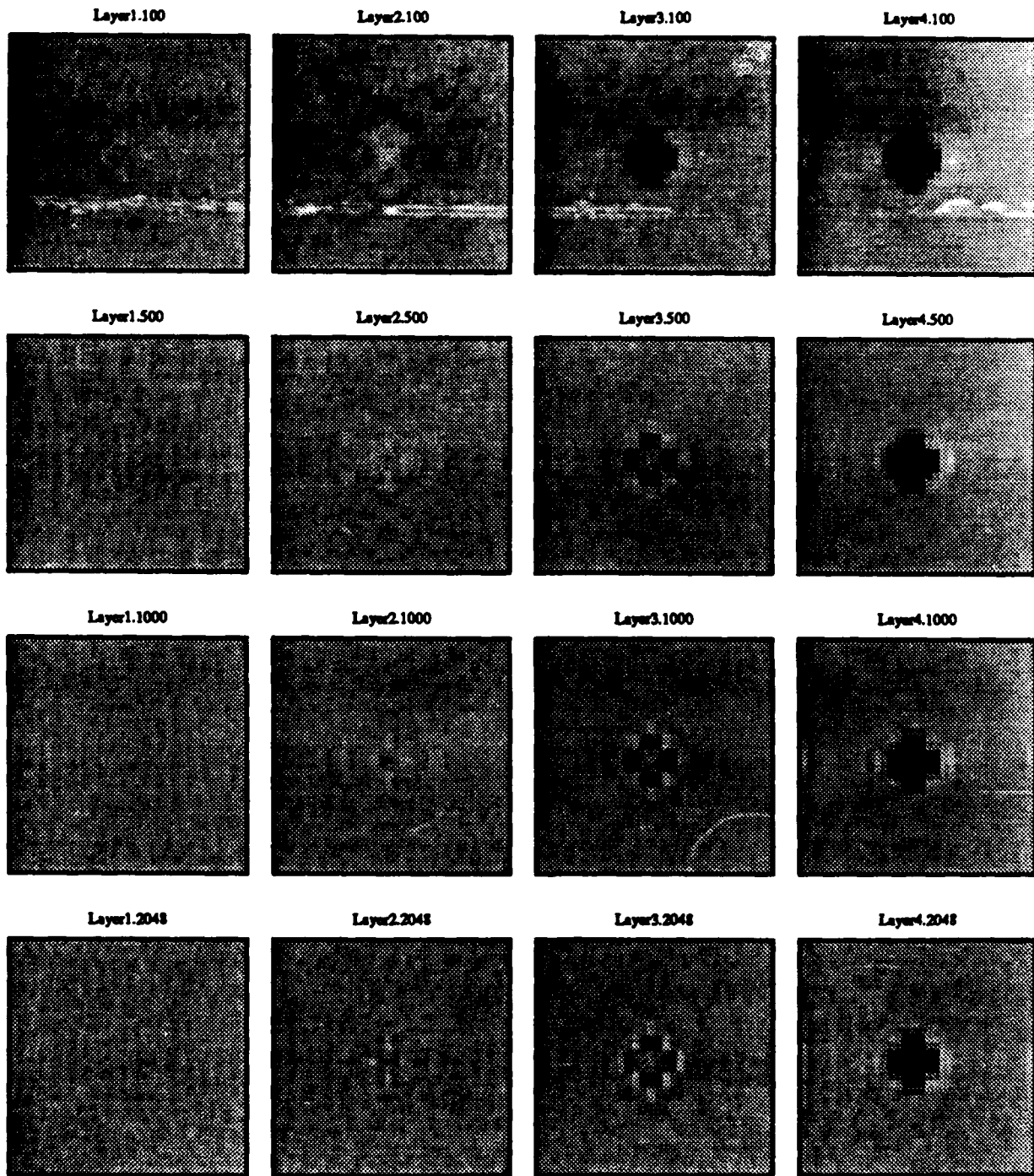


Figure 8
Reconstruction of flaw4
5 Frequencies: 1 3 5 7 9 MHz

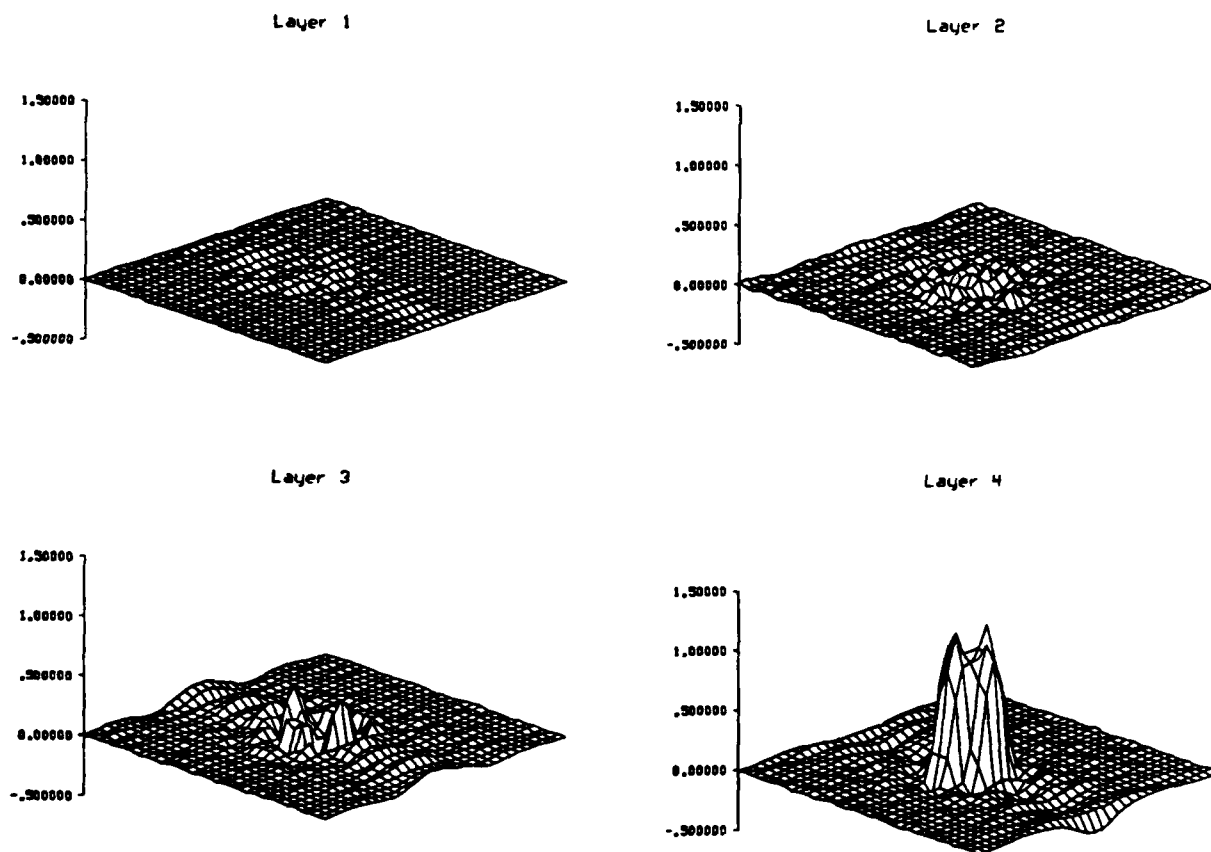


Figure 9
 3D Reconstruction of flaw4
 5 Frequencies: 1 3 5 7 9 MHz
 2048 Unconstrained Iterations

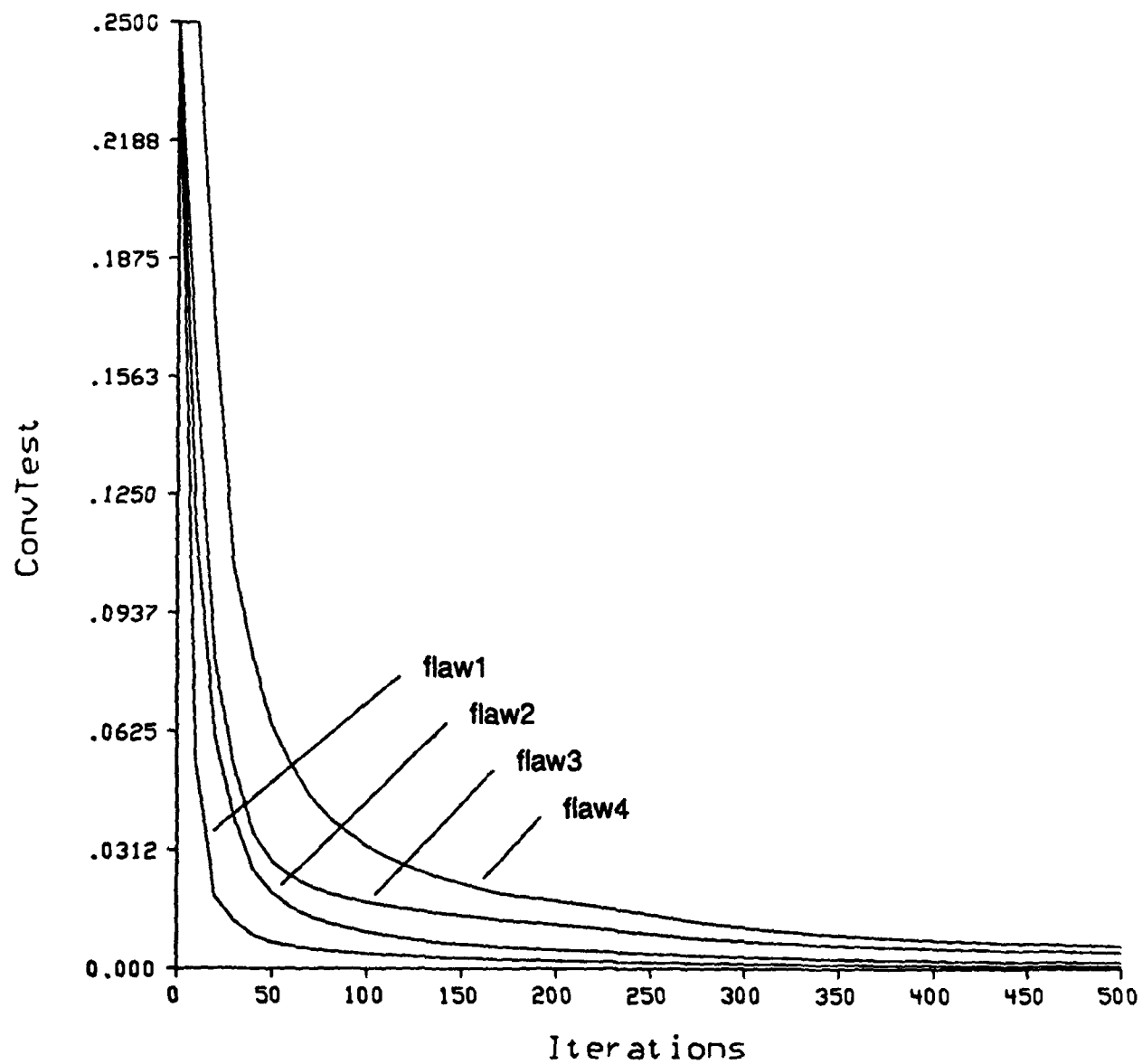


Figure 10
Convergence Measure
5 Frequencies: 1 3 5 7 9 MHz

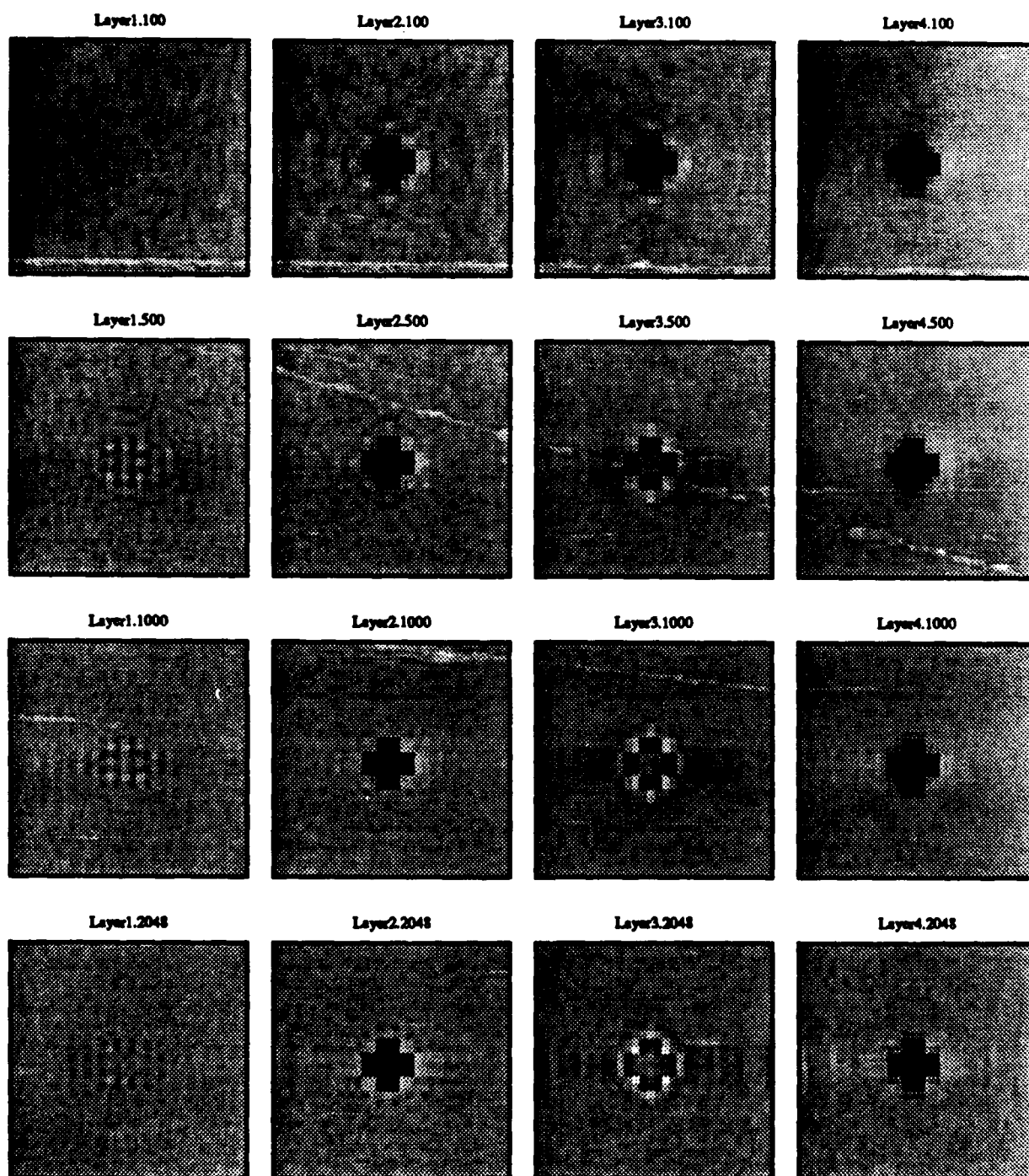


Figure 11
 Reconstruction of flaw24
 5 Frequencies: 1 3 5 7 9 MHz

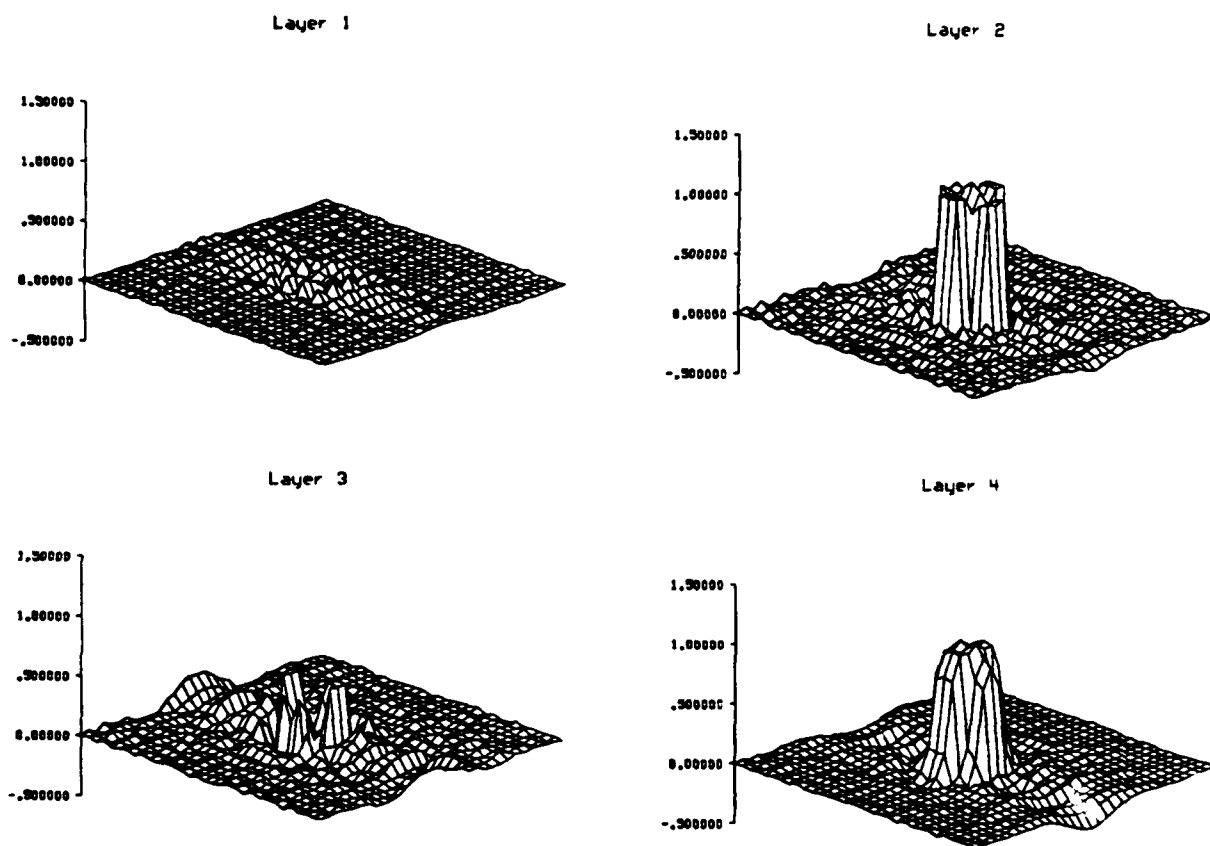


Figure 12
 3D Reconstruction of flaw24
 5 Frequencies: 1 3 5 7 9 MHz
 2048 Unconstrained Iterations

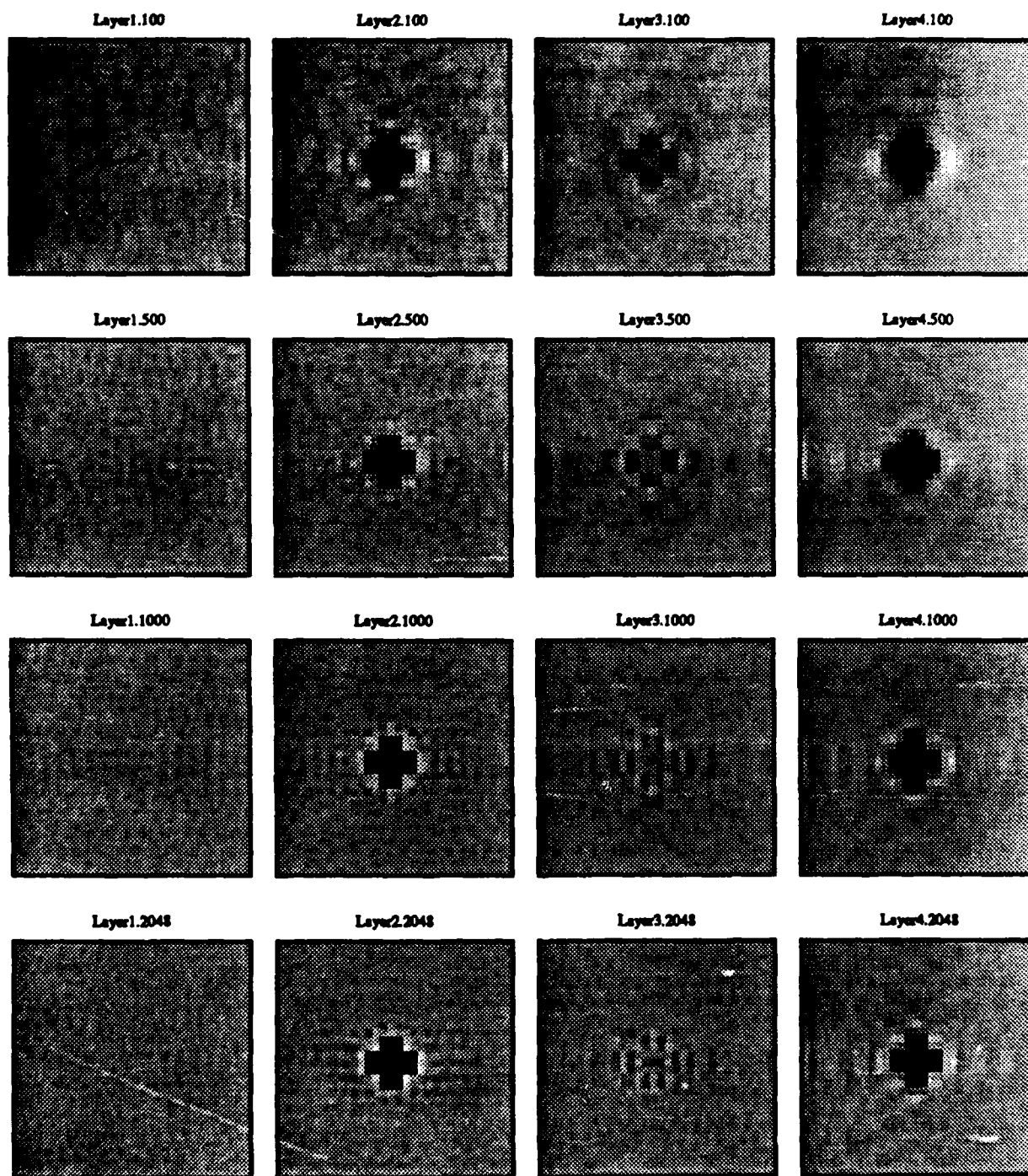


Figure 13
 Reconstruction of flaw24
 5 Frequencies: 1 5 10 20 30 MHz

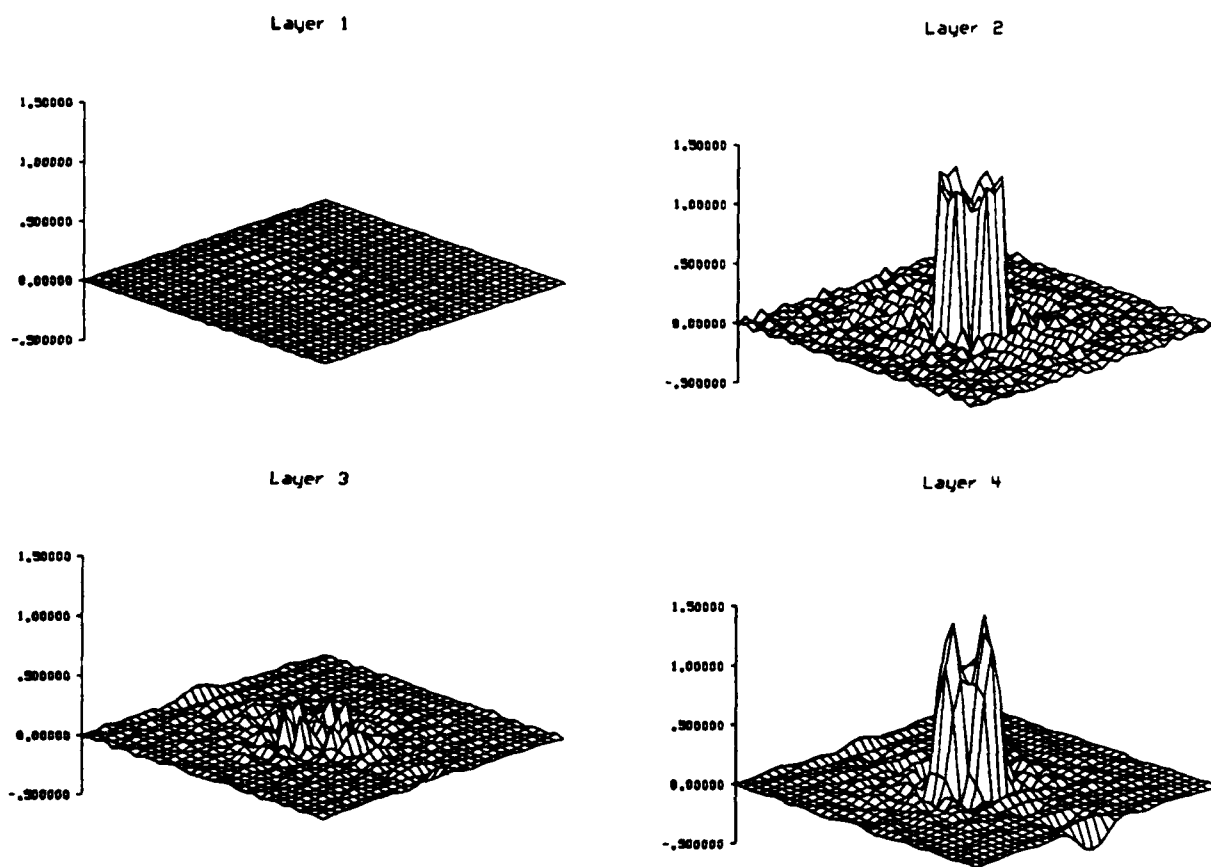


Figure 14
 3D Reconstruction of flaw24
 5 Frequencies: 1 5 10 20 30 MHz
 2048 Unconstrained Iterations

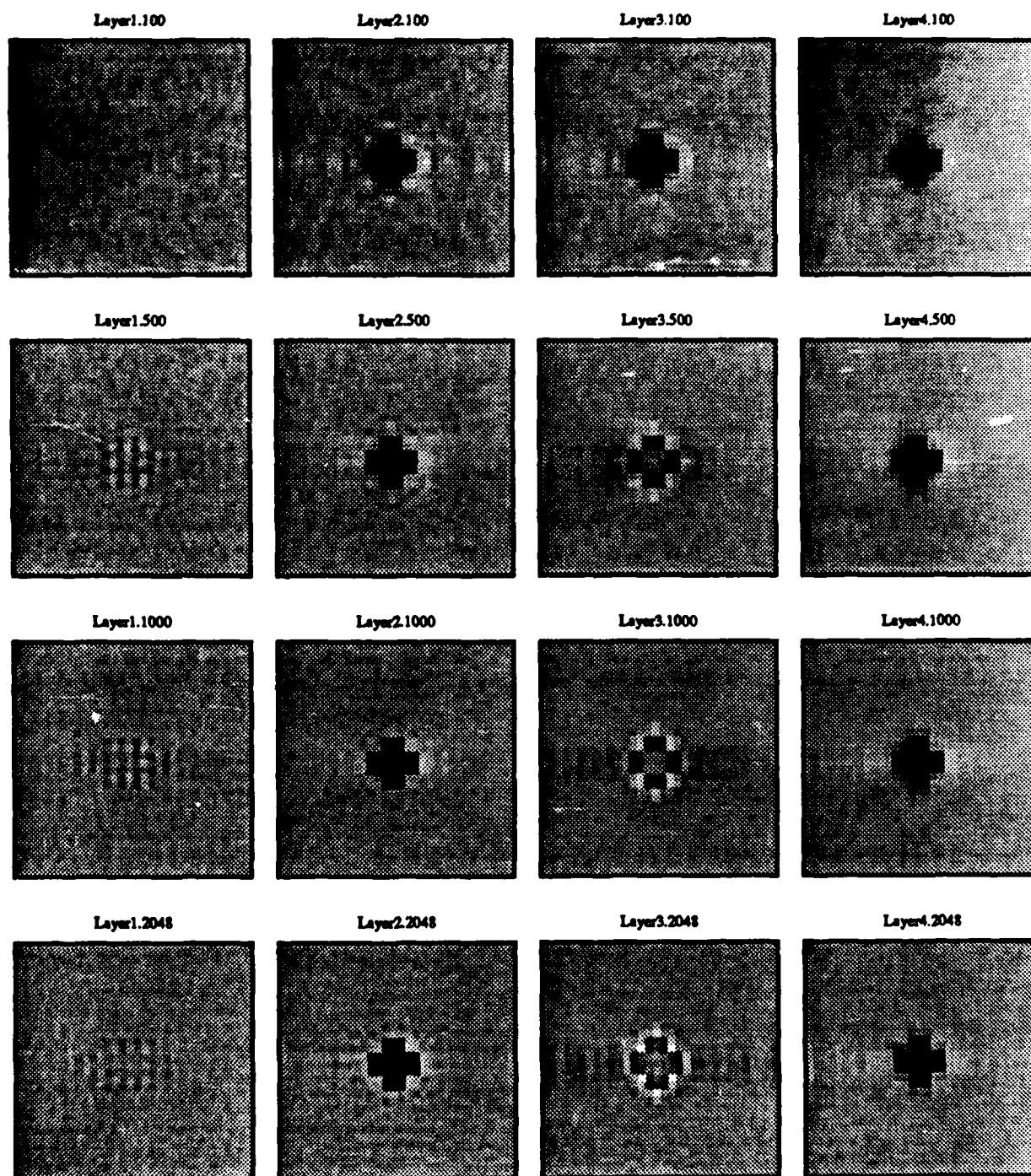


Figure 15
Reconstruction of flaw24
9 Frequencies: 1 2 3 4 5 6 7 8 9 MHz.

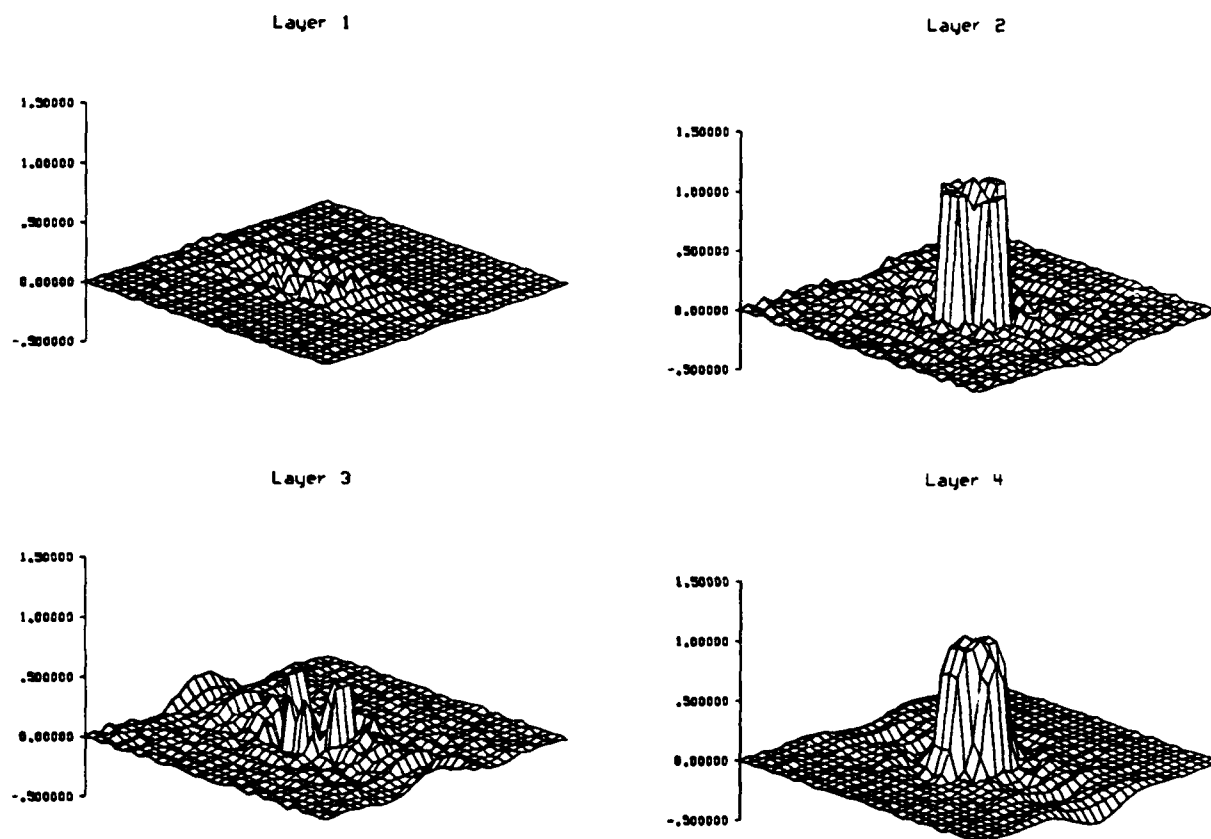


Figure 16
 3D Reconstruction of flaw24
 9 Frequencies: 1 2 3 4 5 6 7 8 9 MHz
 2048 Unconstrained Iterations

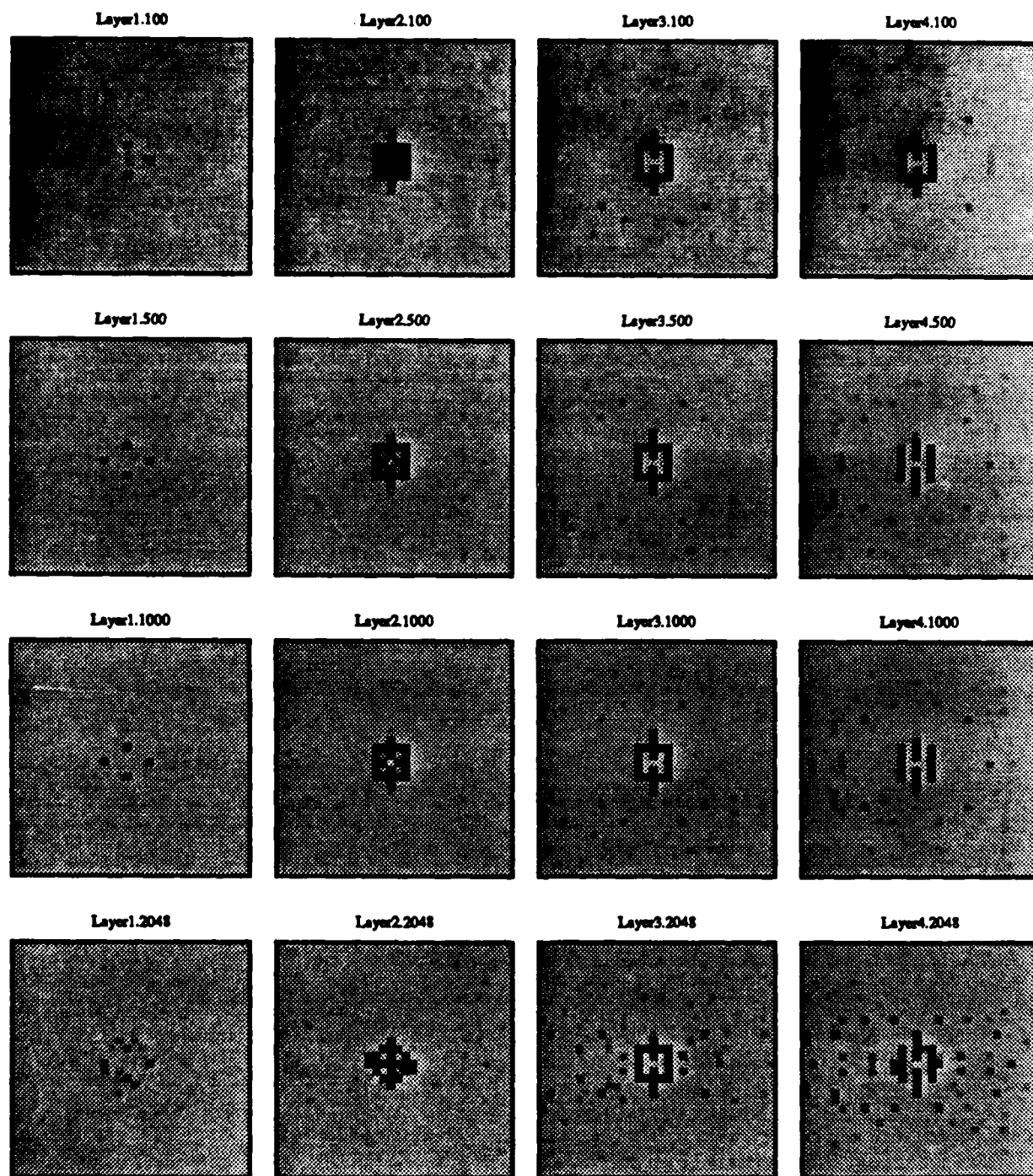


Figure 17
Reconstruction of flaw24
5 Frequencies: 1 3 5 7 9 MHz

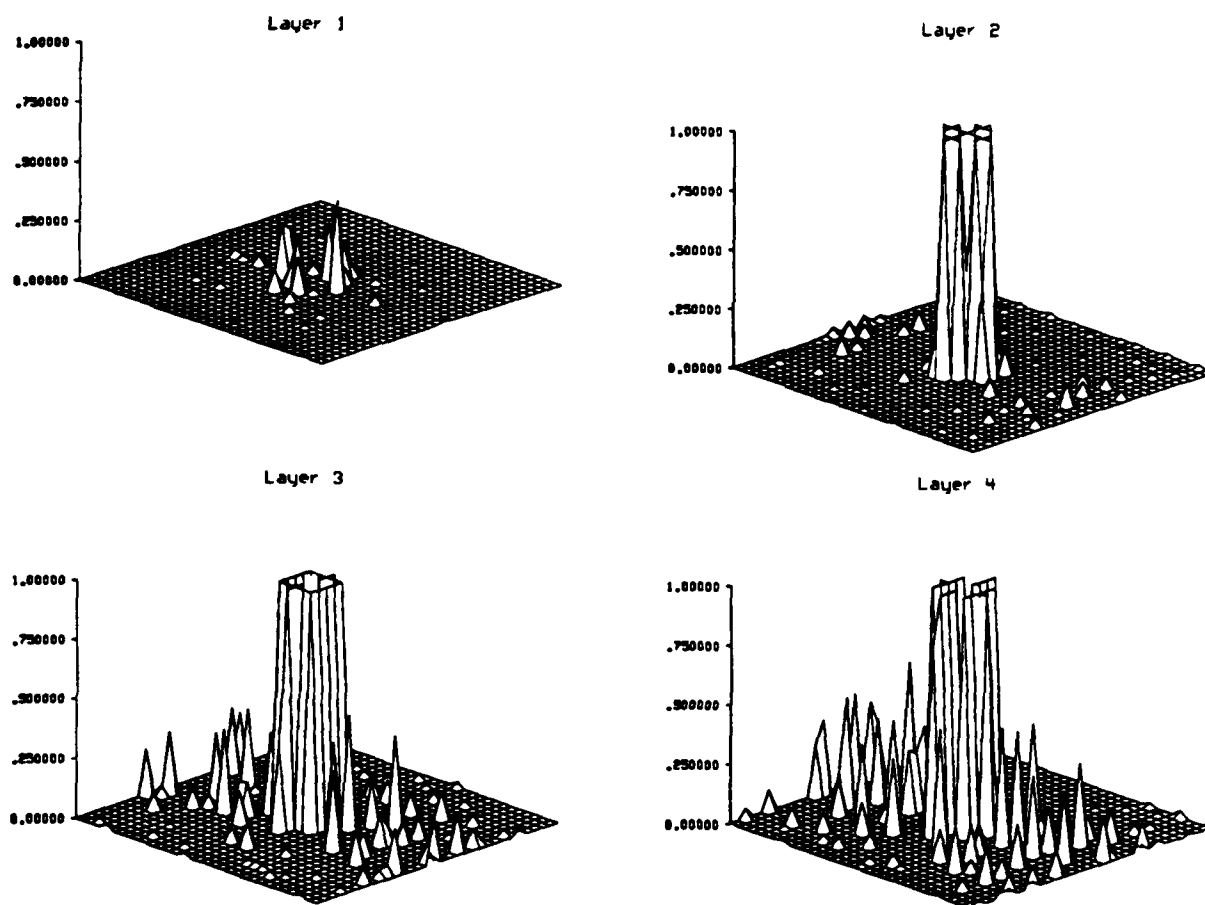


Figure 18
 3D Reconstruction of flaw24
 5 Frequencies: 1 3 5 7 9 MHz
 2048 Constrained Iterations

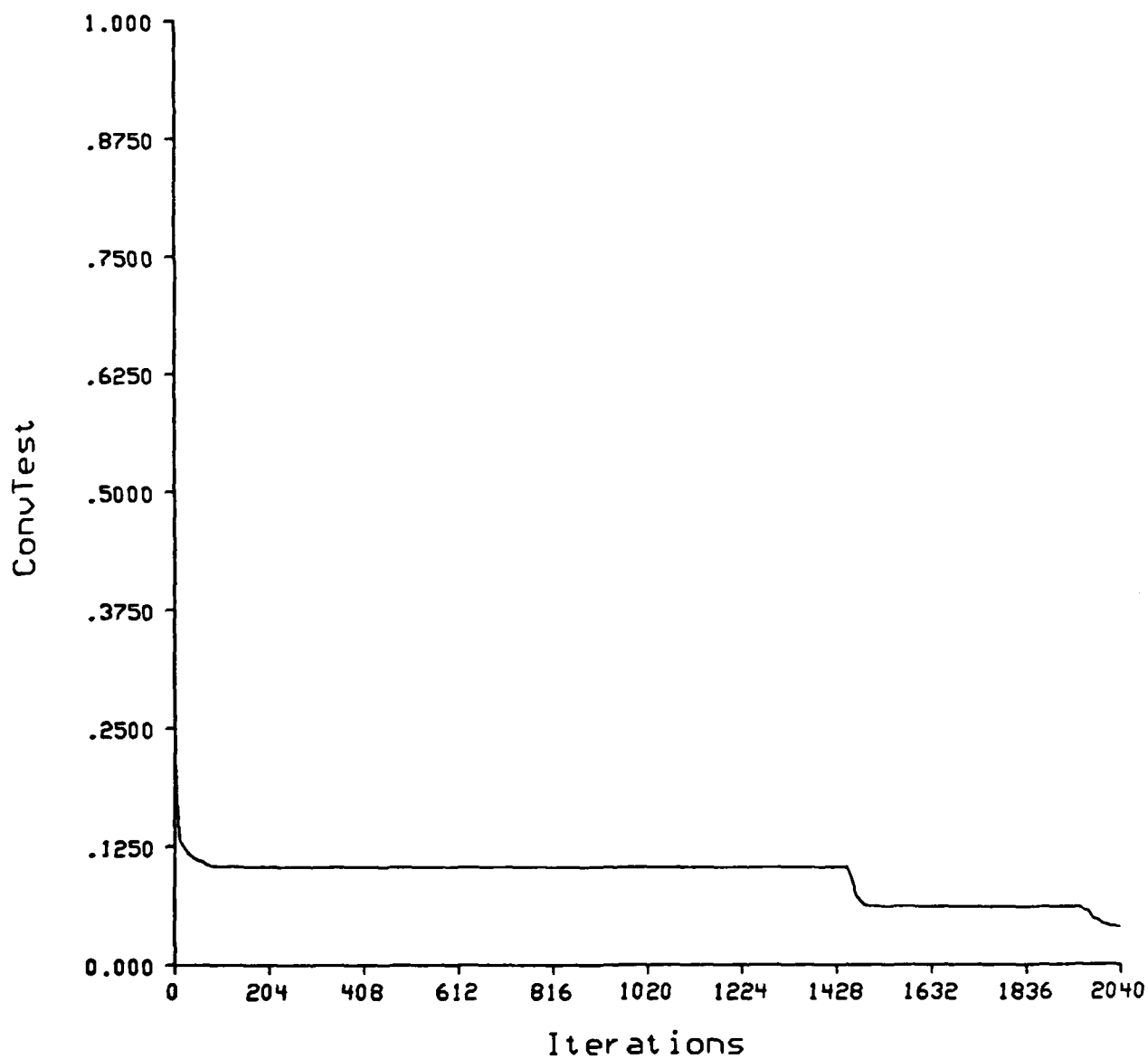


Figure 19
Convergence Measure
5 Frequencies: 1 3 5 7 9 MHz, Constrained

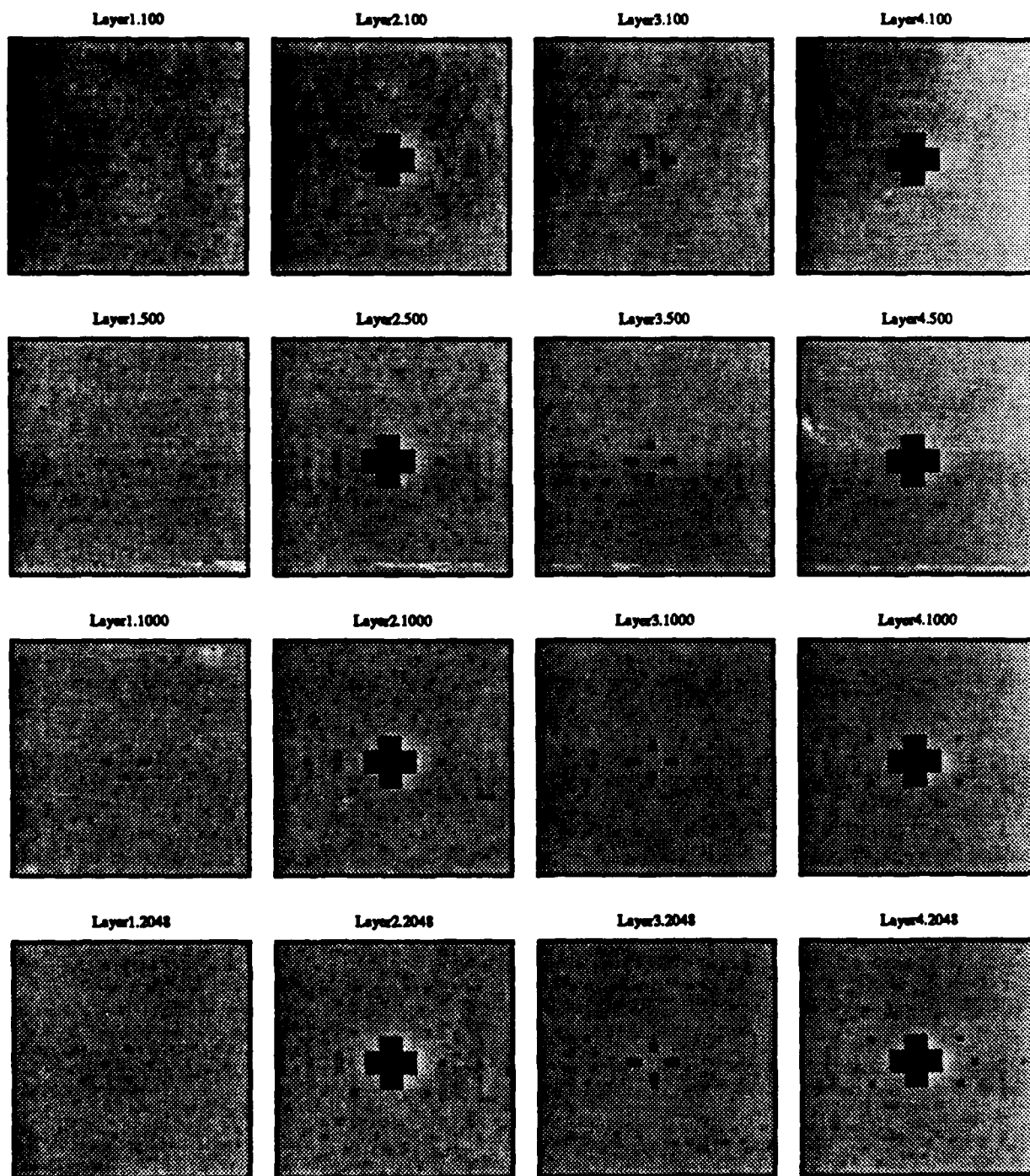


Figure 20
 Reconstruction of flaw24
 5 Frequencies: 1 3 5 7 9 MHz

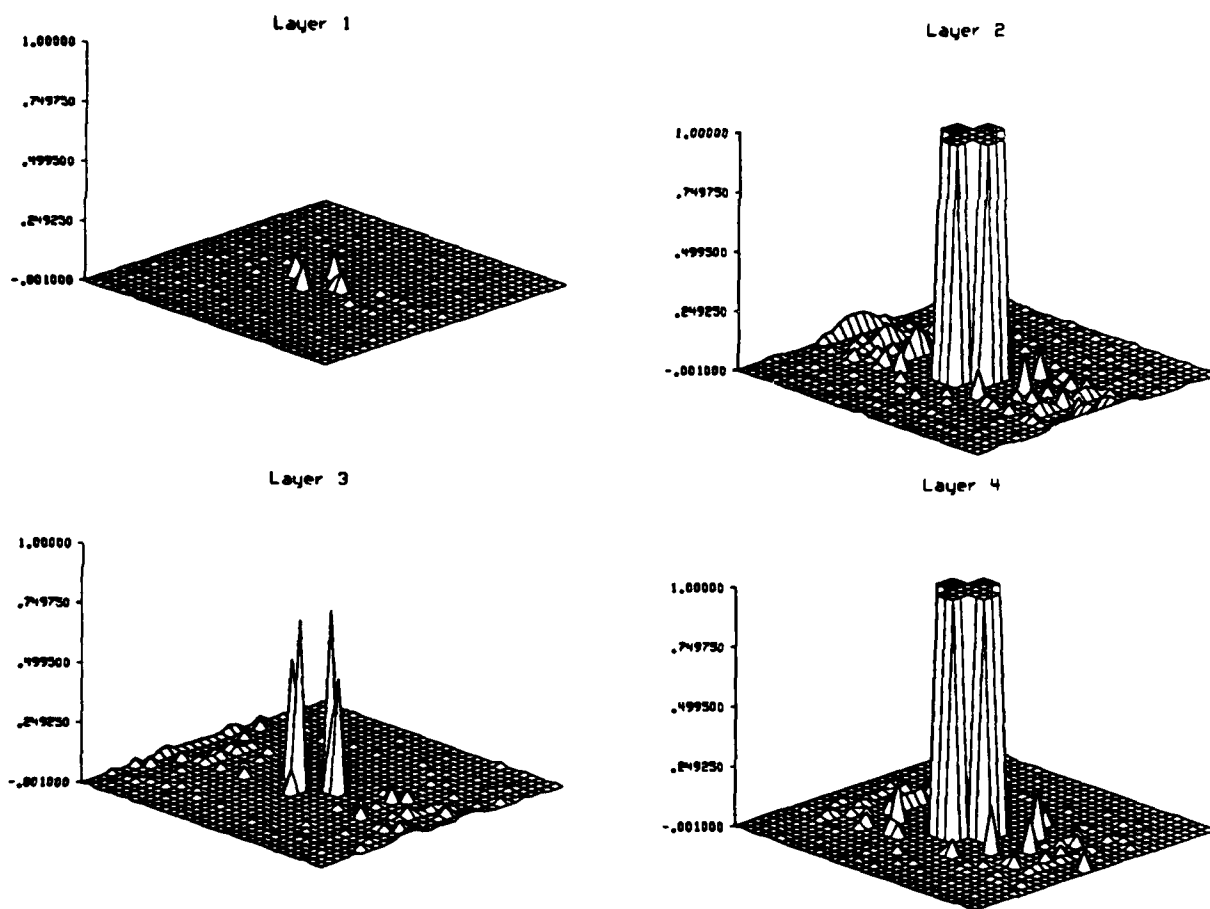


Figure 21
 3D Reconstruction of flaw
 5 Frequencies: 1 3 5 7 9 MHz
 2048 Constrained Iterations

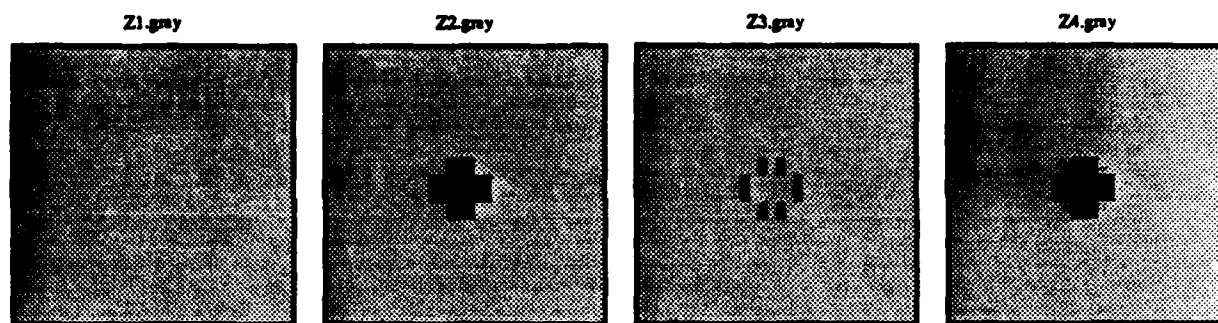


Figure 22
Post-processed Solution
Threshold = 0.23

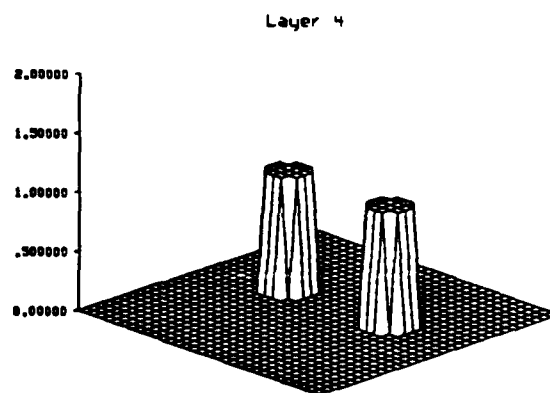
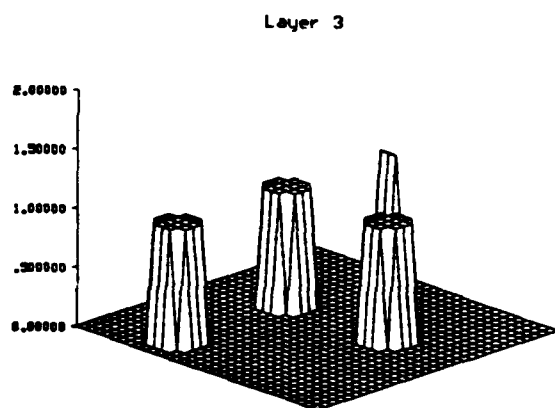
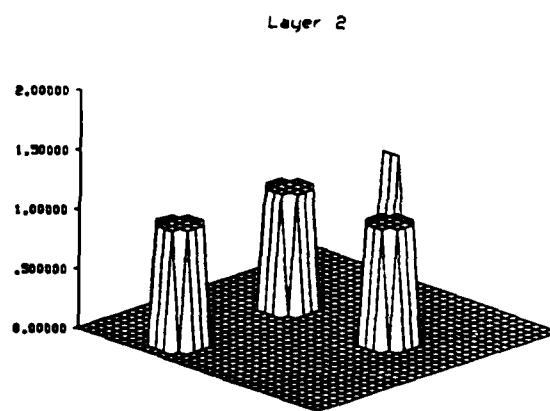
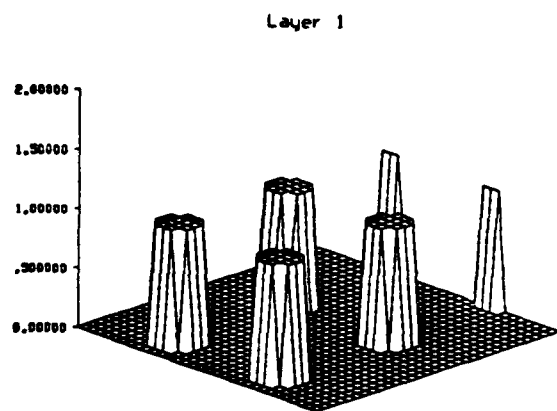


Figure 23: Ten layered graphite epoxy with some drill hole flaws in various depths; layer 1 - layer 4.

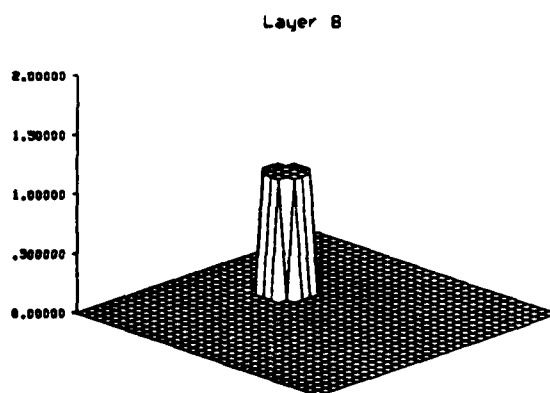
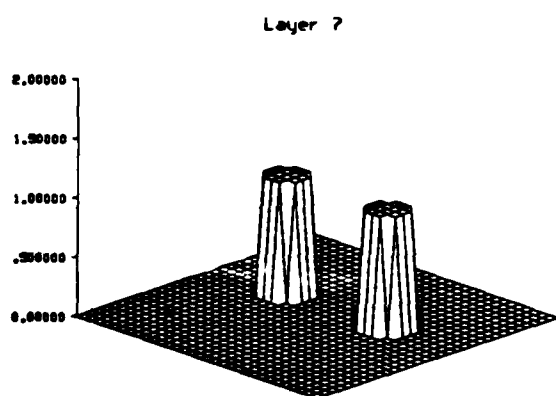
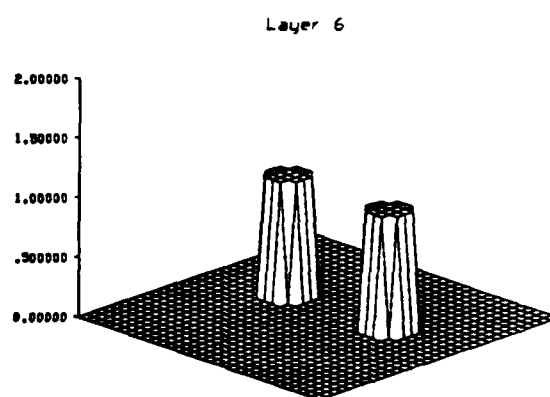
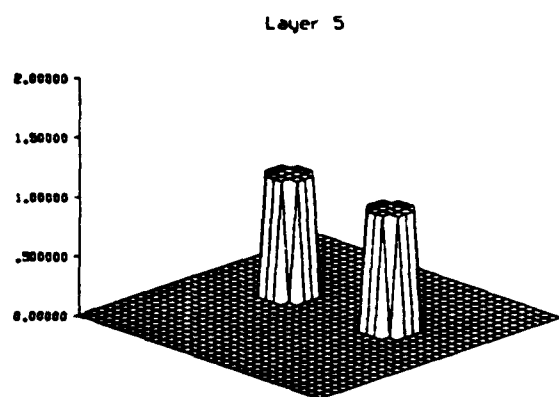


Figure 24: Ten layered graphite epoxy with some drill hole flaws in various depths; layer 5 - layer 8.

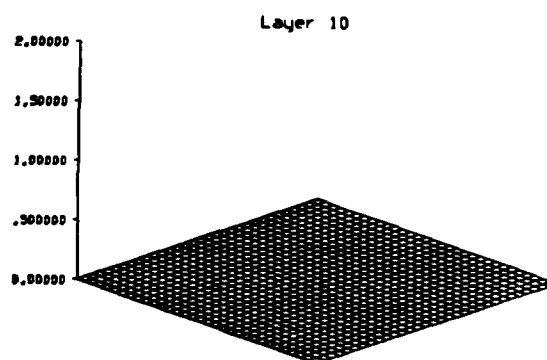
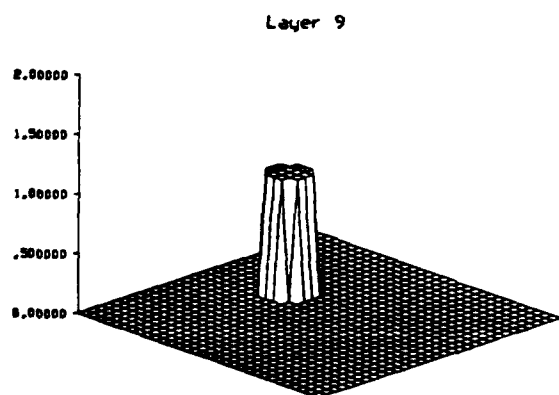


Figure 25: Ten layered graphite epoxy with some drill hole flaws in various depths; layer 9 - layer 10.

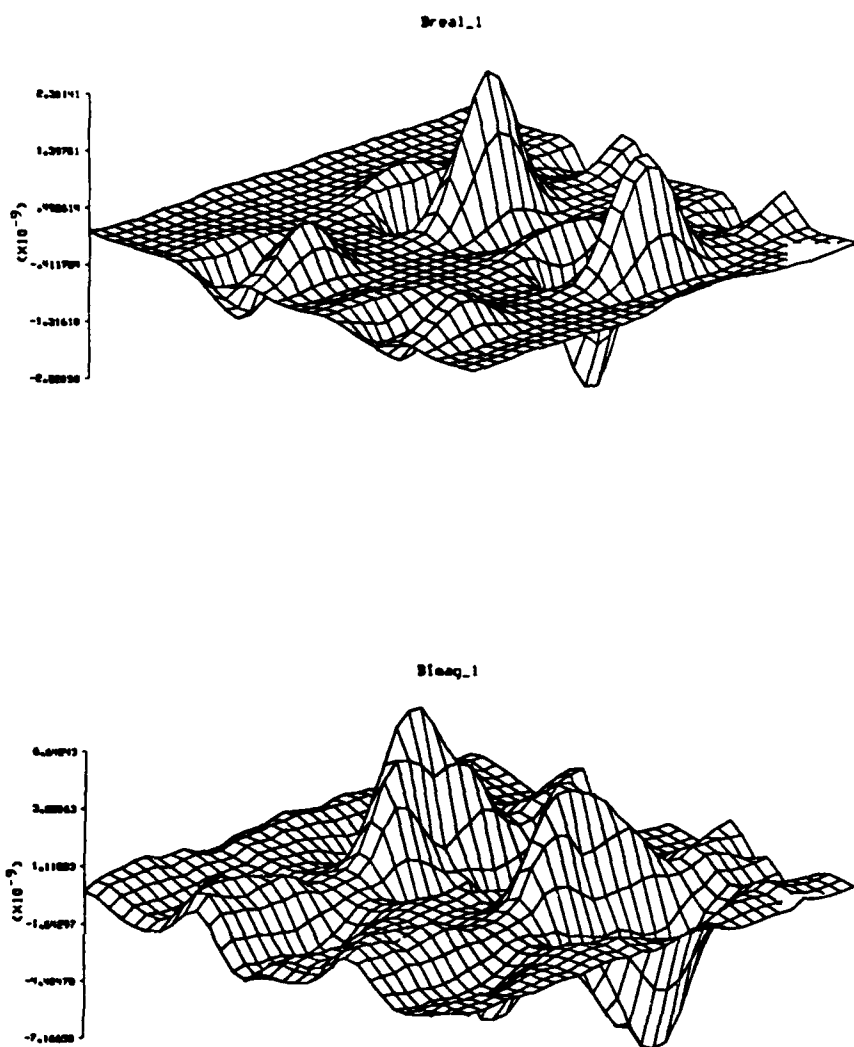


Figure 26: Real and Imaginary parts of the measured data, B , at 2 MHz.

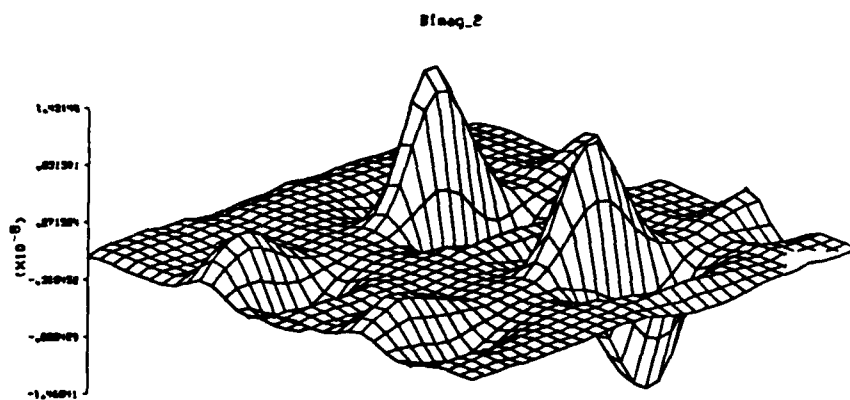
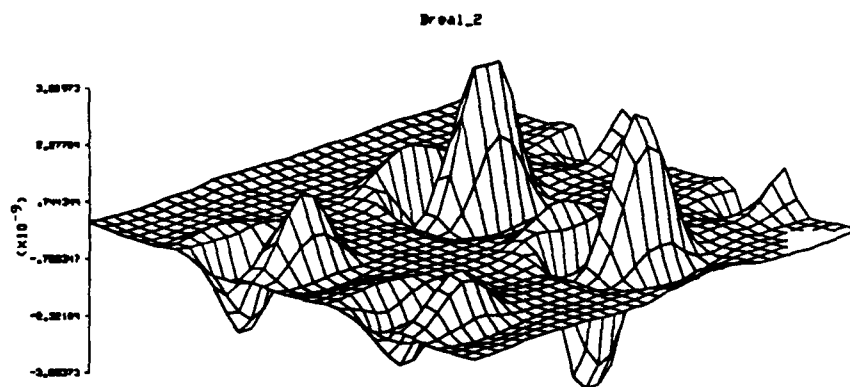


Figure 27: Real and Imaginary parts of the measured data, B , at 4 MHz.

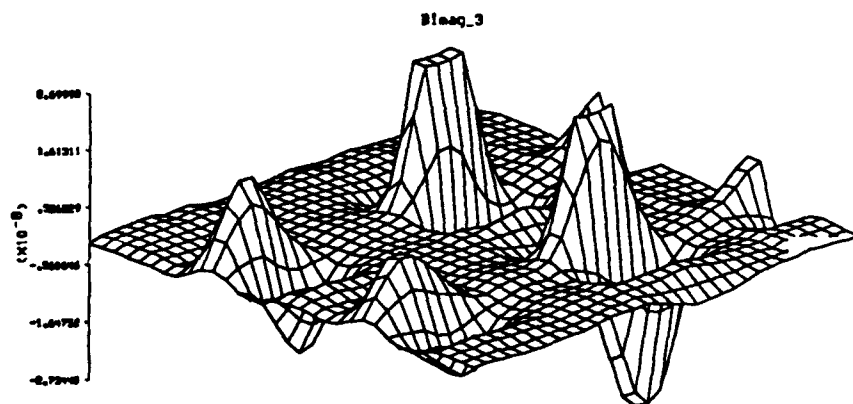
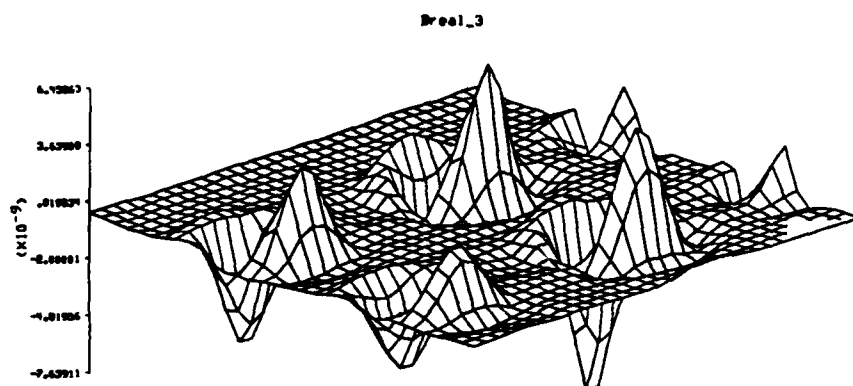


Figure 28: Real and Imaginary parts of the measured data, B , at 8 MHz.

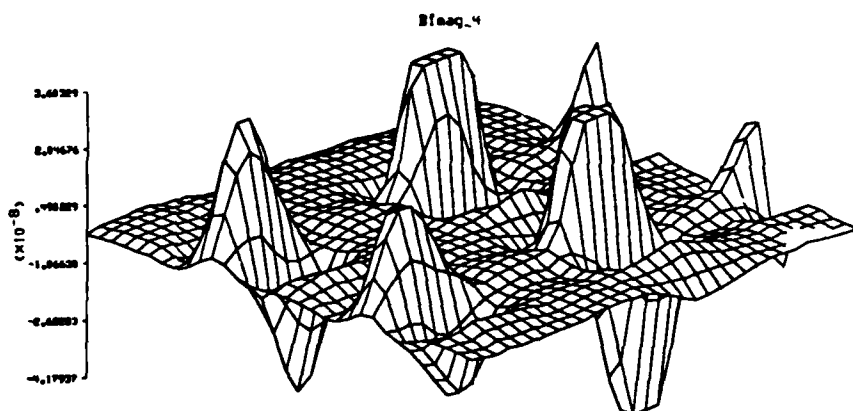
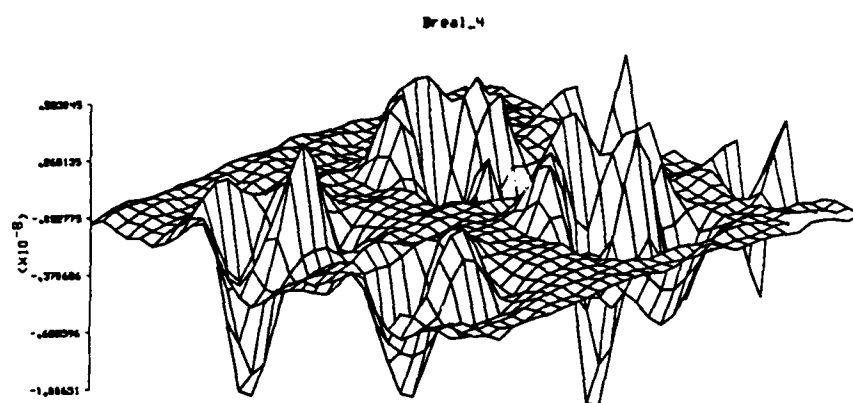


Figure 29: Real and Imaginary parts of the measured data, B , at 12 MHz.

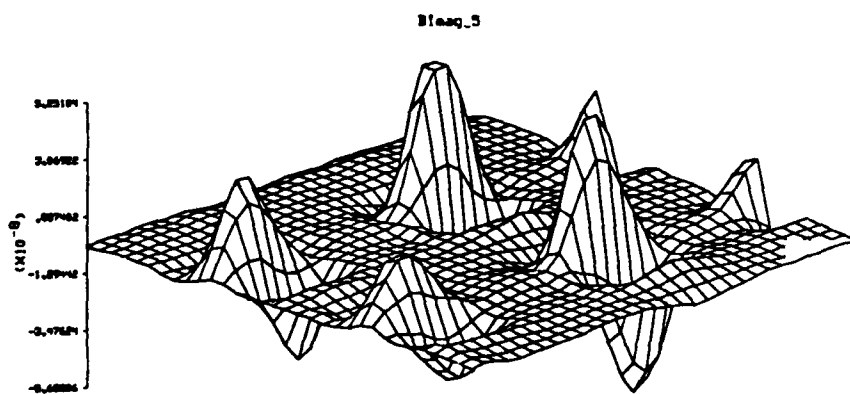
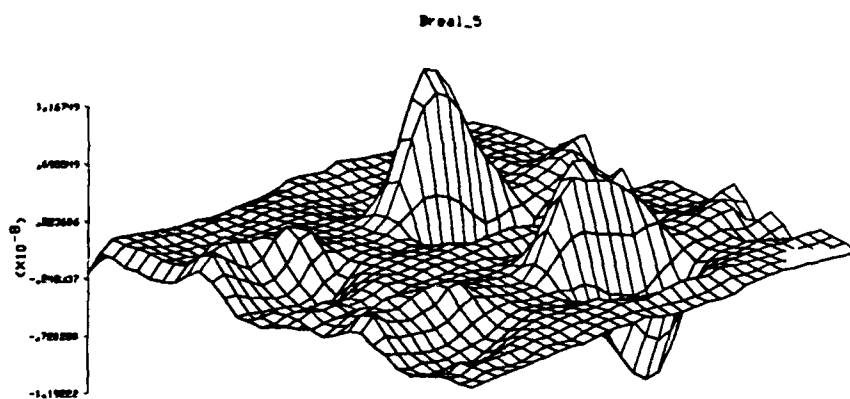


Figure 30: Real and Imaginary parts of the measured data, B , at 16 MHz.

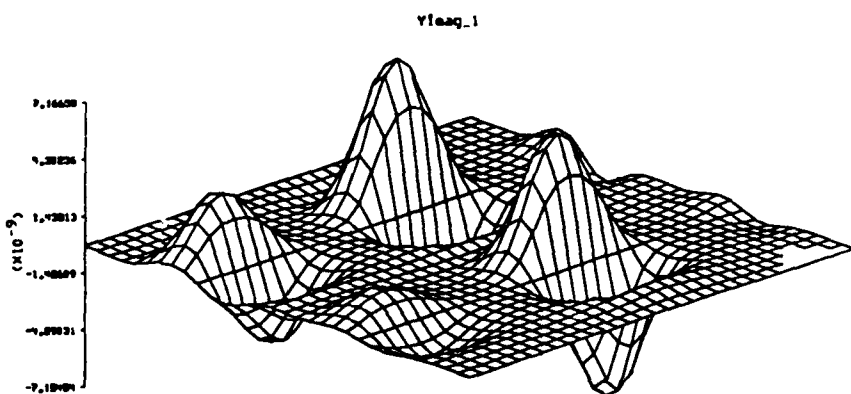
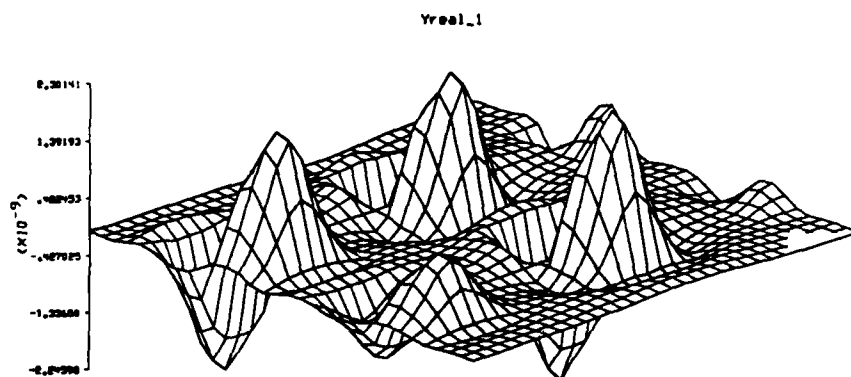


Figure 31: Real and Imaginary parts of the measured data, Y , at 2 MHz.

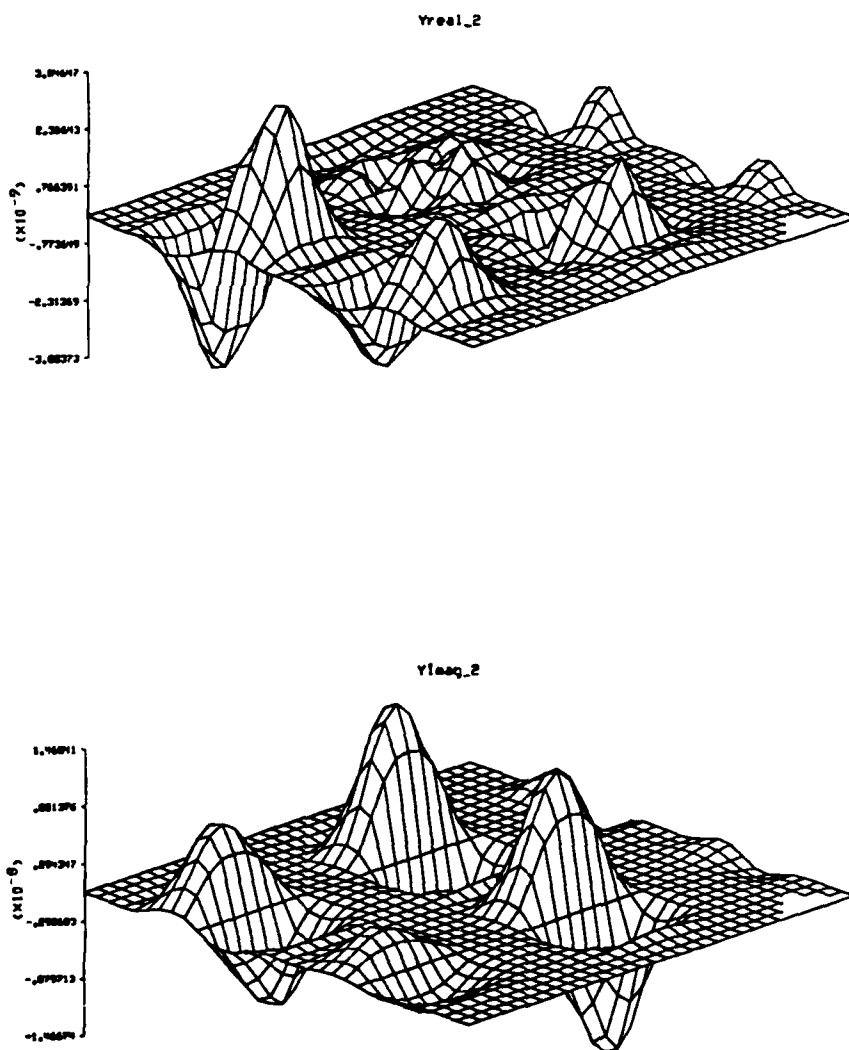


Figure 32: Real and Imaginary parts of the measured data, Y , at 4 MHz.

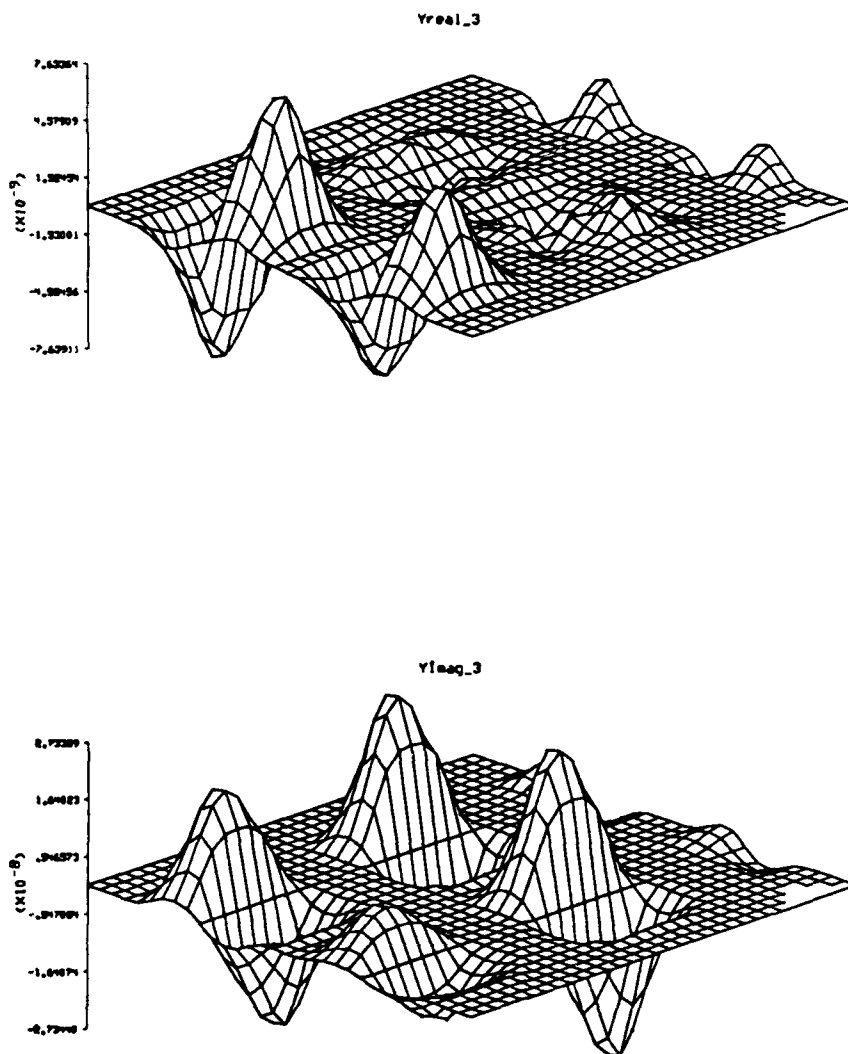


Figure 33: Real and Imaginary parts of the measured data, Y , at 8 MHz.

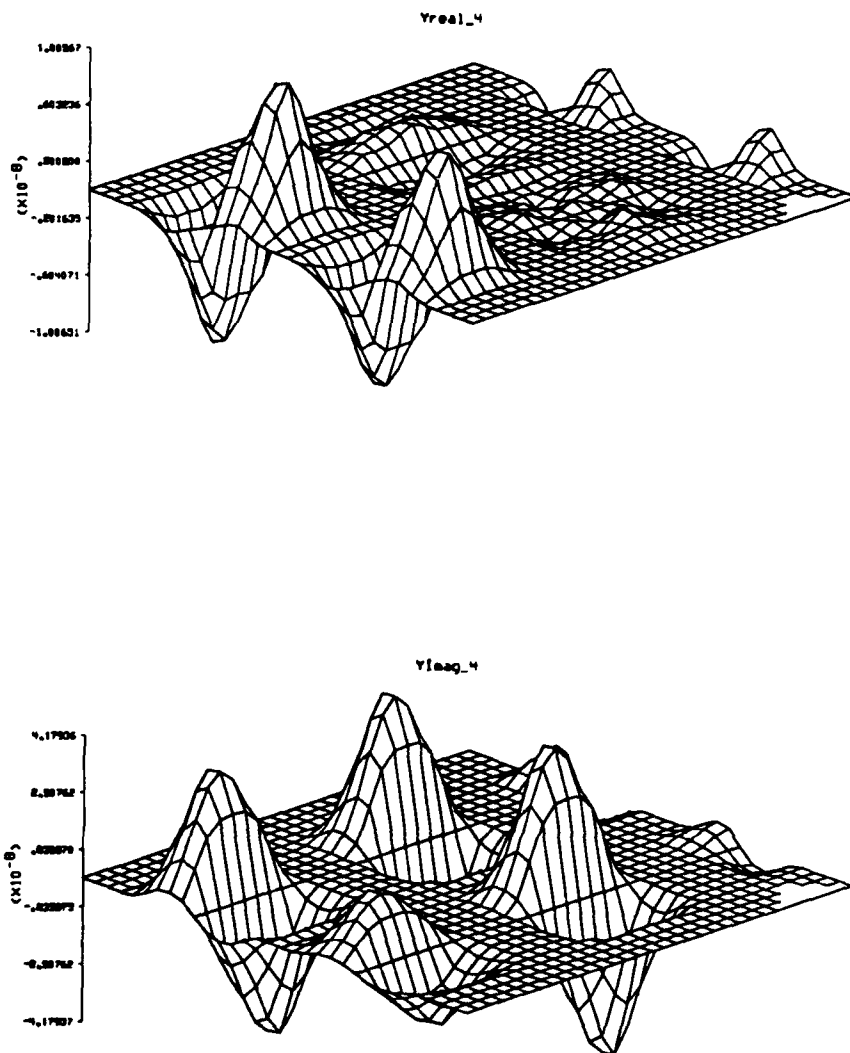


Figure 34: Real and Imaginary parts of the measured data, Y , at 12 MHz.

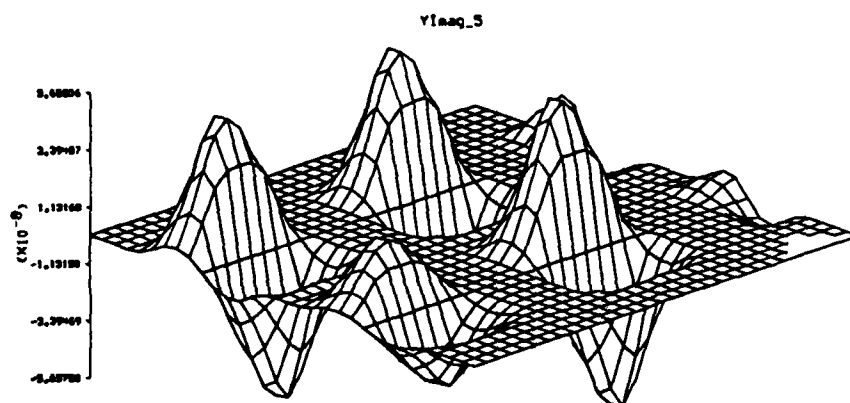
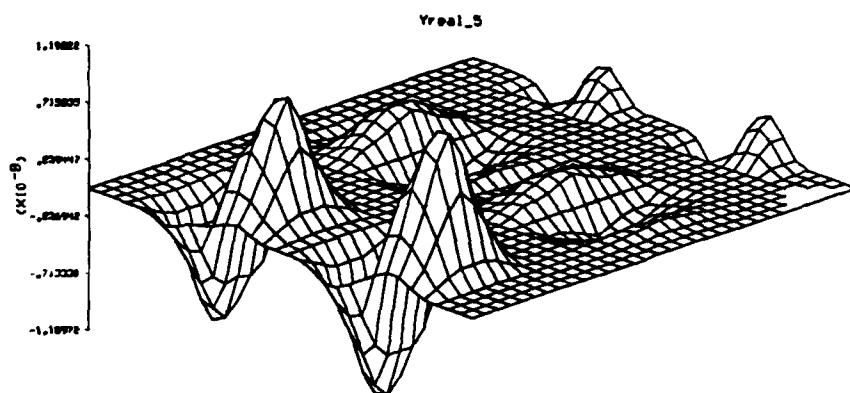


Figure 35: Real and Imaginary parts of the measured data, Y , at 16 MHz.

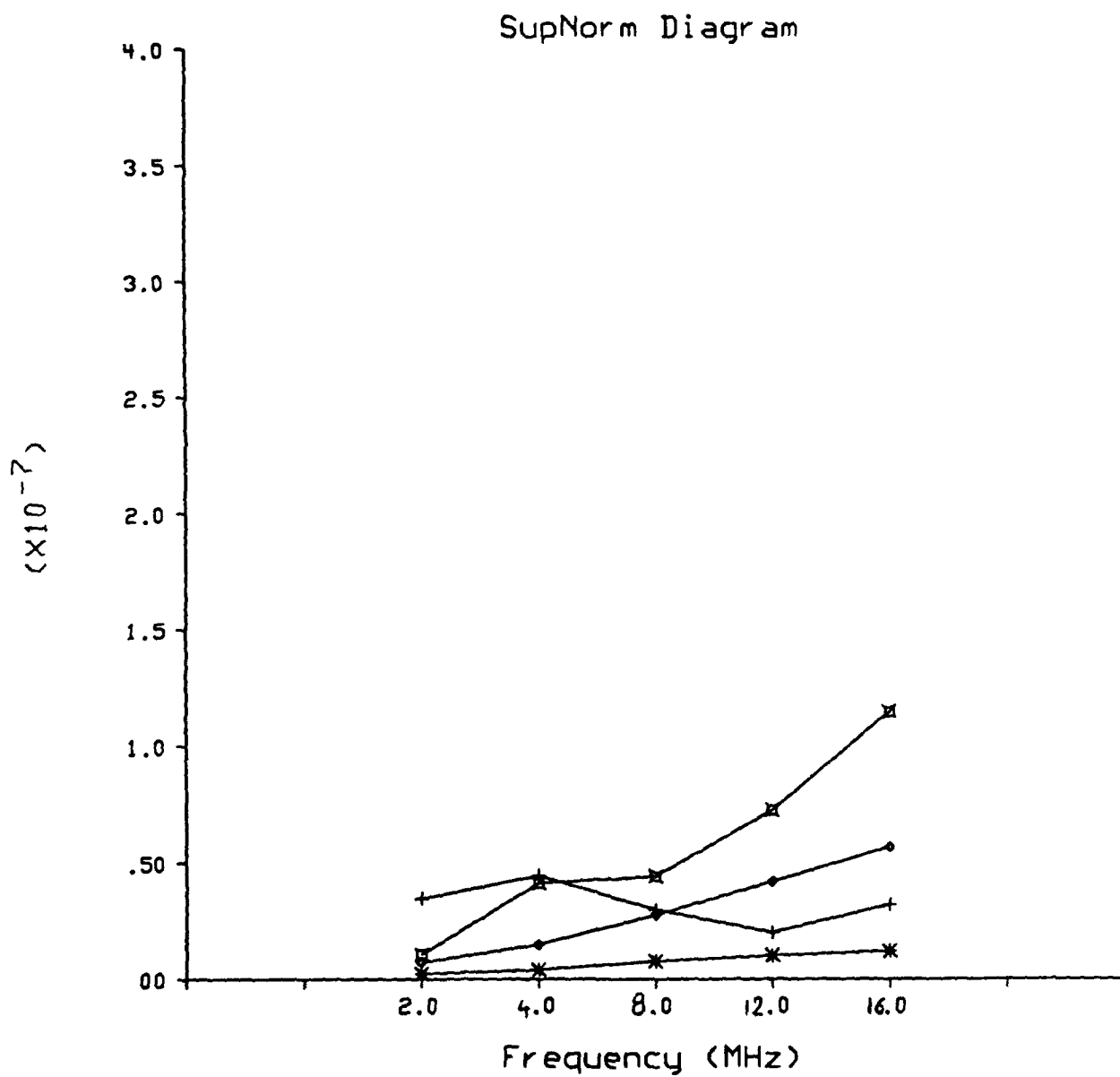


Figure 36: The sup-norms of the real and Imaginary parts of B and Y .
 $+$, \times are real and imaginary sup-norms of B ; $*$, \circ , are real and imaginary
 sup-norms of Y respectively.

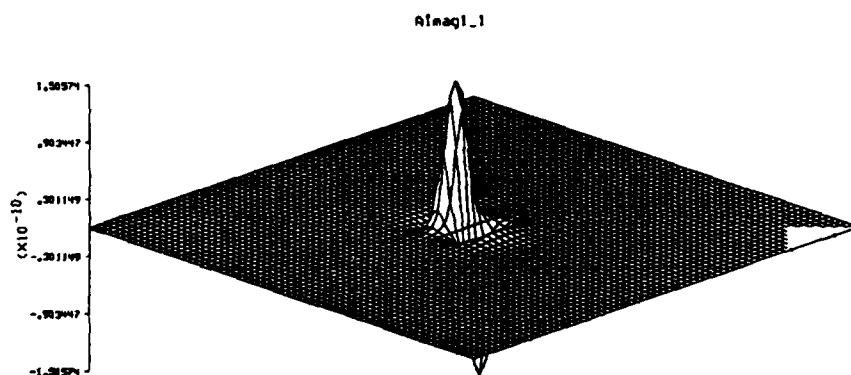
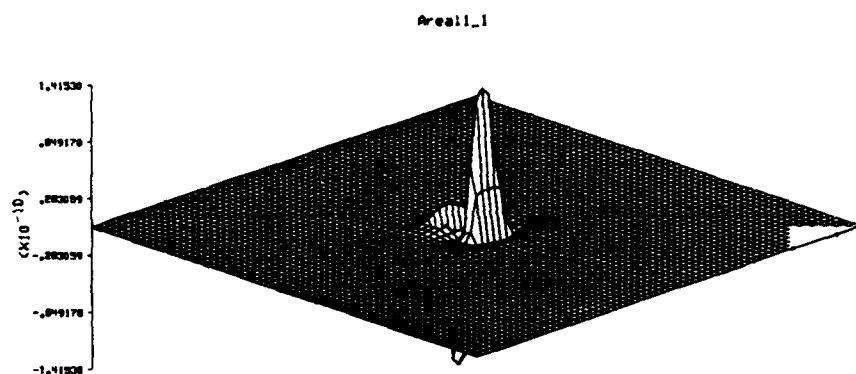


Figure 37: The element of the operator \mathcal{A} for the layer 1 at the frequency 2 MHz.

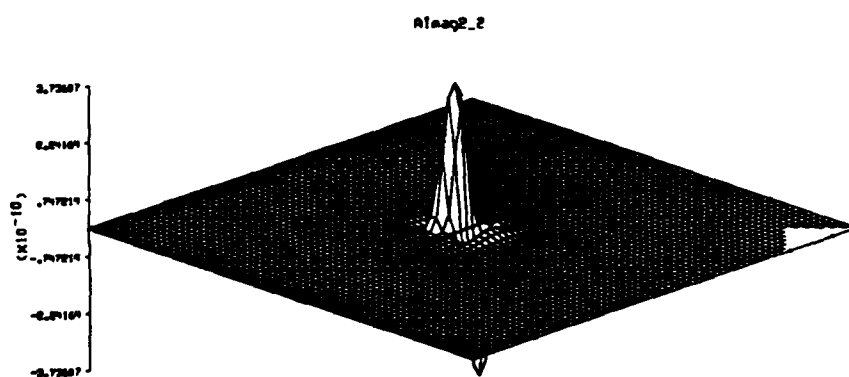
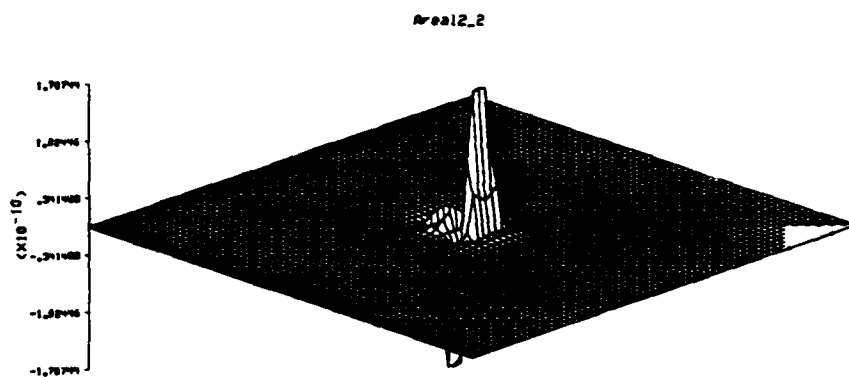


Figure 38: The element of the operator \mathcal{A} for the layer 2 at the frequency 4 MHz.

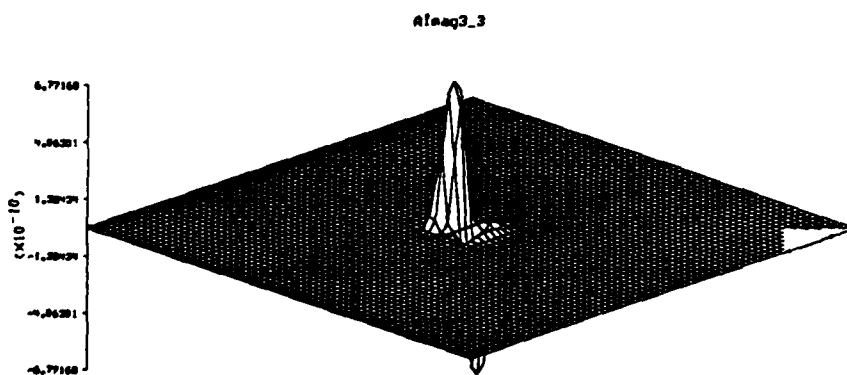
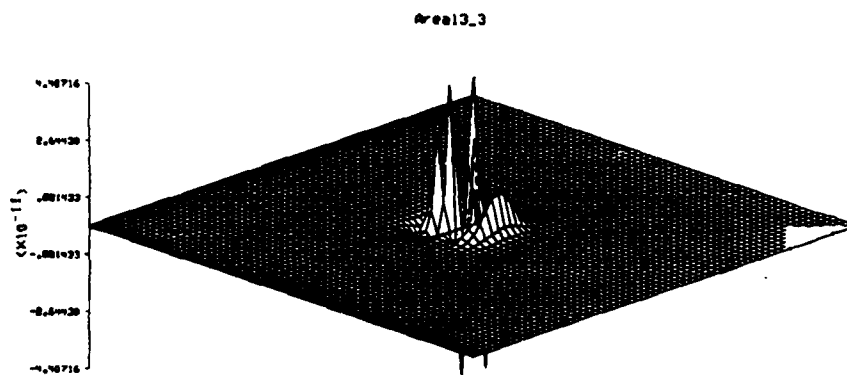


Figure 39: The element of the operator \mathcal{A} for the layer 3 at the frequency 8 MHz.

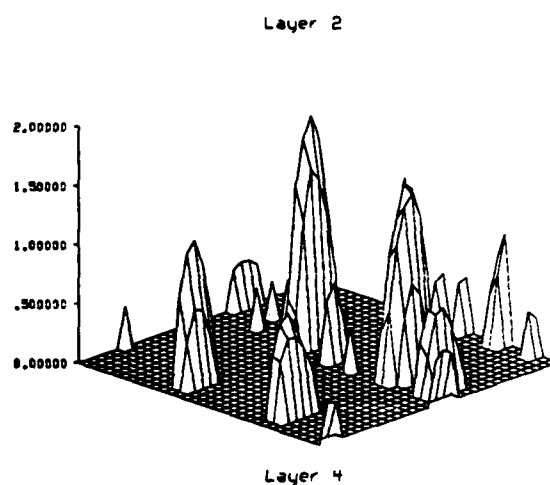
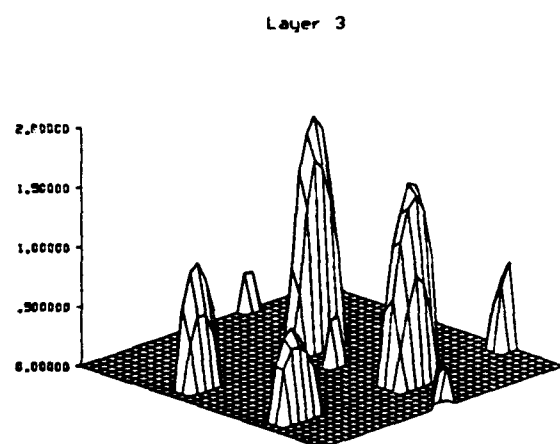
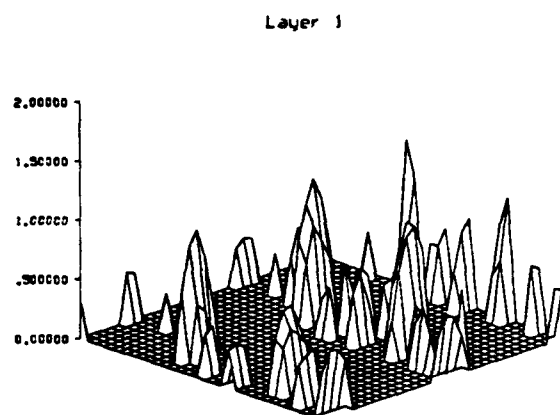


Figure 40: Reconstruction of the flaw; Levenberg-Marquardt parameter is 1.5, the number of iterations is 500 and the threshold value is 0.3; layer 1 - layer 4

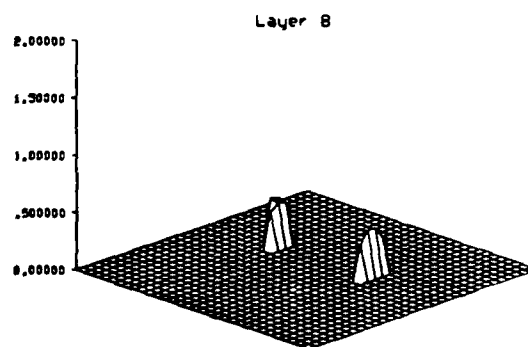
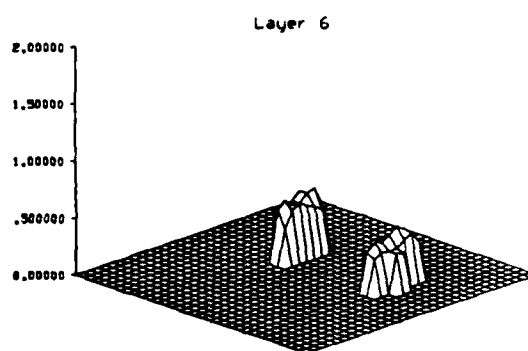
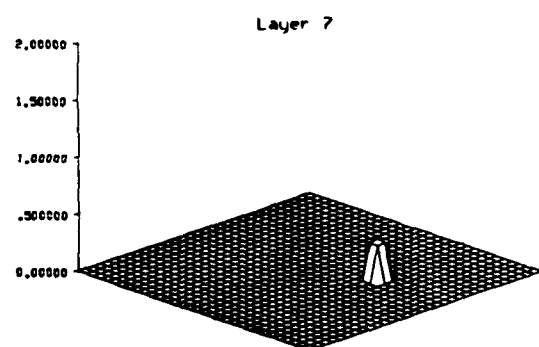
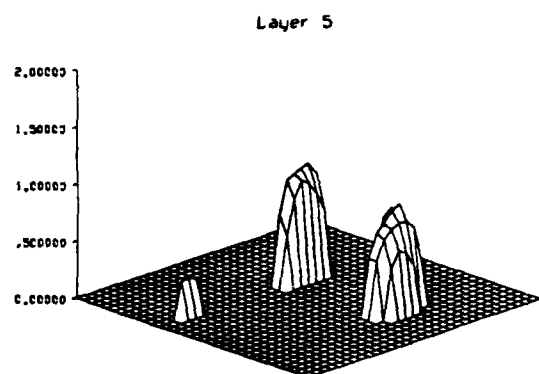


Figure 41: Reconstruction of the flaw; Levenberg-Marquardt parameter is 1.5, the number of iterations is 500 and the threshold value is 0.3; layer 5 - layer 8

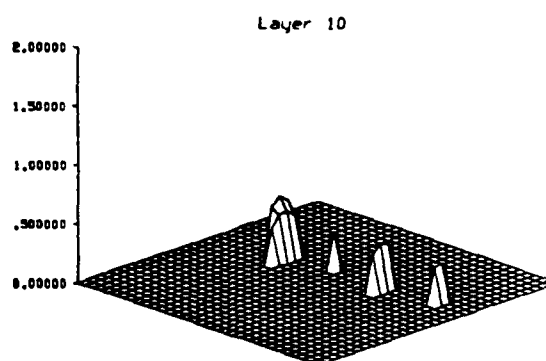
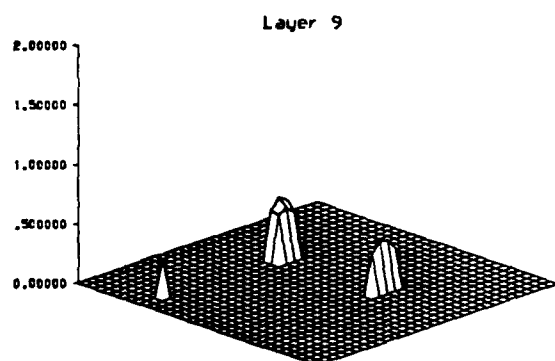


Figure 42: Reconstruction of the flaw; Levenberg-Marquardt parameter is 1.5, the number of iterations is 500 and the threshold value is 0.3; layer 9 - layer 10

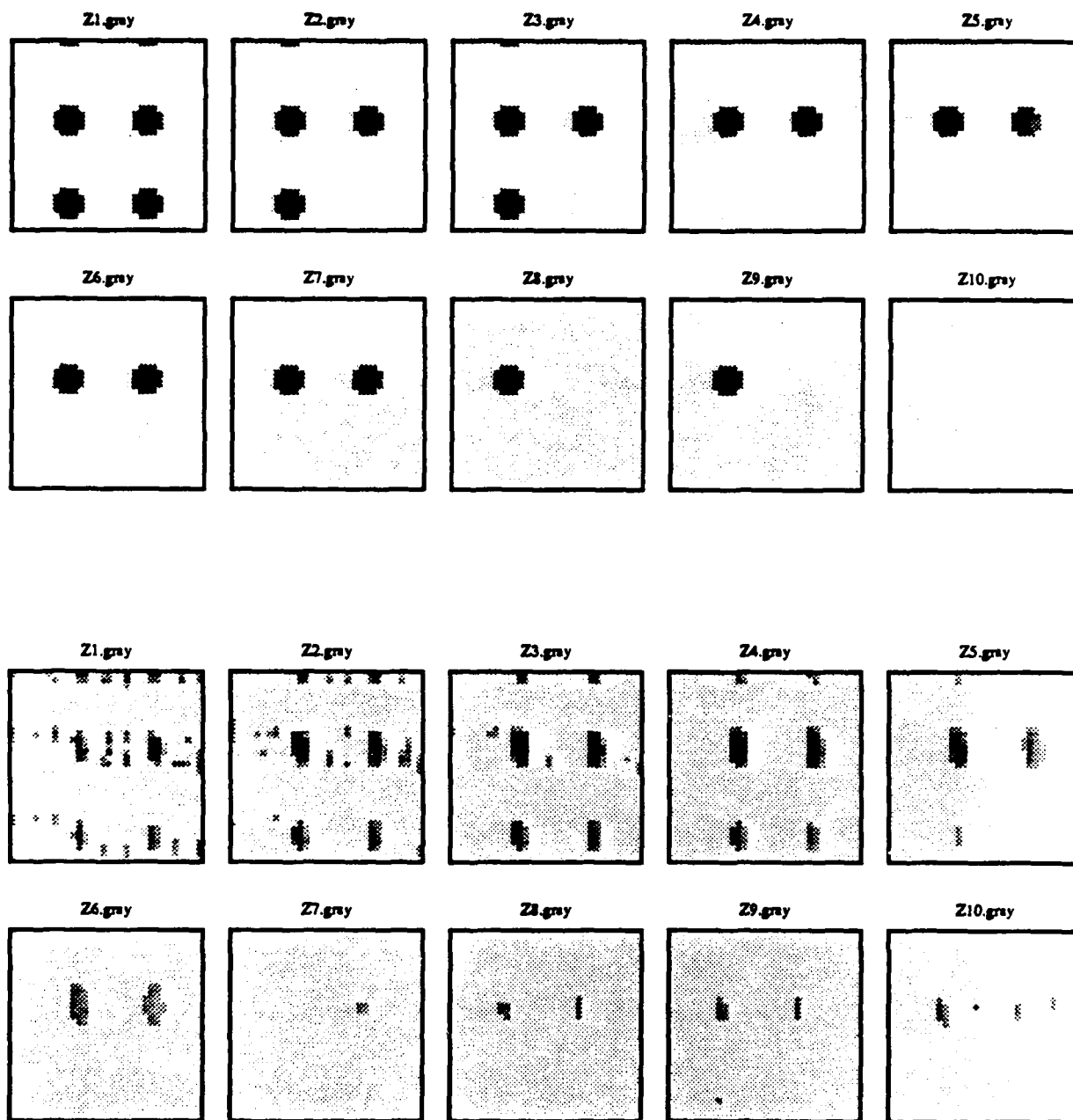


Figure 43: Gray scale of the flaw and its reconstruction; first two rows is the actual flaw, and second two rows are the reconstruction.

CHAPTER IV

RIGOROUS FORMULATION OF THE INVERSE PROBLEM

1. Introduction

Throughout this report we have simplified the model by approximating the anomalous current density, $J^{(a)} = \bar{\sigma}^{(a)} \cdot E$, as $J^{(a)} = \bar{\sigma}^{(a)} \cdot E_0$, where E_0 is the incident electric field produced by the whip (or any other source) in the absence of the flaw. This approximation linearizes the problem, and obviously simplifies the task of inversion. Nevertheless, the true problem is nonlinear, because it involves the product of two unknowns, $\bar{\sigma}^{(a)}$ and E .

In our earlier work in eddy-current inversion we solved the nonlinear problem by resorting to a package of nonlinear equation-solvers, called MINPACK. In addition, we used a variable-metric, nonlinear-programming package, called VMCON, in an attempt to satisfy constraints. These worked well for rather small problems, but for the three-dimensional problems that we are currently addressing, it becomes necessary to use storage-efficient algorithms that allow us to take advantage of special structures of our matrices, such as convolution. Hence, we will go back to the rigorous problem to see how it might be attacked in the light of what we now know about iterative algorithms for solving large problems. There should be no doubt, however, that the rigorous solution of a large nonlinear problem will be time-consuming.

2. The Nonlinear Coupled Integral Equations

Let region 1, where the excitation source and sensors are located, be above the slab, and region 2 be the slab, which contains the anomaly. Assume that we measure the magnetic induction field, B , from which we compute EMF's in the usual way. Then the appropriate pair of coupled integral equations is

$$\begin{aligned} E(r) &= E^{(0)}(r) + \int_{flaw} G_{22}^{(ee)}(r|r') \cdot J_e^{(a)}(r') dr' \\ &= E^{(0)}(r) + \int_{flaw} G_{22}^{(ee)}(r|r') \cdot \bar{\sigma}^{(a)}(r') \cdot E(r') dr' \\ B(r) - B^{(0)}(r) &= \mu_0 \int_{flaw} G_{12}^{(me)}(r|r') \cdot \bar{\sigma}^{(a)}(r') \cdot E(r') dr'. \end{aligned} \quad (1)$$

The superscripts on the Green's functions denote their type, the first denoting the type of field (electric or magnetic), and the second the type of current source (electric or magnetic), whereas the subscripts denote the regions which are coupled by the Green's function; the first subscript denotes the region which contains the field point, and the second the region that contains the source point. The superscript, (0), on E or B denotes the incident field, which is the field that exists in the presence of the slab without the flaw. The left-hand side of the second equation is integrated over the sensor coil to give the measured EMF.

This system is nonlinear (or, more precisely, bilinear) because of the presence of the product $\bar{\sigma}^{(a)}(r') \cdot E(r')$. We have been linearizing the problem by replacing $E(r')$ in the second equation by $E^{(0)}(r')$, and then ignoring the first equation.

To solve this system, we first discretize it in the usual way by means of the method of moments, and then apply an iterative technique to the resulting algebraic equations. The iterations start by replacing \mathbf{E} in the second equation by $\mathbf{E}^{(0)}$, and then solving for $\bar{\sigma}^{(a)}$ by using one of the iterative methods just described. This step uses measured data, and is the 'inverse' phase of the problem.

Once we have an acceptable approximation to $\bar{\sigma}^{(a)}$, we substitute it into the first of (1) and solve the resulting 'direct problem' for an improved version of \mathbf{E} , the electric field within the flawed region. This step will usually converge more rapidly than the inverse phase because the equations are better conditioned. We can use the same iterative technique here that was used during the inverse phase.

The result of the direct phase is then substituted into the second equation, and the second-level inverse problem is solved. The process is continued until the error in the solution is of the order of the error in the measured data.

The process that we have just suggested may not be the most efficient way to solve system (1). We will look at conjugate gradients, and see how to handle the nonlinearity there.

Keep in mind that if we use multifrequencies on this problem, a number of distinct incident fields and Green's functions will have to be computed and stored, one for each frequency. Because of the convolutional nature of the problem, however, we will be able to utilize storage efficiently.

3. Discretization of the Coupled System: Method of Moments

We start by writing the Green's function as a two-dimensional Fourier transform,

$$\mathbf{G}^{(ee)}(\mathbf{x} - \mathbf{x}', \mathbf{y} - \mathbf{y}', z, z') = \frac{1}{4\pi^2} \iint_{-\infty}^{\infty} \tilde{\mathbf{G}}^{(ee)}(z, z') e^{-j[k_x(\mathbf{x} - \mathbf{x}') + k_y(\mathbf{y} - \mathbf{y}')] } dk_x dk_y, \quad (2)$$

with a similar expression for $\mathbf{G}^{(me)}$. From here on we will drop all subscripts that are related to regions 1 and 2.

When (2) is substituted into (1) the integrals over \mathbf{x}' and \mathbf{y}' become Fourier transforms. The resulting integral equations become:

$$\mathbf{E}(\mathbf{r}) = \mathbf{E}^{(0)}(\mathbf{r}) + \frac{1}{4\pi^2} \int dz' \iint_{-\infty}^{\infty} \tilde{\mathbf{G}}^{(ee)}(z, z') \cdot \tilde{\mathbf{J}}_a(z') e^{-j(k_x z + k_y y)} dk_x dk_y \quad (3)(a)$$

$$\mathbf{B}(\mathbf{r}) - \mathbf{B}^{(0)}(\mathbf{r}) = \frac{\mu_0}{4\pi^2} \int dz' \iint_{-\infty}^{\infty} \tilde{\mathbf{G}}^{(me)}(z, z') \cdot \tilde{\mathbf{J}}_a(z') e^{-j(k_x z + k_y y)} dk_x dk_y. \quad (3)(b)$$

The measured data are usually EMF's induced into flat coils that are oriented parallel to the workpiece. In such a case, therefore, we are only interested in $j\omega \times$ the z -component of (3)(b) integrated over the sensor-coil position. This produces another integral relation with a new Green's function to replace (3)(b):

$$EMF(\mathbf{r}) = \frac{j\omega\mu_0}{4\pi^2} \int dz' \iint_{-\infty}^{\infty} \tilde{\mathbf{G}}^{(Ee)}(z, z') \cdot \tilde{\mathbf{J}}_a(z') e^{-j(k_x z + k_y y)} dk_x dk_y, \quad (3)(c)$$

where $\tilde{\mathbf{G}}^{(Ez)}$ is the z row-vector of $\tilde{\mathbf{G}}^{(me)}$ multiplied by the transfer function corresponding to integration over the sensor coil. The Green's functions that appear in (3) are computed in Appendix A.

The discretization of the coupled system of integral equations is done by subdividing the region of space occupied by the anomaly into a regular grid of $(N_x + 1) \times (N_y + 1) \times (N_z + 1)$ cells, each of size $\delta_x \times \delta_y \times \delta_z$, and then expanding the electric field and anomalous conductivity tensor using pulse functions defined over the grid:

$$\mathbf{E}(\mathbf{r}) = \sum_{l=0}^{N_x} \sum_{m=0}^{N_y} \sum_{j=0}^{N_z} \mathbf{E}_{lmj} P_l\left(\frac{x}{\delta_x}\right) P_m\left(\frac{y}{\delta_y}\right) P_j\left(\frac{z}{\delta_z}\right), \quad (4)$$

and

$$\bar{\sigma}^{(a)}(\mathbf{r}) = \sum_{l=0}^{N_x} \sum_{m=0}^{N_y} \sum_{j=0}^{N_z} \bar{\sigma}_{lmj} P_l\left(\frac{x}{\delta_x}\right) P_m\left(\frac{y}{\delta_y}\right) P_j\left(\frac{z}{\delta_z}\right). \quad (5)$$

The pulse function, $P_j(s)$, satisfies

$$P_j(s) = \begin{cases} 1, & \text{if } j \leq s < j+1; \\ 0, & \text{otherwise.} \end{cases} \quad (6)$$

Note that the anomalous current density, which is given by the product of (4) and (5), has exactly the same expansion in pulse functions as either (4) or (5), except, of course, that the expansion coefficients are given by the term-by-term product $\bar{\sigma}_{lmj} \cdot \mathbf{E}_{lmj}$.

We are going to use Galerkin's variant of the method of moments to complete the discretization. In Galerkin's method, we 'test' the integral equations (3) with the same pulse functions that we used to expand the unknowns in (4). For example, we form moments of (3)(a) by multiplying (3)(a) by $P_l(x/\delta_x)P_m(y/\delta_y)P_j(z/\delta_z)/\delta_x\delta_y\delta_z$, and then integrating over each cell. This yields an algebraic system for \mathbf{E}_{lmj} :

$$\mathbf{E}_{lmj}^{(0)} = \mathbf{E}_{lmj} - \sum_{L=0}^{N_x} \sum_{M=0}^{N_y} \sum_{J=0}^{N_z} \mathbf{G}_{jJ}^{(ee)}(l-L, m-M) \cdot \bar{\sigma}_{LMJ} \cdot \mathbf{E}_{LMJ}, \quad (7)$$

where

$$\mathbf{G}_{jJ}^{(ee)}(l-L, m-M) = \frac{\delta_x \delta_y}{4\pi^2 \delta_z} \iint_{-\infty}^{\infty} e^{-j[k_x \delta_x (l-L) + k_y \delta_y (m-M)]} \bar{\bar{\Gamma}}_{jJ}^{(ee)}(k_x, k_y) \left(\frac{\sin(k_x \delta_x / 2)}{k_x \delta_x / 2} \right)^2 \left(\frac{\sin(k_y \delta_y / 2)}{k_y \delta_y / 2} \right)^2 dk_x dk_y. \quad (8)$$

$\tilde{\tilde{\Gamma}}_{jj}^{(ee)}$ is the result of the integrations with respect to z and z' :

$$\begin{aligned}\tilde{\tilde{\Gamma}}_{kj}^{(ee)}(k_x, k_y) &= \int_{z_k^{(-)}}^{z_k^{(+)}} dz \int_{z_j^{(-)}}^{z_j^{(+)}} dz' \tilde{\tilde{\mathbf{G}}}^{(ee)}(z, z') \\ &= \int_{z_k^{(-)}}^{z_k^{(+)}} dz \int_{z_j^{(-)}}^{z_j^{(+)}} dz' \tilde{\tilde{\mathbf{G}}}_I(z - z') \\ &\quad + \int_{z_k^{(-)}}^{z_k^{(+)}} dz \int_{z_j^{(-)}}^{z_j^{(+)}} dz' \tilde{\tilde{\mathbf{G}}}_D(z - z') \\ &\quad + \int_{z_k^{(-)}}^{z_k^{(+)}} dz \int_{z_j^{(-)}}^{z_j^{(+)}} dz' \tilde{\tilde{\mathbf{G}}}_R(z, z').\end{aligned}\tag{9}$$

The subscripts, I, D, R, denote the incident, depolarization, and reflected Green's functions, respectively.

We will show how to compute the integrals of the incident and reflected Green's functions later. The depolarization function, however, can be integrated by inspection; the result is $j(\delta_{kj}\delta_z/\omega\hat{e}_{zz})\mathbf{a}_z\mathbf{a}_z$, where $\delta_{kj} = 1$, if $i = j$; $= 0$, otherwise.

In taking moments of (3') we must keep in mind that the sensors lie in a fixed z -plane above the workpiece. Hence, we multiply by only $P_l(x/\delta x)P_m(y/\delta y)$ and then integrate to get the algebraic system:

$$EMF_{lm} = \sum_{L=0}^{N_x} \sum_{M=0}^{N_y} \sum_{J=0}^{N_z} \mathbf{G}_J^{(Ee)}(l-L, m-M) \cdot \tilde{\tilde{\sigma}}_{LMJ} \cdot \mathbf{E}_{LMJ},\tag{10}$$

where

$$\begin{aligned}\mathbf{G}_J^{(Ee)}(l-L, m-M) &= \frac{j\omega\mu_0\delta_x\delta_y}{4\pi^2} \iint_{-\infty}^{\infty} e^{-j[k_x\delta_x(l-L)+k_y\delta_y(m-M)]} \tilde{\tilde{\Gamma}}_J^{(Ee)}(k_x, k_y) \\ &\quad \left(\frac{\sin(k_x\delta_x/2)}{k_x\delta_x/2}\right)^2 \left(\frac{\sin(k_y\delta_y/2)}{k_y\delta_y/2}\right)^2 dk_x dk_y,\end{aligned}\tag{11}$$

and

$$\tilde{\tilde{\Gamma}}_j^{(Ee)}(k_x, k_y) = \int_{z_j^{(-)}}^{z_j^{(+)}} dz' \tilde{\tilde{\mathbf{G}}}^{(Ee)}(z, z').\tag{12}$$

Keep in mind that $\tilde{\tilde{\Gamma}}^{(Ee)}$, $\mathbf{G}^{(Ee)}$, and $\tilde{\tilde{\mathbf{G}}}^{(Ee)}$ are vectors, not dyads; they take vectors into scalars (EMF).

Equations (7) and (10) are the coupled system of discrete equations that define the rigorous inverse problem. The system is nonlinear (bilinear) in the unknowns, $\tilde{\tilde{\sigma}}_{lmj}$, \mathbf{E}_{lmj} .

Note that in two of the three dimensions, the indices appear in a Toeplitz (or convolution) form. We will discuss the computation of the matrices shortly.

4. Multifrequency or Multiview Reconstruction Methods

Equation (10) indicates that if we measure the EMF's at a single z -level, then we don't have enough data to reconstruct a three-dimensional flaw. The additional data to reconstruct the third dimension can be obtained several ways. For example, we can excite the system from a single coil at a number, N_f , of frequencies, where $N_f \geq N_z + 1$. In that case, the Green's functions and electric field in (7) and (10), as well as the measured EMF's, vary with frequency (but the unknown conductivities are assumed to be independent of frequency).

If we let the integer, n , index the frequency parameter, then (7) and (10) become

$$\mathbf{E}_{lmj}^{(0)}(n) = \mathbf{E}_{lmj}(n) - \sum_{L=0}^{N_x} \sum_{M=0}^{N_y} \sum_{J=0}^{N_z} \mathbf{G}_{JJ}^{(ee)}(l-L, m-M; n) \cdot \bar{\sigma}_{LMJ} \cdot \mathbf{E}_{LMJ}(n) \quad (13)(a)$$

$$EMF_{lm}(n) = \sum_{L=0}^{N_x} \sum_{M=0}^{N_y} \sum_{J=0}^{N_z} \mathbf{G}_J^{(Ee)}(l-L, m-M; n) \cdot \bar{\sigma}_{LMJ} \cdot \mathbf{E}_{LMJ}(n), \quad (13)(b)$$

where $\mathbf{G}_J^{(Ee)}$ is a vector, not a dyad.

This is the "multifrequency reconstruction algorithm". Note that here the Green's functions vary with frequency, as do the measured EMF's and the computed electric fields.

Another method is to excite the system at a single frequency, but with a number of different exciting coils. In this case, only the electric fields and measured EMF's vary with n , which now indexes the location of the exciting coil. Hence, the system of equations becomes

$$\mathbf{E}_{lmj}^{(0)}(n) = \mathbf{E}_{lmj}(n) - \sum_{L=0}^{N_x} \sum_{M=0}^{N_y} \sum_{J=0}^{N_z} \mathbf{G}_{JJ}^{(ee)}(l-L, m-M) \cdot \bar{\sigma}_{LMJ} \cdot \mathbf{E}_{LMJ}(n) \quad (14)(a)$$

$$EMF_{lm}(n) = \sum_{L=0}^{N_x} \sum_{M=0}^{N_y} \sum_{J=0}^{N_z} \mathbf{G}_J^{(Ee)}(l-L, m-M) \cdot \bar{\sigma}_{LMJ} \cdot \mathbf{E}_{LMJ}(n), \quad (14)(b)$$

where $\mathbf{G}_J^{(Ee)}$ is a vector, not a dyad.

This is the "multiview reconstruction algorithm". It has the advantage over the multifrequency algorithm in not requiring the computation and storing of a number of different Green's functions. This is not too important when the linearized theory is used for inversion, but could be quite significant in the present context of the rigorous theory. Another advantage to the multiview algorithm is that it can be applied to problems where the unknown conductivity is frequency dependent.

An advantage of the multifrequency approach, however, is its relative flexibility in the laboratory, especially with regard to hardware implementation. That is, it is probably easier to change frequencies than to change excitation sources.

5. The Conjugate Gradient Algorithm for the Coupled System

We are going to apply the conjugate algorithm to the coupled system of either (13) or (14). This will be an interesting application of conjugate gradients to a nonlinear problem, and in this context we will use some ideas of Stephen J. Norton, "Iterative Seismic Inversion", Geophys. J. Roy. Astr. Soc. (submitted).

We will consider (14) first, and work in the coordinate system in which $\bar{\sigma}$ is diagonal. Then we can rewrite (14)(b) as

$$\begin{aligned} 0 = R_{lmn} &= -EMF_{lm}(n) + \sum_{L=0}^{N_x} \sum_{M=0}^{N_y} \sum_{J=0}^{N_z} \left[G_{Jz}^{(Ee)}(l-L, m-M) \sigma_{LMJz} E_{LMJz}(n) + \right. \\ &\quad \left. G_{Jy}^{(Ee)}(l-L, m-M) \sigma_{LMJy} E_{LMJy}(n) + \right. \\ &\quad \left. G_{Jz}^{(Ee)}(l-L, m-M) \sigma_{LMJz} E_{LMJz}(n) \right] \\ &= -EMF_{lm}(n) + \sum_{J=0}^{N_z} \left[G_{Jz}^{(Ee)} \otimes \sigma_{Jz} E_{Jz}(n) + G_{Jy}^{(Ee)} \otimes \sigma_{Jy} E_{Jy}(n) + G_{Jz}^{(Ee)} \otimes \sigma_{Jz} E_{Jz}(n) \right], \end{aligned} \quad (15)$$

where R_{lmn} is the lmn th component of the residual vector, and \otimes denotes a two-dimensional discrete convolution.

We form the squared-norm of the residuals

$$\Phi(\sigma_{LMJz}, \sigma_{LMJy}, \sigma_{LMJz}) = \sum_{l=0}^{N_x} \sum_{m=0}^{N_y} \sum_{n=0}^{N_z} R_{lmn} R_{lmn}^*, \quad (16)$$

where N_v is the number of "views" (i.e., the number of source locations), and then differentiate with respect to $\bar{\sigma}_{LMJ} = \{\sigma_{LMJz}, \sigma_{LMJy}, \sigma_{LMJz}\}$:

$$\begin{aligned} \frac{\partial \Phi}{\partial \bar{\sigma}_{LMJ}} &= 2\text{Re} \sum_{l=0}^{N_x} \sum_{m=0}^{N_y} \sum_{n=0}^{N_z} R_{lmn} \left[\text{Diag} \left(G_J^{(Ee)*}(l-L, m-M) E_{LMJ}^*(n) \right) + \right. \\ &\quad \left. G_J^{(Ee)*}(l-L, m-M) \cdot \bar{\sigma}_{LMJ} \cdot \frac{\partial E_{LMJ}^*(n)}{\partial \bar{\sigma}_{LMJ}} \right] \\ &= 2\bar{\bar{G}}_{LMJ} \text{grad}_{LMJ}. \end{aligned} \quad (17)$$

In (16) and (17) the asterisk denotes complex conjugation. We are using dyadic notation in (17). For example, the first term within the square brackets is the diagonal part of the dyadic product of the vectors $G_J^{(Ee)*}$ and $E_{LMJ}^*(n)$. We can write (17) in the form of a two-dimensional convolution, also, but we will not need it here.

$E_{LMJ}^*(n)$ satisfies the conjugated version of (14)(a) (but keep in mind that $\bar{\sigma}$ is real); what can we say about the dyad $\partial E_{LMJ}^*(n)/\partial \bar{\sigma}_{LMJ}$? This can probably most easily be computed by using a finite-difference approximation, in which (14)(a) is solved for two values of $\bar{\sigma}$, and then the difference-quotient is formed. It is possible, however, that some insight into the computation of the derivatives can be obtained by directly differentiating (14)(a) with respect to $\bar{\sigma}_{l'm'j'}$, keeping in mind that $\bar{\sigma}$ is diagonal. The result, after a straightforward computation, is

$$\begin{aligned} & G_{jj'}^{(ee)}(l-l', m-m') \cdot \text{Diag}(E_{l'm'j'}(n)) \\ &= \frac{\partial E_{lmj}(n)}{\partial \bar{\sigma}_{l'm'j'}} - \sum_{L=0}^{N_x} \sum_{M=0}^{N_y} \sum_{J=0}^{N_z} G_{JJ'}^{(ee)}(l-L, m-M) \cdot \bar{\sigma}_{LMJ} \cdot \frac{\partial E_{LMJ}(n)}{\partial \bar{\sigma}_{l'm'j'}}. \end{aligned} \quad (18)$$

This is the tensor version of (14)(a). After solving for $\partial E_{LMJ}(n)/\partial \bar{\sigma}_{l'm'j'}$, we keep the "diagonal" entries in which $(l, m, j) = (l', m', j')$. These correspond to local gradients, in which the variations of conductivity and electric field are within the same cell.

Actually solving (18) is out of the question, because of the computations involved. A possibility is to keep only the local gradients in (18), and solve the resulting equation. We might wish to simplify the problem further and approximate the solution for the local gradients by the term on the left-hand side of (18) when $(l, m, j) = (l', m', j')$:

$$U_{lmj}(n) = \begin{bmatrix} G_{jjzz}^{(ee)}(0,0)E_{lmjz}(n) & G_{jjzy}^{(ee)}(0,0)E_{lmjy}(n) & G_{jjxz}^{(ee)}(0,0)E_{lmjz}(n) \\ G_{jjyz}^{(ee)}(0,0)E_{lmjz}(n) & G_{jjyy}^{(ee)}(0,0)E_{lmjy}(n) & G_{jjyz}^{(ee)}(0,0)E_{lmjz}(n) \\ G_{jjzx}^{(ee)}(0,0)E_{lmjz}(n) & G_{jjzy}^{(ee)}(0,0)E_{lmjy}(n) & G_{jjxz}^{(ee)}(0,0)E_{lmjz}(n) \end{bmatrix}. \quad (19)$$

This would be a form of Born approximation for the local gradients.

The conjugate gradient algorithm starts with the iterative step $\bar{\sigma}_{LMJ}^{(k)} = \bar{\sigma}_{LMJ}^{(k-1)} + a_k \bar{f}_{LMJ}^{(k)}$. We choose a_k to minimize $\Phi(\bar{\sigma}_{LMJ}^{(k-1)} + a_k \bar{f}_{LMJ}^{(k)})$ with respect to a_k , for a given $\bar{f}_{LMJ}^{(k)}$. We will shortly determine the optimum $\bar{f}_{LMJ}^{(k)}$.

Let us first derive an expression for the k th residual, (15), using a linearized expression, in which the electric field is replaced by its $(k-1)$ th approximation:

$$\begin{aligned} R_{lmn}^{(k)} &= -EMF_{lm}(n) + \sum_{L=0}^{N_x} \sum_{M=0}^{N_y} \sum_{J=0}^{N_z} G_J^{(Ee)}(l-L, m-M) \cdot (\bar{\sigma}_{LMJ}^{(k-1)} + a_k \bar{f}_{LMJ}^{(k)}) \cdot E_{LMJ}^{(k-1)}(n) \\ &= R_{lmn}^{(k-1)} + a_k \sum_{L=0}^{N_x} \sum_{M=0}^{N_y} \sum_{J=0}^{N_z} G_J^{(Ee)}(l-L, m-M) \cdot \bar{f}_{LMJ}^{(k)} \cdot E_{LMJ}^{(k-1)}(n) \\ &= R_{lmn}^{(k-1)} + a_k F_{lmn}^{(k)}. \end{aligned} \quad (20)$$

Upon substituting this result into (16), we get

$$\begin{aligned}\Phi^{(k)} &= \sum_{l=0}^{N_s} \sum_{m=0}^{N_y} \sum_{n=0}^{N_z} \left(R_{lmn}^{(k-1)} + a_k F_{lmn}^{(k)} \right) \left(R_{lmn}^{(k-1)} + a_k F_{lmn}^{(k)} \right)^* \\ &= \Phi^{(k-1)} + a_k 2\text{Re}[F^{(k)} \cdot R^{(k-1)}] + a_k^2 \|F^{(k)}\|^2,\end{aligned}\quad (21)$$

where we are using vector-matrix inner-product notation. Hence, $\Phi^{(k)}$ is minimized when

$$a_k = -\frac{\text{Re}[R^{(k-1)} \cdot F^{(k)}]}{\|F^{(k)}\|^2}, \quad (22)$$

and when this is substituted into (21) we find the minimum value to be

$$\Phi^{(k)} = \Phi^{(k-1)} - \frac{[\text{Re}(F^{(k)} \cdot R^{(k-1)})]^2}{\|F^{(k)}\|^2}. \quad (23)$$

The greatest decrease occurs when $F^{(k)} = R^{(k-1)}$ in (23). What this means in terms of the direction, $\bar{f}_{LMJ}^{(k)}$, of the change in $\bar{\sigma}_{LMJ}$ can be determined by returning to (20):

$$\begin{aligned}& \text{Re}[R^{(k-1)} \cdot F^{(k)}] \\ &= \text{Re} \sum_{l=0}^{N_s} \sum_{m=0}^{N_y} \sum_{n=0}^{N_z} R_{lmn}^{(k-1)} \left[\sum_{L=0}^{N_s} \sum_{M=0}^{N_y} \sum_{J=0}^{N_z} G_J^{(Ee)*}(l-L, m-M) \cdot \bar{f}_{LMJ}^{(k)} \cdot E_{LMJ}^{(k-1)*}(n) \right] \\ &= \sum_{L=0}^{N_s} \sum_{M=0}^{N_y} \sum_{J=0}^{N_z} \bar{f}_{LMJ}^{(k)} \cdot \left[\text{Re} \sum_{l=0}^{N_s} \sum_{m=0}^{N_y} \sum_{n=0}^{N_z} R_{lmn}^{(k-1)} \text{Diag} \left(G_J^{(Ee)*}(l-L, m-M) E_{LMJ}^{(k-1)*}(n) \right) \right].\end{aligned}\quad (24)$$

Upon comparing the summation term within the large square brackets of (24) with the expression for the gradient, (17), we see that the summation term is the linearized gradient, which is (17) with $\partial E_{LMJ}^*(n)/\partial \bar{\sigma}_{LMJ} = 0$. Hence, (24) shows that the maximum decrease in the norm of the residuals occurs when

$$\bar{f}_{LMJ}^{(k)} = \bar{\bar{G}}\text{rad}_{LMJ}^{(k-1)}. \quad (25)$$

This is the steepest-descent direction.

There is an important orthogonality relation that holds:

$$\sum_{L=0}^{N_s} \sum_{M=0}^{N_y} \sum_{J=0}^{N_z} \bar{f}_{LMJ}^{(k)} \cdot \bar{\bar{G}}\text{rad}_{LMJ}^{(k)} = 0. \quad (26)$$

In order to derive this result, substitute the final version of (20) into the expression, (24), for the linearized gradient and get the following recursion relation:

$$\begin{aligned}\bar{\bar{G}}rad_{LMJ}^{(k)} &= \text{Re} \sum_{l=0}^{N_x} \sum_{m=0}^{N_y} \sum_{n=0}^{N_z} \left[R_{lmn}^{(k-1)} + a_k F_{lmn}^{(k)} \right] \text{Diag} \left(G_J^{(Ee)*}(l-L, m-M) E_{LMJ}^{(k-1)*}(n) \right) \\ &= \bar{\bar{G}}rad_{LMJ}^{(k-1)} + a_k \text{Re} \sum_{l=0}^{N_x} \sum_{m=0}^{N_y} \sum_{n=0}^{N_z} F_{lmn}^{(k)} \text{Diag} \left(G_J^{(Ee)*}(l-L, m-M) E_{LMJ}^{(k-1)*}(n) \right).\end{aligned}\quad (27)$$

When the definition of $F_{lmn}^{(k)}$ from (20) is substituted into (27), and the resulting expression is multiplied by $\bar{f}_{LMJ}^{(k)}$, and then summed, we get

$$\begin{aligned}\sum_{L=0}^{N_x} \sum_{M=0}^{N_y} \sum_{J=0}^{N_z} \bar{f}_{LMJ}^{(k)} \cdot \bar{\bar{G}}rad_{LMJ}^{(k)} &= \sum_{L=0}^{N_x} \sum_{M=0}^{N_y} \sum_{J=0}^{N_z} \bar{f}_{LMJ}^{(k)} \cdot \bar{\bar{G}}rad_{LMJ}^{(k-1)} + a_k \text{Re} \|F^{(k)}\|^2 \\ &= \text{Re} [R^{(k-1)} \cdot F^{(k)}] - \text{Re} [R^{(k-1)} \cdot F^{(k)}] \\ &= 0.\end{aligned}\quad (28)$$

We have used (22) and (24) in arriving at the final result.

The conjugate gradient algorithm starts with a pure gradient step, (25), for $k = 1$, and then continues with

$$\bar{f}_{LMJ}^{(k)} = \bar{\bar{G}}rad_{LMJ}^{(k-1)} + b_k \bar{f}_{LMJ}^{(k-1)}.\quad (29)$$

b_k will be chosen to minimize the denominator in (23), thereby guaranteeing an improved convergence rate.

Before deriving an expression for b_k , we will derive another expression for the numerator of a_k , which appears in (22). We start with (24), and use (29):

$$\begin{aligned}\text{Numerator of } a_k &= \text{Re} [R^{(k-1)} \cdot F^{(k)}] \\ &= \sum_{L=0}^{N_x} \sum_{M=0}^{N_y} \sum_{J=0}^{N_z} [\bar{\bar{G}}rad_{LMJ}^{(k-1)} + b_k \bar{f}_{LMJ}^{(k-1)}] \cdot \bar{\bar{G}}rad_{LMJ}^{(k-1)} \\ &= \|\bar{\bar{G}}rad^{(k-1)}\|^2,\end{aligned}\quad (30)$$

where the final result is due to the orthogonality relation, (26).

The derivation of b_k starts with

$$\begin{aligned}\|F^{(k)}\|^2 &= \sum_{l=0}^{N_x} \sum_{m=0}^{N_y} \sum_{n=0}^{N_z} F_{lmn}^{(k)} F_{lmn}^{(k)*} \\ &= \sum_{L=0}^{N_x} \sum_{M=0}^{N_y} \sum_{J=0}^{N_z} \sum_{L'=0}^{N_x} \sum_{M'=0}^{N_y} \sum_{J'=0}^{N_z} \Gamma_{LMJ;L'M'J'}^{(k)} \bar{f}_{LMJ}^{(k)} \cdot \bar{f}_{L'M'J'}^{(k)},\end{aligned}\quad (31)$$

where

$$\Gamma_{LMJ;L'M'J'}^{(k)} = \sum_{l=0}^{N_s} \sum_{m=0}^{N_y} \sum_{n=0}^{N_z} \text{Diag}(G_J^{(Ee)}(l-L, m-M) E_{LMJ}^{(k-1)}(n)) \cdot \text{Diag}(G_{J'}^{(Ee)*}(l-L', m-M') E_{L'M'J'}^{(k-1)*}(n)) \quad (32)$$

is Hermitian in $(LMJ; L'M'J')$. Equations (31) and (32) are derived from the definition of $F_{lmn}^{(k)}$ in (20), together with an interchange of summations, and a rearrangement of terms.

Upon substituting (29) into (31), and then minimizing the result with respect to b_k , we get for the optimum value of b_k

$$b_k = \frac{-\text{Re} \sum_{L=0}^{N_s} \cdots \sum_{J'=0}^{N_z} \Gamma_{LMJ;L'M'J'}^{(k)} \bar{\bar{G}}_{LMJ}^{(k-1)} \cdot \bar{f}_{L'M'J'}^{(k-1)}}{\sum_{L=0}^{N_s} \cdots \sum_{J'=0}^{N_z} \Gamma_{LMJ;L'M'J'}^{(k)} \bar{f}_{LMJ}^{(k-1)} \cdot \bar{f}_{L'M'J'}^{(k-1)}} \quad (33)$$

It is straightforward to rewrite (27) in terms of $\Gamma_{LMJ;L'M'J'}^{(k)}$:

$$\bar{\bar{G}}_{LMJ}^{(k)} = \bar{\bar{G}}_{LMJ}^{(k-1)} + a_k \text{Re} \sum_{L'=0}^{N_s} \sum_{M'=0}^{N_y} \sum_{J'=0}^{N_z} \bar{f}_{L'M'J'}^{(k)} \Gamma_{LMJ;L'M'J'}^{(k)*} \quad (34)$$

There are two fundamental conjugate gradient orthogonality relations:

$$\sum_{L=0}^{N_s} \cdots \sum_{J'=0}^{N_z} \bar{f}_{LMJ}^{(k)} \cdot \bar{f}_{L'M'J'}^{(k-1)} \text{Re}\{\Gamma_{LMJ;L'M'J'}^{(k)}\} = 0, \quad (35)(a)$$

and

$$\sum_{L=0}^{N_s} \sum_{M=0}^{N_y} \sum_{J=0}^{N_z} \bar{\bar{G}}_{LMJ}^{(k-1)} \cdot \bar{\bar{G}}_{LMJ}^{(k)} = 0. \quad (35)(b)$$

The first relation is easily proved by substituting b_k from (33) into (34), multiplying by $\text{Re}\{\Gamma_{LMJ;L'M'J'}^{(k)}\} \bar{f}_{L'M'J'}^{(k-1)}$, and then summing over (LMJ) and $(L'M'J')$.

In order to prove the second relation, we multiply (34) by $\bar{\bar{G}}_{LMJ}^{(k-1)}$ and sum

$$\begin{aligned} \sum_{L=0}^{N_s} \sum_{M=0}^{N_y} \sum_{J=0}^{N_z} \bar{\bar{G}}_{LMJ}^{(k-1)} \cdot \bar{\bar{G}}_{LMJ}^{(k)} &= \sum_{L=0}^{N_s} \sum_{M=0}^{N_y} \sum_{J=0}^{N_z} \bar{\bar{G}}_{LMJ}^{(k-1)} \cdot \bar{\bar{G}}_{LMJ}^{(k-1)} \\ &\quad + a_k \text{Re} \sum_{L=0}^{N_s} \cdots \sum_{J'=0}^{N_z} \bar{\bar{G}}_{LMJ}^{(k-1)} \cdot \bar{f}_{L'M'J'}^{(k)} \Gamma_{LMJ;L'M'J'}^{(k)*} \end{aligned} \quad (36)(a)$$

Next substitute $\overline{\text{Grad}}_{LMJ}^{(k-1)} = \tilde{f}_{LMJ}^{(k)} - b_k \tilde{f}_{LMJ}^{(k-1)}$, which follows from (29), into the second term on the right-hand side of (36)(a), and rewrite the right-hand side as

$$\|\overline{\text{Grad}}^{(k-1)}\|^2 + a_k \text{Re} \sum_{L=0}^{N_s} \cdots \sum_{J'=0}^{N_s} [\Gamma_{LMJ;L'M'J'}^{(k)*} \tilde{f}_{LMJ}^{(k)} \cdot \tilde{f}_{L'M'J'}^{(k)} - b_k \Gamma_{LMJ;L'M'J'}^{(k)*} \tilde{f}_{LMJ}^{(k-1)} \cdot \tilde{f}_{L'M'J'}^{(k)}]. \quad (36)(b)$$

The second term under the summation sign vanishes because of the first orthogonality relation, (35)(a), and the first term under the summation sign is equal to $\|F^{(k)}\|^2$, because of (31). Therefore, when we recall that $a_k = -\|\overline{\text{Grad}}^{(k-1)}\|^2 / \|F^{(k)}\|^2$, which follows from (22) and (30), we see that (35)(b) vanishes, which proves the theorem.

Our last task is to derive a simpler expression for b_k . In order to do this we must assume that the change in the model (i.e., conductivity) is sufficiently small to permit us to say that the electric field within the anomalous region does not change too much from iteration to iteration. If this is the case, we can write $\Gamma^{(k)} \approx \Gamma^{(k-1)}$, so that

$$b_k = \frac{-\text{Re} \sum_{L=0}^{N_s} \cdots \sum_{J'=0}^{N_s} \Gamma_{LMJ;L'M'J'}^{(k-1)} \overline{\text{Grad}}_{LMJ}^{(k-1)} \cdot \tilde{f}_{L'M'J'}^{(k-1)}}{\|F^{(k-1)}\|^2}, \quad (37)$$

where we have used (31) and (33).

Next, take the complex conjugate of (34), replace a_k in the resulting expression by (22) and (30), replace k by $k-1$, and get, after rearranging:

$$\text{Re} \sum_{L'=0}^{N_s} \sum_{M'=0}^{N_s} \sum_{J'=0}^{N_s} \tilde{f}_{L'M'J'}^{(k-1)} \Gamma_{LMJ;L'M'J'}^{(k-1)} = \frac{\|F^{(k-1)}\|^2}{\|\overline{\text{Grad}}^{(k-2)}\|^2} [\overline{\text{Grad}}_{LMJ}^{(k-1)} - \overline{\text{Grad}}_{LMJ}^{(k-2)}]. \quad (38)$$

Upon taking the dot product of (38) with $\overline{\text{Grad}}_{LMJ}^{(k-1)}$, and then summing over LMJ , we get

$$\text{Re} \sum_{L=0}^{N_s} \cdots \sum_{J'=0}^{N_s} \Gamma_{LMJ;L'M'J'}^{(k-1)} \tilde{f}_{L'M'J'}^{(k-1)} \cdot \overline{\text{Grad}}_{LMJ}^{(k-1)} = \frac{\|F^{(k-1)}\|^2}{\|\overline{\text{Grad}}^{(k-2)}\|^2} \|\overline{\text{Grad}}^{(k-1)}\|^2, \quad (39)$$

where we have used (35)(b). Upon comparing (39) with (37), the result follows immediately:

$$b_k = -\frac{\|\overline{\text{Grad}}^{(k-1)}\|^2}{\|\overline{\text{Grad}}^{(k-2)}\|^2}. \quad (40)$$

Note that a_k and b_k are negative here, whereas they were positive in our previous notes on the conjugate gradient algorithm. This is due to the fact that we have defined our residual vector to be the negative of the previous definition.

We can summarize these results by saying that the nonlinear conjugate algorithm is similar to the linear one, except that the operators must be updated at each iteration, because the electric field is updated. In addition, we may have to ensure that the increments in the solution vector are not too large.

Let Y be the array of complex scalars, $\{EMF_{lm}(n)\}$, where lmn index the array elements, and define the operator

$$\begin{aligned} A^{(k)}(\bar{f}) &= \sum_{L=0}^{N_e} \sum_{M=0}^{N_y} \sum_{J=0}^{N_z} G_J^{(Ee)}(l-L, m-M) \cdot \bar{f}_{LMJ} \cdot E_{LMJ}^{(k-1)}(n) \\ &= \sum_{L=0}^{N_e} \sum_{M=0}^{N_y} \sum_{J=0}^{N_z} \text{Diag} \left(G_J^{(Ee)}(l-L, m-M) E_{LMJ}^{(k-1)}(n) \right) \cdot \bar{f}_{LMJ}, \end{aligned} \quad (41)$$

together with its adjoint

$$A^{*(k)}(R) = \text{Re} \sum_{l=0}^{N_e} \sum_{m=0}^{N_y} \sum_{n=0}^{N_z} R_{lmn} \text{Diag} \left(G_J^{(Ee)*}(l-L, m-M) E_{LMJ}^{(k-1)*}(n) \right). \quad (42)$$

Note that A produces an array of complex scalars from an array of real vectors, whereas A^* produces an array of real vectors from an array of complex scalars. The electric field at the k th step is computed from (14)(a), using the k th approximation of $\bar{\sigma}_{LMJ}$.

We can derive a recursion relation for the electric field when $\bar{\sigma}_{LMJ}^{(k)} = \bar{\sigma}_{LMJ}^{(k-1)} + a_k \bar{f}_{LMJ}^{(k)}$ in the following way. Substitute this expression into (14)(a), in which the electric field is replaced by its k th approximation. Subtract from this result (14)(a), in which the electric field and conductivity tensor are replaced by their $(k-1)$ th approximations. Then, if we say that $E_{LMJ}^{(k)} \approx E_{LMJ}^{(k-1)}$, we get the final result

$$E_{lmj}^{(k)} = E_{lmj}^{(k-1)} + a_k \sum_{L=0}^{N_e} \sum_{M=0}^{N_y} \sum_{J=0}^{N_z} G_J^{(ee)}(l-L, m-M) \cdot \bar{f}_{LMJ} \cdot E_{LMJ}^{(k-1)}. \quad (43)$$

The second term on the right hand side of (43) is the correction vector induced in the electric field, due to the correction term in the conductivity. Clearly, (43) gives $E^{(k)}$ explicitly in terms of $E^{(k-1)}$. Hence, this is an explicit recursion relation for the electric field vector. We can get an implicit relation by simply replacing the electric field vector in the correction term of (43) by $E^{(k)}$, which means that we would have a large system to solve in (43). Therefore, the explicit recursion relation has an obvious advantage over the implicit. We should also remember that (43) was derived under the assumption that the changes in conductivity are not large, from iteration to iteration. This means that a_k is small.

The conjugate gradient algorithm starts with an initial guess, X_0 , from which we compute $R_0 = Y - A^{(1)}X_0$, $P_1 = Q_0 = A^{*(1)}R_0$. In addition, we have a convergence

parameter, ϵ . Then for $k = 1, \dots$, if $Test = \|R_k\|/\|Y\| < \epsilon$, stop; X_k is the optimal solution of (14)(b). Otherwise, update X_k by the following steps:

$$\begin{aligned}
 S_k &= A^{(k)} P_k \\
 a_k &= \frac{\|Q_{k-1}\|^2}{\|S_k\|^2} \\
 X_k &= X_{k-1} + a_k P_k \\
 R_k &= R_{k-1} - a_k S_k \\
 Q_k &= A^{*(k)} R_k \\
 b_k &= \frac{\|Q_k\|^2}{\|Q_{k-1}\|^2} \\
 P_{k+1} &= Q_k + b_k P_k.
 \end{aligned} \tag{44}$$

comment (1): For a linear problem, solved in infinite precision arithmetic, the algorithm terminates at the M th step when $Q_{M+1} = 0$, so that X_{M+1} is the least-squares solution of $Y = AX$. We have already shown that the vectors Q_0, Q_1, Q_2, \dots , are mutually orthogonal, as are the vectors, S_1, S_2, S_3, \dots . In addition

$$S_k^T P_j = \begin{cases} 0, & \text{if } j < k; \\ \|Q_k\|^2, & \text{otherwise.} \end{cases}$$

comment (2): This suggests that we monitor the iterates $\{Q_k\}$ for loss of orthogonality, and restart when the condition $|Q_k^T Q_{k+1}| \geq \epsilon_1 Q_k^T Q_{k+1}$ is satisfied, where $\epsilon_1 = 0.2$ (say). When this occurs, we set $b_k = 0$ in the last line, and then continue (i.e., we restart with a pure gradient step).

comment (3): Allen McIntosh, *Fitting Linear Models: An Application of Conjugate Gradient Algorithms*, Springer-Verlag, 1982, gives an alternative expression for b_k :

$$b_k = \frac{Q_k^T (Q_k - Q_{k-1})}{\|Q_{k-1}\|^2},$$

which seems to produce Q_k 's that are more orthogonal, when using the criterion of comment (2). This definition requires, however, that an extra array to store Q_{k-1} be made available. This is no problem if we monitor for orthogonality for the purpose of restarting, because that array is required anyway.

The Toeplitz operations that are a part of A and A^* are evaluated by using the FFT, as described in Appendix A of Chapter II. This, together with the fact that the storage requirements are reasonably modest, are the reasons why the conjugate gradient algorithm becomes attractive for large problems in our model.

APPENDIX A

Internal Green's Functions, G_{12} , G_{22} , in the Bulk Model

We are going to sketch a procedure that organizes the computations in such a way that the z' dependence is displayed explicitly, so that integrations with respect to z' are computed more easily. There is a bit of preliminary work that must be done. We will use our previous equations and notation as much as possible.

$$a \begin{bmatrix} -\alpha_{10} \\ -\alpha_{20} \\ 0 \\ 1 \end{bmatrix} e^{-\lambda_0 z} + b \begin{bmatrix} 0 \\ 1 \\ -\beta_{10} \\ \beta_{20} \end{bmatrix} e^{-\lambda_0 z}$$

$$z=0$$

$$c \bar{v}_1 e^{\lambda_1(z-z')} + d \bar{v}_2 e^{-\lambda_1(z-z')} + e \bar{v}_3 e^{\lambda_3(z-z')} + f \bar{v}_4 e^{-\lambda_3(z-z')}$$

$$z=z'$$

$$c' \bar{v}_1 e^{\lambda_1(z-z')} + d' \bar{v}_2 e^{-\lambda_1(z-z')} + e' \bar{v}_3 e^{\lambda_3(z-z')} + f' \bar{v}_4 e^{-\lambda_3(z-z')}$$

$$z=-z_0$$

$$g \begin{bmatrix} \alpha_{10} \\ \alpha_{20} \\ 0 \\ 1 \end{bmatrix} e^{\lambda_0(z+z_0)} + h \begin{bmatrix} 0 \\ 1 \\ \beta_{10} \\ -\beta_{20} \end{bmatrix} e^{\lambda_0(z+z_0)}$$

We rewrite the equation of continuity at the bottom interface in the following form, which is suggestive of a scattering operator:

$$[\bar{v}_2 | \bar{v}_4 | -\bar{v}_{10} | -\bar{v}_{30}] \begin{bmatrix} \bar{d}' \\ \bar{f}' \\ g \\ h \end{bmatrix} = -[\bar{v}_1 | \bar{v}_3] \begin{bmatrix} \bar{c}' \\ \bar{e}' \end{bmatrix}, \quad (\text{A.1})$$

where

$$\begin{aligned} \bar{d}' &= d' e^{\lambda_1(z_0+z')} \\ \bar{f}' &= f' e^{\lambda_3(z_0+z')} \\ \bar{c}' &= c' e^{-\lambda_1(z_0+z')} \\ \bar{e}' &= e' e^{-\lambda_3(z_0+z')}. \end{aligned} \quad (\text{A.2})$$

Equation (A.1) defines the scattering operator at the bottom interface:

$$\begin{bmatrix} \tilde{d}' \\ \tilde{f}' \\ g \\ h \end{bmatrix} = \bar{\bar{S}}_b \begin{bmatrix} \tilde{c}' \\ \tilde{e}' \end{bmatrix}, \quad (\text{A.3})$$

where

$$\begin{aligned} \bar{\bar{S}}_b &= [\bar{v}_2|\bar{v}_4| - \bar{v}_{10}| - \bar{v}_{30}]^{-1} [-\bar{v}_1| - \bar{v}_3] \\ &= \begin{bmatrix} B_{11} & B_{12} \\ B_{21} & B_{22} \\ B_{31} & B_{32} \\ B_{41} & B_{42} \end{bmatrix}. \end{aligned} \quad (\text{A.4})$$

It is easy to express these equations in terms of the expansion coefficients defined at $z = z'(-)$:

$$\begin{bmatrix} d' \\ f' \\ g \\ h \end{bmatrix} = \bar{\bar{S}}^{(-)} \begin{bmatrix} c' \\ e' \end{bmatrix}, \quad (\text{A.5})$$

where

$$\begin{aligned} \bar{\bar{S}}^{(-)} &= \begin{bmatrix} e^{-\lambda_1(z_0+z')} & 0 & 0 & 0 \\ 0 & e^{-\lambda_3(z_0+z')} & 0 & 0 \\ 0 & 0 & 1 & 0 \\ 0 & 0 & 0 & 1 \end{bmatrix} \bar{\bar{S}}_b \begin{bmatrix} e^{-\lambda_1(z_0+z')} & 0 \\ 0 & e^{-\lambda_3(z_0+z')} \end{bmatrix} \\ &= \begin{bmatrix} B_{11}e^{-2\lambda_1(z_0+z')} & B_{12}e^{-(\lambda_1+\lambda_3)(z_0+z')} \\ B_{21}e^{-(\lambda_1+\lambda_3)(z_0+z')} & B_{22}e^{-2\lambda_3(z_0+z')} \\ B_{31}e^{-\lambda_1(z_0+z')} & B_{32}e^{-\lambda_3(z_0+z')} \\ B_{41}e^{-\lambda_1(z_0+z')} & B_{42}e^{-\lambda_3(z_0+z')} \end{bmatrix}. \end{aligned} \quad (\text{A.6})$$

A similar analysis, starting at the top interface and working down to $z'(+)$, yields

$$\begin{bmatrix} a \\ b \\ c \\ e \end{bmatrix} = \bar{\bar{S}}^{(+)} \begin{bmatrix} d \\ f \end{bmatrix}, \quad (\text{A.7})$$

where

$$\bar{\bar{S}}^{(+)} = \begin{bmatrix} T_{11}e^{\lambda_1 z'} & T_{12}e^{\lambda_3 z'} \\ T_{21}e^{\lambda_1 z'} & T_{22}e^{\lambda_3 z'} \\ T_{31}e^{2\lambda_1 z'} & T_{32}e^{(\lambda_1+\lambda_3)z'} \\ T_{41}e^{(\lambda_1+\lambda_3)z'} & T_{42}e^{2\lambda_3 z'} \end{bmatrix}, \quad (\text{A.8})$$

and

$$\begin{bmatrix} T_{11} & T_{12} \\ T_{21} & T_{22} \\ T_{31} & T_{32} \\ T_{41} & T_{42} \end{bmatrix} = [\bar{v}_{20}|\bar{v}_{40}| - \bar{v}_1| - \bar{v}_3]^{-1} [\bar{v}_2|\bar{v}_4] \quad (\text{A.9})$$

is the scattering operator at the top interface. The discontinuity equation at $z = z'$ becomes

$$\begin{bmatrix} c - c' \\ d - d' \\ e - e' \\ f - f' \end{bmatrix} = [\bar{v}_1 | \bar{v}_2 | \bar{v}_3 | \bar{v}_4]^{-1} \bar{U} \cdot \bar{J}, \quad (\text{A.10})$$

or

$$\begin{aligned} c - c' &= h_1 \\ d - d' &= h_2 \\ e - e' &= h_3 \\ f - f' &= h_4, \end{aligned} \quad (\text{A.11})$$

and the h 's are independent of z_0 and z' . Don't forget that we have a different set of h 's for each type of current (electric or magnetic), and for each orientation of the current source.

Now, on to the algebra! When written out, (A.7) and (A.5) become:

$$\begin{aligned} a &= S_{11}^{(+)} d + S_{12}^{(+)} f \\ b &= S_{21}^{(+)} d + S_{22}^{(+)} f \\ c &= S_{31}^{(+)} d + S_{32}^{(+)} f \\ e &= S_{41}^{(+)} d + S_{42}^{(+)} f \\ d' &= S_{11}^{(-)} c' + S_{12}^{(-)} e' \\ f' &= S_{21}^{(-)} c' + S_{22}^{(-)} e' \\ g &= S_{31}^{(-)} c' + S_{32}^{(-)} e' \\ h &= S_{41}^{(-)} c' + S_{42}^{(-)} e', \end{aligned} \quad (\text{A.12})$$

and when (A.11) is substituted into the middle four equations in (A.12), we get, after some steps

$$\begin{aligned} \alpha_{11} d - \alpha_{12} f &= r_1 \\ -\alpha_{21} d + \alpha_{22} f &= r_2, \end{aligned} \quad (\text{A.13})$$

where

$$\begin{aligned} \alpha_{11} &= 1 - S_{11}^{(-)} S_{31}^{(+)} - S_{12}^{(-)} S_{41}^{(+)} \\ \alpha_{12} &= S_{11}^{(-)} S_{32}^{(+)} + S_{12}^{(-)} S_{42}^{(+)} \\ \alpha_{21} &= S_{21}^{(-)} S_{31}^{(+)} + S_{22}^{(-)} S_{41}^{(+)} \\ \alpha_{22} &= 1 - S_{21}^{(-)} S_{32}^{(+)} - S_{22}^{(-)} S_{42}^{(+)} \\ r_1 &= h_2 - S_{11}^{(-)} h_1 - S_{12}^{(-)} h_3 \\ r_2 &= h_4 - S_{21}^{(-)} h_1 - S_{22}^{(-)} h_3. \end{aligned} \quad (\text{A.14})$$

When we expand α_{11} and α_{22} , using (A.6) and (A.8), we find that they are independent of z' , but we find that α_{12} is proportional to $\exp(\lambda_1 - \lambda_3)z'$ and α_{21} is proportional to

$\exp(-(\lambda_1 - \lambda_3)z')$. Hence, when we solve (A.13) using Cramer's rule, the denominator determinant is independent of z' (as we knew it had to be). This means that z' appears only in various exponential terms in the numerator of the solution. This makes it easy to integrate.

Let's continue. After solving (A.13) we substitute (d, f) into the first two equations in (A.12), and get what we are really looking for: the field above the slab. The result is

$$\begin{aligned}
 a = N_1 & \left[\frac{T_{11}(1 - B_{21}T_{32}e^{-(\lambda_1+\lambda_3)z_0} - B_{22}T_{42}e^{-2\lambda_3z_0})}{D} \right. \\
 & \left. + \frac{T_{12}(B_{21}T_{31}e^{-(\lambda_1+\lambda_3)z_0} + B_{22}T_{41}e^{-2\lambda_3z_0})}{D} \right] \\
 & + N_2 \left[\frac{T_{11}(B_{11}T_{32}e^{-2\lambda_1z_0} + B_{12}T_{42}e^{-(\lambda_1+\lambda_3)z_0})}{D} \right. \\
 & \left. + \frac{T_{12}(1 - B_{11}T_{31}e^{-2\lambda_1z_0} - B_{12}T_{41}e^{-(\lambda_1+\lambda_3)z_0})}{D} \right] \\
 b = N_1 & \left[\frac{T_{21}(1 - B_{21}T_{32}e^{-(\lambda_1+\lambda_3)z_0} - B_{22}T_{42}e^{-2\lambda_3z_0})}{D} \right. \\
 & \left. + \frac{T_{22}(B_{21}T_{31}e^{-(\lambda_1+\lambda_3)z_0} + B_{22}T_{41}e^{-2\lambda_3z_0})}{D} \right] \\
 & + N_2 \left[\frac{T_{21}(B_{11}T_{32}e^{-2\lambda_1z_0} + B_{12}T_{42}e^{-(\lambda_1+\lambda_3)z_0})}{D} \right. \\
 & \left. + \frac{T_{22}(1 - B_{11}T_{31}e^{-2\lambda_1z_0} - B_{12}T_{41}e^{-(\lambda_1+\lambda_3)z_0})}{D} \right], \tag{A.15}
 \end{aligned}$$

where

$$\begin{aligned}
 N_1 &= e^{\lambda_1 z'} h_2 - h_1 B_{11} e^{-2\lambda_1 z_0} e^{-\lambda_1 z'} - h_3 B_{12} e^{-(\lambda_1+\lambda_3)z_0} e^{-\lambda_3 z'} \\
 N_2 &= e^{\lambda_3 z'} h_4 - h_1 B_{21} e^{-(\lambda_1+\lambda_3)z_0} e^{-\lambda_1 z'} - h_3 B_{22} e^{-2\lambda_3 z_0} e^{-\lambda_3 z'} \\
 D &= (1 - B_{11}T_{31}e^{-2\lambda_1z_0} - B_{12}T_{41}e^{-(\lambda_1+\lambda_3)z_0})(1 - B_{21}T_{32}e^{-(\lambda_1+\lambda_3)z_0} - B_{22}T_{42}e^{-2\lambda_3z_0}) \\
 &\quad - (B_{21}T_{31}e^{-(\lambda_1+\lambda_3)z_0} + B_{22}T_{41}e^{-2\lambda_3z_0})(B_{11}T_{32}e^{-2\lambda_1z_0} + B_{12}T_{42}e^{-(\lambda_1+\lambda_3)z_0}). \tag{A.16}
 \end{aligned}$$

Equation (A.15) is needed for computing G_{12} , where the subscripts refer to regions of space (1 being above the slab, and 2 being the interior of the slab). In order to compute G_{22} , we need the coefficients c , e , d' , f' . These are gotten, after solving (A.13), by using (A.11) and (A.12):

$$\begin{aligned}
 c &= S_{31}^{(+)} d + S_{32}^{(+)} f \\
 e &= S_{41}^{(+)} d + S_{42}^{(+)} f \\
 d' &= d - h_2 \\
 f' &= f - h_4. \tag{A.17}
 \end{aligned}$$

There is another way of getting the results of this note that reflects the physics of the problem. It is less complicated algebraically, and will produce expressions that are easily integrated with respect to z' . The technique is based upon the notion of incident and reflected Green's functions, and uses the scattering operators that have already been defined.

We start with (A.11) and decompose the fields within the slab into incident and reflected parts. Because the h 's in (A.11) are independent of z_0 and z' , being properties of only the exciting point source and the material within the slab, they are used to define the incident field within the slab:

$$F_I = \begin{cases} h_2 \bar{v}_2 e^{-\lambda_1(z-z')} + h_4 \bar{v}_4 e^{-\lambda_3(z-z')}, & \text{if } z' < z < 0 \\ -h_1 \bar{v}_1 e^{\lambda_1(z-z')} - h_3 \bar{v}_3 e^{\lambda_3(z-z')}, & \text{if } -z_0 < z < z'. \end{cases} \quad (\text{A.18})$$

Note that the incident field is decomposed into an upward-traveling wave above z' , and a downward-traveling wave below z' .

The incident field contains all those singularities of the Green's function that are associated with the source and sink points. The reflected Green's function, therefore, is regular, and is the response due to the presence of the boundaries at $z = 0$ and $z = -z_0$. The reflected field is given by the remainder of the total proposed field and the incident field:

$$\begin{aligned} F_R &= c \bar{v}_1 e^{\lambda_1(z-z')} + e \bar{v}_3 e^{\lambda_3(z-z')} + d' \bar{v}_2 e^{-\lambda_1(z-z')} + f' \bar{v}_4 e^{-\lambda_3(z-z')} \\ &= c'' \bar{v}_1 e^{\lambda_1 z} + e'' \bar{v}_3 e^{\lambda_3 z} + d'' \bar{v}_2 e^{-\lambda_1 z} + f'' \bar{v}_4 e^{-\lambda_3 z} \end{aligned} \quad (\text{A.19})$$

where

$$\begin{aligned} d'' &= d' e^{\lambda_1 z'}, & f'' &= f' e^{\lambda_3 z'} \\ c'' &= c e^{-\lambda_1 z'}, & e'' &= e e^{-\lambda_3 z'}. \end{aligned} \quad (\text{A.20})$$

Note that F_R is continuous across z' , and that the (c'', e'') terms are downward-traveling (which means that they originate at the upper boundary, $z = 0$), whereas the (d'', f'') terms are upward-traveling (which means that they originate at the lower boundary, $z = -z_0$).

Eventually we will have to integrate F_R with respect to z and z' . The integral with respect to z is trivial, being simply the integral of the exponential terms. The integral with respect to z' , on the other hand involves the coefficients, c'' , d'' , e'' , f'' , and these are only implicitly defined in terms of z' . This is the same problem that motivated these notes in the first place; now we are going to develop another formalism for expressing these coefficients in terms of z' , in order to evaluate the integrals.

In terms of our new notation, (A.3) and (A.4) are equivalent to

$$\begin{aligned} \begin{bmatrix} d'' \\ f'' \end{bmatrix} &= - \begin{bmatrix} B_{11} e^{-2\lambda_1 z_0} & B_{12} e^{-(\lambda_1 + \lambda_3) z_0} \\ B_{21} e^{-(\lambda_1 + \lambda_3) z_0} & B_{22} e^{-2\lambda_3 z_0} \end{bmatrix} \begin{bmatrix} h_1 e^{-\lambda_1 z'} \\ h_3 e^{-\lambda_3 z'} \end{bmatrix} \\ &+ \begin{bmatrix} B_{11} e^{-2\lambda_1 z_0} & B_{12} e^{-(\lambda_1 + \lambda_3) z_0} \\ B_{21} e^{-(\lambda_1 + \lambda_3) z_0} & B_{22} e^{-2\lambda_3 z_0} \end{bmatrix} \begin{bmatrix} c'' \\ e'' \end{bmatrix}, \end{aligned} \quad (\text{A.21})$$

and (A.7) and (A.8) produce

$$\begin{bmatrix} c'' \\ e'' \end{bmatrix} = \begin{bmatrix} T_{31} & T_{32} \\ T_{41} & T_{42} \end{bmatrix} \begin{bmatrix} h_2 e^{\lambda_1 z'} \\ h_4 e^{\lambda_3 z'} \end{bmatrix} + \begin{bmatrix} T_{31} & T_{32} \\ T_{41} & T_{42} \end{bmatrix} \begin{bmatrix} d'' \\ f'' \end{bmatrix}. \quad (\text{A.22})$$

The physics implied by (A.21) and (A.22) is interesting. The first term in (A.21) corresponds to the reflection from the lower boundary of the downward-going part of the incident field, and the second term represents the reflection from the lower boundary of the downward-going wave that has been reflected from the top boundary. In (A.22) the terms correspond to reflections from the top surface.

Equations (A.21) and (A.22) can be solved for c'' , d'' , e'' , f'' in several ways. One way is to use an iterative scheme, which starts out by assuming that $c'' = 0$, $e'' = 0$ and then computing $[d'', f'']$ from (A.21). This result is then substituted into (A.22), from which an updated value of $[c'', e'']$ is obtained. This completes the first cycle; the second cycle starts with the updated $[c'', e'']$ being substituted back into (A.21). This iterative method mimics the multiple reflections that are produced in this system.

An alternative method of solution is simply to create a 4×4 linear system from (A.21) and (A.22), which is then solved conventionally. No matter how (A.21) and (A.22) are solved, these results are all that are needed to compute G_{22} (don't forget the depolarizing term). In order to compute G_{12} , we need $[a, b]$, as before. Rather than use (A.15), we can derive a second equation from (A.7) and (A.8):

$$\begin{bmatrix} a \\ b \end{bmatrix} = \begin{bmatrix} T_{11} & T_{12} \\ T_{21} & T_{22} \end{bmatrix} \begin{bmatrix} h_2 e^{\lambda_1 z'} \\ h_4 e^{\lambda_3 z'} \end{bmatrix} + \begin{bmatrix} T_{11} & T_{12} \\ T_{21} & T_{22} \end{bmatrix} \begin{bmatrix} d'' \\ f'' \end{bmatrix}. \quad (\text{A.23})$$

This equation can be solved once $[d'', f'']$ is known.

Because the coefficient matrices in (A.21), (A.22) are independent of z' , we can easily derive an equation for the integrals of $[c'', d'', e'', f'']$ with respect to z' . In fact, the equation is (A.21), (A.22), with the inhomogeneous terms replaced by the appropriate integrals with respect to z' . Such integrals are easily computed because of the presence of the exponentials.

Let's charge on and solve (A.21) and (A.22) the old-fashioned way, by elimination of pairs of unknowns. For example, if we substitute (A.22) into (A.21), thereby eliminating $[c'', e'']$ in favor of $[d'', f'']$, we get

$$[\bar{I} - \bar{B} \bar{T}] \begin{bmatrix} d'' \\ f'' \end{bmatrix} = \bar{B} \bar{T} \begin{bmatrix} h_2 e^{\lambda_1 z'} \\ h_4 e^{\lambda_3 z'} \end{bmatrix} - \bar{B} \begin{bmatrix} h_1 e^{-\lambda_1 z'} \\ h_3 e^{-\lambda_3 z'} \end{bmatrix}, \quad (\text{A.24})$$

where \bar{B} is the matrix that appears in (A.21), and \bar{T} is the matrix that appears in (A.22).

The solution of (A.24) is

$$\begin{bmatrix} d'' \\ f'' \end{bmatrix} = [\bar{I} - \bar{B} \bar{T}]^{-1} \bar{B} \bar{T} \begin{bmatrix} h_2 e^{\lambda_1 z'} \\ h_4 e^{\lambda_3 z'} \end{bmatrix} - [\bar{I} - \bar{B} \bar{T}]^{-1} \bar{B} \begin{bmatrix} h_1 e^{-\lambda_1 z'} \\ h_3 e^{-\lambda_3 z'} \end{bmatrix}, \quad (\text{A.25})$$

and when this is substituted into (A.22), we get

$$\begin{bmatrix} c'' \\ e'' \end{bmatrix} = \left[\bar{I} + \bar{T} [\bar{I} - \bar{B} \bar{T}]^{-1} \bar{B} \right] \bar{T} \begin{bmatrix} h_2 e^{\lambda_1 z'} \\ h_4 e^{\lambda_3 z'} \end{bmatrix} - \bar{T} [\bar{I} - \bar{B} \bar{T}]^{-1} \bar{B} \begin{bmatrix} h_1 e^{-\lambda_1 z'} \\ h_3 e^{-\lambda_3 z'} \end{bmatrix}. \quad (\text{A.26})$$

Because we are only solving 2×2 systems, the inverses can be easily carried out by using Cramer's rule, as was done in solving (A.23).

The solution vector can be written as

$$\begin{bmatrix} c'' \\ e'' \\ d'' \\ f'' \end{bmatrix} = \begin{bmatrix} R_{11} & R_{12} & R_{13} & R_{14} \\ R_{21} & R_{22} & R_{23} & R_{24} \\ R_{31} & R_{32} & R_{33} & R_{34} \\ R_{41} & R_{42} & R_{43} & R_{44} \end{bmatrix} \begin{bmatrix} h_2 e^{\lambda_1 z'} \\ h_4 e^{\lambda_3 z'} \\ h_1 e^{-\lambda_1 z'} \\ h_3 e^{-\lambda_3 z'} \end{bmatrix}, \quad (\text{A.27})$$

where the matrix elements are independent of z' , and are called reflection coefficients. Note that there is a matrix of reflection coefficients for each of the three components of electric or magnetic current density, because h depends upon the current source.

In terms of the 2×2 matrices defined earlier, we have

$$\begin{aligned} \begin{bmatrix} R_{11} & R_{12} \\ R_{21} & R_{22} \end{bmatrix} &= \left[\bar{I} + \bar{T} [\bar{I} - \bar{B} \bar{T}]^{-1} \bar{B} \right] \bar{T} \\ \begin{bmatrix} R_{13} & R_{14} \\ R_{23} & R_{24} \end{bmatrix} &= -\bar{T} [\bar{I} - \bar{B} \bar{T}]^{-1} \bar{B} \\ \begin{bmatrix} R_{31} & R_{32} \\ R_{41} & R_{42} \end{bmatrix} &= [\bar{I} - \bar{B} \bar{T}]^{-1} \bar{B} \bar{T} \\ \begin{bmatrix} R_{33} & R_{34} \\ R_{43} & R_{44} \end{bmatrix} &= -[\bar{I} - \bar{B} \bar{T}]^{-1} \bar{B}. \end{aligned} \quad (\text{A.28})$$

The Dyadic Green's Function $\tilde{G}_{22}^{(ee)}(z, z')$

The "electric-electric" dyadic Green's function has the following interpretation: its first column is the electric field vector produced by a point source of electric current that is oriented in the x -direction, its second column is the electric field vector produced by a point source of electric current that is oriented in the y -direction, and similarly for the third column. Of course, we are still working in the Fourier domain, so that the only spatial variables are (z, z') , where z is the field point, and z' the source point. Hence, we can write

$$\begin{aligned} \tilde{G}^{(ee)}(z, z') &= \\ &\begin{bmatrix} \tilde{E}_x^{(z)} & \tilde{E}_x^{(y)} & \tilde{E}_x^{(z)} \\ \tilde{E}_y^{(z)} & \tilde{E}_y^{(y)} & \tilde{E}_y^{(z)} \\ (-k_z \tilde{H}_y^{(z)} + k_y \tilde{H}_z^{(z)})/\omega \hat{e}_{zz} & (-k_z \tilde{H}_y^{(y)} + k_y \tilde{H}_z^{(y)})/\omega \hat{e}_{zz} & (-k_z \tilde{H}_y^{(z)} + k_y \tilde{H}_z^{(z)})/\omega \hat{e}_{zz} \end{bmatrix} \\ &+ j \frac{\delta(z - z')}{\omega \hat{e}_{zz}} \mathbf{a}_z \mathbf{a}_z. \end{aligned} \quad (\text{A.29})$$

The superscripts on the field components in each column denote the direction of the applied electric point-current source. The delta function term that appears in the zz component of the dyad is due to the fact that \tilde{E}_z contains a term that is directly proportional to the z -component of the applied electric current density. Hence, when this current density is a delta function, as it is when computing the dyadic Green's function, the same delta function appears in the Green's function. This term is the "depolarization" Green's function.

The tangential components of the electromagnetic field that appear in (A.29) are computed from (A.18) and (A.19), where the coefficients in (A.19) are given in (A.27). We conclude, therefore, that the matrix in (A.29) consists of two parts: an incident part, due to (A.18), and a reflected part, due to (A.19). Hence, we write $\tilde{G}^{(ee)}(z, z') = \tilde{G}_I(z - z') + \tilde{G}_D(z - z') + \tilde{G}_R(z, z')$. Note that the incident and depolarization Green's dyadics depend upon the difference between the source and field points.

Let's go into the computation of the dyadic Green's function in a little more detail. We start with (A.18) and (A.19), keeping in mind that there are three different h 's (corresponding to each possible orientation of the point source of current) for the electric Green's function, and three different h 's for the magnetic Green's function. We are interested in only the electric dyadic Green's function now. Hence, each h will give us a column of the Green's dyad; how do we get the rows? Remember that the eigenvectors stand for

$$\bar{v} = \begin{bmatrix} E_x \\ E_y \\ H_x \\ H_y \end{bmatrix}. \quad (\text{A.30})$$

Hence, the entries of (A.29) can be easily picked out of this vector structure. For example, the first column of the incident part of (A.29) is obtained upon referring to (A.18):

$$\begin{aligned} \tilde{E}_z^{(z)} &= h_2^{(z)} v_2^{(1)} e^{-\lambda_1(z-z')} + h_4^{(z)} v_4^{(1)} e^{-\lambda_3(z-z')} & z' < z \\ &= -h_1^{(z)} v_1^{(1)} e^{\lambda_1(z-z')} - h_3^{(z)} v_3^{(1)} e^{\lambda_3(z-z')} & z < z' \end{aligned} \quad (\text{A.31})(a)$$

$$\begin{aligned} \tilde{E}_y^{(z)} &= h_2^{(z)} v_2^{(2)} e^{-\lambda_1(z-z')} + h_4^{(z)} v_4^{(2)} e^{-\lambda_3(z-z')} & z' < z \\ &= -h_1^{(z)} v_1^{(2)} e^{\lambda_1(z-z')} - h_3^{(z)} v_3^{(2)} e^{\lambda_3(z-z')} & z < z' \end{aligned} \quad (\text{A.31})(b)$$

$$\begin{aligned} \tilde{H}_z^{(z)} &= h_2^{(z)} v_2^{(3)} e^{-\lambda_1(z-z')} + h_4^{(z)} v_4^{(3)} e^{-\lambda_3(z-z')} & z' < z \\ &= -h_1^{(z)} v_1^{(3)} e^{\lambda_1(z-z')} - h_3^{(z)} v_3^{(3)} e^{\lambda_3(z-z')} & z < z' \end{aligned} \quad (\text{A.31})(c)$$

$$\begin{aligned} \tilde{H}_y^{(z)} &= h_2^{(z)} v_2^{(4)} e^{-\lambda_1(z-z')} + h_4^{(z)} v_4^{(4)} e^{-\lambda_3(z-z')} & z' < z \\ &= -h_1^{(z)} v_1^{(4)} e^{\lambda_1(z-z')} - h_3^{(z)} v_3^{(4)} e^{\lambda_3(z-z')} & z < z' \end{aligned} \quad (\text{A.31})(d)$$

$$\tilde{E}_z^{(z)} = \frac{1}{\omega \epsilon_{zz}} \left[-k_z \tilde{H}_y^{(z)} + k_y \tilde{H}_z^{(z)} \right]$$

$$\begin{aligned}
&= \frac{1}{\omega \hat{\epsilon}_{zz}} \left[(-k_x v_2^{(4)} + k_y v_2^{(3)}) h_2^{(z)} e^{-\lambda_1(z-z')} \right. \\
&\quad \left. + (-k_x v_4^{(4)} + k_y v_4^{(3)}) h_4^{(z)} e^{-\lambda_3(z-z')} \right] \quad z' < z \\
&= \frac{1}{\omega \hat{\epsilon}_{zz}} \left[(k_x v_1^{(4)} - k_y v_1^{(3)}) h_1^{(z)} e^{\lambda_1(z-z')} \right. \\
&\quad \left. + (k_x v_3^{(4)} - k_y v_3^{(3)}) h_3^{(z)} e^{\lambda_3(z-z')} \right] \quad z < z'. \quad (A.31)(e)
\end{aligned}$$

In order to compute the reflected part, we start with (A.19), and get

$$\tilde{E}_z^{(z)} = c''(z) v_1^{(1)} e^{\lambda_1 z} + e''(z) v_3^{(1)} e^{\lambda_3 z} + d'''(z) v_2^{(1)} e^{-\lambda_1 z} + f'''(z) v_4^{(1)} e^{-\lambda_3 z} \quad (A.32)(a)$$

$$\tilde{E}_y^{(z)} = c''(z) v_1^{(2)} e^{\lambda_1 z} + e''(z) v_3^{(2)} e^{\lambda_3 z} + d'''(z) v_2^{(2)} e^{-\lambda_1 z} + f'''(z) v_4^{(2)} e^{-\lambda_3 z} \quad (A.32)(b)$$

$$\tilde{H}_x^{(z)} = c''(z) v_1^{(3)} e^{\lambda_1 z} + e''(z) v_3^{(3)} e^{\lambda_3 z} + d'''(z) v_2^{(3)} e^{-\lambda_1 z} + f'''(z) v_4^{(3)} e^{-\lambda_3 z} \quad (A.32)(c)$$

$$\tilde{H}_y^{(z)} = c''(z) v_1^{(4)} e^{\lambda_1 z} + e''(z) v_3^{(4)} e^{\lambda_3 z} + d'''(z) v_2^{(4)} e^{-\lambda_1 z} + f'''(z) v_4^{(4)} e^{-\lambda_3 z} \quad (A.32)(d)$$

$$\begin{aligned}
\tilde{E}_z^{(z)} &= \frac{1}{\omega \hat{\epsilon}_{zz}} \left[-k_x \tilde{H}_y^{(z)} + k_y \tilde{H}_x^{(z)} \right] \\
&= \frac{1}{\omega \hat{\epsilon}_{zz}} \left[(-k_x v_1^{(4)} + k_y v_1^{(3)}) c''(z) e^{\lambda_1 z} + (-k_x v_3^{(4)} + k_y v_3^{(3)}) e''(z) e^{\lambda_3 z} \right. \\
&\quad \left. + (-k_x v_2^{(4)} + k_y v_2^{(3)}) d'''(z) e^{-\lambda_1 z} + (-k_x v_4^{(4)} + k_y v_4^{(3)}) f'''(z) e^{-\lambda_3 z} \right], \quad (A.32)(e)
\end{aligned}$$

where $[c''(z), e''(z), d'''(z), f'''(z)]$ is given by (A.27), with the h 's given by $[h_2^{(z)}, h_4^{(z)}, h_1^{(z)}, h_3^{(z)}]$.

It should be clear, now, how to compute the other two columns of the incident dyadic Green's function.

The Vector Green's Function $\tilde{G}_{12}^{(Ee)}(z, z')$

We start with the dual of the bottom row of the dyad in (A.29), which produces the z -component of the magnetic field:

$$\begin{aligned}
\tilde{H}_z(z, z') &= \\
&[(-k_y \tilde{E}_x^{(z)} + k_x \tilde{E}_y^{(z)})/\omega \mu_0 \quad (-k_y \tilde{E}_x^{(y)} + k_x \tilde{E}_y^{(y)})/\omega \mu_0 \quad (-k_y \tilde{E}_x^{(z)} + k_x \tilde{E}_y^{(z)})/\omega \mu_0]. \quad (A.33)
\end{aligned}$$

If $\tilde{S}(k_x, k_y)$ is the transfer function corresponding to integration over the sensor coil, then

$$\tilde{G}_{12}^{(Ee)}(z, z') = \tilde{S}(k_x, k_y) \tilde{H}_z(z, z'). \quad (A.34)$$

This is the expression that is used in (12) (see the comment below (3)(c), also). The electric field is evaluated in region 1 of the figure ($z > 0$), so that we need $[a, b]$ from either (A.15) or (A.37).

Consider (10); with a whip source that produces a y -directed electric field, E_0 , in the principal-axis system, we have

$$EMF_{lm} = \sum_{L=0}^{N_x} \sum_{M=0}^{N_y} \sum_{J=0}^{N_z} G_J^{(Ee)(y)}(l-L, m-M) E_{0LMJ} \bar{\sigma}_{LMJ}^{(yy)}. \quad (\text{A.35})$$

Now $G_J^{(Ee)(y)}$ is given in (11) and (12), which uses the y -component of (A.33) and (A.34)

$$\tilde{G}^{(Ee)(y)}(z, z') = \tilde{S}(k_x, k_y)(-k_y \tilde{E}_x^{(y)} + k_x \tilde{E}_y^{(y)})/\omega\mu_0, \quad (\text{A.36})$$

where, from the figure,

$$\begin{aligned} \tilde{E}_x^{(y)} &= -a^{(y)}\alpha_{10}e^{-\lambda_0 z} \\ \tilde{E}_y^{(y)} &= -a^{(y)}\alpha_{20}e^{-\lambda_0 z} + b^{(y)}e^{-\lambda_0 z}. \end{aligned} \quad (\text{A.37})$$

← $a^{(y)}$ and $b^{(y)}$ are given by either (A.15) or (A.23) with $[h] = [h^{(y)}]$. For example, in (A.16) we have

$$\begin{aligned} N_1 &= e^{\lambda_1 z'} h_2^{(y)} - h_1^{(y)} B_{11} e^{-2\lambda_1 z_0} e^{-\lambda_1 z'} - h_3^{(y)} B_{12} e^{-(\lambda_1 + \lambda_3)z_0} e^{-\lambda_3 z'} \\ N_2 &= e^{\lambda_3 z'} h_4^{(y)} - h_1^{(y)} B_{21} e^{-(\lambda_1 + \lambda_3)z_0} e^{-\lambda_1 z'} - h_3^{(y)} B_{22} e^{-2\lambda_3 z_0} e^{-\lambda_3 z'}, \end{aligned} \quad (\text{A.38})$$

whereas (A.23) and (A.27) produce

$$\begin{aligned} \begin{bmatrix} a^{(y)} \\ b^{(y)} \end{bmatrix} &= \begin{bmatrix} T_{11} & T_{12} \\ T_{21} & T_{22} \end{bmatrix} \left(\bar{I} + \begin{bmatrix} R_{31} & R_{32} \\ R_{41} & R_{42} \end{bmatrix} \right) \begin{bmatrix} h_2^{(y)} e^{\lambda_1 z'} \\ h_4^{(y)} e^{\lambda_3 z'} \end{bmatrix} \\ &+ \begin{bmatrix} T_{11} & T_{12} \\ T_{21} & T_{22} \end{bmatrix} \begin{bmatrix} R_{33} & R_{34} \\ R_{43} & R_{44} \end{bmatrix} \begin{bmatrix} h_1^{(y)} e^{-\lambda_1 z'} \\ h_3^{(y)} e^{-\lambda_3 z'} \end{bmatrix}. \end{aligned} \quad (\text{A.39})$$

Clearly, we are using separation of variables, in which the coefficients, $[a, b]$, carry the z' dependence. Hence, in evaluating the integrals over z' in (12), we need only integrate these coefficients with respect to z' . The results are readily apparent from (A.38) and (A.39), because the z' dependence is explicitly stated in the exponentials; the coefficient matrices are independent of z' .

CHAPTER V

**LABORATORY DATA COLLECTION
AND MODEL INTERFACE
FOR FLAW INVERSION**

Jeff C. Treece

1. INTRODUCTION

Collecting and storing laboratory data became a fairly complicated task as a large amount of data were taken under a wide range of physical circumstances. This chapter gives an overview of the software and hardware involved in the complete data acquisition process. We first discuss the data collection software, which touches on the hardware design for a complete understanding of the motivation behind the software. We also review the sensors and excitations used for the project; these sensors are mentioned here to complete the documentation of handling and keeping track of the data. Finally, we present some sample laboratory data.

2. DATA COLLECTION SOFTWARE

The data acquisition itself was just one part of the overall process, and began with a "C" language data acquisition program designed to run on MS-DOS computers. We used two different MS-DOS computers during the project, and the software was developed to operate well with almost any type of MS-DOS computer, even one without a hard drive. During the project, we upgraded from a PC-XT compatible computer to 12MHz PC-AT compatible laboratory computer, allowing us to acquire data much more efficiently. Some changes to the data acquisition program were required to get the program to run on the new computer; these changes are documented in the Sixth and Seventh Quarterly Reports.

Data collected in the laboratory went through many handling steps before its usage in the computer modeling program. This section outlines the steps that we used in acquiring and storing the data collected in our laboratory at Indiana University (IU). The laboratory was set up and operated through IU's "Partners in Applied Research" (PAR) program. Hardware used in the project was developed prior to this work, and is discussed in the reports for our contract with Naval Surface Warfare Center, contract number N60921-86-C-0172, which expired in December 1988 [S1]. It will be necessary to refer to features of the hardware in this report, but for detailed information, the reader is encouraged to study the reports for the NSWC project and Reference [T2]. It is sufficient for this project to model the electronics system as in the block diagram of Figure V-1. It is very important to note that the signals produced by the electronics are not the true in-phase and quadrature EMF readings required by the model [S2], but are derived from the EMF values after some amount of amplitude scaling and phase-angle rotation. The actual EMF values must be determined from the laboratory measurements by forming a linear combination of the measured "zero" and "ninety" signals. Reference to Figure V-1 is made later in this chapter when discussing the algorithms that we used for computing the actual EMF values.

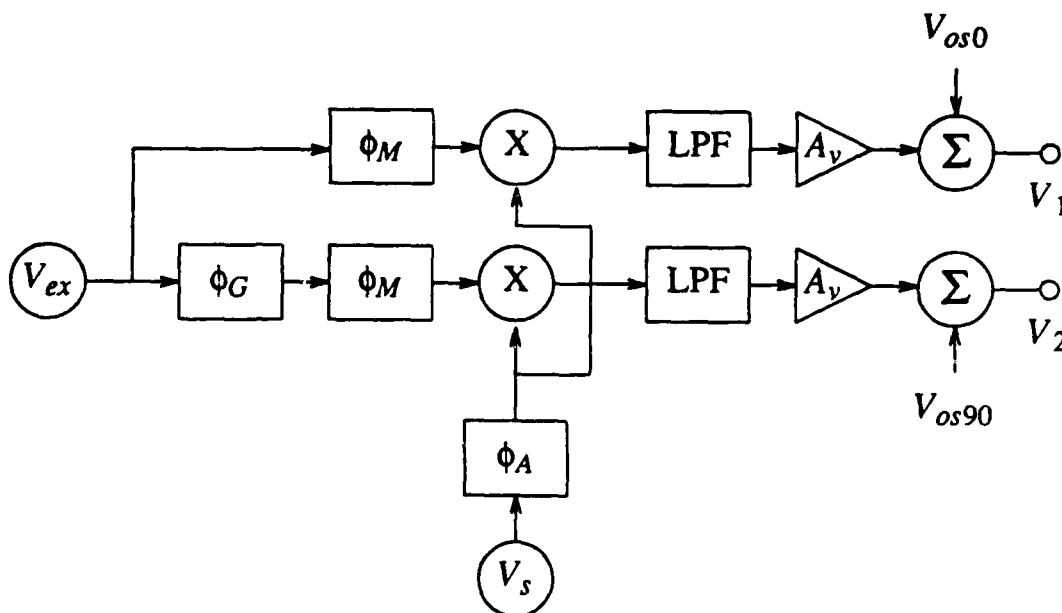


Figure V-1. Model of the mixer circuit.

2 a. Steps in the Acquisition Process

To obtain a sufficiently large base of data from different flaws requires special tools and methods for compactly storing and retrieving the data. All data collected were eventually stored on our Alliant UNIX machine, and the UNIX environment was used to access the growing database, process and plot the data, and maintain information about the laboratory experiments. The following list summarizes the steps acquiring data and making it ready for the model.

1. Collect measurements in remote laboratory. We will use the term "test" to denote a given set of measurements resulting from one scan over a sample of material. A test typically consists of measurements at a multitude of frequencies on a grid of points in the $X-Y$ space, and is stored on a floppy disk or a hard drive in a number of different files.
2. Transfer the data from laboratory computer to Alliant computer. This task was best performed by first using an archive program to consolidate the data into one file (we used the public-domain program *zoo*), then copying the archive file to an IU UNIX machine that could be used to send data to our Alliant by UUCP (UNIX-to-UNIX copy). Alternatively we sometimes hand-carried floppy diskettes to an IBM-AT networked to our Alliant.
3. Store the data in an orderly manner. Our method was to use a unique directory in the labdata account, named by the year and date that the test was performed, that contained a few standard files: the compressed archive in one of several formats, *tar*, *zoo*,

or *ar*, *Read.me*, overview information about the measurement; *db.entry*, database information in a specific format; and *header*, specific information about the measurement. *Read.me* and *header* were also added to the archive.

4. Add *db.entry* to the database so that page number, data measurement statistics, sample, excitation, and other information could be accessed through the database program.
5. Run a program called *profile* developed by Bishara Shamee and Jeff Treece to make a profile page of grayscale images to add to our booklet of data.

2 b. Phase Shifts and Gain Errors

Note that there are two DC outputs of the circuit represented by Figure V-1, whose phase and amplitude depend in part on several phase errors and the amplifier gain. In short:

$$V_{\alpha} = \sin(\omega t) \quad (V-0)$$

$$V_s = A \sin(\omega t + \phi_s) \quad (V-1)$$

$$\begin{aligned} V_1 &= A \text{ LPF } \left\{ \sin(\omega t + \phi_M) \sin(\omega t + \phi_s + \phi_A) \right\} \\ &= A' \cos(\phi_M - \phi_s - \phi_A) + V_{os0} \end{aligned} \quad (V-2)$$

$$\begin{aligned} V_2 &= A \text{ LPF } \left\{ \sin(\omega t + \phi_M + \phi_G) \sin(\omega t + \phi_s + \phi_A) \right\} \\ &= A' \cos(\phi_M + \phi_G - \phi_s - \phi_A) + V_{os90} \end{aligned} \quad (V-3)$$

Where V_1 and V_2 are the outputs of the in-phase and quadrature mixers, respectively, and ϕ_s is the phase of the signal applied to the mixer input. Equations (V-2) and (V-3) can be used to calculate system parameters when some of the variables are known. Also, it is possible to calculate the mixer phase shift using the *SPICE* circuit analysis program. One can also extract the amplifier phase shifts from the data sheets. Finally, another set of two equations can be obtained after modifying the mixer circuit to bypass the amplifier (thus bypass the amplifier phase shift). These equations and calculations yield an over-determined system, however, the equations are non-linear, and several ideal assumptions have been made. Moreover, the laboratory measurements are taken with some degree of experimental error. The solution to the set of equations was attempted using *MINPACK*. A more complete discussion of this calculation was presented in the Seventh Quarterly Report.

2 c. New Method of Finding Phase Shifts, Based on Field Model

The *MINPACK* method of determining phase shifts, reviewed in this chapter and described in the Seventh Quarterly Report, has certain drawbacks, one of which is its complexity. The complexity of the process makes the error margin uncertain. Because of this fact and that we wanted to test results using an independent method, we briefly looked at a second method of calculating phase shift and gain multipliers for the lab data. The second method was based simply on calculating the expected EMF values ¹ and determining from the calculations the proper scaling factor and phase angle for the actual frequencies measured.

To calculate the expected EMF, we must know, apriori, the properties of the material. For this, we selected various metals, whose conductivities were documented in [W1]. We selected thin planar samples of the metals and measured the transmitted

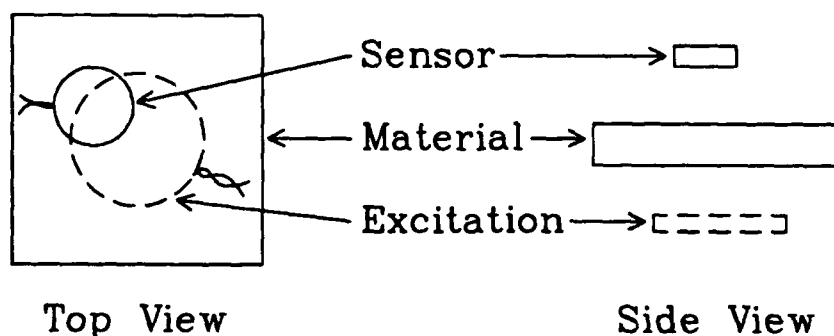


Figure V-2. Sensor and excitation arrangement for calibration experiments.

field using the setup of Figure V-2. We were able to compute the expected field using the experiment geometry and sample conductivity as inputs to the model. The outputs of the model were assumed the correct EMF values, and the outputs of the lab system were assumed to be V_1 and V_2 as shown in Figure V-1. A simple linear transformation can be used to transform V_1 and V_2 into the calculated EMF values. Then, assuming the same hardware setup for other tests, other laboratory data can be converted using the same linear transformation.

Plots of Figure V-3 show laboratory data and model calculations for the field transmitted through a sheet of aluminum foil. Similar experiments were repeated for other samples: copper, stainless steel, iron, and thick aluminum. Thick samples were desirable because the thickness was convenient to measure, but were undesirable because they attenuated the signal at high frequencies (demonstrating their EM shielding properties). Consistent results were obtained, indicating that a good agreement is seen after scaling the lab data by a factor of about 10 and correcting the phase by almost 180

¹ The calculation itself is not simple, but the concept is simple. The calculation is based on work reported in Chapter I.

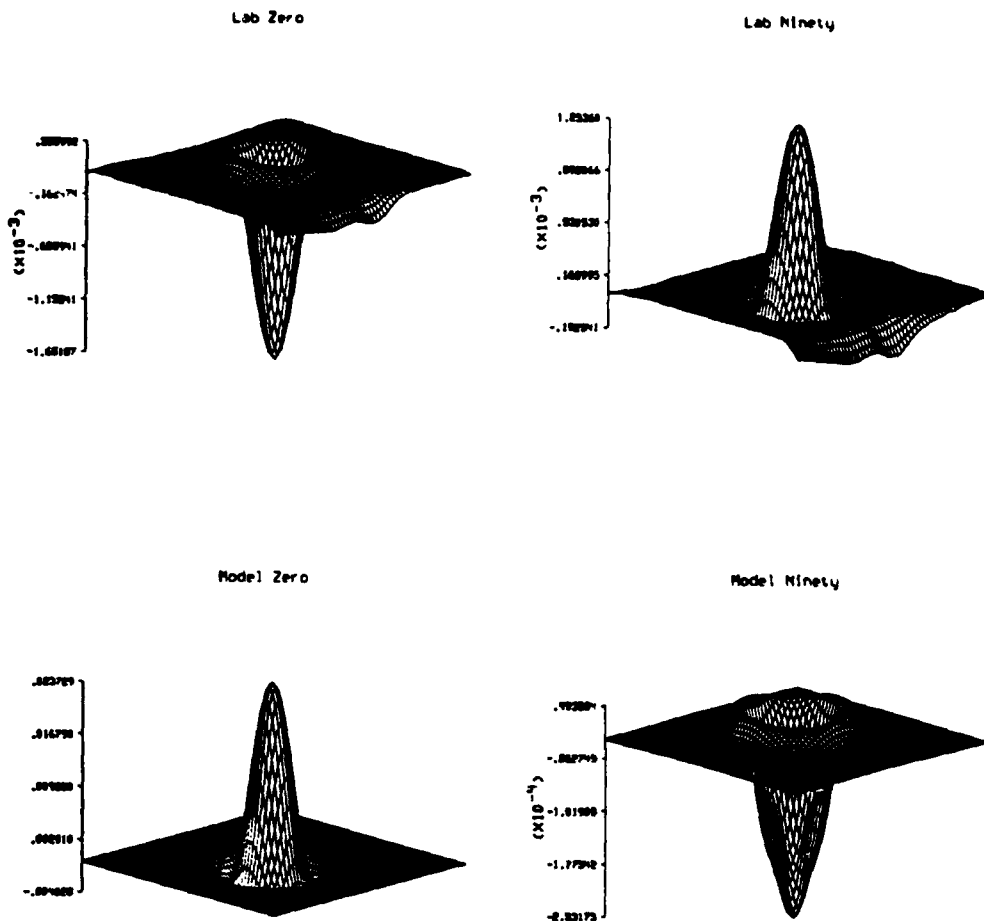


Figure V-3. Laboratory data (top) and model calculations (bottom) for transmitted field through thin sheet of aluminum at 5MHz. On the left is the "zero" signal; on the right is the "ninety" signal. Scaling and rotating (phase angle) the lab data gives a close approximation of the model calculations. The required rotation and scaling are not alarming. See text for a full explanation.

degrees. The 180 degree phase error is not disturbing: such an "error" could easily be the result of connecting the sensor or excitation with the wires reversed or losing a minus sign in a calculation. The consistency of these experiments indicates that this method might be an excellent way to calibrate the laboratory data. The two biggest problems in obtaining accurate results seem to be getting an accurate conductivity estimate and

accurately measuring the thickness of the material.

2 d. Using High-Frequency Data

At high frequencies, phase shifts and gain errors in the laboratory hardware can not be ignored. In competition with the hardware limitations are the needs of the computer model, which uses a multi-frequency algorithm that benefits from a wide range of frequencies. By compensating in software for phase shifts and gain errors and redesigning some of the sensors and exciting coils, we were able to collect data over a wider range of frequencies than expected at the onset of the project. The inductance of our *sleeve* excitation source was about $80\mu\text{H}$, and the sleeve had a self-resonance frequency in the 1-2MHz range. In order to expand our usable frequency range, we first looked for an excitation source with less inductance (though data collected with the sleeve are *not* useless: it is, however, more difficult to characterize the current that is driven through the coil, and thus determine the phase and magnitude of the excitation current). We next used a *whip* excitation, which had nearly the same cross-sectional geometry as the sleeve, but was formed of only one turn of wire instead of about forty. We were able to collect data using the whip at frequencies up to 25MHz. Smaller sensors also allow us to make measurements at higher frequencies -- sometimes up to 50MHz². We were not able to collect data above 50MHz because that is the highest frequency we could generate with our HP8116A signal generator.

The small excitations do not produce uniform fields, and the first version of the computer model assumed uniform fields. Later, changes were made to the model (see Chapters I and III) that allowed us to use data from whip, ring and other sensors and excitations. We discovered several trade-offs when using the smaller sensors: they typically gave higher resolution, measured only the near-surface region of the sample, tended to be more sensitive to lift-off, and gave a smaller flaw signal. Since the small sensors gave higher resolution measurements, we were often able to detect micro-features of the material, such as fiber weave structure and fiber orientation.

The software phase and gain compensation took place in three stages: we first characterized the laboratory hardware by performing experiments, then calculated parameters required for rotating and scaling, and then we converted the data by calculating actual EMF values, taking the excitation current into account. The first step was hardware-dependent: for each new sensor/excitation arrangement, new experiments were required to characterize the phase shifts. For this reason, EMF values could be accurately calculated for only certain sensors and excitation (the ones for which we performed the required experiments). The second step was accomplished by running a program using the data of the first step as input. The program calculated best-fit values for a number of unknowns. The entire method is described in detail in the Fifth Quarterly Report for contract number N60921-86-C-0172, between Sabbagh Associates and Naval Surface Warfare Center [S1]. An alternative method for the second step was

² The data at high frequencies had much more error, that is the phase and amplitude were much less accurate than at the low frequencies.

contemplated near the end of this project, and some preliminary results are presented in Section 0. At certain frequencies, the final step can possibly fail (see Seventh Quarterly Report, Appendix D, Section e). If the final calculation fails due to large specific values of phase shifts, the data are not useful at that frequency for use in the model.

3. SENSORS, EXCITATIONS, SAMPLES, AND DESCRIPTIONS

We tested new sensors to optimize the design for flaw and feature detection. Certain sensor configurations were particularly good at detecting certain features. For example, a directed current, such as our *whip* excitation, was found to be good at detecting fiber "tows."³ Certain innovative sensors, such as the "figure-eight" sensor/excitation described in the sensors listing, were useful for detecting flaws and other small features. We have noted that certain sensor designs are optimum for particular applications; we have already discussed an excitation that is good at detecting signals from tows, which indicates micro-structure of the material. However, carrying the example further, large tow signals hinder detection of flaws, so those sensors that are good at detecting tows might not be good at detecting impact damage.

3 a. List of Sensors Used

SENSORS

1. Sensor "HW1"
Pancake coil, 13 turns, 28 AWG. Diameter 0.16"
2. Sensor "HW1a"
HW1's replacement. Pancake coil, 13 turns, 28 AWG.
Outer diameter 0.125"; Inner diameter 0.06"
3. Sensor "HW2"
Pancake coil, 4 turns, 34 AWG. Diameter 0.09"
4. Sensor "HW3"
Pancake coil, 3 turns, 34 AWG. Diameter 0.06"
5. Sensor "HW4"
Pancake coil 3 turns, 34 AWG. Diameter 0.06"
6. Sensor "HW5"
Pancake coil, 3 turns, 34 AWG. Diameter 0.03"
7. Sensor "HW6"

³ Tows are the result of the bunches of fibers that are used when the materials are made. Conductivity is better in the tow regions than between tows, resulting in a striped image. Some such images are presented in the Fifth, Sixth, and Seventh Quarterly Reports. *Tow* is spinners' cant, now used by makers of graphite-epoxy. *Satin weave*, which has warp and woof without a twill, is another borrowed textile phrase, taken from weavers at the loom.

Pancake coil, 3 turns, 34 AWG. Diameter 0.04"

8. Sensor "HW7"

Pancake coil, 2 turns, 34 AWG. Diameter ?"

9. Sensor "mac01"

Circuit board sensor, 0.6" x 0.565". 10 turns, each having a width of 20 mils.

10. Sensor "mac08"

A circuit board sensor made up of 8 mac01's with a spacing of 30 mils between each sensor. Center-to-center distance between sensors is 0.6".

11. Sensor "jrb2"

0.375" diameter barrel, probe tip 0.25" diameter. This probe has a black housing with three gold stripes. There is a female connector for coaxial cable in back, and a small (less than 0.06" diameter) coil at front. The number of turns in the probe tip is unknown. Inductance ? henries. Resistance ? ohms.

12. Sensor "jrb2ns"

This is simply the jrb2 probe without its ferrite shield.

13. Sensor "HW8"

Pancake coil, 5 turns, 28 AWG.

Outer diameter 0.375"; Inner diameter 0.03"

14. Sensor "HW9"

Pancake coil, 5 turns, 36 AWG. Diameter 0.03"

15. Sensor "HW10"

Pancake coil, 5 turns, 36 AWG. Diameter 0.035"

16. Sensor "HW11"

Pancake coil, 5 turns, 40 AWG. Diameter 0.03"

17. Sensor "HW12"

Pancake coil, 5 turns, 40 AWG. Diameter 0.025"

18. Sensor "cap1"

Circuit-board sensor. 0.745" x 0.385"

Fingers separated by 20 mils. 2 groups of fingers. The inner group has four fingers, each outer group has two. The outer groups are connected.

19. Sensor "cap2"

Circuit-board sensor. 0.65" x 0.65"

Fingers separated by roughly 30 mils. Two separate groups of three fingers each. The fingers zig-zag twice.

20. Sensor "cap3"

Circuit-board sensor. 0.5" x 0.75"

Fingers separated by roughly 20 mils. Two separate groups of five fingers each.

21. Sensor "cap4"

Circuit-board sensor. 0.6" x 0.575"

Six groups of two fingers roughly 20 mils apart. The groups are separate.

22. Sensor "cap5"

Circuit-board sensor. 0.6" x 0.55"

Two separate groups of three fingers, each separated by 40 mils.

23. Sensor "cap6"

Circuit-board sensor. 0.75" x 0.55"

Both sides are different. One side has two groups of three fingers, the other side has three groups of two fingers, where the outer two groups are connected. The fingers are roughly 50 mils apart.

24. Sensor "cap7"

Circuit-board sensor. 0.275" x 0.575"

Six separate groups of two fingers separated by 20 mils.

25. Sensor "cap8"

Circuit-board sensor. 0.39" x 0.37"

Both sides are different. One side has four groups of two, the other side has one group of four flanked by two groups of two. The fingers are 20 mils apart. One finger in the four finger group is broken.

26. Sensor "HW13"

Pancake coil, 5 turns, 40 AWG. Outer diameter 0.15"

27. Sensor "HW14"

Pancake coil, 5 turns, 32 AWG. Outer diameter 0.1"

28. Sensor "HW15"

Pancake coil, 5 turns, 32 AWG. Outer diameter 0.09" +/- 0.01"

29. Sensor "HW16"

Pancake coil, 5 turns, 32 AWG. Outer diameter 0.09" +/- 0.01"

30. Sensor "HW17"

Pancake coil, 5 turns, 32 AWG. Outer diameter 0.09" +/- 0.01"

31. Sensor "280"

Sue Vernon's 86.280 probe. The barrel is a highlighter pen. A coax female connector is on one end, and an iron cup, 835 mils in diameter, is on the other. Epoxy seals the cup. Inner diameter = 350 mils. Barrel = 2,875 mils long. Inductance =? Henries. Resistance =? ohms.

A label says:

86.280 29I

1 c 6 03

32. Sensor "335"

Sue Vernon's 86.335 probe. The barrel is a highlighter pen. A coax female connector is on one end, and an iron cup, 1" in diameter, is on the other. Epoxy seals the cup. Inner diameter = 450 mils. Barrel = 2,140 mils long. Inductance =? Henries. Resistance =? ohms.

A label says:

86.335 26 16 pa

400 3b9

33. Sensor "disk"

A disk drive head. See the lab book for details. This is basically a split-core transformer, as far as we can tell.

34. Sensor "HW18"

One loop, 34 AWG, 0.2" diameter.

35. Sensor "HW19"

One loop, 34 AWG, 0.1" diameter.

36. Sensor "eyel"

Two loops with one turn in each loop. The windings oppose so that the background signal is eliminated, outer diameter .13" +/- 0.01", 34 AWG

37. Sensor "X1"

Four handwounds in series. Each Hw has two turns of 38 AWG wire around the peg of a dual-row header. The four sensors were then bent into an x shape such that opposing legs canceled each other in a

uniform field. This sensor was then placed in a ring excitation.

38. Sensor "rings"

Two handwounds with two turns of 34 AWG wire that were wrapped around a peg of a dual-row header. The windings oppose so that the background signal is eliminated.

39. Sensor "D1"

Two handwounds with two turns of 34 AWG wire that were wrapped around a peg of a dual-row header. The windings oppose so that the background signal is eliminated.

40. Sensor "microl"

Small micro sensor made at Purdue.

40. Sensor "micros"

Small micro sensors connected in series, placed side by side.

50. Sensor "HW20"

Two loops, 34 AWG, .70" +/- 0.01" diameter.

51. Sensor "HW21"

Two loops, 34 AWG, .59" +/- 0.01" diameter.

3 b. A List of the Excitations

EXCITATIONS

1. Excitation "linch loop"
diameter 1", 34 AWG.

2. Excitation "big sleeve"
A 11" x 3.88" x 0.25" piece of Plexi-glass, wound by 28 AWG wire 16 times. Each winding is 0.125" apart.

3. Excitation "junk sleeve"

4. Excitation "large sleeve"
9" in length when flat. 39 conductors (standard computer ribbon cable) connected together to form a solenoid. Width 1.94".

5. Excitation "small sleeve"
9.5" when laid flat. 14 conductors (standard computer ribbon cable) connected together to form another solenoid. 0.7" width.

6. Excitation "bridge"
A circuit board sensor, mac08, is attached to a Plexi-glass backing, which measures 9.06" x 5.06" x 0.24". The mac08 leads run out of the bottom edge of the Plexi-glass, back to another board with one 200 ohm potentiometer and 2 other resistors for each lead.

7. Excitation "HW2"
See above entry in SENSORS. Used as an excitation, HW2 was arranged in a "ring" configuration.

8. Excitation "HW6"
See above entry in SENSORS and "HW2".

9. Excitation "harp"
An 11" x 2" x 0.25" rectangular solenoid wrapped around Plexi-glass. It has 17 turns of 28 AWG wire, each spaced roughly 0.125" apart.
10. Excitation "loop4"
28 AWG, diameter 0.875". Loop excitations are used in anisotropy tests.
11. Excitation "loop21"
12. Excitation "large loop"
28 AWG, diameter 2.22"
13. Excitation "small loop"
28 AWG, diameter 1.11"
14. Excitation "mac01"
See above entry in SENSORS.
15. Excitation "monster"
28 AWG wire. 10" x 10.6". A 30 turn solenoid whose windings are in the direction of the larger axis. The windings are spaced five to six sixteenths of an inch apart.
16. Excitation "ring1"
28 AWG, diameter 0.625"
17. Excitation "ring2"
18. Excitation "ring3"
Slightly bent. 28 AWG, diameter 1"
19. Excitation "ring4"
28 AWG, diameter 0.1"
20. Excitation "ring5"
34 AWG, diameter 1.5" \pm 0.06"
21. Excitation "ring6"
22. Excitation "ring7"
36 AWG, diameter 0.625" \pm 0.06"
23. Excitation "ring8"
36 AWG, diameter 0.6" \pm 0.06"
24. Excitation "ring9"
36 AWG, diameter 0.625" \pm 0.06"
25. Excitation "ring10"
36 AWG, diameter 0.64" \pm 0.06"
26. Excitation "ring20"
40 AWG, diameter 0.125"
Has broken lead wire.
27. Excitation "ring21"
A double ring, one superimposed upon the other. 34 AWG, diameters 1" \pm 0.06".
28. Excitation "whip"
A single loop of 28 AWG wire. The loop is 8" when stretched flat.
29. Excitation "window"
A circuit board, 7.06" x 7" x 0.06", with copper on top. The left and right edges are solid copper columns, each one 0.375" wide. Joining the

two are regularly-spaced copper rows, each 0.06" wide, that completely fill the board from top to bottom. There are 100 rows in all.

30. Excitation "loop5"
28 AWG, diameter 0.25".

31. Excitation "ring11"
36 AWG, diameter 0.625" \pm 0.06"

32. Excitation "ring12"
36 AWG, diameter 0.625" \pm 0.06"

33. Excitation "fig8"
A sideways figure 8. The leads are attached to loop B. Diameter of loop A is 0.625" \pm 0.06". Diameter of loop B is 0.625" \pm 0.09". The fig8 is made out of 36 AWG wire.

34. Excitation "280"
See the above entry in SENSORS.

35. Excitation "335"
See the above entry in SENSORS.

36. Excitation "whip2"
A single loop of 28 AWG wire. The wire is 0.75" long when stretched to a separation of roughly 60 mils.

37. Excitation "ring23"
34 AWG, diameter 0.2"

38. Excitation "ring24"
34 AWG, diameter 0.1"

39. Excitation "ring25"
34 AWG, diameter 0.12"

40. Excitation "ring26"
34 AWG, diameter 0.06"

41. Excitation "ring27"

42. Excitation "ring28"
34 AWG, diameter 0.33"

43. Excitation "Rings"
Two handwounds of 34 AWG wire that were wrapped around a peg of a dual-row header. The windings oppose each other.

44. Excitation "micro2"
Small micro sensor made at Purdue.

3 c. Samples

DESCRIPTIONS OF SAMPLES

1. Sample "1"

Sample 1 is the well-known satin weave square sample that has twelve flat-bottom drilled holes. The dimensions are 6.125" wide by 6.125" long by 0.11" thick. The top side has twelve visible holes (6 0.5" diameter and 6 0.25" diameter). The top side is smoother than the bottom side. Weaves of dimensions approximately 0.1" are visible from both sides. The pattern appears to be "under-4, over-1." See the lab notes for more details.

2. Sample "pan12"

6.125" x 6.125" x 0.11" satin weave. Same weave pattern as Sample 1. Yellow alignment lines run horizontally as shown in the lab notes. The top side is smoother than the bottom side.

3. Sample "3"

6.1" x 6.1" x 0.1" satin weave. There is a hole almost precisely in the center of the top side (top side is the side that is "roughest"). The hole is 0.2" in diameter, appears to be flat-bottomed, and is approximately 55mils deep.

4. Sample "pi1"

6" x 6" x 0.065" checkered cloth pattern, but not satin weave. Top side is rougher than the bottom side. The panel flexes more easily along the y axis than along the x axis, as in the lab notes. A tag attached to the sample says:

10 layers
11 mil ohm
T = 67 -
wt = 57.1140 gm
v = 39.837 p = 1.434
high resistivity reasons unknown

5. Sample "pa4"

5.9" x 5.9" x 0.08". Top side has eleven holes of various sizes; see the lab notes. The panel seems rigid in both directions.

6. Sample "4"

6" x 6" x 0.085". The top side is smooth, the bottom side is cloth-patterned. The bottom has "5245C" and "#4" written in yellow grease pencil. There is a yellow X connecting the four corners of the sample. We will call the "5245C" edge the "0" direction. From the top, one can see predominate (fiber?) lines, diagonal from upper-left to lower-right. A blue grease pencil arrow points to the left on the top side. The board bends easier about the "0" direction axis than about the axis of the blue arrow. The board is warped in the "easy" direction (about 50 mils in the center).

7. Sample "2"

11.375"x 11.5" x 0.085" cloth pattern. The top says "top/front." The panel has blue grease pencil Xs near the center on both sides. Horizontal grooves of various widths (from 0.125" to 1", two sets) have been stamped on the top in four rows. The grooves average less than 5 mils deep. 7" from the left edge, and 1" and 2" from the bottom edge, are 2 depressions. The lower one is roughly 10 mils deep, the upper one is around 5 mils deep. 2" above the second depression is a third, 0.5" long and roughly 5 mils deep. On the back face, a crack extends from top to bottom, 3.875" inward from the right edge. The sample is warped near this crack, by (on the average) 5 mils. The whole sample bends

along the axes parallel with the crack much easier than along other axes.

8. Sample "RAE1"

13" x 12.875" x 0.215" cloth pattern. The front has "RAE1" and "0-90" on a sticker in the top right corner. Various irregular depressions are circled with yellow grease pencil, see the lab notes for more details.

9. Sample "RAE2"

4.94" x 4.38" x 0.125" rigid cloth weave. The panel has blue tape saying "RAE2" in the upper right corner. The back shows fibers in x patterns. The front has two circled regions. See the lab notes for more details.

10. Sample "RAE3"

6.125" x 4.31" x 0.195" rigid cloth weave. The front and back are plain except for a circled depression on the front. The depression is located 2.5" up and 3.5" over from the bottom left corner.

11. Sample "RAE4"

7.125" x 6.125" x 0.395" rigid cloth weave. The panel has no diagonal fibers. No obvious flaws are on it. Blue tape saying "RAE4" is in the upper right corner.

12. Sample "RAE5"

12.25" x 11" x 0.32" rigid cloth weave. There is a tape saying "RAE5" in the upper right corner. Also in the top right corner is written "0+/-45." The panel has 5 layers of roughly 0.06" each. The front has two circled depressions. The upper left circle says "28.3 J."

13. Sample "5"

12" x 11.88" x 0.15". Top is smooth, bottom is a canvas-type of surface. A blue X is drawn on the front. Lines run from left to right on the top. The top is scraped in the bottom left quadrant. The edges are rough and irregular. Fibers run vertically. The panel is rigid, except for vertical axes. Two cracks are in the back. One is 0.75" from the right edge, the other is 6.75" from the right edge. This is the unidirectional sample made by Olaf Rask.

14. Sample "bar"

2" x 12" x 1.44". The top is cloth weave, the bottom is satin weave. The sample is obviously layered. The middle of the bottom is warped upward by roughly 15mils. The top says "4-10" and has two circular depressions: one squarely in the center, and one 4 inches beneath the first. The top has shallow grooves spaced around 1" apart; these grooves are apparently joints.

15. Sample "A"

9" x 9" x 0.11". The top is smooth, the bottom is a tight canvas weave. Fibers run diagonally, + and - 22.5 degrees. A red "A" and an arrow indicating fiber direction are drawn in the upper left quadrant. The panel has no obvious flaws.

16. Sample "B"

9" x 9" x 0.11. This panel has the same physical attributes as Sample A. A red "B" and an arrow are drawn in the upper left quadrant, as with Sample A. Again, no visible flaws are present.

17. Sample "ceramic"

Two ceramic disks, one white, one black. The white one has a circular depression in it, 85 mils in diameter and 30 mils deep. The white disk has a 465 mil diameter and is 242 mils deep; the black disk is 465 mils in diameter and 212 mils deep. The black disk is abraded near the edges.

18. Sample "xas"
12" x 12" x 0.17". This sample is described fully in the notes included in the package from England. It is a 32-ply carbon-epoxy slab with nine 0.2-ply-wide delaminations ranging in diameter from 0.8" in the upper left to 2" in the lower right. A label in the upper right corner of the top face says:

070 688 / B.C.
XAS 914
32 ply 0/90/+or-45
with delaminations

19. Sample "carba"

20. Sample "carbb"

21. Sample "C302"
10" x 13.25" x .14" carbon carbon weave sample. This sample has it's lower right corner cut out. The sample is warped down the middle, however it is not obvious. The front of the sample is labeled with C302 written on it, also the direction of the warp is indicated here. The sample also has a purple square painted on the front.

22. Sample "copper"
3.995" x 3.930" x .024" piece of copper.

23. Sample "lead"
4.5" x 4.6" x .106" piece of lead.

24. Sample "stainless"
16.88" x 7.9" x .062" piece of stainless steel.

25. Sample "slide"
1.074" x 3.135" x .274 carbon-carbon. The top side has two large flaws, also the top right corner is ground down. Backside has a glossy appearance.

SOLAR CELLS

1. 2L65-66-503
Solarcell marked with "O" on the bottom in black. Has obvious defect going across the cell, 80 mils up from the centerline (silver strip at the bottom).
2. 5J79-63-501
No defects are obvious, though there is a slight hump 80 mils up from the centerline, with the silver strip at the bottom. Also, there may be a defect along the upper right side. See lab notes for more details.
3. 5J69-20-06-501
There seems to be a defect 175 mils below the centerline, and the cell's appearance is "patchy," more reflective than cells #1, #2, or #4.
4. 4L96-44-501
No obvious flaws, though there is a slightly raised area about 200 mils above the centerline.
5. 4M59-30-501
6. 5K19-41-501
7. 2M16-49-503
8. 5K15-43-501

9. 2L87-08-501

There is an obvious diagonal crack from the lower left edge going up to the right.

10. 3M61-41-503

There is a lengthwise raised area 300 mils from the right edge.

11. 4M11-59-501

This cell has a crack on the lower right edge. There is also a smashed spot in the lower right.

12. 4M59-35-501

There is a crack at the upper left edge.

13. 3M62-65-501

No glaring defects.

14. 4M78-48-501

No obvious defects.

15. 3M72-22-501

Nothing obvious.

16. 4M59-45-501

Nothing obvious.

17. 4048-37

Exposure.

18. 4048-60

19. 4048-14

20. 4048-54

21. 4048-07

CIRCUIT BOARDS

1.

7.94" x 3.625" x 0.06" Copper-colored rectangle. See the lab notes for a picture of it.

2.

9" x 3" x 0.06". Top is silver-green, bottom is dark green. There are many large holes, but few pinholes. There are 2 solder globs on the top and the bottom. See the lab notes.

3.

4.5" x 5.44" x 0.06"

This board is green. There is a 2.63" x 0.38" projection out of the bottom, located 0.63" from the left edge. The top has a 5 x 7 grid of contacts. Six chips are still on the board. The back "looks like a parking lot." See the lab notes for a diagram.

4.

9" x 3" x 0.06"

This board is a clone of #2, except it has no solder globs, and its pinholes are smaller.

5.

5.44" x 3.38" x 0.06" green board. The top and bottom both have rows of

silver near the top and bottom, roughly 0.125" wide, but the top has a silver column at the left edge, 0.125" wide. In the middle of both sides are pinholes, arranged in 6 groups of 16. These pinholes cover a rectangular area totaling 4" x 1". The bottom left corner of the pinhole rectangle is 0.75" from the left and 0.75" from the bottom.

6.

8.5" x 5" x 0.06" green board. The top face say "top" in the lower left corner. There is a gold strip on the left edge of the top and bottom. The top has sparse wiring, the bottom somewhat more wiring. The only holes are close to the left and right edges, in the center. See the lab notes for more details.

7.

4.06" x 2.44" x 0.05" brown board. The left has a contact projection with dimensions 1.5" x 0.25", located 0.5" up from the bottom edge. The front says "s2193626" near the lower left. The upper right and lower left corners have 0.625" long, 0.063" high cuts extending into the board from the right along the top and bottom edges. Again, see the lab notes for a diagram.

8.

6.69" x 6" x 0.06" board, dark green front, silvered back. There is a contact projection on the left edge of the top. It is 0.25" wide, 2.5" long, and starts 1.75" from the bottom.

9.

8.25" x 2.88" x 0.07" board. The front says "44112" near a resistor in the upper left. A 4.12" x 0.375" contact projection starts 2" from the right edge, near a capacitor. Two rows of 22 vertical, soldered, pinhole columns cover the front and back faces. Two 0.125" diameter holes are positioned at 2" and 6.25" from the left side, 0.5" from the top.

10. copper3

16.25" x 10" x 0.06" brown board. The front face of this board has "10424" in the upper right quadrant. The back face has a mailing label along the top edge. There is a rectangular hole in the upper left corner of the front. Gold contacts are along the bottom edge. The wiring and pinhole rows are predominately vertical on both sides. The board is made up of 6 layers. The top and bottom edges of the front are warped upwards by roughly 0.3", and the left and right edges are warped downwards by around 0.1". The board is flexible in all directions.

3 d. Database Descriptions

FEATURES

1. tows

Linear disturbance in data due to the sample's fiber direction. When two or more fiber directions are present, a weave-like pattern appears in the data.

2. flaws

Any man-made or natural cut, crack or blemish located on the sample being analyzed.

3. anisotropy

Used to obtain directional properties of a sample. A pattern is

obtained by using a single current loop placed either on top
(1) Reflected or on the bottom of the sample (2) transmitted.

4. foil
A piece of foil used to represent a "target". This piece of foil can be any size, shape and at any location. (See Read.me files for detailed information on location.)
5. aluminum
A piece of aluminum used as a sample.
6. orientation
Aluminum "targets" cut in various shapes and sizes. These "targets" are then placed on the sample being analyzed. Useful for giving true directions of sample with respect to the positioner.
7. monosensor
A single sensor being used for eddy current detection, as opposed to using several sensors.
8. solarcell
A semiconductor solarcell was used as the sample.
9. subtraction
The subtraction of one data set from another. This is generally performed on data coming from two samples of identical makeup and orientation, except one of the two samples may have a man-made flaw.
10. saturated
Measured signal at the A/D converter exceeded the maximum readable value. The data obtained at these points are generally useless. A sure indication is areas in the grayscale that are all-black or all-white.
11. traces
Copper traces on a pc board.
12. weaves
Weave patterns can be seen on plots associated with satin weave graphite epoxy composite materials.
13. SBIR88
These data were used in a proposal for the SBIR 1988 solicitation.
14. 0.1ufcap
A .1uf capacitor was placed at the output of the lowpass filter on amplifier. The resistor value used in the LPF was 10k.
15. 2.7ufcap
The lowpass filter at the output was using a 2.7uf capacitor. The resistor used was 10k.
16. 0.01ufcap
The lowpass filter at the output was using a .01uf capacitor. The resistor used was 10k.
17. transmitted
The anisotropy test was done in transmission (the sensor and excitation were on opposite sides of the material).
18. reflected
The anisotropy measurement was reflected (the sensor and excitation were on the same side of the material).
19. tee
The sensor arrangement was "tee." For a tee arrangement, the sensor

and excitation are pancake coils, and the sensor is placed tangentially to the material. The excitation is placed tangentially to the sensor (in a plane parallel to the sample).

20. impact
Damage is visible in the measurement that was the result of impact.
21. cracks
This primarily applies to solar cells. A crack in the material shows up in the measurements.
22. incase
This feature primarily applies to solar cells. The measurements were made while the samples were still in their cases.
23. blast
The data was taken, but the real reason for the measurement was to expose the sample to a "blast" of excitation.
24. striping
Discontinuities in the Y direction in the plots caused by multiple sensors covering adjacent areas of the sample.
25. lemon
An anisotropy test feature. The reflected or transmitted field has an "oval" appearance (stretched in one direction).
26. fourfold
An anisotropy test feature. The reflected or transmitted field has four or more "lobes".
27. balazs
The data collected is bad for some reason. For example, a sensor may have come loose during the test and only half of the data are valid.
28. metal
data were collected from transmitted field through a metal sheet so that calibration data could be collected to determine gain and phase shift of the amplifiers

4. DATA-HANDLING SOFTWARE

The phase angle and gain depends on many things, including the particular sensors and excitations used. The numerical accuracy of the data, and hence the success of the inversion algorithms, hinges on the proper characterization of these sensors and hardware. An improved method of storing data was developed during this project that involved using a different coding of data and a different data compression algorithm.

As mentioned above, proper handling an appropriate usage of the data can be as complicated a task as actually acquiring the data. One difficult problem is documenting the experiments well enough that the phase shifts, gain, and physical parameters can be accessed when required by the conversion program. In addition to having the information available, proper usage of the data demands that the user have knowledge of how the data conversion tools operate. Another difficulty is locating the data required after it has been stored away in its archive.

Documentation consisted of more than notes about sensor size, distances, and physical locations of samples and sensors; we also performed experiments to characterize the hardware. Results from the experiments were used data-handling software. Descriptions of sensors, samples, excitations, and data features were updated for the laboratory database, and a menu-driven program was developed to locate particular data based on features or other keywords. Documentation was improved for the software tools required for extracting and managing data to help the user understand the operation of the relatively complicated data conversion utilities.

4 a. Keeping Track of the Data

Our method insured a standard way of storing the data, and reduced the amount of disk space required, making it easy to recover raw data for a numerical experiment. By placing vital information in the database, one later has the ability to search for specific samples or other keywords and immediately locate the data. The ability to select certain features of the data helped us to gain insight about the data collection process. We can, for example, locate all tests that demonstrate the "tow" feature, and then see what sensors and excitations were used to gather those data. A listing produced by the database program is included in this report. Sample entries from the laboratory data have appeared in previous quarterly reports, and do not appear here. The complete summary of all data appears in a collection of outputs from *profile*, that we appropriately call the *Tons-o-Data* data book. One such entry was made for every test made for this project and others. Also included in this report is a description of the operation of the database-searching utilities. Standard UNIX and public software utilities were used to locate and manipulate the data: *awk*, *sed*, *tar*, *grep*, *ar*, *zoo*, *compress*, and *troff*. The following listing is an introductory notice that gives the user an idea of how the database operates.

INSTRUCTIONS FOR "DATA" USAGE

You have accessed a simple (really) database that will give you information about data acquired in the lab. Some on-line definition files can be viewed from the main menu. These definition files explain characteristics of sensors, samples, excitations, and features from the entire collection of lab data. A few simple database operators allow you to pick out particular sets of data based on your selection of features or other stored information. A report will be generated that can be sent to the printer, a computer file, or the terminal screen. In order to effectively use the database, you should understand how the information is stored...

- 1) Raw information about lab measurements is edited into a form-like file that is human readable. That file is called "db".
- 2) The raw file is condensed into a more compact file that is not very readable. Information is stored one-data-set-per-line. Separate bits of information within the line are separated with the "@" sign. The compact file is called "db.condensed".

To retrieve information, the compact file is "grep"ed for patterns that match the keywords specified by the database user. The keywords can be a list of words, and can involve logical operators: OR, AND, and NOT. For example, one can search for all data listing features "flaws" but NOT

"balazs." Note that since the file is grepped on a line-by-line basis, there is no way of telling what field the pattern matches. The pattern "1" will match "1" in the SAMPLE field (see fields below), but will also match "1988" in the DATE field. If you wish to match fields precisely, you can surround the pattern with "@"; thus the pattern "@1@" matches the "1" in the SAMPLE field (unfortunately "@1@" matches "1" in other fields such as "AVERAGES" -- see below).

The fields appearing in the db file are listed below:

- | | |
|----------------|---|
| 1) (empty) | Empty; nothing in this field |
| 2) PAGE | Page number in the Tons-o-Data manual |
| 3) SAMPLE | The official sample name |
| 4) DIRECTORY | The pathname to the data on the Alliant |
| 5) DATE | Date recorded by data acquisition program |
| 6) SENSOR | The official sensor name |
| 7) EXCITATION | The official excitation name |
| 8) ORIENTATION | Orientation of sample, if applicable |
| 9) TOPORBOTTOM | Top --> sensor scanned over top of sample |
| 10) RANGE | Two numbers representing lower and upper frequency |
| 11) TEST | Name of the test performed (e.g. "flaw") |
| 12) QUALITY | One word describing data quality (good, fair, poor) |
| 13) DIMENSIONS | Size of scan in inches -- X and Y |
| 14) RESOLUTION | Step size in inches -- X and Y |
| 15) AVERAGE | Number of points averages together per measurement |
| 16) VERSION | Laboratory hardware ID number |
| 17) FEATURES | Features demonstrated by the data |

For more information, refer to documentation for the data-taking program and documentation for the conversion program.

4 b. Data Conversion

To correct in software for phase and gain errors, a program was run in the lab to record the outputs of the A/D converters (all channels) under simplified conditions. These data were used determine the phase-shift and gain effects present in the circuitry. A program called `adcounts.c` reads the A/D converters on the lab computer at a number of frequencies to provide required phase and gain information. A second program is a c-shell program on the Alliant UNIX computer that takes `adcounts` output and formats a "parameter" file to be used by the parameter-calculating program. A third program, `calcparms.f`, uses the *MINPACK* equations and the parameter file, `parms.dat` to determine amounts of scaling and rotation. The output of the `calcparms` program is called `calcparms.dat`. A fourth program, `makesystem` takes the `calcparms.dat` file and produces `mixer.parms`. Finally, `mixer.parms` is used by `convert` when the phase and gain calculations are made. This process is further described above, in the *DATA COLLECTION* section.

`convert` was used to translate raw laboratory data, stored in a compact coded format, into user-ready EMF data, processed as needed to compensate for the phase and gain errors described above. A great deal of input is required by `convert` before the EMF values can be extracted. The values of N_x and N_y , along with the number of sensors used and the ordering of the data files, are *always* required when attempting to reorder the data. `convert` must also know the storage format of the data: several different storage formats were used throughout this project (see *Image Compression and*

Archival). Also, the laboratory setup and parameters are needed to use the data in the model (e.g. the list of frequencies and excitation voltages used). If the user attempts to compensate phase and gain or normalize to the exciting coil current, then the values of amplifier gains and exciting coil voltages are required. Other information is useful for keeping track of how the data is collected: date of the measurement, version of data-taking program used, number of measurements averaged to get one data value, sensor used, excitation coil used, the sample material measured, and the physical dimensions (in inches, for example) of the area covered by the test.

In early versions of the data-taker program, the data files were named with digits indicating the sensor number and Y value of the pass. This storage is very different than the storage method of later versions. Whenever a such a revision is made to the lab software, the required method of conversion changes. If a new there is a new hardware setup, the sensor order is possibly reversed, and in some cases, sensors can be hooked up with reverse polarity. Thus for every hardware or software revision, a new *hardware ID number* was created that was used as an input to `convert`. The program can decide from the unique ID how to reorder the data and invert certain channels if required. All of the above parameters are read by `convert` in the form of a *header*, which is always created by the data-taker program. The following list is a summary of the information found in header:

```
Hardware ID Number
Date of Experiment
Description (Sample, Sensor, Excitation)
Beginning X Value in Inches
Ending X
Number of Data Values in X
Beginning Y Value in Inches
Ending Y
Number of Data Values in Y
Number of Frequencies Used
Number of Sensors Used
Number of Data Points Averaged
List of Frequencies in KHz
List of Exciting Coil Voltages
List of Gain Settings (0=H; 1=L)
Data-taker Version ID
```

Included in the list of inputs to `convert` is the revision level of the data-taking program. The revision of the data-taker is important because a number of factors within the data-taker can affect the accuracy of the measurements. If a measurement is repeated for verification, it is important to use the original revision of the program. Also, when the laboratory numbers are compared to model calculations, the accuracy of the measurements is an important consideration. Under some conditions, the data-taker might give erroneous results, and the revision level helps debug problems with the data.

A number of hardware system parameters must be determined before the phase and amplitude of the signal can be calculated (see *DATA COLLECTION*). These parameters are assumed to be stored in a file called `mixer.parms` in the lab data home directory. When `convert` runs, it searches for the file and allows phase and gain calculations if the file is present. If the file is not present, then the program will warn the user that no phase/gain calculation can be attempted. Sometimes, `convert` can not perform the

requested calculation of EMF values. In this case, the files are still created but are not normalized: the result is "raw" values from the A/D converter. Thus, the user must pay attention to any warnings given by the program.

The contents of `mixer.parms` are calculated by `calcparms`: *mixer phase shift, exciting coil current, exciting coil magnitude, amplifier phase shift (H and L gains), individual channel DC offsets (H and L gains), and individual channel gains (H and L gains)*. The values of the parameters change with different exciting coils, sensors, cables, and mixer circuits; thus, a new `mixer.parms` file is required each time a new experiment is set up (whenever the actual phase and magnitude is required). Since it is not always feasible to produce a new parameter file every time an experiment is run, we often "live with" the phase and gain errors that result. Any time that the "standard" parameter file is not accurate enough, additional data can be taken to improve the experiment's accuracy. It is impossible for `convert` to estimate the accuracy of the conversion, except when the frequency is known to be out of range.

Documentation for `convert` exists for the FORTRAN version of the program. When the format of data storage was changed (data-taker Revision 1.17), `convert` was re-written in C language to assure better portability to other computers, such as MS-DOS machines. The operation of the C version of `convert` closely follows the documentation in two internal documents: *A Guide to Using Convert*, and *Convert Usage Instructions*, both written by Jeff Treece. Some amount of usage instruction is given when invoking `convert -h`.

4 c. Image Compression and Archival

Counts measured from the A/D converters were originally stored in *jeffcode*.⁴ A slightly more compact storage would result from storing a pair of readings in three bytes, but it would be impossible to edit or view the file with standard text tools. The disk-space savings would be 25 percent, ignoring the newline character at the end of every line in the coded file. The standard file format for all hardware Revision Numbers 4.1 and 4.4, prior to software Revision 1.17, has two lines of *jeffcode* numbers for each *X* value in the file: one line contains the in-phase measurements and the other line contains the quadrature measurements. Each of the two lines has a coded measurement, occupying two characters, for each frequency recorded. Each line is terminated with the UNIX newline character (10 decimal). *Jeffcode* must be first decoded since it is not a native machine data type. Coding and decoding *jeffcode* can be done using bit operations to speed up the process, but the process always takes some amount of computation. A decoded number is always in the range of 0-4095 decimal, inclusive, and represents the number of counts measured by the A/D converter. The analog input range of the A/D converter is -10V to 10V; thus the counts are converted into a voltage by the equation $V = -10 + C \times 20/4096$, where *C* is the number of counts measured by the A/D

⁴ *Jeffcode* is described in previous quarterly reports. It was created for convenience, not for efficiency. Every byte of the coded file is a readable ASCII character, making it possible to edit and view the file.

converter.

Data for each measurement are stored in a compressed archive. Three archive programs have been used: UNIX's `ar`, UNIX's `tar`, and the public domain program `zoo`. `Zoo` has its own internal data compression; when the other two are used, the resulting archive file compressed with UNIX's `compress` utility. Data from the lab stored in *jeffcode* does not typically have a good compression rate (not much disk space is saved) because the like-features of the data are dissociated: the spatial structure of the image is not maintained. One way to improve the compression is to store the gradient (along columns) of the file. This simple operation improves compression by saving only variations and not the absolute numbers.

Another way to improve compression is to store the data in a reordered space. The normal ordering (adjacent *X* values stored in successive memory locations) makes the most sense; if stored this way, regions of small variations compress well. There are other advantages to storing data in the sensible ordering; for example, the data can be read directly into arrays using low-level read statements, resulting in much more efficient I/O in processing programs. Compression can often be improved by separating least-significant bits and most-significant bits into separate files. The most significant bits have little variation, and compress very well. This discussion applies only to general-purpose data compression utilities, such as `compress`. There may exist other compression utilities that take advantage of the geometry of the data file that would perform adequately without reordering the data. Prior to Revision 1.17 of the data-taker, storage was in *jeffcode*; after that time, the data were written with the four most-significant bits in one file and the eight least-significant bits in another file. The naming convention for the data files became:

A number of experiments were performed using the techniques discussed above. Timing results are not very accurate because they were performed on a UNIX machine while it was tending to other tasks. The timing can be used to get a rough idea of the computer resources required to store and extract the data. Experiments using several different methods yielded the following results:

Lab Data Files:

name10.0h
 Base Name |
 Frequency |
 Phase |
 Bit Significance

Output of Convert:

name10.00
 Base Name |
 Frequency |
 Phase

Figure V-4. File naming convention for the data files and convert output files. The "Base Name" is up to five characters, and is determined when the data is taken. "Frequency" is an integer, starting with 0, that indicates the frequency index (0 is the first frequency, 1 is the second, and so on). "Phase" is either 0 or 1 in the lab data files and 00 or 90 in the convert output files, and represents whether the data are in-phase or quadrature. "Bit Significance" is either h or l, and indicates whether the file contains most-significant bits or least-significant bits. Lab data files are stored in character format (one byte per datum), and convert output files are stored in single-precision floating point binary format.

#	Storage Method	JC	DF	Size	Time *
1.	Raw Jeffcode	y	n	424	35.1
2.	Differenced Jeffcode	y	y	252	30.3
3.	Reordered Jeffcode	y	n	220	25.9
4.	Differenced Reordered Jeffcode	y	y	200	24.3
5.	Reordered 2-byte Integer	n	n	276	27.4
6.	Differenced Reordered 2-byte Integer	n	y	208	27.8
7.	Reordered 2-byte Integer Separate Files	n	n	216	25.5
8.	Differenced Reordered 2-byte Integer Separate Files	n	y	176	28.3
9.	1.5-byte Character No Compression	n	n	384	2.6
10.	2-byte Character No Compression	n	n	500	
11.	1.5-byte Character Differenced Reordered	n	y	168	33.3
12.	1.5-byte Character	n	n	204	32.3
13.	2-byte Character Differenced in X-Y Reordered Separate Files	n	y	140	26.1

* Very approximate

Table V-1. Experimental timings and disk usage values for various storage methods.

The column labeled "JC" indicates whether or not the method uses *jeffcode*; if so, some computation is required to extract the data. Likewise, the column "DF" indicates whether or not the data is differenced. Again, a "y" in this column indicates that additional computation is required to extract the original data. The size is given in k-bytes used by the archive file. The time column tells how much time was required for extraction, in seconds. The time column is very approximate since the time depends on system load and other factors. "Jeffcode" is the data format produced by the laboratory program. "Reordered" means that the data has been re-written into a "normal" ordering (see above). whose rows and columns correspond to X- and Y-indices of the data. "2-byte" and "1.5-byte" indicate how many bytes are used to store one datum. "Integer" indicates that the counts of the A/D converter are re-formatted into the machine representation for an integer. "Character" indicates that the data are stored as-is from the A/D converter, bit-for-bit. "Separate Files" indicates that the most-significant and least-significant bits are stored in two different files. In terms of disk storage space required, method 13 is the best. In terms of extraction time, methods 9 and 10 are the best. Other methods, such as 2-byte character, might be more convenient for accessing and using the data. The new version of software uses method 7.

5. SAMPLE LABORATORY DATA

It is beyond the scope of this report to present all 500 plus pages of the *Tons-o-Data* booklet. We have presented some of these data in previous quarterly reports, and a relatively complete discussion of the data is presented in the final report for the NSW project, mentioned previously in this chapter. For the purpose of this report, a few key sets of data are presented (the data presented here bears special significance because it is considered in model calculations in Chapter III). The images are presented here as they appear in the *Tons-o-Data* booklet. The data used by the model are these data, rotated and scaled as discussed above.

5 a. Data Database Listing

A fairly complete summary of the stored data is presented here. The database listing starting on the following page was produced by the database programs, and represents one of the forms of output that a user can request when searching for particular data. Page numbers in the listing refer to the page numbers from the *Tons-o-Data* booklet, as in the *Sample 1* and *Sample 3* data presented in this chapter.

Page	Directory	Sample	Features	Sensor	Source	Q	Res.	Range	Test
001	1987/aug19/amp1a.ref	A	reflected anisotropy 2.7ufcap	mac08	small loop	good	0.1 0.1	500 16000	anisotropy
003	1987/aug19/amp1b.ref	B	reflected anisotropy 2.7ufcap	mac08	small loop	good	0.1 0.1	500 16000	anisotropy
005	1987/aug19/amp1a.tran	A	anisotropy transmitted 2.7ufcap lemon	mac08	small loop	good	0.1 0.1	500 16000	anisotropy
007	1987/aug19/amp1b.tran	B	anisotropy transmitted 2.7ufcap lemon	mac08	small loop	good	0.1 0.1	500 16000	anisotropy
009	1987/dec01	B	flaws lows SBIR88 2.7ufcap impact	mac08	whip	good	0.1 0.1	1000 25000	flaws
011	1987/dec10	aluminum	reflected anisotropy aluminum 2.7ufcap saturation	mac08	1 inch loop	fair	0.1 0.1	1000 25000	anisotropy
013	1987/dec11	aluminum	reflected anisotropy aluminum 2.7ufcap	mac08	1 inch loop	good	0.1 0.1	1000 25000	anisotropy
015	1987/dec14	aluminum	reflected anisotropy aluminum 2.7ufcap	mac08	1 inch loop	good	0.1 0.1	50 1250	anisotropy
017	1987/dec02/sample1	1	flaws 2.7ufcap monosen- sor saturated	mac08	whip	good	0.1 0.1	1000 25000	flaws
019	1987/dec02/sampleA_B	AB	flaws lows foil 2.7ufcap monosensor	mac08	whip	good	0.1 0.1	1000 25000	flaws
021	1987/dec07	1	flaws monosensor SBIR88 2.7ufcap	mac08	whip	good	0.1 0.1	1000 25000	flaws
023	1987/jul10	1	flaws 2.7ufcap striping	mac08	bridge	good	0.1 0.1	100 9000	bridge
025	1987/jul14/templ1.110mils	1	flaws 2.7ufcap striping	mac08	bridge	fair	0.1 0.1	100 9000	bridge
027	1987/jul14/pen12.5mils	pen12	flaws 2.7ufcap striping	mac08	bridge	fair	0.1 0.1	100 9000	bridge
029	1987/jul15	2	flaws 2.7ufcap striping	mac08	bridge	fair	0.1 0.1	100 9000	bridge
031	1987/jul16	2	flaws 2.7ufcap striping	mac08	bridge	fair	0.1 0.1	100 25000	bridge
033	1987/jul23	1	flaws 2.7ufcap striping	mac08	bridge	fair	0.1 0.1	1000 31000	bridge
035	1987/jul24	1	flaws 2.7ufcap striping	mac08	large sleeve	fair	0.1 0.1	100 9000	flaws
037	1987/jul08	1	flaws 2.7ufcap striping	mac08	bridge	fair	0.1 0.1	100 9000	bridge
039	1987/jul09/bamp12	2	flaws 2.7ufcap striping	mac08	bridge	poor	0.1 0.1	100 9000	bridge
041	1987/jul09/backside.bamp1	1	flaws 2.7ufcap striping	mac08	bridge	fair	0.1 0.1	100 9000	bridge
043	1987/jun12/sample5.loopz	5	anisotropy 2.7ufcap lemon transmitted	mac08	small loop	good	0.1 0.1	100 9000	anisotropy
045	1987/jun15/amp15_ansi_topside	5	reflected anisotropy 2.7ufcap	mac08	small loop	good	0.1 0.1	100 9000	anisotropy
047	1987/jun15/amp12_ansi_topside	2	reflected anisotropy 2.7ufcap striping balazs	mac08	small loop	poor	0.1 0.1	100 9000	anisotropy
049	1987/jun15/loop_only		anisotropy 2.7ufcap	mac08	small loop	good	0.1 0.1	100 9000	anisotropy
051	1987/jun02/sample3	3	flaws 2.7ufcap striping	mac08	large sleeve	good	0.1 0.1	100 9000	flaws
053	1987/jun02/sample.pa4	pa4	flaws 2.7ufcap striping	mac08	large sleeve	good	0.1 0.1	100 9000	flaws
055	1987/jun26/loop.ref		anisotropy 2.7ufcap reflected	mac08	small loop	good	0.1 0.1	100 9000	anisotropy
057	1987/jun26/amp15.tran	5	anisotropy transmitted 2.7ufcap	mac08	small loop	good	0.1 0.1	100 9000	anisotropy
059	1987/jun26/amp15.ref	5	anisotropy 2.7ufcap reflected	mac08	small loop	good	0.1 0.1	100 9000	anisotropy

Page	Directory	Sample	Features	Sensor	Source	Q	Res.	Range	Test
061	1987/jun03/sample4	4	anisotropy 2.7ufcap transmitted fourfold	mac08	small loop	good	0.1 0.1	100 9000	anisotropy
063	1987/jun03/pan12	pan12	anisotropy 2.7ufcap transmitted fourfold	mac08	small loop	good	0.1 0.1	100 9000	anisotropy
065	1987/jun30/asm1	1	flaws 2.7ufcap striping balazs	mac08	junk sleeve	poor	0.1 0.1	100 9000	flaws
067	1987/jun30/asm2	1	flaws 2.7ufcap striping balazs	mac08	junk sleeve	poor	0.1 0.1	100 9000	flaws
069	1987/jun08		anisotropy 2.7ufcap	mac08	small loop	good	0.1 0.1	100 9000	anisotropy
071	1987/may19	1	flaws 2.7ufcap striping	mac08	large sleeve	good	0.1 0.1	100 5000	flaws
073	1987/may20/tmp2a	2	flaws 2.7ufcap striping	mac08	large sleeve	poor	0.1 0.1	100 5000	flaws
075	1987/may20/tmp2b	2	flaws 2.7ufcap striping	mac08	large sleeve	poor	0.1 0.1	100 5000	flaws
077	1987/may21/tmp2a	2	flaws 2.7ufcap striping balazs	mac08	large sleeve	poor	0.1 0.1	100 5000	flaws
079	1987/may21/tmp2b	2	flaws 2.7ufcap striping balazs	mac08	large sleeve	poor	0.1 0.1	100 5000	flaws
081	1987/may25/may25.iso	2	anisotropy 2.7ufcap reflected	mac08	large loop	good	0.1 0.1	100 5000	anisotropy
083	1987/may26/emplP11	pi1	anisotropy 2.7ufcap reflected fourfold	mac08	large loop	good	0.1 0.1	100 5000	anisotropy
085	1987/may26/emplP12	pi2	anisotropy 2.7ufcap reflected	mac08	large loop	good	0.1 0.1	100 5000	anisotropy
087	1987/may27/sample4r	4	anisotropy 2.7ufcap reflected fourfold	mac08	small loop	good	0.1 0.1	100 5000	anisotropy
089	1987/may27/sample4z	4	anisotropy transmitted 2.7ufcap fourfold	mac08	small loop	good	0.1 0.1	100 5000	anisotropy
091	1987/may27/pan12z	pan12	anisotropy transmitted 2.7ufcap fourfold	mac08	small loop	good	0.1 0.1	100 5000	anisotropy
093	1987/may27/empl4.aniso	4	anisotropy 2.7ufcap reflected fourfold	mac08	small loop	good	0.1 0.1	100 5000	anisotropy
095	1987/may28/pi1_2	pi1	anisotropy 2.7ufcap transmitted fourfold	mac08	small loop	good	0.1 0.1	100 9000	anisotropy
097	1987/may28/pi1c	pi1	anisotropy 2.7ufcap transmitted fourfold	mac08	small loop	good	0.1 0.1	100 5000	anisotropy
099	1987/may28/empl2.aniso	2	anisotropy 2.7ufcap transmitted lemon	mac08	small loop	good	0.1 0.1	100 9000	anisotropy
101	1987/nov11	AB	flaws tows 2.7ufcap striping	mac08	whip	fair	0.1 0.1	1000 25000	flaws
103	1987/dec22/monster1	1	flaws 2.7ufcap striping	mac08	monster	fair	0.1 0.1	1000 25000	flaws
105	1987/nov02/sa_whip_112.5	A	tows 2.7ufcap striping	mac08	whip	good	0.1 0.1	1000 25000	flaws
107	1987/dec22/harp1	1	flaws 2.7ufcap striping	mac08	harp	good	0.1 0.1	1000 25000	flaws
109	1987/nov02/sa_whip_22.5	A	tows 2.7ufcap striping	mac08	whip	good	0.1 0.1	1000 25000	flaws
111	1988/jan06	solar1	solarcell monosensor flaws 2.7ufcap striping cracks	HW1	whip	fair	0.05 0.05	1000 25000	crack
113	1987/nov02/sa_whip_45	A	tows 2.7ufcap striping	mac08	whip	good	0.1 0.1	1000 25000	flaws
115	1987/nov20	AB	flaws tows foil 2.7ufcap monosensor	mac08	whip	good	0.1 0.1	1000 25000	flaws
117	1987/nov03/emplA	A	flaws subtraction 2.7ufcap striping	mac08	whip	fair	0.1 0.1	1000 25000	flaws

Page	Directory	Sample	Features	Sensor	Source	Q	Res.	Range	Test
119	1987/nov03/amp1B	B	flaws subtraction 2.7ufcap striping	mac08	whip	fair	0.1 0.1	1000 25000	flaws
121	1987/nov05	AB	flaws tows 2.7ufcap striping	mac08	whip	fair	0.1 0.1	1000 25000	flaws
123	1987/nov06		orientation 2.7ufcap foil	mac08	whip	good	0.1 0.1	1000 25000	orientation
125	1987/oct13	2	flaws 2.7ufcap striping	mac08	whip	good	0.1 0.1	1000 30200	flaws
127	1987/oct15	1	flaws 2.7ufcap striping	mac08	whip	good	0.1 0.1	1000 25000	flaws
129	1987/oct02/defroster1	1	flaws 2.7ufcap striping	mac08	window	fair	0.1 0.1	1000 25000	flaws
131	1987/oct23	B	flaws tows 2.7ufcap striping impact	mac08	sleeve	fair	0.1 0.1	1000 25000	flaws
133	1987/oct29	B	flaws tows 2.7ufcap striping impact	mac08	whip	fair	0.1 0.1	1000 25000	flaws
135	1987/oct03/defroster1	1	flaws 2.7ufcap striping	mac08	window	fair	0.1 0.1	1000 25000	flaws
137	1987/oct03/sb_try_0	B	flaws tows 2.7ufcap striping impact	mac08	whip	good	0.1 0.1	1000 25000	flaws
139	1988/jan11	1	flaws 2.7ufcap monosen- sor	HW1	ring1	good	0.1 0.1	1000 25000	flaws
141	1987/oct30	A	tows 2.7ufcap striping	mac08	whip	good	0.1 0.1	1000 25000	flaws
143	1987/sep15/TMR_2	B	anisotropy 2.7ufcap reflected lemon	mac08	small loop	good	0.1 0.1	500 16000	anisotropy
145	1987/sep15/TMR_1	B	anisotropy 2.7ufcap reflected lemon	mac08	small loop	good	0.1 0.1	500 16000	anisotropy
147	1987/sep23/sb_try1	B	flaws tows 2.7ufcap striping impact	mac08	large sleeve	fair	0.1 0.1	500 16000	flaws
149	1987/sep23/sb_try2_0	B	flaws tows 2.7ufcap striping impact	mac08	large sleeve	good	0.1 0.1	500 16000	flaws
151	1987/sep23/sb_try3_90	B	flaws tows 2.7ufcap striping impact	mac08	large sleeve	fair	0.1 0.1	500 16000	flaws
153	1987/sep28/sb_try1_90	B	flaws tows 2.7ufcap striping impact	mac08	large sleeve	fair	0.1 0.1	500 16000	flaws
155	1987/sep29/sa_try1_0	A	tows 2.7ufcap striping	mac08	large sleeve	fair	0.1 0.1	500 16000	flaws
157	1987/sep30/linedata	1	flaws 2.7ufcap	mac08	whip	good	0.1 0.1	1000 25000	flaws
159	1987/sep30/defroster	1	flaws SBIR88 2.7ufcap striping	mac08	window	fair	0.1 0.1	1000 25000	flaws
161	1987/apr23/amp3.nd	3	flaws 2.7ufcap striping	mac08	large sleeve	poor	0.1 0.1	100 5000	flaws
163	1987/apr23/amp12	2	flaws 2.7ufcap striping	mac08	large sleeve	poor	0.1 0.1	100 5000	flaws
165	1987/apr23/sample3.diag	3	flaws 2.7ufcap striping	mac08	large sleeve	good	0.1 0.1	100 5000	flaws
167	1987/apr13	2	flaws 2.7ufcap striping balazs	mac08	small sleeve	poor	0.1 0.1	100 5000	flaws
169	1987/apr16	3	flaws 2.7ufcap striping	mac08	small sleeve	fair	0.1 0.1	100 5000	flaws
171	1987/apr22/amp12.90	2	flaws 2.7ufcap striping	mac08	small sleeve	poor	0.1 0.1	100 5000	flaws
173	1987/apr22/amp13.90	3	flaws 2.7ufcap striping	mac08	small sleeve	fair	0.1 0.1	100 5000	flaws
175	1987/apr30	1	flaws SBIR88 2.7ufcap	mac08	small sleeve	good	0.1 0.1	100 5000	flaws
177	1987/apr08	2	flaws 2.7ufcap striping	mac08	small sleeve	good	0.1 0.1	100 5000	flaws
179	1987/apr09/50mil	mac08	flaws 2.7ufcap striping	mac08	small sleeve	good	0.05 0.05	100 5000	flaw
181	1987/apr09/100mil	2	flaws 2.7ufcap striping	mac08	small sleeve	good	0.1 0.1	100 5000	flaws

Page	Directory	Sample	Features	Sensor	Source	Q	Res.	Range	Test
183	1987/mar25	1	flaws 2.7ufcap striping	mac08	small sleeve	good	0.1 0.1	100 5000	flaws
185	1987/mar26	1	flaws 2.7ufcap striping saturated	mac08	small sleeve	good	0.1 0.1	100 5000	flaws
187	1987/mar27/impl2	2	flaws 2.7ufcap striping	mac08	small sleeve	poor	0.1 0.1	100 5000	flaws
189	1987/mar27/impl1 diag	1	flaws 2.7ufcap striping	mac08	small sleeve	good	0.1 0.1	100 5000	flaws
191	1987/mar27/impl1 back	1	flaws 2.7ufcap striping saturated	mac08	small sleeve	good	0.1 0.1	100 5000	flaws
193	1987/may18	1	flaws 2.7ufcap striping balazs	mac08	large sleeve	fair	0.1 0.1	100 5000	flaws
195	1987/may07	bar	flaws 2.7ufcap striping inspect balazs	mac08	big sleeve	poor	0.1 0.1	100 5000	flaws
197	1988/jan12	copper1	traces monosensor 2.7ufcap saturated	HW1	ring1	fair	0.02 0.02	100 25000	pcboard
199	1988/jan13/solarcell1	solar1	solarcell monosensor cracks saturated 2.7ufcap flaws	HW2	ring2	fair	0.01 0.01	100 30000	crack
201	1988/jan13/pcboard	pcboard1	traces monosensor 2.7ufcap saturated	HW2	ring2	good	0.02 0.02	200 25000	pcboard
203	1988/jan13/solarcell1.2	solar1	cracks flaws monosensor solarcell saturated 2.7ufcap	HW2	ring2	fair	0.02 0.02	1000 50000	crack
205	1988/jan14/solarcell2	solar2	monosensor solarcell saturated 2.7ufcap	HW2	ring2	fair	0.02 0.02	1000 50000	crack
207	1988/jan14/solarcell3	solar3	flaws cracks monosensor solarcell 2.7ufcap	HW2	ring2	good	0.02 0.02	1000 50000	crack
209	1988/jan14/solarcell2.2	solar2	monosensor solarcell 2.7ufcap	HW2	ring2	fair	0.02 0.02	1000 50000	crack
211	1988/jan14/solarcell4	solar4	flaws monosensor solar-cell 2.7ufcap cracks	HW2	ring2	fair	0.02 0.02	1000 50000	crack
213	1988/jan14/sample1	1	flaws monosensor weaves 2.7ufcap	HW2	ring2	good	0.1 0.1	500 50000	flaws
215	1988/jan15/pcboard2	copper1	traces monosensor 2.7ufcap	HW2	ring2	good	0.01 0.01	500 50000	trace
217	1988/jan28	1	flaws 0.1ufcap monosensor weaves	HW1	HW2	good	0.1 0.1	500 50000	flaws
219	1988/jan29	copper2	traces monosensor 0.1ufcap	HW2	ring2	good	0.0198 0.02	500 50000	pcboard
221	1988/jan19/pcboard	copper1	traces monosensor 0.1ufcap	HW2	ring2	good	0.1 0.1	500 50000	pcboard
223	1988/jan21/copper1	1	traces monosensor 0.1ufcap	HW7	ring6	fair	0.1 0.1	500 50000	pcboard
225	1988/jan22	solar4	monosensor solarcell 0.1ufcap	HW5	HW6	poor	0.1 0.1	20000 50000	crack
227	1988/feb10	1	flaws monosensor 0.1ufcap	HW1a	ring3	fair	0.1 0.1	500 50000	flaws
229	1988/feb06	1	flaws monosensor 0.1ufcap	mac01	mac01	good	0.1 0.1	100 6000	flaws
231	1988/feb11	1	flaws monosensor 0.1ufcap weaves	HW3	ring4	good	0.1 0.1	500 50000	flaws
233	1988/jan30	2	flaws 0.1ufcap monosensor	HW3	ring2	good	0.1 0.1	500 50000	flaws
235	1988/jan20	1	flaws 0.1ufcap monosensor weaves	HW5	HW6	good	0.1 0.1	500 50000	flaw
237	1988/jan19/sample1	1	flaws monosensor 0.1ufcap weaves	HW2	ring2	good	0.1 0.1	1000 50000	flaw
239	1988/feb13	solar5	monosensor solarcell 0.1ufcap	HW3	ring4	good	0.1 0.1	1000 50000	crack

Page	Directory	Sample	Features	Sensor	Source	Q	Res.	Range	Test
241	1988/feb14/solarcell6	solar6	solarcell monosensor flaws 0.1ufcap cracks	HW3	ring4	good	0.1 0.1	1000 50000	crack
243	1988/feb14/solarcell7	solar7	solarcell monosensor flaws 0.1ufcap cracks	HW3	ring4	good	0.1 0.1	1000 50000	crack
245	1988/feb15/solarcell8	solar8	solarcell monosensor 0.1ufcap	HW3	ring4	good	0.1 0.1	1000 50000	crack
247	1988/feb17/ampbb	B	flaws monosensor 0.1ufcap impact tows	HW3	ring4	fair	0.1 0.1	1000 50000	flaw
249	1988/feb17/ampib	B	flaws monosensor 0.1ufcap impact tows	HW3	ring4	fair	0.1 0.1	1000 50000	flaw
251	1988/feb17/amp12	2	flaws monosensor 0.1ufcap	HW3	ring4	poor	0.1 0.1	1000 50000	flaw
253	1988/feb16/solarcell6h	solar6	solarcell monosensor flaws 0.1ufcap cracks	HW3	ring4	good	0.1 0.1	1000 50000	crack
255	1988/feb16/solarcell6	solar6	solarcell monosensor flaws 0.1ufcap cracks	HW3	ring4	good	0.1 0.1	500 50000	crack
257	1988/feb15/copper3	copper3	traces monosensor 0.1ufcap	HW3	ring4	good	0.1 0.1	100 40000	pcboard
259	1988/feb22/Smp1b22	B	flaws monosensor tows 0.1ufcap impact	HW3	ring4	good	0.1 0.1	1000 50000	flaw
261	1988/feb25	1	flaws monosensor 0.1ufcap saturated	HW3	ring5	good	0.1 0.1	500 50000	flaw
263	1988/jan07	posensor	traces monosensor 0.1ufcap	HW1	whip	fair	0.00958 0.01	100 30000	trace
265	1988/mar04/norm	1	flaws monosensor 0.1ufcap	HW3	ring5	good	0.2 0.2	500 20000	flaw
267	1988/mar04/slow	1	flaws monosensor 0.1ufcap	HW3	ring5	good	0.2 0.2	500 20000	flaw
269	1988/mar21	1	flaws monosensor 0.1ufcap tee weaves	HW3	ring1	good	0.1 0.1	1000 50000	flaw
271	1988/mar22/tee2	2	flaws monosensor 0.1ufcap tee saturated	HW3	ring1	fair	0.1 0.1	1000 50000	flaw
273	1988/mar22/teeb	B	monosensor 0.1ufcap tee tows impact	HW3	ring1		0.1 0.1	1000 50000	flaw
275	1988/mar23	1	flaws monosensor 0.1ufcap tee weaves saturated	HW3	ring1	good	0.1 0.1	1000 50000	flaw
277	1988/apr01	solar1	solarcell cracks monosensor 0.1ufcap tee flaws saturated	HW3	ring1	fair	0.025 0.025	500 50000	crack
279	1988/apr04	copr10	traces monosensor 0.1ufcap tee	HW3	ring1	good	0.05 0.05	500 50000	trace
281	1988/apr15	AB	foil monosensor 0.1ufcap tows flaws	mac01	whip	good	0.075 0.075	500 9000	target
283	1988/apr18	solar1	solarcell cracks monosensor 0.1ufcap flaws saturated	mac01	whip	fair	0.05 0.05	500 25000	crack
285	1988/apr19	solar1	belaze cracks solarcell monosensor 0.1ufcap flaws saturated	mac01	whip	fair	0.05 0.05	500 25000	crack
287	1988/apr20	solar9	cracks monosensor solar- cell incase 0.1ufcap flaws	HW3	ring20	poor	0.05 0.05	1000 50000	crack
289	1988/apr22	solar9	cracks monosensor incase solarcell 0.1ufcap flaws	HW3	ring20	fair	0.05 0.05	1000 50000	crack
291	1988/apr25/rac1.1	rac1	tows saturated 0.1ufcap monosensor	mac01	whip	fair	0.1 0.1	500 50000	flaw

Page	Directory	Sample	Features	Sensor	Source	Q	Res.	Range	Test
293	1988/apr25/me1.2	me1	tows monosensor 0.1ufcap balazs	mac01	whip	fair	0.1 0.1	500 50000	flaw
295	1988/apr25/me2	me2	tows monosensor 0.1ufcap saturated	mac01	whip	fair	0.1 0.1	500 50000	flaw
297	1988/apr25/me3	me3	impact tows saturated monosensor 0.1ufcap	mac01	whip	fair	0.1 0.1	500 50000	flaw
299	1988/apr25/me4	me4	tows monosensor 0.1ufcap balazs	mac01	whip	fair	0.1 0.1	500 50000	flaw
301	1988/apr25/me5	me5	tows monosensor 0.1ufcap	mac01	whip	good	0.1 0.1	500 50000	flaw
303	1988/apr28	solar9	cracks monosensor 0.1ufcap solarcell flaws	jrb2	ring21	good	0.05 0.05	500 50000	crack
305	1988/may02/me4	me4	anisotropy monosensor 0.1ufcap transmitted fourfold	jrb2ns	loop21	fair	0.2 0.2	500 50000	anisotropy
307	1988/may02/me5	me5	anisotropy monosensor 0.1ufcap transmitted lemon fourfold	jrb2ns	loop21	fair	0.2 0.2	500 50000	anisotropy
309	1988/may02/solar	solar9	cracks monosensor 0.1ufcap solarcell flaws	jrb2ns	ring21	good	0.05 0.05	500 50000	crack
311	1988/may09/sampleA	A	anisotropy 0.1ufcap monosensor transmitted lemon	mac01	loop4	good	0.1 0.1	500 50000	anisotropy
313	1988/may09/target	AB	0.1ufcap monosensor foil saturated tows flaws	mac01	loop4	fair	0.075 0.075	500 50000	target
315	1988/may10/sampleA_B	AB	0.1ufcap monosensor foil tows flaws	mac01	loop4	fair	0.075 0.075	500 50000	target
317	1988/may11/me2	me2	monosensor 0.1ufcap transmitted anisotropy fourfold	mac01	loop4	good	0.1 0.1	500 50000	anisotropy
319	1988/may11/aniso_A	A	monosensor 0.1ufcap reflected anisotropy lemon saturated	mac01	loop4	fair	0.1 0.1	500 50000	anisotropy
321	1988/may11/aniso_AB	AB	monosensor 0.1ufcap transmitted anisotropy saturated lemon	mac01	loop4	fair	0.1 0.1	500 50000	anisotropy
323	1988/may12/me1	me1	monosensor 0.1ufcap transmitted anisotropy fourfold	mac01	loop4	good	0.1 0.1	500 50000	anisotropy
325	1988/may11/me3	me3	monosensor 0.1ufcap transmitted anisotropy saturated	mac01	loop4	fair	0.1 0.1	500 50000	anisotropy
327	1988/may12/A_reflected	A	monosensor 0.1ufcap reflected anisotropy saturated lemon	mac01	loop4	fair	0.1 0.1	500 50000	anisotropy
329	1988/may10/target_X	AB	monosensor 0.1ufcap flaws foil saturated tows	mac01	loop4	fair	0.1 0.1	500 50000	flaw
331	1988/may12/mpi4	4	monosensor 0.1ufcap transmitted anisotropy fourfold	mac01	loop4		0.1 0.1	500 50000	anisotropy
333	1988/may13/sample5	5	monosensor 0.1ufcap transmitted anisotropy saturated lemon	mac01	loop4	fair	0.1 0.1	500 50000	anisotropy
335	1988/may16/sampleA_B	AB	monosensor 0.1ufcap transmitted anisotropy fourfold	mac01	loop4	good	0.1 0.1	500 50000	anisotropy
337	1988/may17/me1	me1	monosensor 0.1ufcap impact flaws saturated	HW9	ring7	poor	0.1 0.1	500 50000	flaw

Page	Directory	Sample	Features	Sensor	Source	Q	Res.	Range	Test
339	1988/may17/me45.1	me1	monosensor 0.1ufcap impact flaws balazs saturated tows	HW9	ring7	poor	0.1 0.1	500 50000	flaw
341	1988/may17/me45.2	me1	monosensor 0.1ufcap impact flaws tows	HW9	ring7	fair	0.1 0.1	500 50000	flaw
343	1988/may17/bias1	solar17	monosensor solarcell 0.1ufcap blast	HW9	ring7	good	0.1 0.1	500 50000	blast
345	1988/may17/bias2	solar17	monosensor solarcell 0.1ufcap blast	HW9	ring7	good	0.1 0.1	500 50000	blast
347	1988/may17/bias3	solar17	monosensor solarcell 0.1ufcap blast	HW9	ring7	good	0.1 0.1	500 50000	blast
349	1988/may17/solar9-11	solar9	monosensor solarcell 0.1ufcap cracks flaws	HW9	ring7	good	0.1 0.1	500 50000	crack
351	1988/may18/solar1-4	solar1	monosensor solarcell 0.1ufcap cracks flaws	HW9	ring7	fair	0.1 0.1	500 50000	crack
353	1988/may26/fig8test	1	flaws monosensor 0.1ufcap weaves	HW3	fig8	good	0.1 0.1	500 50000	flaw
355	1988/may25/sampleab	AB	anisotropy transmitted fourfold monosensor 0.1ufcap	mac01	loop5	good	0.1 0.1	500 50000	anisotropy
357	1988/may26/me1 clean	me1	anisotropy transmitted monosensor 0.1ufcap fourfold saturated	mac01	loop5	fair	0.1 0.1	500 50000	anisotropy
359	1988/may26/me1 flaw23J	me1	anisotropy transmitted monosensor 0.1ufcap fourfold flaws impact	mac01	loop5	fair	0.1 0.1	500 50000	anisotropy
361	1988/jun01	1	monosensor 0.1ufcap weaves	HW10	ring7	good	0.1 0.1	500 50000	flaw
363	1988/jun03/cap1	1	monosensor 0.1ufcap saturated flaws	cap1	cap1	fair	0.1 0.1	500 50000	flaw
365	1988/jun03/cap1r	1	monosensor 0.1ufcap flaws	cap1	cap1	fair	0.1 0.1	500 50000	flaw
367	1988/jun03/cap2	1	monosensor 0.1ufcap flaws	cap2	cap2	fair	0.1 0.1	500 50000	flaw
369	1988/jun03/cap5	1	monosensor 0.1ufcap flaws	cap5	cap5	fair	0.1 0.1	500 50000	flaw
371	1988/jun06/vernon	1	monosensor 0.1ufcap saturated flaws	280	335	fair	0.1 0.1	500 50000	flaw
373	1988/jun06/cap2a	1	monosensor 0.1ufcap flaws	cap2	cap2	fair	0.1 0.1	500 50000	flaw
375	1988/jun06/cap6	1	monosensor 0.1ufcap flaws	cap6	cap6	fair	0.1 0.1	500 50000	flaw
377	1988/jun07/vernon280	1	monosensor 0.1ufcap flaws	280	whip	fair	0.1 0.1	500 50000	flaw
379	1988/jun07/vernon335	1	monosensor 0.1ufcap flaws	335	whip	fair	0.1 0.1	500 50000	flaw
381	1988/jun09/eightchannels	1	0.1ufcap flaws striping	mac08	harp	fair	0.1 0.1	500 50000	flaw
383	1988/jun13/harp3_sch	1	0.1ufcap striping flaws	mac08	harp	fair	0.1 0.1	500 50000	flaw
385	1988/jun13/solar	solar5	cracks solarcell monosensor 0.1ufcap blast flaws	HW13	ring7	good	0.05 0.05	500 50000	crack
387	1988/jun14/quad_ring	1	flaws weaves striping 0.1ufcap saturation balazs	HW9	ring7	fair	0.1 0.1	500 50000	flaw
389	1988/jun14/RAE1	me1	flaws impact striping saturation 0.1ufcap balazs	HW9	ring7	fair	0.1 0.1	500 50000	flaw
391	1988/jun14/quad_ring2	me1	flaws impact striping saturation 0.1ufcap balazs	HW9	ring7	fair	0.1 0.1	500 50000	flaw

Page	Directory	Sample	Features	Sensor	Source	Q	Res.	Range	Test
393	1988/jun09/switched0_1	1	flaws striping 0.1ufcap	mac08	harp	fair	0.1 0.1	500 50000	flaw
395	1988/jun16/test1	1	balazs striping 0.1ufcap flaws	HW14	ring7	fair	0.1 0.1	500 50000	flaw
397	1988/jun21/test6	1	flaws striping 0.1ufcap	mac08	harp	fair	0.1 0.1	500 50000	flaw
399	1988/jun21/drive_head	1	flaws 0.1ufcap monosen- sor	disk	disk	good	0.1 0.1	50 5000	flaw
401	1988/jun24/me1 bottom_cap6	me1	flaws 0.1ufcap monosen- sor	cap6	cap6	fair	0.1 0.1	500 50000	flaw
403	1988/jun24/ceramic_disks	ceram	flaws 0.1ufcap monosen- sor	cap6	cap6	fair	0.05 0.05	500 50000	flaw
405	1988/jun22/solar	solar6	flaws 0.1ufcap monosen- sor solarcell	disk	disk	good	0.05 0.05	50 5000	flaw
407	1988/jun23/me1_cap6	me1	flaws 0.1ufcap monosen- sor	cap6	cap6	fair	0.1 0.1	500 50000	flaw
409	1988/jun23/me1_disk	me1	flaws 0.1ufcap monosen- sor	disk	disk	fair	0.1 0.1	50 5000	flaw
411	1988/jun28/me1_4channels	me1	flaws 0.1ufcap striping	HW14	ring7	fair	0.1 0.1	500 50000	flaw
413	1988/jun28/xas_4channels	xas	flaws 0.1ufcap striping	HW14	ring7	fair	0.1 0.1	500 50000	flaw
415	1988/jul11/sample1_weaves	1	flaws 0.1ufcap monosen- sor weaves saturated	HW2	ring1	fair	0.05 0.05	500 50000	flaw
417	1988/jul11/new_filter_caps	1	flaws 0.01ufcap weaves monosensor	HW2	ring1	good	0.05 0.05	500 50000	flaw
419	1988/jul11/no_filter_caps	1	flaws 0.1ufcap monosen- sor weaves	HW2	ring1	good	0.05 0.05	500 50000	flaw
421	1988/jul15/sampleb_hw2	b	flaws 0.1ufcap tows monosensor	HW2	ring1	fair	0.05 0.05	500 50000	flaw
423	1988/jul19/sampleb_new_flaw	b	flaws 0.1ufcap tows monosensor	HW2	ring1	good	0.05 0.05	500 50000	flaw
425	1988/jul19/sampleb_new_flaw_back	b	flaws 0.1ufcap tows monosensor	HW2	ring1	good	0.05 0.05	500 50000	flaw
427	1988/jul20/whip_over_sampleb	b	flaws 0.1ufcap tows monosensor	HW2	whip	fair	0.05 0.05	500 50000	flaw
429	1988/jul20/whip_over_back	b	flaws 0.1ufcap tows monosensor	HW2	whip	fair	0.05 0.05	500 50000	flaw
431	1988/jul21/carba_run2	carba	flaws 0.1ufcap weaves monosensor	HW2	HW8	fair	0.05 0.05	500 50000	flaw
433	1988/jul20/carba_run1	carba	monosensor .1ufcap	HW2	ring1	fair	0.05 0.05	500 50000	flaw
435	1988/jul21/carba_run3	carba	monosensor .1ufcap balazs	HW2	whip2	poor	0.05 0.05	500 50000	flaw
437	1988/jul22/carba_whip2	carba	monosensor balazs	HW2	whip2	poor	0.05 0.05	500 50000	flaw
439	1988/jul22/carba_cap9	carba	monosensor balazs	cap9	cap9	poor	0.05 0.05	500 50000	flaw
441	1988/jul22/carba_tee	carba	monosensor balazs	HW3	ring22	fair	0.05 0.05	1000 50000	weave
443	1988/jul22/carbb_tee	carbb	monosensor balazs	HW3	ring22	fair	0.05 0.05	1000 50000	flaw
445	1988/jul25/carbb_weaves	carbb	weaves 0.1ufcap monosensor balazs	HW2	ring1	fair	0.05 0.05	500 50000	flaw
447	1988/jul26/carbb_fold	carbb	flaws 0.1ufcap monosen- sor balazs	disk	disk	poor	0.05 0.05	50 5000	flaw
449	1988/jul26/xas_quad4	xas	flaws 0.1ufcap monosen- sor balazs tows	HW2	ring1	fair	0.1 0.1	500 50000	flaw
451	1988/jul26/xas_diam5	xas	flaws 0.1ufcap monosen- sor balazs tows	HW2	ring1	fair	0.1 0.1	500 50000	flaw
453	1988/jul25/carba_weaves	carba	monosensor 0.1ufcap balazs weaves	HW2	ring1	fair	.050 .050	500 50000	weave

Page	Directory	Sample	Features	Sensor	Source	Q	Res.	Range	Test
455	1988/jul22/solar_10a	solar9	monosensor .1ufcap cracks flaws solarcell	HW3	ring22	good	.025 .025	1000 50000	crack
457	1988/jul25/solar	solar5	monosensor 0.1ufcap cracks flaws solarcell	HW2	ring1	good	.025 .025	1000 50000	flaw
459	1988/jul25/solar2	solar5	flaw monosensor 0.1ufcap solarcell	disk	disk	fair	.025 .025	500 50000	crack
461	1988/jul26/solar3	solar7	balazs monosensor 0.1ufcap flaws cracks solarcell	disk	disk	fair	.025 .025	500 50000	crack
463	1988/jul27/solar1	solar5	cracks flaws 0.1ufcap monosensor solarcell	HW18	ring23	good	.025 .025	1000 50000	crack
465	1988/jul27/solar_y	solar5	flaw .1ufcap monosensor solarcell	HW18	ring23	good	.025 .025	1000 50000	flaw
467	1988/jul27/xas	xas	monosensor tows .1ufcap	HW18	ring23	fair	.099 .099	1000 50000	flaw
469	1988/jul29/carb9	carba	monosensor .1ufcap weaves	HW18	ring23	fair	0.100 0.100	500 50000	weave
471	1988/jul29/carba	carba	monosensor .1ufcap weaves balazs	HW19	ring24	fair	0.100 0.100	500 50000	weave
473	1988/aug01/carba_detailed_weaves	carba	weaver .1ufcap monosensor	HW19	ring24	good	.050 .050	500 50000	weave
475	1988/aug01/carbb_groove_grooveside	carbb	monosensor .1ufcap	HW19	ring24	fair	.050 .050	500 50000	flaw
477	1988/aug01/solar_q	solar5	flaws .1ufcap monosensor solarcell	HW19	ring24	good	.025 .025	500 50000	flaw
479	1988/aug08/solar_x	solar8	flaws .1ufcap monosensor solarcell	HW19	ring24	good	.025 .025	500 50000	flaw
481	1988/aug08/cc_fiber_joint	carbb	monosensor .1ufcap flaws	HW19	ring24	fair	.050 .050	1000 50000	flaw
483	1988/aug09/be_on_top	b	flaws monosensor	HW19	ring24	fair	.050 .050	500 50000	flaw
485	1988/aug09/be_on_bottom	b	flaws tows monosensor	HW19	ring24	fair	.050 .050	500 50000	flaw
487	1988/aug10/B_top	b	flaws tows monosensor	HW8	whip	good	.050 .050	500 50000	flaw
489	1988/aug10/B_bottom	b	flaws tows monosensor	HW8	whip	fair	.050 .050	500 50000	flaw
491	1988/aug11/B_top_ring	b	flaws tows monosensor	HW8	ring8	good	.050 .050	500 50000	flaw
493	1988/aug11/B_bottom_ring	b	flaws tows monosensor	HW8	ring8	good	.050 .050	500 50000	flaw
495	1988/jan15/pcbboard1	copper1	traces monosensor 0.1ufcap	HW2	ring2	good	.010 .010	500 50000	flaw
497	1988/apr26/rac1b	rac1	monosensor 0.1ufcap	mac01	whip		0.100 0.100	500 50000	
499	1988/apr27/rac3	rac3	monosensor 0.1ufcap	jrb1	ring21		0.100 0.100	500 50000	
501	1988/apr27/rac3s	rac3	monosensor 0.1ufcap	jrb2	ring21		0.100 0.100	500 50000	
503	1988/jun01/hw10	1	monosensor 0.1ufcap	HW10	ring7		.099 .099	500 50000	
505	1988/jul01/sample1_new.f.caps	1	monosensor 0.1ufcap	HW2	ring2		.099 .099	500 50000	
507	1988/jul07/diam4	xas	monosensor 0.1ufcap subtraction transmitted	mac01	loop5		0.100 0.100	500 50000	
509	1988/jul07/diam5	xas	monosensor 0.1ufcap subtraction transmitted	mac01	loop5		0.100 0.100	500 50000	
511	1988/jul07/quad1	xas	monosensor 0.1ufcap subtraction transmitted	mac01	loop5		0.100 0.100	500 50000	
513	1988/jul07/quad2	xas	monosensor 0.1ufcap subtraction transmitted	mac01	loop5		0.100 0.100	500 50000	

Page	Directory	Sample	Features	Sensor	Source	Q	Res.	Range	Test
515	1988/jul07/quad3	xas	monosensor 0.1ufcap subtraction transmitted	mac01	loop5		0.100 0.100	500 50000	
517	1988/jul07/quad4	xas	monosensor 0.1ufcap subtraction transmitted	mac01	loop5		0.100 0.100	500 50000	
519	1988/jul11/no_tantalum_caps	1	monosensor 0.1ufcap	HW2	ring1		.050 .050	500 50000	
521	1988/jul13/dlam4	xas	monosensor 0.1ufcap subtraction transmitted	mac01	loop5		.050 .050	500 50000	
523	1988/jul13/dlam5	xas	monosensor 0.1ufcap subtraction transmitted	mac01	loop5		.050 .050	500 50000	
525	1988/jul13/quad1	xas	monosensor 0.1ufcap subtraction transmitted	mac01	loop5		.050 .050	500 50000	
527	1988/jul13/quad2	xas	monosensor 0.1ufcap subtraction transmitted	mac01	loop5		.050 .050	500 50000	
529	1988/jul13/quad3	xas	monosensor 0.1ufcap subtraction transmitted	mac01	loop5		.050 .050	500 50000	
531	1988/jul13/quad4	xas	monosensor 0.1ufcap subtraction transmitted	mac01	loop5		.050 .050	500 50000	
533	1988/jul15/d5no1	xas	monosensor 0.1ufcap subtraction transmitted	mac01	loop5		0.100 0.100	500 50000	
535	1988/jul15/d5no2	xas	monosensor 0.1ufcap subtraction transmitted	mac01	loop5		0.100 0.100	500 50000	
537	1988/jul18/dlam4	xas	monosensor 0.1ufcap subtraction transmitted	mac01	loop5		0.100 0.100	500 50000	
539	1988/jul18/dlam5	xas	monosensor 0.1ufcap subtraction transmitted	mac01	loop5		0.100 0.100	500 50000	
541	1988/jul18/quad1	xas	monosensor 0.1ufcap subtraction transmitted	mac01	loop5		0.100 0.100	500 50000	
543	1988/jul18/quad2	xas	monosensor 0.1ufcap subtraction transmitted	mac01	loop5		0.100 0.100	500 50000	
545	1988/jul18/quad3	xas	monosensor 0.1ufcap subtraction transmitted	mac01	loop5		0.100 0.100	500 50000	
547	1988/jul18/quad4	xas	monosensor 0.1ufcap subtraction transmitted	mac01	loop5		0.100 0.100	500 50000	
549	1988/jul27/diff/dlam2	xas	monosensor 0.1ufcap subtraction transmitted	HW18	loop5		0.100 0.100	1000 50000	
551	1988/jul27/diff/dlam8	xas	monosensor 0.1ufcap subtraction transmitted	HW18	loop5		0.100 0.100	1000 50000	
553	1988/jul27/diff/quad1	xas	monosensor 0.1ufcap subtraction transmitted	HW18	loop5		0.100 0.100	1000 50000	
555	1988/jul27/diff/quad2	xas	monosensor 0.1ufcap subtraction transmitted	HW18	loop5		0.100 0.100	1000 50000	
557	1988/jul27/diff/quad3	xas	monosensor 0.1ufcap subtraction transmitted	HW18	loop5		0.100 0.100	1000 50000	
559	1988/jul27/diff/quad4	xas	monosensor 0.1ufcap subtraction transmitted	HW18	loop5		0.100 0.100	1000 50000	
561	1988/jul28/dlam2	xas	monosensor 0.1ufcap subtraction transmitted	HW4	loop5		0.100 0.100	500 50000	
563	1988/jul28/dlam8	xas	monosensor 0.1ufcap subtraction transmitted	HW4	loop5		0.100 0.100	500 50000	

Page	Directory	Sample	Features	Sensor	Source	Q	Res.	Range	Test
565	1988/jul28/quad1	XAS	monosensor 0.1ufcap subtraction transmitted	HW4	loop5		0.100 0.100	500 50000	
567	1988/jul28/quad2	XAS	monosensor 0.1ufcap subtraction transmitted	HW4	loop5		0.100 0.100	500 50000	
569	1988/jul28/quad3	XAS	monosensor 0.1ufcap subtraction transmitted	HW4	loop5		0.100 0.100	500 50000	
571	1988/jul28/quad4	XAS	monosensor 0.1ufcap subtraction transmitted	HW4	loop5		0.100 0.100	500 50000	
573	1988/aug08/diff/dlam2	XAS	monosensor 0.1ufcap subtraction transmitted	HW4	loop5		0.100 0.100	500 50000	
575	1988/aug08/diff/dlam8	XAS	monosensor 0.1ufcap subtraction transmitted	HW4	loop5		0.100 0.100	500 50000	
577	1988/aug08/diff/quad1	XAS	monosensor 0.1ufcap subtraction transmitted	HW4	loop5		0.100 0.100	500 50000	
579	1988/aug08/diff/quad2	XAS	monosensor 0.1ufcap subtraction transmitted	HW4	loop5		0.100 0.100	500 50000	
581	1988/aug08/diff/quad3	XAS	monosensor 0.1ufcap subtraction transmitted	HW4	loop5		0.100 0.100	500 50000	
583	1988/aug08/diff/quad4	XAS	monosensor 0.1ufcap subtraction transmitted	HW4	loop5		0.100 0.100	500 50000	
585	1988/aug09/diff/dlam2	XAS	monosensor 0.1ufcap subtraction transmitted	HW8	loop5		0.100 0.100	500 50000	
587	1988/aug09/diff/dlam8	XAS	monosensor 0.1ufcap subtraction transmitted	HW8	loop5		0.100 0.100	500 50000	
589	1988/aug09/diff/quad1	XAS	monosensor 0.1ufcap subtraction transmitted	HW8	loop5		0.100 0.100	500 50000	
591	1988/aug09/diff/quad2	XAS	monosensor 0.1ufcap subtraction transmitted	HW8	loop5		0.100 0.100	500 50000	
593	1988/aug09/diff/quad3	XAS	monosensor 0.1ufcap subtraction transmitted	HW8	loop5		0.100 0.100	500 50000	
595	1988/aug09/diff/quad4	XAS	monosensor 0.1ufcap subtraction transmitted	HW8	loop5		0.100 0.100	500 50000	
597	1988/aug10/diff/dlam2	XAS	monosensor 0.1ufcap subtraction transmitted	HW8	loop5		0.100 0.100	500 50000	
599	1988/aug10/diff/dlam8	XAS	monosensor 0.1ufcap subtraction transmitted	HW8	loop5		0.100 0.100	500 50000	
601	1988/aug10/diff/quad1	XAS	monosensor 0.1ufcap subtraction transmitted	HW8	loop5		0.100 0.100	500 50000	
603	1988/aug10/diff/quad2	XAS	monosensor 0.1ufcap subtraction transmitted	HW8	loop5		0.100 0.100	500 50000	
605	1988/aug10/diff/quad3	XAS	monosensor 0.1ufcap subtraction transmitted	HW8	loop5		0.100 0.100	500 50000	
607	1988/aug10/diff/quad4	XAS	monosensor 0.1ufcap subtraction transmitted	HW8	loop5		0.100 0.100	500 50000	
609	1988/aug11/diff/dlam2	XAS	monosensor 0.1ufcap subtraction transmitted	HW8	loop5		0.100 0.100	500 50000	
611	1988/aug11/diff/dlam8	XAS	monosensor 0.1ufcap subtraction transmitted	HW8	loop5		0.100 0.100	500 50000	

Page	Directory	Sample	Features	Sensor	Source	Q	Res.	Range	Test
613	1988/aug11/diff/quad1	xas	monosensor 0.1ufcap subtraction transmitted	HW8	loop5		0.100 0.100	500 50000	
615	1988/aug11/diff/quad2	xas	monosensor 0.1ufcap subtraction transmitted	HW8	loop5		0.100 0.100	500 50000	
617	1988/aug11/diff/quad3	xas	monosensor 0.1ufcap subtraction transmitted	HW8	loop5		0.100 0.100	500 50000	
619	1988/aug11/diff/quad4	xas	monosensor 0.1ufcap subtraction transmitted	HW8	loop5		0.100 0.100	500 50000	
621	1988/aug12/d4mg	xas	monosensor 0.1ufcap subtraction transmitted	HW19	ring24		0.100 0.100	500 50000	
623	1988/aug12/d5mg	xas	monosensor 0.1ufcap subtraction transmitted	HW19	ring24		0.100 0.100	500 50000	
625	1988/aug12/d7mg	xas	monosensor 0.1ufcap subtraction transmitted	HW19	ring24		0.100 0.100	500 50000	
627	1988/aug12/q2mg	xas	monosensor 0.1ufcap subtraction transmitted	HW19	ring24		0.100 0.100	500 50000	
629	1988/aug12/q3mg	xas	monosensor 0.1ufcap subtraction transmitted	HW19	ring24		0.100 0.100	500 50000	
631	1988/aug12/q4mg	xas	monosensor 0.1ufcap subtraction transmitted	HW19	ring24		0.100 0.100	500 50000	flaw
633	1988/aug20/solar	solar5	monosensor 0.1ufcap solarcell	HW20	ring25		.010 .010	1000 50000	crack
635	1988/aug22/xas	xas	monosensor 0.1ufcap tows	HW20	ring25		.019 .020	1000 50000	flaw
637	1988/aug23/xas2	xas	monosensor 0.1ufcap tows	HW20	ring25		.019 .020	1000 50000	flaw
639	1988/aug30/dlam	dlam	monosensor 0.1ufcap	HW20	ring25		.050 .050	1000 50000	
641	1988/aug31/xasmo	xas	monosensor 0.1ufcap	HW20	ring25		.041 .040	1000 50000	
643	1988/sep01/xas02	xas	monosensor 0.1ufcap	HW20	ring25		.040 .040	1000 50000	
645	1988/sep11/xas07	xas	monosensor 0.1ufcap	big	test		.082 .082	1000 50000	
647	1988/sep12/xas08	xas	monosensor 0.1ufcap	big	test		.082 .081	1000 50000	
649	1988/sep13/xas09	xas	monosensor 0.1ufcap	big	test		.082 .081	1000 50000	
651	1988/sep16/xas10	xas	monosensor 0.1ufcap	HW19	ring24		.082 .081	1000 50000	
653	1988/sep26/dlam2	xas	monosensor 0.1ufcap subtraction transmitted	mac01	loop5		0.100 0.100	500 50000	
655	1988/sep26/dlam5	xas	monosensor 0.1ufcap subtraction transmitted	mac01	loop5		0.100 0.100	500 50000	
657	1988/sep26/xasq1	xas	monosensor 0.1ufcap subtraction transmitted	mac01	loop5		0.100 0.100	500 50000	
659	1988/sep26/xasq2	xas	monosensor 0.1ufcap subtraction transmitted	mac01	loop5		0.100 0.100	500 50000	
661	1988/sep26/xasq3	xas	monosensor 0.1ufcap subtraction transmitted	mac01	loop5		0.100 0.100	500 50000	
663	1988/sep26/xasq4	xas	monosensor 0.1ufcap subtraction transmitted	mac01	loop5		0.100 0.100	500 50000	
665	1988/sep28/dlam2	xas	monosensor 0.1ufcap subtraction transmitted	mac01	loop5		0.100 0.100	500 50000	
667	1988/sep28/dlam5	xas	monosensor 0.1ufcap subtraction transmitted	mac01	loop5		0.100 0.100	500 50000	

Page	Directory	Sample	Features	Sensor	Source	Q	Res.	Range	Test
669	1988/sep28/quad1	xas	monosensor 0.1ufcap subtraction transmitted	mac01	loop5		0.100 0.100	500 50000	
671	1988/sep28/quad2	xas	monosensor 0.1ufcap subtraction transmitted	mac08	loop5		0.100 0.100	500 50000	
673	1988/sep28/quad3	xas	monosensor 0.1ufcap subtraction transmitted	mac01	loop5		0.100 0.100	500 50000	
675	1988/sep28/quad4	xas	monosensor 0.1ufcap subtraction transmitted	mac01	loop5		0.100 0.100	500 50000	
677	1988/oct03/diam2	xas	monosensor 0.1ufcap subtraction transmitted	mac01	loop5		0.100 0.100	500 50000	
679	1988/oct03/diam5	xas	monosensor 0.1ufcap subtraction transmitted	mac01	loop5		0.100 0.100	500 50000	
681	1988/oct03/quad1	xas	monosensor 0.1ufcap subtraction transmitted	mac01	loop5		0.100 0.100	500 50000	
683	1988/oct03/quad2	xas	monosensor 0.1ufcap subtraction transmitted	mac01	loop5		0.100 0.100	500 50000	
685	1988/oct03/quad3	xas	monosensor 0.1ufcap subtraction transmitted	mac01	loop5		0.100 0.100	500 50000	
687	1988/oct03/quad4	xas	monosensor 0.1ufcap subtraction transmitted	mac01	loop5		0.100 0.100	500 50000	
689	1988/oct04/diam3	xas	monosensor 0.1ufcap subtraction transmitted	mac01	loop5		0.100 0.100	500 50000	
691	1988/oct04/diam8	xas	monosensor 0.1ufcap subtraction transmitted	mac01	loop5		0.100 0.100	500 50000	
693	1988/oct04/quad1	xas	monosensor 0.1ufcap subtraction transmitted	mac01	loop5		0.100 0.100	500 50000	
695	1988/oct04/quad2	xas	monosensor 0.1ufcap subtraction transmitted	mac01	loop5		0.100 0.100	500 50000	
697	1988/oct04/quad3	xas	monosensor 0.1ufcap subtraction transmitted	mac01	loop5		0.100 0.100	500 50000	
699	1988/oct04/quad4	xas	monosensor 0.1ufcap subtraction transmitted	mac01	loop5		0.100 0.100	500 50000	
701	1988/oct10	solar	solarcell monosensor 0.1ufcap	eye1	ring27		.050 .050	1000 30000	
703	1988/oct11	solar9	solarcell monosensor 0.1ufcap	x1	ring28		.050 .050	1000 35000	
705	1988/oct12/solar1a	4p8243	monosensor solarcell 0.1ufcap	x1	ring28		.019 .020	1000 35000	
707	1988/oct12/solar2a	2r0031	monosensor solarcell 0.1ufcap	x1	ring28		.019 .020	1000 35000	crack
709	1988/oct12/solar3a	4P8668	solarcell monosensor 0.1ufcap	x1	ring28		.019 .020	1000 35000	crack
711	1988/oct12/solar4a	5e4535	monosensor 0.1ufcap solarcell	x1	ring28		.019 .020	1000 35000	crack
713	1988/oct12/solar6a	solar6	monosensor 0.1ufcap solarcell	x1	ring28		.019 .020	1000 35000	crack
715	1988/oct13/solar7a	2r1513	monosensor 0.1ufcap solarcell	x1	ring28		.019 .020	1000 35000	crack
717	1988/oct13/solar8a	3q3944	monosensor 0.1ufcap solarcell	HW7	ring7		.019 .020	1000 25000	crack
719	1988/oct14/jctom	idunno	monosensor 0.1ufcap	HW7	ring7		.019 .020	1000 50000	
721	1988/oct14/solar9a	4r2028	monosensor 0.1ufcap solarcell	HW7	ring7		.019 .020	1000 25000	crack

Page	Directory	Sample	Features	Sensor	Source	Q	Res.	Range	Test
723	1988/oct17/solarJ2	3Q3944	monosensor 0.1ufcap solarcell	HW7	ring8		.019 .020	1000 50000	crack
725	1988/oct17/solarJ3	4r3563	monosensor 0.1ufcap solarcell	HW7	ring8		.019 .020	1000 50000	crack
727	1988/oct17/solarJ4	5h4535	monosensor 0.1ufcap solarcell	HW7	ring8		.019 .020	1000 50000	crack
729	1988/oct17/solarJT	4r2028	monosensor 0.1ufcap solarcell	HW7	ring8		.019 .020	1000 50000	crack
731	1988/oct18/solarJ5	4p8668	monosensor 0.1ufcap solarcell	HW7	ring8		.019 .020	1000 50000	crack
733	1988/oct18/solarS1	2p8645	monosensor 0.1ufcap solarcell	HW7	ring7		.019 .020	1000 50000	crack
735	1988/oct19/solarS2	4r2028	monosensor 0.1ufcap solarcell	HW7	ring7		.019 .020	1000 50000	crack
737	1988/oct19/solarS3	4p8243	monosensor 0.1ufcap solarcell	HW7	ring7		.019 .020	1000 50000	crack
739	1988/oct20/solarS4	2r1514	monosensor 0.1ufcap solarcell	HW7	ring8		.019 .020	1000 50000	crack
741	1988/oct20/solarS5	2r0031	monosensor 0.1ufcap solarcell	HW7	ring8		.019 .020	1000 50000	crack
743	1988/oct24/solarS6	2p6262	monosensor 0.1ufcap solarcell	HW7	ring8		.019 .020	1000 50000	crack
745	1988/oct25/solarI0	2r1514	monosensor 0.1ufcap solarcell	d1	rings1		.019 .020	1000 20000	crack
747	1988/oct25/solarS8	4r2028	monosensor 0.1ufcap solarcell	d1	rings1		.019 .020	1000 20000	crack
749	1988/oct25/solarS9	4r3563	monosensor 0.1ufcap solarcell	d1	rings1		.019 .020	1000 20000	crack
751	1988/oct26/solarI1	4p8268	monosensor 0.1ufcap solarcell	d1	rings1		.019 .020	1000 20000	crack
753	1988/oct26/solarI2	3q3934	monosensor 0.1ufcap solarcell	d1	rings1		.019 .020	1000 20000	crack
755	1988/oct26/solarI3	4p8243	monosensor 0.1ufcap solarcell	d1	rings1		.019 .020	1000 20000	crack
757	1988/oct27/dlams	zas	monosensor 0.1ufcap tows	d1	rings1		0.100 0.100	1000 20000	flaw
759	1988/oct27/dlamb	zas	monosensor 0.1ufcap	d1	rings1		.050 .050	1000 20000	flaw
761	1988/oct27/solarI4	2p6262	monosensor 0.1ufcap solarcell	d1	rings1		.019 .020	1000 20000	crack
763	1988/oct28/delamC	zas	monosensor 0.1ufcap	d1	rings1		0.100 0.100	1000 20000	flaw
765	1988/oct28/delamD	zas	monosensor 0.1ufcap	d1	rings1		.049 .049	1000 20000	flaw
767	1988/oct28/micro	3q3944	monosensor 0.1ufcap solarcell	micro1	micro2		.019 .020	1000 50000	crack
769	1988/oct31/micr3	4r2028	monosensor 0.1ufcap	micro1	micro2		.019 .020	1000 50000	crack
771	1988/oct31/micro1	2r1514	monosensor 0.1ufcap solarcell	micro1	micro2		.019 .020	1000 50000	crack
773	1988/oct31/micro2	4r3563	monosensor 0.1ufcap solarcell	micro1	micro2		.019 .020	1000 50000	crack
775	1988/nov01/blenz	2p8645	monosensor 0.1ufcap solarcell	micro1	micro2		.019 .020	26464 26464	crack
777	1988/nov01/blenz1	4r2028	monosensor 0.1ufcap solarcell	micro1	micro2		.019 .020	26464 26464	crack
779	1988/nov01/micr4	4p8243	monosensor 0.1ufcap solarcell	micro1	micro2		.019 .020	1000 50000	crack
781	1988/nov01/micr5	5h4535	monosensor 0.1ufcap solarcell	micro1	micro2		.019 .020	1000 50000	crack
783	1988/nov01/micr6	2p8645	monosensor 0.1ufcap solarcell	micro1	micro2		.019 .020	1000 50000	crack
785	1988/nov02/blenz2	4p8668	monosensor 0.1ufcap solarcell	micro1	micro2		.019 .020	26464 26464	crack

Page	Directory	Sample	Features	Sensor	Source	Q	Res.	Range	Test
787	1988/nov03/blenz5	5b4535	monosensor 0.1ufcap solarcell	micro1	micro2		.019 .020	26464 26464	crack
789	1988/nov03/blenz5	5b4535	monosensor 0.1ufcap solarcell	micro1	micro2		.019 .020	26464 26464	crack
791	1988/nov03/micr4	2p6262	monosensor 0.1ufcap solarcell	micro1	micro2		.019 .020	26464 26464	crack
793	1988/nov04/hfq10	4p8243	monosensor 0.1ufcap solarcell	micro1	micro2		.019 .020	1000 1000	crack
795	1988/nov04/hfq60	4p8243	monosensor 0.1ufcap solarcell	micro1	micro2		.019 .020	6000 6000	crack
797	1988/nov04/hfq70	4p8243	monosensor 0.1ufcap solarcell	micro1	micro2		.019 .020	7000 7000	crack
799	1988/nov04/hfq80	4p8243	monosensor 0.1ufcap solarcell	micro1	micro2		.019 .020	8000 8000	crack
801	1988/nov09/hfq01	4p8243	monosensor 0.1ufcap solarcell	micros	ring28		.019 .020	19464 19464	crack
803	1988/nov11/hfq02	4r3563	monosensor 0.1ufcap solarcell	micros	ring28		.019 .020	1000 45000	crack
805	1988/nov14/cent2	4r2028	monosensor 0.1ufcap solarcell	micros	ring3		.019 .020	1000 50000	crack
807	1988/nov14/centr	4r2028	monosensor 0.1ufcap solarcell	micros	HW3		.019 .020	1000 50000	crack
809	1988/nov17/back1	4r2028	monosensor 0.1ufcap solarcell	micros	ring28		.019 .020	9000 9000	crack
811	1988/nov17/back2	4p8243	monosensor 0.1ufcap solarcell	micros	ring3		.019 .020	24464 24464	crack
813	1988/nov17/grnd1	4p8243	monosensor 0.1ufcap solarcell	micros	ring3		.019 .020	5000 50000	crack
815	1988/nov17/grnd2	4p8243	monosensor 0.1ufcap solarcell	micros	ring3		.019 .020	5000 50000	crack
817	1988/nov21/ald1b	ald1	monosensor 0.1ufcap	micros	ring3		.050 .050	1000 50000	flaw
819	1988/nov22/ald1	ald1	monosensor 0.1ufcap	HW19	ring24		.050 .050	1000 50000	flaw
821	1988/nov22/ald1d	ald1	monosensor 0.1ufcap	HW19	ring24		.050 .050	1000 50000	flaw
823	1988/nov23/cc_301b	C302	monosensor 0.1ufcap	HW14	ring3		0.100 0.100	1000 50000	flaw
825	1988/nov23/cc_302a	C302	monosensor 0.1ufcap	HW14	ring3		0.100 0.100	1000 50000	flaw
827	1988/nov28/dlama	zas	monosensor 0.1ufcap tows	micros	loop5		.050 .050	1000 50000	flaw
829	1988/nov28/dlamb	zas	monosensor 0.1ufcap tows	micros	loop5		.050 .050	1000 50000	flaw
831	1988/nov30/tnpb1	B	monosensor 0.1ufcap	mac01	whip		.019 .020	1000 28000	flaw
833	1988/dec02/tnpb2	B	monosensor 0.1ufcap	HW14	whip		.019 .020	1000 45000	flaw
835	1988/dec02/tnpb3	B	monosensor 0.1ufcap	HW14	whip		.019 .020	1000 45000	flaw
837	1988/dec07/tnpb4	B	monosensor 0.1ufcap	HW14	loop5		.019 .020	1000 50000	flaw
839	1988/dec07/tnpb5	B	monosensor 0.1ufcap	HW14	loop5		.019 .020	1000 50000	flaw
841	1988/dec08/tnpb6	B	monosensor 0.1ufcap	HW14	loop5		.019 .020	1000 50000	flaw
843	1988/dec09/tnpb7	B	monosensor 0.1ufcap	HW20	ring25		.019 .020	5000 50000	flaw
845	1988/dec12/tnpb8	B	monosensor 0.1ufcap	HW21	ring25		.019 .020	5000 50000	flaw
847	1988/dec12/tnpb9	B	monosensor 0.1ufcap	HW21	ring25		.050 .050	5000 50000	flaw
849	1988/dec13/tnpb3a	3	monosensor 0.1ufcap	mac01	whip		.050 .050	1000 25000	flaw
851	1988/dec13/tnpb3b	3	monosensor 0.1ufcap	mac01	whip		.050 .050	1000 25000	flaw
853	1988/dec13/tnpb10	B	monosensor 0.1ufcap	HW3	whip		.019 .020	5000 50000	flaw

Page	Directory	Sample	Features	Sensor	Source	Q	Res.	Range	Test
855	1988/dec13/apb11	B	monosensor 0.1ufcap	HW3	whip		.050 .050	5000 50000	flaw
857	1988/dec15/sts01	stainless	monosensor 0.1ufcap transmitted metal	mac01	ring1		.050 .050	5000 50000	anisotropy
859	1988/dec16/cop01	copper	monosensor 0.1ufcap transmitted metal	mac01	ring1		.050 .050	100 4000	anisotropy
861	1988/dec16/sts02	stainless	monosensor 0.1ufcap transmitted metal	mac01	ring1		.050 .050	100 4000	anisotropy
863	1988/dec19/alum1	alum	monosensor 0.1ufcap transmitted metal	mac01	ring1		.050 .050	100 4000	anisotropy
865	1988/dec19/lead1	lead	monosensor 0.1ufcap transmitted metal	mac01	ring1		.050 .050	100 4000	anisotropy
867	1989/jan11	foil	metal transmitted monosensor 0.1ufcap	mac01	ring1		.050 .050	100 4000	anisotropy
869	1989/jan12	foil	metal monosensor 0.1ufcap transmitted	mac01	ring1	good	.050 .050	5000 50000	anisotropy

5 b. Sample 1 Data

Laboratory data considered in Chapter III was taken from *Sample 1*, a satin weave sample with twelve flat-bottom drilled holes of two different diameters and six different depths. A complete discussion of the modeling and inversion of these data appears in Chapter III. Here, images from the *Tons-o-Data* booklet are presented before any rotating or scaling, as outlined above, is done to the data.

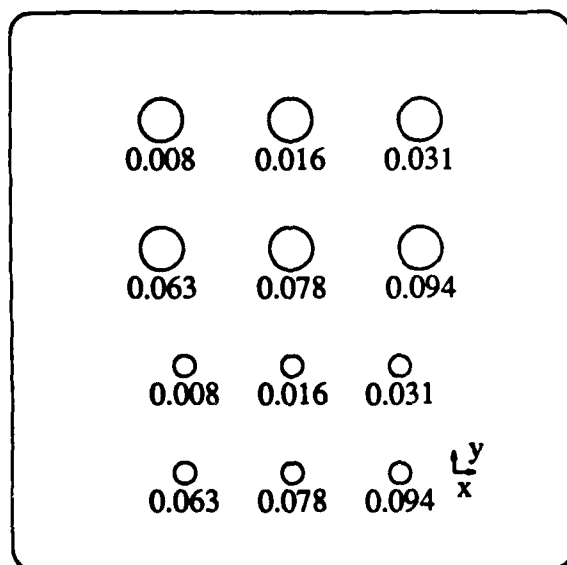


Figure V-5. Drawing of *Sample 1*, satin weave graphite epoxy panel with twelve flat-bottom holes of two diameters: 0.5" and 0.25". Depths of the holes are as indicated.

The layout of *Sample 1* appears in Figure V-5. Depths of the holes are shown in inches. The overall size of the sample is 6" by 6". The larger holes are 0.5" diameter; the smaller holes are 0.25" diameter. All holes in this sample are flat-bottom machined. Pages from data profiles are presented in Figure V-6.

5 c. Sample 3 Data

Sample 3 is a satin weave sample of graphite with one 0.25" diameter flaw in the center. Thus, it is a convenient comparison with model calculations: it is easy to describe the flaw to the model, and relatively easy to interpret the results since they are known to come from a single flaw rather than a number of flaws. Some tests were done with *Sample 1*, both right-side-up and up-side-down. The topside images are presented here because they represent a convenient measurement to be considered for model calculations.

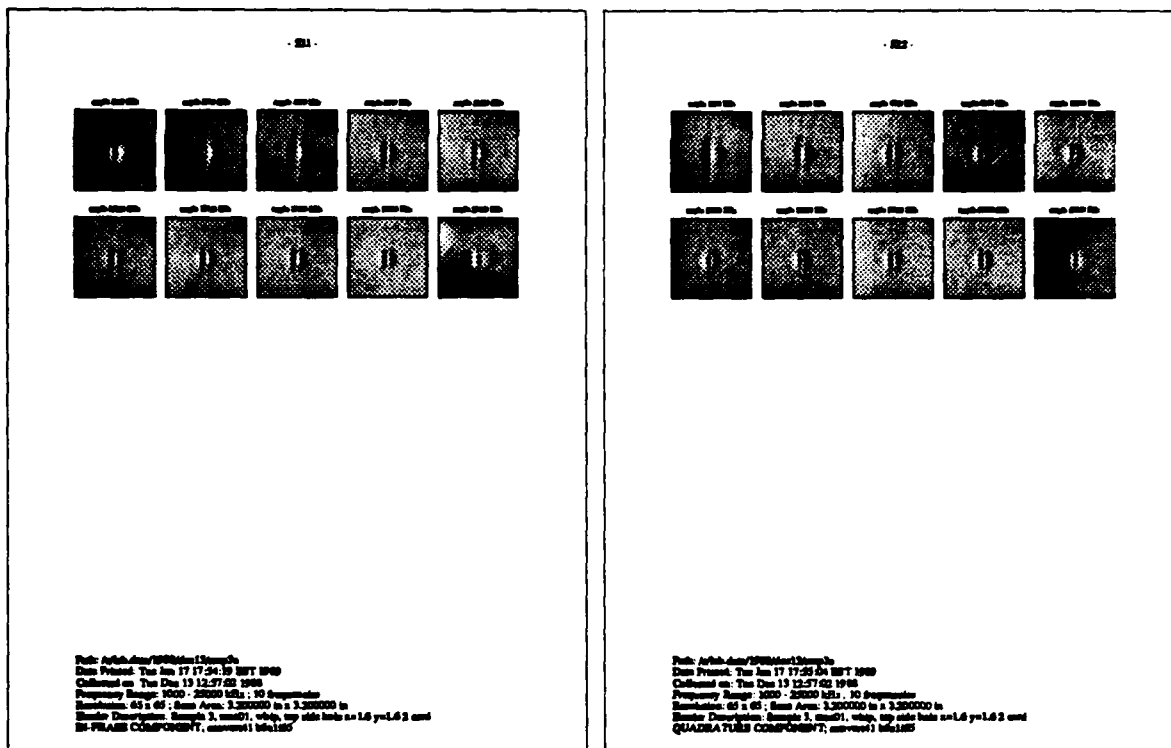


Figure V-7. Data from *Sample 3*, a satin weave with a single flat-bottom machined hole in the center. These data are convenient for reconstruction because of the relative simplicity of the flaw geometry. The actual flaw is approximately 0.1" deep and 0.25" in diameter. Data here are "raw" laboratory data, without normalization and phase angle rotation.

[W1] H. P. Westman, Editor, "Reference Data for Radio Engineers", Fourth Edition, International Telephone and Telegraph Corporation, 1956.